Distribution Agreement

In presenting this thesis or dissertation as a partial fulfillment of the requirements for an advanced degree from Emory University, I hereby grant to Emory University and its agents the non-exclusive license to archive, make accessible, and display my thesis or dissertation in whole or in part in all forms of media, now or hereafter known, including display on the world wide web. I understand that I may select some access restrictions as part of the online submission of this thesis or dissertation. I retain all ownership rights to the copyright of the thesis or dissertation. I also retain the right to use in future works (such as articles or books) all or part of this thesis or dissertation.

Signature:

_____ _____

Salma Ferdous Date

The role of *Lsd1* in the development of the retina and retinoblastoma

By

Salma Ferdous
Doctor of Philosophy

Graduate Division of Biological and Biomedical Science
Genetics and Molecular Biology

John M. Nickerson
Advisor

Jeffrey H. Boatright
Committee Member

Jeremy M. Boss
Committee Member

Andrew Escayg
Committee Member

Hans E. Grossniklaus
Committee Member

Accepted:

Lisa A. Tedesco, Ph.D.
Dean of the James T. Laney School of Graduate Studies

Date

The role of *Lsd1* in the development of the retina and retinoblastoma

By

Salma Ferdous
B.S. The University of Texas at Austin, 2010

Advisor: John M. Nickerson, PhD

An abstract of
A dissertation submitted to the Faculty of the James T. Laney School of Graduate Studies of
Emory University
in partial fulfillment of the requirements for the degree of
Doctor of Philosophy in
Graduate Division of Biological and Biomedical Science
Genetics and Molecular Biology
2021

Abstract

The role of *Lsd1* in the development of the retina and retinoblastoma
By Salma Ferdous

The increasing importance of epigenetics on neuronal developmental and diseases, also known as “neuroepigenetics” is becoming widely recognized. Neurological abnormalities are frequently associated with many Mendelian disorders related to the epigenetic machinery, indicating that neurons may be uniquely sensitive to epigenetic dysregulation. Lysine specific demethylase 1 (*Lsd1*), also known as Kdm1A, was the first histone demethylase to be discovered. Through interactions with other proteins, *Lsd1* is able to demethylate H3K4, H3K9, and H4K20 as well as other non-histone proteins, such as p53. *Lsd1* is known to be important in neuronal development, particularly due to a neuron-specific isoform, neuro *Lsd1* (n*Lsd1*). *Lsd1* overexpression is observed in many different cancers and the development of *Lsd1* inhibitors has become a promising new research area. Although *Lsd1* has been extensively studied in brain development and disease, there is relatively little known about its role in the visual system, particularly in the retina. The purpose of this study was to increase our understanding of the role of *Lsd1* in retinal development and determine whether *Lsd1* may be a viable therapeutic target in retinoblastoma, a pediatric ocular cancer. Using transgenic mouse models and human retinoblastoma samples, we determined the normal expression of *Lsd1* during and after murine retina development. We found that *Lsd1* is expressed in all retinal progenitor cells (RPCs) and has peak expression at post-natal 7 (P7). Afterwards, expression decreases until reaching a maintenance basement level at post-natal day 36 (P36). *Lsd1* has variable expression in the adult mouse retina in different mature retinal neuronal types. Based on these results, we explored how the deletion of *Lsd1* would affect proper retinal development in transgenic mice. Although heterozygous *Lsd1* mice do not show any visual abnormalities, homozygous deletion of *Lsd1* in RPCs results in severe retinal degeneration, causing significant decreases in visual function and defects in retinal morphology. Lastly, we investigated the expression pattern of *Lsd1* in human and mouse retinoblastoma samples and found that *Lsd1* is overexpressed in highly differentiated and proliferating tumor cells. Therefore, *Lsd1* may be a potential molecular target for the development of new therapeutic options in retinoblastoma.

The role of *Lsd1* in the development of the retina and retinoblastoma

By

Salma Ferdous
B.S. The University of Texas at Austin, 2010

Advisor: John M. Nickerson, PhD

A dissertation submitted to the Faculty of the James T. Laney School of Graduate Studies of Emory University
in partial fulfillment of the requirements for the degree of
Doctor of Philosophy in
Graduate Division of Biological and Biomedical Science
Genetics and Molecular Biology
2021

Acknowledgments

I would like to thank my parents for all of their sacrifice, love, and support throughout the years. I want to thank all of the personnel, past and present, in the Nickerson Lab and in the Department of Ophthalmology who have helped me grow as a scientist. Finally, I want to thank all of the wonderful friends that I made in GMB, Emory, and Atlanta who have supported me throughout this journey and helped me grow as a person.

Dissertation Table of Contents

Table of Figures

Table of Supplemental Figures

Table of Supplemental Tables

Chapter I: Introduction

Chapter I: Introduction

The purpose of this dissertation is to explore the role of *Lsd1* both in retinal development (Aim 1) and as a potential therapeutic target in retinoblastoma, a pediatric ocular cancer (Aim 2).

Premise for Aim 1: The role of Lsd1 in normal retinal development

Previous work has shown that, in general, histone methylation patterns are quite dynamic during retinogenesis and retinal progenitor cell differentiation[1,2]. Additionally, researchers such as *Popova et al*. have shown that inhibition of *Lsd1* in retinal explants impairs the proper differentiation of rod photoreceptors[3]. Therefore, we hypothesize that *Lsd1* will be dynamically expressed during and after retinal development and that different mature retinal neuronal subtypes will express *Lsd1* at different levels, indicating that *Lsd1* may play unique roles in the differentiation of these different neuronal subtypes. We also hypothesize that the inhibition of *Lsd1* during critical stages of retinal development will impair proper proliferation or differentiation of retinal progenitor cells, resulting in either retinal degeneration or an improper distribution of different neuronal populations.

Premise for Aim 2: Lsd1 is a potential therapeutic target in retinoblastoma

The retinoblastoma susceptibility gene (*Rb1*) was the first human tumor suppressor gene identified[4,5]. *Rb1* suppresses transcription through the binding of chromatin remodeling and histone deacetylase proteins and plays an important role in restricting cellular division[6]. Mutations in *Rb1* can cause cone precursors to undergo a cancerous transformation[7,8], leading to retinoblastoma, a pediatric ocular cancer. Epigenetics have been found to be important in both Mendelian and complex ocular diseases[9] including retinoblastoma[10–13], and tumors related to

retinoblastoma, such as neuroblastoma and medulloblastoma[14,15], have been shown to be sensitive to *Lsd1* inhibitors[16–21]. Therefore, we hypothesize that *Lsd1* may be overexpressed in retinoblastoma tumors, making *Lsd1* inhibitors a potential novel therapeutic treatment[22].

Outline of the Dissertation

This dissertation is separated into 7 distinct chapters. This introduction serves as the first chapter. The second chapter is a review covering the importance of epigenetic modifications, especially histone demethylases such as *Lsd1*, in the development of neuronal tissues such as the brain and eye. The third chapter is a primary scientific article, published in the journal Investigative Ophthalmology and Visual Sciences (IOVS), that investigates the expression levels and localization of *Lsd1* and its substrates H3K4me1 and H3K3me2 during and after retinal development. The fourth chapter investigates whether the genetic deletion of *Lsd1*, either in a whole-body heterozygous manner or a retina-specific homozygous manner, will have any negative effects on visual function or morphology. These first few chapters collectively are linked in Aim 1 of this dissertation. The fifth chapter is linked to Aim 2 of this dissertation and investigates whether or not *Lsd1* is a possible therapeutic target in retinoblastoma and whether *Lsd1* inhibitors could be a possible treatment option. The sixth chapter is a primary scientific article that is currently under review at the journal IOVS and is unrelated to *Lsd1*. This chapter investigates how natural aging gradually affects visual function and retinal morphology. Finally, the seventh chapter is an overall summary and discussion of the entire dissertation.

References

1 Raoss RC, Tchedre KT, Malik MTA, Coleman N, Fang Y, Marquez VE, et al. Dynamic patterns of histone lysine methylation in the Developing Retina. Investig Ophthalmol Vis Sci 2010;51:6784–92. PMCID:20671280.

2 Aldiri I, Xu B, Wang L, Chen X, Hiler D, Griffiths L, et al. The Dynamic Epigenetic Landscape of the Retina During Development, Reprogramming, and Tumorigenesis. Neuron 2017;94:550-568.e10.

3 Popova EY, Pinzon-Guzman C, Salzberg AC, Zhang SS-M, Barnstable CJ. LSD1-Mediated Demethylation of H3K4me2 Is Required for the Transition from Late Progenitor to Differentiated Mouse Rod Photoreceptor. Mol Neurobiol 2016;53:4563–81. PMCID:26298666.

4 Friend SH, Bernards R, Rogelj S, Weinberg RA, Rapaport JM, Albert DM, et al. A human DNA segment with properties of the gene that predisposes to retinoblastoma and osteosarcoma. Nature 1986;323:643–6. PMCID:2877398.

5 Bookstein R, Lee EYHP, To H, Young LJ, Sery TW, Hayes RC, et al. Human retinoblastoma susceptibility gene: Genomic organization and analysis of heterozygous intragenic deletion mutants. Proc Natl Acad Sci U S A 1988;85:2210–4.

6 Mendoza PR, Grossniklaus HE. The Biology of Retinoblastoma. Prog Mol Biol Transl Sci. 2015;134:503-16. doi: 10.1016/bs.pmbts.2015.06.012. Epub 2015 Jul 14. PMID: 26310174

7 Bremner R, Sage J. Cancer: The origin of human retinoblastoma. Nature. 2014 Oct 16;514(7522):312-3. doi: 10.1038/nature13748. Epub 2014 Sep 24. PMID: 25252972; PMCID: PMC5438154

.

8 Xu XL, Singh HP, Wang L, Qi D-L, Poulos BK, Abramson DH, et al. Rb suppresses human cone precursor-derived retinoblastoma tumors. Nature 2014;514:385–8. PMCID:25252974.

9 Oliver VF, van Bysterveldt KA, Merbs SL. Epigenetics in Ocular Medicine. Med Epigenetics 2016:391–412.

10 Poulaki V, Mitsiades CS, Kotoula V, Negri J, McMullan C, Miller JW, et al. Molecular sequelae of histone deacetylase inhibition in human retinoblastoma cell lines: Clinical implications. Investig Ophthalmol Vis Sci 2009;50:4072–9. PMCID:19387079.

11 Zhang Y, Wu D, Xia F, Xian H, Zhu X, Cui H, et al. Downregulation of HDAC9 inhibits cell proliferation and tumor formation by inducing cell cycle arrest in retinoblastoma. Biochem Biophys Res Commun 2016;473:600–6.

12 Jin Q, He W, Chen L, Yang Y, Shi K, You Z. MicroRNA 1013p inhibits proliferation in retinoblastoma cells by targeting EZH2 and HDAC9. Exp Ther Med 2018;16:1663–70.

13 Yu N, Chen P, Wang Q, Liang M, Qiu J, Zhou P, et al. Histone deacetylase inhibitors differentially regulate c-Myc expression in retinoblastoma cells. Oncol Lett 2020;19:460–8.

14 Kohe SE, Bennett CD, Gill SK, Wilson M, McConville C, Peet AC. Metabolic profiling of the three neural derived embryonal pediatric tumors retinoblastoma, neuroblastoma and medulloblastoma, identifies distinct metabolic profiles. Oncotarget 2018;9:11336–51.

15 Capper D, Jones DTW, Sill M, Hovestadt V, Schrimpf D, Sturm D, et al. DNA methylation-based classification of central nervous system tumours. Nature. 2018 Mar 22;555(7697):469-474. doi: 10.1038/nature26000. Epub 2018 Mar 14. PMID: 29539639;

PMCID: PMC6093218.

16 Schulte JH, Lim S, Schramm A, Friedrichs N, Koster J, Versteeg R, et al. Lysine-specific demethylase 1 is strongly expressed in poorly differentiated neuroblastoma: Implications for therapy. Cancer Res 2009;69:2065–71. PMCID:19223552.

17 Althoff K, Beckers A, Odersky A, Mestdagh P, Köster J, Bray IM, et al. MiR-137 functions as a tumor suppressor in neuroblastoma by downregulating KDM1A. Int J Cancer 2013;133:1064–73.

18 Ambrosio S, Saccà CD, Amente S, Paladino S, Lania L, Majello B. Lysine-specific demethylase LSD1 regulates autophagy in neuroblastoma through SESN2-dependent pathway. Oncogene 2017;36:6701–11.

19 Pajtler KW, Weingarten C, Thor T, Künkele A, Heukamp LC, Büttner R, et al. The KDM1A histone demethylase is a promising new target for the epigenetic therapy of medulloblastoma. Acta Neuropathol Commun 2014;2:1–13.

20 Callegari K, Maegawa S, Bravo-Alegria J, Gopalakrishnan V. Pharmacological inhibition of LSD1 activity blocks REST-dependent medulloblastoma cell migration. Cell Commun Signal 2018;16:1–13.

21 Lee C, Rudneva VA, Erkek S, Zapatka M, Chau LQ, Tacheva-Grigorova SK, et al. Lsd1 as a therapeutic target in Gfi1-activated medulloblastoma. Nat Commun 2019;10:332.

22 Mendoza PR, Grossniklaus HE. Therapeutic Options for Retinoblastoma. Cancer Control 2016;23:99–109. PMCID:25661903.

Chapter II: The contribution of histone demethylases, specifically Lsd1, in the development of two neuronal tissues, the brain and the eye

Abstract

The purpose of this review is to provide an overview of the contribution of histone demethylases, specifically *Lsd1*, in the development of two neuronal tissues, the brain and the eye. Since Waddington's seminar discovery that environmental changes could lead to heritable changes in an organism without actual manipulation of the organism's genome, researchers have uncovered the vast influence of epigenetic modifications on both proper cellular development and disease progression. In particular histone methylation patterns have been shown to be dynamic and influenced by both histone methyltransferases and demethylases. Lysine specific demethylase 1 (*Lsd1*) is able to demethylate mono- and di- methyl groups on H3K4, H3K9, and H4K20 as well as demethylate non-histone proteins. Although it is ubiquitously expressed throughout the body, *Lsd1* has been shown to have an acutely important role in the development of neurons, particularly due to a neuron specific isoform, neuro*Lsd1* (n*Lsd1*). The brain has served as the primary neuronal tissue where this neuron specific role of *Lsd1* has been studied. There are numerous devastating consequences of *Lsd1* deletion or dysregulation in both brain development and diseases. Although the eye is an extension of the brain, much less is known about the role of *Lsd1* in the proper development of the retina and its possible role in both complex and Mendelian ocular disorders. Given the important role of epigenetics in both of these areas, it is paramount for future research to study *Lsd1* in an eye specific context in order to further both our basic science understanding of its role as well as determining whether it may be a viable therapeutic target for ocular disease.

General epigenetics

Conrad Waddington's seminal paper "The genetic assimilation of the bithorax phenotype" provided the scientific community with the first experimental evidence that environmental changes could produce heritable changes in an organism without actual manipulation of the organism's genome[1]. From this groundbreaking research, the field of epigenetics was born[2]. Now, 65 years after Waddington's original experiments, researchers are still uncovering the vast influence of epigenetic modifications on both normal development and disease progression through the regulation and dysregulation of transcription, cellular replication, and chromatin organization within cells. Epigenetic modifications can be broadly grouped in DNA methylation and histone modifications. The N-terminal "tails" of histone proteins can be post-transcriptionally modified via chemical additions of methyl, acetyl, or phosphate groups, just to name a few (Figure 2.1). These modifications can alter chromatin organization and allow for or prevent the recognition and binding of other proteins, namely transcription factors, leading to transcriptional regulation.

Histone methylation

In particular, the addition of methyl groups to the fourth lysine position on H3 histone proteins (H3K4) is associated with transcriptional activation. On a single lysine, up to three methyl groups can be added, and although mono-, di-, and tri-methylation result in active transcription, they are generally located on different genomic areas. Mono-methylation is normally found at active and primed enhancer elements, whereas di-methylation is found at gene promoters, and tri-methylation is found at gene promoters and poised genes[3–5].

The first histone lysine methyltransferase was discovered in 2000[6]. Since then, a total of six proteins that act as histone methyltransferases on H3K4, KMT2A – KMT2F, have been found in mammals. Four short years later, a histone demethylase (*Kdm1A*, also known as *Lsd1*) was discovered[7]. There are two major classes of histone demethylases for H3K4[8] including LSD1/LSD2, which act on mono- and di- methyl groups[7], and the JMJC domain proteins, including JARID1A-D, which act on tri-methyl groups[9].

Methylation patterns are dynamic, and their impact are far reaching. *Black et al.* wrote an excellent review on the establishment, regulation, and biological impact of histone lysine methylation[10]. Specifically, methylation patterns on H3K4 differ depending on cell type and sub-type[4]. Neurons are post-mitotic terminally differentiated cells that receive sensory input from the outside world and transform it into electrical signals that are relayed throughout the body. The central nervous system is comprised mainly of the brain and spinal cord. In the brain the regulation of H3K4 methylation patterns has been extensively studied for both development and disease and is reviewed by *Shen et al*[11]. The eye, specifically the neurosensory retina and optic nerve, are considered to be extensions of the brain due to their embryonic origins. In vertebrate embryonic development, the retina and optic nerve are outgrowths of the embryonic diencephalon[12]. The different cell types in the retina and brain allow for the processing and transmission of different types of information. In general, the influence of epigenetic regulation on neuronal developmental and diseases, also known as "neuroepigenetics" is being widely recognized and histone methylation in particular has been heavily studied[13]. There are over 40 Mendelian disorders related to the epigenetic machinery. Over 90% of these disorders are associated with neurological dysfunction, indicating that neurons may be uniquely sensitive to

epigenetic dysregulation[14,15].

Lysine specific demethylase 1 (Lsd1)

Prior to the discovery of Lysine specific demethylase 1 (*Lsd1*) in 2004, histone methylation was widely considered to be a permanent modification[7]. Through nucleosome binding, *Lsd1* can act upon mono- and di-methyl H3K4 and H3K9 modifications (Figure 2.2)[7,16]. *Lsd1* is unable to bind to tri-methylated modifications due to the requirement of a free lone pair of electrons for the flavin-dependent amine oxidation reaction to occur[17]. Within the nucleosome, *Lsd1* forms a complex with other epigenetic proteins, such as HDAC1[18], and its H3K4 demethylase activity is dependent on its association with CoREST[19]. In addition to acting upon H3K4 methyl groups, *Lsd1* is also able to demethylate H3K9[20] and H4K20[21] as well as other non-histone proteins[22]. *Lsd1* is deposited maternally into the zygote at fertilization and aids in epigenetic reprogramming[23]. It is also essential for global regulation of the transcriptome by maintaining the homeostasis of enhancers[24].

Neuronal specific isoform of Lsd1 (nLSD1)

Although *Lsd1* is expressed ubiquitously throughout the body, there are 4 isoforms in mammals. Apart from the canonical isoform, the other three isoforms feature the inclusion of one or both alternatively spliced micro-exons, E2a or E8a (Figure 2.3). The inclusion of E2a can occur in all tissues, however, the inclusion of E8a, a micro-exon encoding a tetrapeptide Asp-Thr-Val-Lys, is exclusive to neuronal tissues[25]. During perinatal brain development, this neuro-specific *Lsd1* (n*Lsd1*) is the predominate *Lsd1* isoform, but post development, it makes up roughly 30% - 40% of transcribed *Lsd1* in the brain[25,26]. n*Lsd1* can be phosphorylated at the Thr369 residue, which

transforms the enzyme into a dominant negative isoform that is unable to repress gene transcription, ultimately promoting neurite growth and branching[27]. Reductions in n*Lsd1* levels in the brain, both in n*Lsd1* homozygous knockout mice and n*Lsd1* heterozygous animals, cause an anxiety behavior that is likely due to the hypomethylation and hypoacetylation of stress-related genes[28]. n*Lsd1* also plays a role in spatial learning and long-term memory formation[26]. One of the most interesting aspects of n*Lsd1* is that the addition of the E8a micro-exon changes substrate specificity for this enzyme. n*Lsd1* knockdown increases H3K9 di-methylation, but not H3K4 di-methylation in SH-SY5Y human neuronal cells derived from neuroblastoma[20]. The H3K9 demethylation capability of n*Lsd1* is due to its association with a novel binding complex which includes the protein Supervilin[20]. In mouse primary cortical neurons, n*Lsd1* knockout had no significant impact on H3K4 or H3K9 methylation levels, but there was a significant increase in H4K20 methylation[21].

Consequences of Lsd1 deletion or dysregulation in both brain development and disease

As mentioned above, dysregulation or total ablation of *Lsd1* in the brain does have serious consequences. Mutations in *Lsd1* have been associated with a wide array of diseases and disorders, including neurodevelopmental diseases, psychiatric disorders, and addiction disorders[3]. *Lsd1* is in the top 2% of evolutionarily constrained genes, which are genes that are intolerant to functional variation[29]. Therefore, global homozygous deletion of *Lsd1* will result in embryonic lethality, whereas heterozygous deletion seems to have no profound consequences[30]. Human patients who have dominant missense mutations in *Lsd1* have been shown to have neurodevelopmental delays and craniofacial abnormalities[31]. These missense mutations result in decreased protein stability and enzymatic activity, ultimately causing the observed pathology[32].

A male patient with dual *de novo* mutations in *Lsd1* and ANKRD11 has also been shown to have features of both KBG and Kabuki syndromes[33].

In adult mice, tamoxifen-induced conditional deletion of *Lsd1* causes paralysis, degeneration of the hippocampus and cortex, and learning and memory defects[34]. siRNA knockout of *Lsd1* can reduce cell proliferation in wild-type mouse brains specifically in the hippocampal dentate gyri[35]. *Lsd1* is known to interact with TLX, which is a master regulator of neural stem cell proliferation and maintenance[36,37]. *Lsd1* is also ubiquitously expressed in the developing cortex and *Lsd1* inhibition affects pyramidal cortical neuron development[38]. In a tauopathy mouse, which can serve as a model for disorders such as Alzheimer's Disease, *Lsd1* is abnormally sequestered into the cytoplasm rather than being in the nucleus and further depletion of *Lsd1* caused an acceleration of the neurodegeneration[39].

In addition to *Lsd1* mutations causing neurological defects, *Lsd1* has also been shown to be aberrantly regulated in brain cancers, such as neuroblastoma. In poorly differentiated neuroblastoma tumor cells, *Lsd1* is overexpressed and inhibition of *Lsd1* via siRNAs, pharmacological drug inhibitors, or miR137 has been shown to decrease tumor cell growth and increase tumor cell death[40–42]. In medulloblastoma, *Lsd1* is overexpressed and medulloblastoma tumor cells, both *in vitro* and *in vivo*, decreased in size, proliferation, and viability after being treated with *Lsd1* inhibitors[43–45]. This role of *Lsd1* in different cancer types is partially due to its ability to regulate tumor suppressor genes, including p53[46,47]. Molecularly, the overexpression of *Lsd1* can lead to an overactive cell cycle by increasing the phosphorylation of the RB1 protein [48,49]. Due to the overexpression of *Lsd1* that is observed in many different cancers, *Lsd1* has been

extensively researched as a potential therapeutic target and numerous inhibitors are being developed[50–56].

Retinal development, structure, and function

In contrast to the brain, which mostly completes development during embryonic stages, the mouse retina continues developing after birth[57]. The vertebrate retina originates from the pseudostratified neuroepithelium, which consists of retina progenitor cells (RPCs)[12]. RPCs can differentiate into distinct classes of retinal neurons in a conserved, but overlapping, pattern due to the influence of numerous cell fate determinants[58,59]. Individual RPCs are very heterogenous in their individual transcriptome[60,61] and this allows for multipotency before they become specified and ultimately committed towards a particular cell fate[62]. Thus, the differentiation of the retina is both simultaneously dynamic and regimented[63].

The mature mouse retina is comprised of nine distinct layers and contains 7 major cells types[64]. There are 6 neuronal types including rod photoreceptors, cone photoreceptors, amacrine cells, bipolar cells, and horizontal cells, and 1 glial type, muller glial cells, that are organized in a laminar structure[65] (Figure 2.4). The posterior-most layer is the outer nuclear layer (ONL), which is comprised of the two different types of photoreceptors. Rods make up 97% of the photoreceptors in the mouse retina and are used for vision during dim light conditions. Meanwhile, cones comprise the remaining 3% of photoreceptors and are used for color vision[66]. These photoreceptors absorb light energy in the form of photons and convert it into electrical potential[67]. Adjacent to the ONL is the inner nuclear layer (INL), which contains the nuclei of three neuronal subtypes: amacrine, bipolar, horizontal cells as well as muller glial cells[68]. These

cells are second-order neurons that are responsible for the synthesis and transmission of the electrical potential from the photoreceptors to the third-order neurons in the retinal ganglion cell layer (RGCL)[67]. The RGCL contains two types of neurons, displaced amacrine cells and retinal ganglions cells. There are many subtypes of retinal ganglion cells[69,70] and these cells integrate a large amount of electrical signals before transmitting that information to the visual cortex in the brain via axons that project through the optic nerve head[67]. *Wassle and Boycott*[65] and *Seabrook et al.*[71] have excellent in-depth reviews on the structure and architecture of the mammalian and mouse retina respectively and *Hoon et al.*[67] reviews retinal circuity and function.

The role of Lsd1 in the visual system - current knowledge and unanswered questions

Although *Lsd1* has been extensively studied in brain neuronal development and many different cancers types, there is a severe dearth of knowledge on the role of *Lsd1* specifically within the visual system. To our knowledge, there are less than 10 manuscripts on the role of *Lsd1* in the eye or in ocular diseases. In *Drosophila*, inhibition of *Lsd1* increased *white* eye color pigment expression although this is likely more related to the role of *Lsd1* in heterochromatin formation rather than a true role in ocular biology[72]. In mouse retinas *Lsd1* expression begins at embryonic day 17.5 in the mouse retina and expression peaks at post-natal day 2 before decreasing in the adult retina[73]. Pharmacological inhibition of *Lsd1* with tranylcypromine (TCP) in mouse post-natal day 0 retinal explants resulted in large transcriptomic abnormalities and blocked the differentiation of retinal progenitor cells into rod photoreceptors[73]. Intravitreal injections of TCP also protected retinal ganglion cells from dying from oxidative stress or NMDA-induced excitotoxicity both *in vitro* and *in vivo*[74]. Lastly, in a diabetic retinopathy mouse model, *Lsd1* was found to be upregulated[75] and acts as a scaffold to a lncRNA HOTAIR that can regulate the

transcription of VE-cadherin and VEGFA in retinal endothelial cells[76]. Inhibition of *Lsd1* in the diabetic retinopathy model via siRNAs prevented retinal endothelial cell apoptosis, mitochondrial damage, and reactive oxygen species generation[77].

Overall, histone modifications, such as H3K4 methylation, and epigenetic proteins, such as the histone demethylase *Lsd1*, are critical for the proper development and functional health of neurons, both in the brain and the eye. In the brain, the canonical isoform of *Lsd1* and neuron specific isoform, n*Lsd1*, have been shown to regulate the transcriptome by demethylating several histone positions, such as H3K4, H3K9, and H4K20 as well as other non-histone proteins. In both human and animal models, dysregulation of the *Lsd1* isoform contribute to a number of disorders, including neurodevelopmental diseases, psychiatric disorders, and addiction disorders, and correction of this dysfunction is a critical avenue for their treatment development. Dysfunctional *Lsd1* has also been shown to play a critical role in the progression of cancers, including brain-specific cancers such as medulloblastoma and neuroblastoma. Although the eye is an extension of the brain, much less is known about the role of *Lsd1* in the normal development of the retina and its possible role in both complex and Mendelian ocular disorders. Given the important role of epigenetics in both of these areas, it is paramount for future research to study *Lsd1* in an eye specific context in order to further both our basic science understanding of its role as well as determining whether it may be a viable therapeutic target for ocular disease.

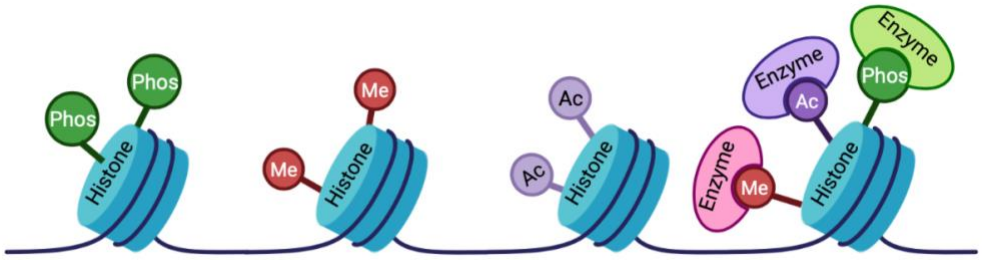

Figure 2.1: Schematic diagram of different general histone modifications, including phosphorylation, methylation, and acetylation (Created in Biorender).

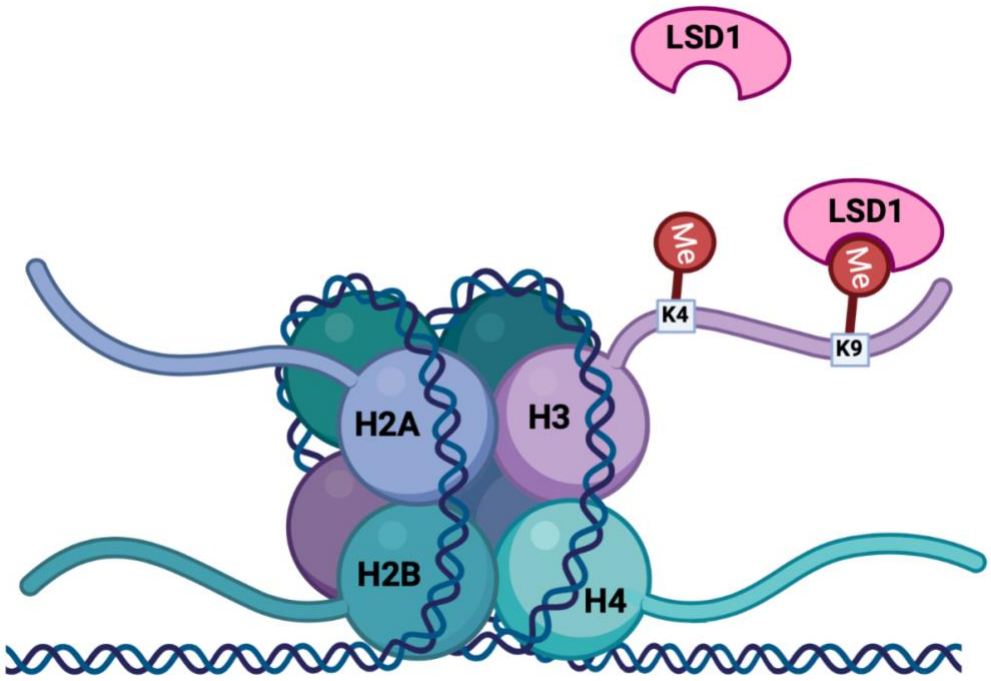

Figure 2.2: Schematic diagram of the ability for Lsd1 to bind to methyl groups on the lysine at position 4 and position 9 on the H3 histone protein. For simplicity, LSD1 is shown alone and bound to only one methyl group; however, in the nucleus, LSD1 forms complexes with other proteins and is able to demethylate both di- and mono-methyl modifications (Created in Biorender).

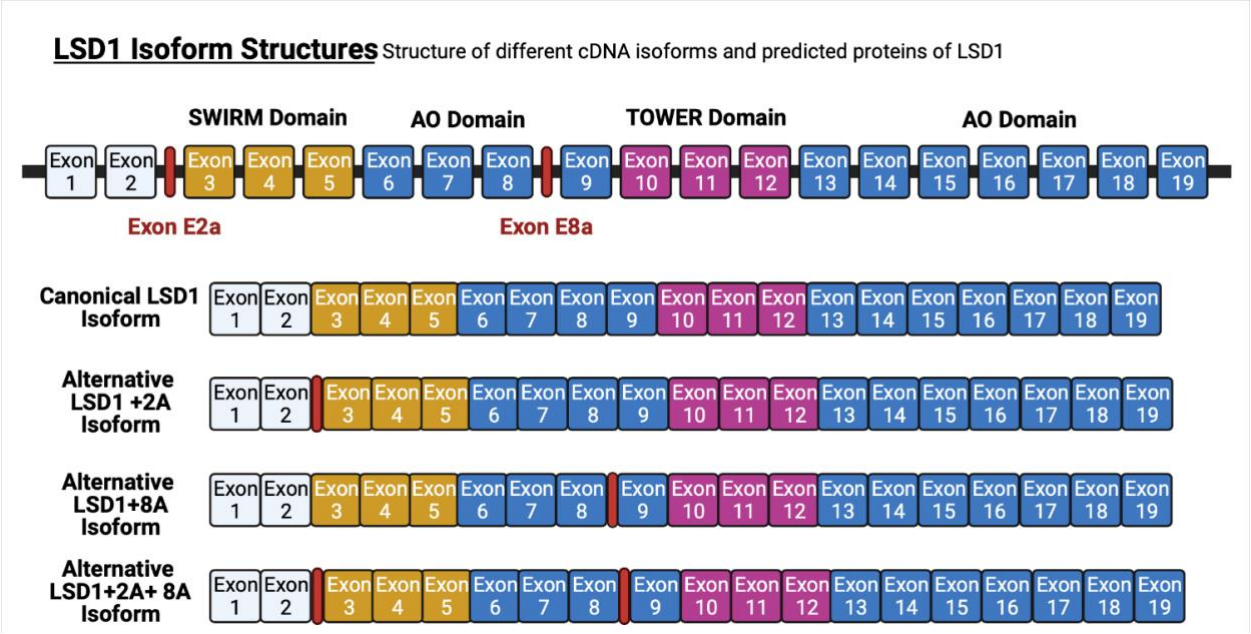

Figure 2.3: Schematic diagram of the structures of different cDNA isoforms and predicted proteins of LSD1 (Created in Biorender).

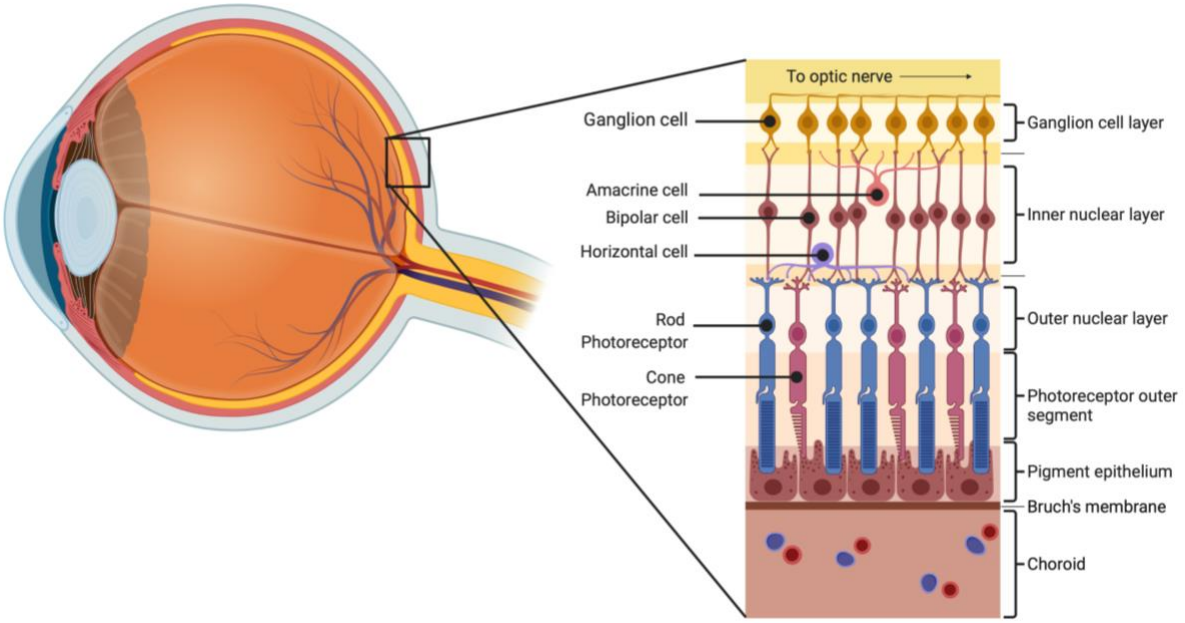

Figure 2.4: Schematic diagram of basic retinal anatomy, highlighting both specific cell types as well as the different cellular layers (Created in Biorender).

References

1 Waddington CH. The genetic assimilation of the bithorax phenotype. Evolution (N Y) 1956;10:1–13.

2 Noble D. Conrad Waddington and the origin of epigenetics. J Exp Biol 2015;218:816–8. PMCID:25788723.

3 Collins BE, Greer CB, Coleman BC, Sweatt JD. Histone H3 lysine K4 methylation and its role in learning and memory. Epigenetics and Chromatin 2019;12:1–16. PMCID:30616667.

4 Koch CM, Andrews RM, Flicek P, Dillon SC, Karaöz U, Clelland GK, et al. The landscape of histone modifications across 1% of the human genome in five human cell lines. Genome Res 2007;17:691–707. PMCID:17567990.

5 Soares LM, He PC, Chun Y, Suh H, Kim TS, Buratowski S. Determinants of Histone H3K4 Methylation Patterns. Mol Cell 2017;68:773-785.e6. PMCID:29129639.

6 Rea S, Eisenhaber F, O'Carroll D, Strahl BD, Sun ZW, Schmid M, et al. Regulation of chromatin structure by site-specific histone H3 methyltransferases. Nature 2000;406:593–9. PMCID:10949293.

7 Shi Y, Lan F, Matson C, Mulligan P, Whetstine JR, Cole PA, et al. Histone demethylation mediated by the nuclear amine oxidase homolog LSD1. Cell 2004;119:941–53. PMCID:15620353.

8 Shi YG, Tsukada Y. The discovery of histone demethylases. Cold Spring Harb Perspect Biol 2013;5:2–4. PMCID:24003214.

9 Seward DJ, Cubberley G, Kim S, Schonewald M, Zhang L, Tripet B, et al. Demethylation of trimethylated histone H3 Lys4 in vivo by JARID1 JmjC proteins. Nat

Struct Mol Biol 2007;14:240–2. PMCID:17310255.

10 Black J, Rechem C Van, Whetstine JR. Histone Lysine Methylation Dynamics: Establishment, Regulation, and Biological Impact. Mol Brain Res 2012;48:1–32. PMCID:1000000221.

11 Shen E, Shulha H, Weng Z, Akbarian S. Regulation of histone H3K4 methylation in brain development and disease. Philos Trans R Soc B Biol Sci 2014;369: PMCID:25135975.

12 Centanin L, Wittbrodt J. Retinal neurogenesis. Dev 2014;141:241–4.

13 Christopher MA, Kyle SM, Katz DJ. Neuroepigenetic mechanisms in disease. Epigenetics Chromatin 2017;10:47. PMCID:29037228.

14 Fahrner J, Bjornsson H. Mendelian Disorders of the Epigenetic Machinery: Tipping the Balance of Chromatin States. Annu Rev Genomics Hum Genet 2014;15:269–93. PMCID:24655651.

15 Bjornsson HT. The Mendelian disorders of the epigenetic machinery. Genome Res 2015;25:1473–81.

16 Dhall A, Shelton PMM, Delachat AMF, Leonen CJA, Fierz B, Chatterjee C. Nucleosome Binding by the Lysine Specific Demethylase 1 (LSD1) Enzyme Enables Histone H3 Demethylation. Biochemistry 2020;59:2479–83. PMCID:32567837.

17 Forneris F, Binda C, Dall'Aglio A, Fraaije MW, Battaglioli E, Mattevi A. A highly specific mechanism of histone H3-K4 recognition by histone demethylase LSD1. J Biol Chem 2006;281:35289–95. PMCID:16987819.

18 Song Y, Dagil L, Fairall L, Robertson N, Wu M, Ragan TJ, et al. Mechanism of Crosstalk between the LSD1 Demethylase and HDAC1 Deacetylase in the CoREST

Complex. Cell Rep 2020;30:2699-2711.e8. PMCID:32101746.

19 Lee MG, Wynder C, Cooch N, Shiekhattar R. An essential role for CoREST in nucleosomal histone 3 lysine 4 demethylation. Nature 2005;437:432–5. PMCID:16079794.

20 Laurent B, Ruitu L, Murn J, Hempel K, Ferrao R, Xiang Y, et al. A Specific LSD1/KDM1A Isoform Regulates Neuronal Differentiation through H3K9 Demethylation. Mol Cell 2015;57:957–70. PMCID:26928661.

21 Wang J, Telese F, Tan Y, Li W, Jin C, He X, et al. LSD1n is an H4K20 demethylase regulating memory formation via transcriptional elongation control. Nat Neurosci 2015;18:1256–64. PMCID:26214369.

22 Gu F, Lin Y, Wang Z, Wu X, Ye Z, Wang Y, et al. Biological roles of LSD1 beyond its demethylase activity. Cell Mol Life Sci 2020;77:3341–50. PMCID:32193608.

23 Wasson JA, Simon AK, Myrick DA, Wolf G, Driscoll S, Pfaff SL, et al. Maternally provided LSD1/KDM1A enables the maternal-to-zygotic transition and prevents defects that manifest postnatally. Elife 2016;5:1–25. PMCID:26814574.

24 Agarwal S, Bonefas KM, Garay PM, Brookes E, Murata-Nakamura Y, Porter RS, et al. LSD1/KDM1A Maintains Genome-wide Homeostasis of Transcriptional Enhancers. Genome Res 2021;31:1–12.

25 Zibetti C, Adamo A, Binda C, Forneris F, Toffolo E, Verpelli C, et al. Alternative splicing of the histone demethylase LSD1/KDM1 contributes to the modulation of neurite morphogenesis in the mammalian nervous system. J Neurosci 2010;30:2521–32. PMCID:20164337.

26 Rusconi F, Grillo B, Toffolo E, Mattevi A, Battaglioli E. NeuroLSD1: Splicing-

Generated Epigenetic Enhancer of Neuroplasticity. Trends Neurosci 2016;40:1–11. PMCID:27986293.

27 Toffolo E, Rusconi F, Paganini L, Tortorici M, Pilotto S, Heise C, et al. Phosphorylation of neuronal Lysine-Specific Demethylase 1LSD1/KDM1A impairs transcriptional repression by regulating interaction with CoREST and histone deacetylases HDAC1/2. J Neurochem 2014;128:603–16. PMCID:24111946.

28 Rusconi F, Grillo B, Ponzoni L, Bassani S, Toffolo E, Paganini L, et al. LSD1 modulates stress-evoked transcription of immediate early genes and emotional behavior. Proc Natl Acad Sci U S A 2016;113:1511974113-. PMCID:26976584.

29 Samocha KE, Robinson EB, Sanders SJ, Stevens C, Sabo A, McGrath LM, et al. A framework for the interpretation of de novo mutation in human disease. Nat Genet 2014;46:944–50.

30 Wang J, Scully K, Zhu X, Cai L, Zhang J, Prefontaine GG, et al. Opposing LSD1 complexes function in developmental gene activation and repression programs. Nature 2007;446:882–7. PMCID:17392792.

31 Chong JX, Yu J, Lorentzen P, Park KM, Jamal SM, Tabor HK, et al. Gene discovery for Mendelian conditions via social networking: de novo variants in KDM1A cause developmental delay and distinctive facial features. Genet Med 2016;18:788–95. PMCID:26656649.

32 Pilotto S, Speranzini V, Marabelli C, Rusconi F, Toffolo E, Grillo B, et al. LSD1/KDM1A mutations associated to a newly described form of intellectual disability impair demethylase activity and binding to transcription factors. Hum Mol Genet 2016;25:2578–87. PMCID:27094131.

33 Tunovic S, Barkovich J, Sherr EH, Slavotinek AM. De novo ANKRD11 and KDM1A gene mutations in a male with features of KBG syndrome and Kabuki syndrome. Am J Med Genet Part A 2014;164:1744–9. PMCID:24838796.

34 Christopher MA, Myrick DA, Barwick BG, Engstrom AK, Porter-Stransky KA, Boss JM, et al. LSD1 protects against hippocampal and cortical neurodegeneration. Nat Commun 2017;8:1–13. PMCID:28993646.

35 Sun G, Alzayady K, Stewart R, Ye P, Yang S, Li W, et al. Histone Demethylase LSD1 Regulates Neural Stem Cell Proliferation. Mol Cell Biol 2010;30:1997–2005. PMCID:20123967.

36 Yokoyama A, Takezawa S, Schule R, Kitagawa H, Kato S. Transrepressive Function of TLX Requires the Histone Demethylase LSD1. Mol Cell Biol 2008;28:3995–4003. PMCID:18391013.

37 Islam MM, Zhang C-L. TLX: A master regulator for neural stem cell maintenance and neurogenesis. Biochim Biophys Acta - Gene Regul Mech 2015;1849:210–6.

38 Fuentes P, Cánovas J, Berndt FA, Noctor SC, Kukuljan M. CoREST/LSD1 control the development of pyramidal cortical neurons. Cereb Cortex 2012;22:1431–41. PMCID:21878487.

39 Engstrom AK, Walker AC, Moudgal RA, Myrick DA, Kyle SM, Bai Y, et al. The inhibition of LSD1 via sequestration contributes to tau-mediated neurodegeneration. Proc Natl Acad Sci U S A 2020;117:29133–43. PMCID:33139560.

40 Schulte JH, Lim S, Schramm A, Friedrichs N, Koster J, Versteeg R, et al. Lysine-specific demethylase 1 is strongly expressed in poorly differentiated neuroblastoma: Implications for therapy. Cancer Res 2009;69:2065–71. PMCID:19223552.

41 Althoff K, Beckers A, Odersky A, Mestdagh P, Köster J, Bray IM, et al. MiR-137 functions as a tumor suppressor in neuroblastoma by downregulating KDM1A. Int J Cancer 2013;133:1064–73.

42 Ambrosio S, Saccà CD, Amente S, Paladino S, Lania L, Majello B. Lysine-specific demethylase LSD1 regulates autophagy in neuroblastoma through SESN2-dependent pathway. Oncogene 2017;36:6701–11.

43 Pajtler KW, Weingarten C, Thor T, Künkele A, Heukamp LC, Büttner R, et al. The KDM1A histone demethylase is a promising new target for the epigenetic therapy of medulloblastoma. Acta Neuropathol Commun 2014;2:1–13.

44 Callegari K, Maegawa S, Bravo-Alegria J, Gopalakrishnan V. Pharmacological inhibition of LSD1 activity blocks REST-dependent medulloblastoma cell migration. Cell Commun Signal 2018;16:1–13.

45 Lee C, Rudneva VA, Erkek S, Zapatka M, Chau LQ, Tacheva-Grigorova SK, et al. Lsd1 as a therapeutic target in Gfi1-activated medulloblastoma. Nat Commun 2019;10:332.

46 Amente S, Milazzo G, Sorrentino MC, Ambrosio S, Palo G Di, Lania L, et al. Lysine-specific demethylase (LSD1/KDM1A) and MYCN cooperatively repress tumor suppressor genes in neuroblastoma. Oncotarget 2015;6:14572–83. PMCID:26062444.

47 Huang J, Sengupta R, Espejo AB, Lee MG, Dorsey JA, Richter M, et al. p53 is regulated by the lysine demethylase LSD1. Nature 2007;449:105–8. PMCID:17805299.

48 Cho HS, Suzuki T, Dohmae N, Hayami S, Unoki M, Yoshimatsu M, et al. Demethylation of RB regulator MYPT1 by histone demethylase LSD1 promotes cell cycle progression in cancer cells. Cancer Res 2011;71:655–60. PMCID:21115810.

49 He Y, Zhao Y, Wang L, Bohrer LR, Pan Y, Wang L, et al. LSD1 promotes S-phase entry

and tumorigenesis via chromatin co-occupation with E2F1 and selective H3K9 demethylation. Oncogene 2018;37:534–43.

50 Højfeldt JW, Agger K, Helin K. Histone lysine demethylases as targets for anticancer therapy. Nat Rev Drug Discov 2013;12:917–30. PMCID:24232376.

51 Sareddy GR, Nair BC, Krishnan SK, Gonugunta VK, Zhang Q guang, Suzuki T, et al. KDM1 is a novel therapeutic target for the treatment of gliomas. Oncotarget 2013;4:18–28.

52 Zheng Y-C, Ma J, Wang Z, Li J, Jiang B, Zhou W, et al. A Systematic Review of Histone Lysine-Specific Demethylase 1 and Its Inhibitors. Med Res Rev 2015;35:1032–71. PMCID:20099266.

53 Morera L, Lübbert M, Jung M. Targeting histone methyltransferases and demethylases in clinical trials for cancer therapy. Clin Epigenetics 2016;8:57. PMCID:27222667.

54 Duan YC, Ma YC, Qin WP, Ding LN, Zheng YC, Zhu YL, et al. Design and synthesis of tranylcypromine derivatives as novel LSD1/HDACs dual inhibitors for cancer treatment. Eur J Med Chem 2017;140:392–402.

55 Ji YY, Lin SD, Wang YJ, Su MB, Zhang W, Gunosewoyo H, et al. Tying up tranylcypromine: Novel selective histone lysine specific demethylase 1 (LSD1) inhibitors. Eur J Med Chem 2017;141:101–12.

56 Karakaidos P, Verigos J, Magklara A. Lsd1/kdm1a, a gate-keeper of cancer stemness and a promising therapeutic target. Cancers (Basel) 2019;11:1–22.

57 Young R. Cell Proliferation During Postnatal Development of the Retina in the Mouse. Dev Brain Res 1985;21:229–39.

58 Cepko CL, Austin CP, Yang X, Alexiades M, Ezzeddine D. Cell fate determination in the

vertebrate retina 1996;93:589–95.

59 Livesey FJ, Cepko CL. Vertebrate neural cell-fate determination: Lessons from the retina. Nat Rev Neurosci 2001;2:109–18. PMCID:11252990.

60 Trimarchi JM, Stadler MB, Cepko CL. Individual retinal progenitor cells display extensive heterogeneity of gene expression. PLoS One 2008;3: PMCID:18270576.

61 Cepko C. Intrinsically different retinal progenitor cells produce specific types of progeny. Nat Rev Neurosci 2014;15:615–27. PMCID:25096185.

62 Bassett EA, Wallace VA. Cell fate determination in the vertebrate retina. Trends Neurosci 2012;35:565–73. PMCID:22704732.

63 Young RW. Cell differentiation in the retina of the mouse. Anat Rec 1985;212:199–205. PMCID:6501608.

64 Jeon C-J, Strettoi E, Masland RH. The Major Cell Populations of the Mouse Retina. J Neurosci 1998;18:8936–46.

65 Wassle H, Boycott BB. Functional architecture of the mammalian retina. Physiol Rev 1991;71:447–80. PMCID:2006220.

66 Carter-Dawson LD, LaVail MM. Rods and cones in the mouse retina. I. Structural analysis using light and electron microscopy. J Comp Neurol 1979;188:245–62. PMCID:500858.

67 Hoon M, Okawa H, Della Santina L, Wong ROL. Functional architecture of the retina: Development and disease. Prog Retin Eye Res 2014;42:44–84. PMCID:24984227.

68 Dubin MW. The inner plexiform layer of the vertebrate retina: A quantitative and comparative electron microscopic analysis. J Comp Neurol 1970;140:479–505. PMCID:4098652.

69 Sumbul U, Song S, Mcculloch K, Becker M, Lin B, Sanes JR, et al. A genetic and computational approach to structurally classify neuronal types. Nat Commun 2014;5:1–26.

70 Sanes JR, Masland RH. The Types of Retinal Ganglion Cells: Current Status and Implications for Neuronal Classification. Annu Rev Neurosci 2015;38:221–46. PMCID:25897874.

71 Seabrook TA, Burbridge TJ, Crair MC, Huberman AD. Architecture, Function, and Assembly of the Mouse Visual System. Annu Rev Neurosci 2017;40:499–538. PMCID:28772103.

72 Hoyer-Fender S. Transgenerational effect of drug-mediated inhibition of LSD1 on eye pigment expression in Drosophila. BMC Ecol 2020;20:1–12. PMCID:33228645.

73 Popova EY, Pinzon-Guzman C, Salzberg AC, Zhang SS-M, Barnstable CJ. LSD1-Mediated Demethylation of H3K4me2 Is Required for the Transition from Late Progenitor to Differentiated Mouse Rod Photoreceptor. Mol Neurobiol 2016;53:4563–81. PMCID:26298666.

74 Tsutsumi T, Iwao K, Hayashi H, Kirihara T, Kawaji T, Inoue T, et al. Potential Neuroprotective Effects of an LSD1 Inhibitor in Retinal Ganglion Cells via p38 MAPK Activity. Investig Opthalmology Vis Sci 2016;57:6461. PMCID:27893888.

75 Zhong Q, Kowluru RA. Epigenetic modification of Sod2 in the development of diabetic retinopathy and in the metabolic memory: Role of histone methylation. Investig Ophthalmol Vis Sci 2013;54:244–50. PMCID:23221071.

76 Zhao D, Zhao Y, Wang J, Wu L, Liu Y, Zhao S, et al. Long noncoding RNA Hotair facilitates retinal endothelial cell dysfunction in diabetic retinopathy. Clin Sci

2020;134:2419–34. PMCID:32812634.

77 Zhong Q, Kowluru RA. Regulation of matrix metalloproteinase-9 by epigenetic modifications and the development of diabetic retinopathy. Diabetes 2013;62:2559–68. PMCID:23423566.

Chapter III: Characterization of LSD1 expression within the murine eye

Salma Ferdous, Hans E. Grossniklaus, Jeffrey H. Boatright, John M. Nickerson

Adapted from an original publication with permission of Investigative Ophthalmology & Visual Sciences:

Ferdous S, Grossniklaus HE, Boatright JH, Nickerson JM. Characterization of LSD1 Expression Within the Murine Eye. Invest Ophthalmol Vis Sci. 2019 Nov 1;60(14):4619-4631. doi: 10.1167/iovs.19-26728. PMID: 31675426; PMCID:PMC6827424

Abstract

The purpose of this study was to extend the current understanding of endogenous lysine specific demethylase 1 (LSD1) expression spatially and temporally in the retina. Towards that end, we determined the localization and levels of LSD1 and its substrates H3K4me1 and H3K4me2 (H3K4me1/2) within the murine eye. Immunofluorescent microscopy for LSD1, H3K4me1, and H3K4me2 was conducted on murine formalin-fixed paraffin-embedded eye sections across development in addition to western immunoblotting to assess localization and protein levels. Retinal LSD1 protein levels were highest at P7, whereas its substrates H3K4me1 and H3K4me2 had equally high levels at P2 and P14. Concentrations of all three proteins gradually decreased over developmental time until reaching a basement level of ~60% of maximum at P36. LSD1 and H3K4me1/2 were expressed uniformly in all retinal progenitor cells. By P36, there was variability in LSD1 expression in GCL, uniform expression in INL, and dichotomous expression between photoreceptors in ONL. This contrasted with H3K4me1/2 expression, which remained uniform. Additionally, LSD1 was widely expressed in the lens, cornea, and retinal pigment epithelium. Consistent with its known role in neuronal differentiation, LSD1 is highly and uniformly expressed throughout all retinal progenitor cells. Variability in LSD1 expression, particularly in photoreceptors, may be indicative of their unique transcriptomes and epigenetic patterns of rods and cones. Murine rod nuclei exhibit LSD1 expression in a ring or shell, rather than throughout the nucleus, consistent with their unique inverted chromatin organization. LSD1 has substantial expression throughout adulthood, especially in cone nuclei. By providing insight into endogenous LSD1 expression, our current findings could directly inform future studies to determine the exact role of *Lsd1* in the development and maintenance of specific structures and cell types within the eye.

Introduction

Epigenetic modifications, such as DNA methylation and histone modifications, including acetylation, methylation, and phosphorylation, are dynamic and can change due to environmental influence[1,2]. These dynamic changes contribute to the regulation of gene expression without altering the DNA sequence itself. Aberrant epigenetic alterations have been implicated in the development of ocular disorders, such as uveal melanoma, age-related macular degeneration, and glaucoma through the dysregulation of key biological processes such as cell proliferation, oxidative stress, angiogenesis, and inflammation[3].

Lysine specific demethylase 1 (*Lsd1*) (OMIM #609132), also known as *Kdm1a* and *Aof2*, was the first histone demethylase to be discovered. This protein acts specifically to demethylate the active mark H3K4 mono- and di-methylation (H3K4me1 and H3K4me2) and the repressive mark H3K9 mono- and di-methylation (H3K9me1 and H3K9me2) depending on its associated complex; thus, LSD1 can switch between a transcriptional repressor and activator[4,5]. Inhibitors of LSD1 and its complex members have been explored for anti-cancer therapies and have shown promising results in clinical trials[6–8].

Lsd1 and its downstream targets are involved in a wide range of biological functions, including embryonic development[9], neurogenesis[10,11], tumor-cell growth and metastasis[12,13], stress-induced emotional behaviors[14], and maternal reprogramming at fertilization[15]. Three patients with *de novo* missense mutations in *Lsd1* display numerous clinical symptoms, including ocular defects such as blue sclera, exotropia, and strabismus[16,17]. In addition, patients with mutations in related epigenetic proteins, including *KMT2D* (OMIM #602113) or *KDM6A* (OMIM #300128), are

often diagnosed with Kabuki syndrome. Kabuki syndrome 1 and 2 (OMIM #147920 and OMIM #300867) are characterized by intellectual disability and distinctive craniofacial features, and recently a patient with a suspected deleterious mutation in *Lsd1* exhibited Kabuki-like clinical features[17].

Within the central nervous system, *Lsd1* is involved in terminal differentiation of neurons. Inducible deletion of *Lsd1* in adult mice lead to paralysis and hippocampal and cortex cell death as well as associated learning and memory problems[18]. This may be in part facilitated through interactions in both the brain and retina between LSD1 and TLX, also known as NR2E1 (OMIM #603849), a master regulator of neural stem cell maintenance and neurogenesis[19,20].

Despite the retina being a component of the central nervous system, little is known about the role of *Lsd1* in ocular development or maintenance. Recently, Popova and colleagues found that *Lsd1* is highly expressed in late progenitor retinal cells as they become post-mitotic and begin to differentiate and that inhibition of LSD1 blocks the differentiation of the retinoblast into rod photoreceptors[21]. *Tsutsumi et al.* found potential neuroprotective effects of an LSD1 inhibitor that may protect retinal ganglion cells, which may have implications in glaucoma[22]. These studies have examined the effects of LSD1 inhibition in the retina and we aimed to extend the current understanding of endogenous LSD1 expression spatially and temporally and compare and contrast our work with theirs.

In this study, we evaluated the protein levels and localization of *Lsd1* and its associated substrates H3K4me1 and H3K4me2 within the developing murine eye. Additionally, we looked

at LSD1 expression within the adult human retina. Such "mapping" of *Lsd1* could provide useful and necessary information for subsequent studies in the important field of epigenetic changes in retinal development and retinal diseases. We hypothesized that due to its role in neuron terminal differentiation, initiation of Lsd1 expression induces terminal differentiation in at least some retinal progenitor cells (RPCs). We also hypothesized that LSD1 would not be needed after retinal cells have terminally differentiated; thus, LSD1 levels would likely dramatically decrease. Testing these hypotheses are the goal of future experiments.

Methods

Animal studies: Mouse housing, experiments, and handling were approved by the Emory University Institutional Animal Care and Use Committee, and the studies were conducted in adherence with Association for Research in Vision and Ophthalmology (ARVO) and followed guidance and principles of the Association for Assessment and Accreditation of Laboratory Animal Care (AAALAC). C57BL/6J (WT) and Thy1-YFPH mice were maintained on a 12-h light/dark cycle at 23 °C, and standard mouse chow (Lab Diet 5001; PMI Nutrition Inc., LLC, Brentwood, MO) and water were provided *ad libitum*. The mice were managed and housed by Emory University Division of Animal Resources. Adult mice were euthanized using CO_2 gas asphyxiation for 5 minutes followed by cervical dislocation. Weanling pups (aged <P21) were sacrificed using decapitation. Animals ranged in age from P2 – P330.

Human studies: Within the records of the L.F. Montgomery Laboratory at the Emory Eye Center, enucleation specimens ranging from January 1940 to August 2017 were identified that contained intact retinas. Many of these samples were enucleated due to a diagnosis of retinoblastoma. For the purposes of this study, only samples that contained parts of retina with normal morphology

and three nuclear layers were included for further LSD1 expression analysis. These studies were determined to be exempt by the Emory Institutional Review Board in full compliance with tenets of Helsinki and ARVO guidelines.

Immunofluorescence: All antibodies are listed in Table 1 below.

Unless otherwise noted, one to three drops of DAPI nuclear stain plus fluorshield (Sigma #F6057) was applied on top of each immunofluorescence slide (both sections and flatmounts) and a coverslip (#22 Thermo Fisher #152250) was placed on top of the slide. The edges of the coverslip were sealed with nail polish and allowed to dry overnight in darkness at room temperature before imaging.

Sections:

Murine eyes were enucleated and placed in zinc + formaldehyde (Z-fix; Anatech LTD, Battle Creek MI #SKU622) for fixation for 1 hour at room temperature. Afterwards the eyes were washed 3X in 1X phosphate buffer solution (PBS) (Corning 46-013-CM), dehydrated using increasing percentages of ethanol and xylene, and embedded in paraffin. Five micron-thick sections were cut using a microtome, placed on superfrost glass micro slides (VWR #48311-703) and allowed to air dry vertically at ambient room temperature overnight. The slides were then incubated in fresh xylenes for 8 minutes, 5 minutes, and 2 minutes before being washed in decreasing ethanol percentages for 2 minutes each (100%, 90%, 80% 70%, 60%, 50%) and then twice in 1X PBS for 2 minutes each. Afterwards, the slides were heated for 30 minutes in citrate buffer (10mM sodium citrate, 0.05% (V/V) Tween 20 pH 6.0) in a 95 °C water bath for antigen retrieval. Coplin jars with the slides were removed from the water bath and cooled to room

temperature in a beaker filled with distilled room temperature water for 15 minutes. Slides were washed one final time for 5 minutes in 1X PBS before being placed in a humid chamber. A boundary was drawn around each individual retinal section using a pap pen (Research Products International #195505). Slides were incubated in 1X Powerblock solution (Fisher Scientific #NC9495720) for 1 hour. Primary antibodies were diluted using 1X Powerblock and 1X PBS (dilutions indicated in Table 1). Sections were incubated in primary antibody overnight at 4°C in a humidified chamber. The next day, slides were washed 3X in 1X PBS for 5 minutes each and then incubated in secondary antibodies for 2 hours at room temperature (in a sealed humidified black plastic box). Slides were again washed 3X in 1X PBS for 5 minutes each.

Retina Flatmounts:

Murine eyes from P30 Thy1-YFPH mice were enucleated and placed in pre-chilled 10 mL of 97% methanol (Sigma Aldrich #34860) + 3% glacial acetic acid solution for 4 days at -80°C[23]. These mice endogenously express yellow fluorescent protein under the control of the *Thy1* promoter, a retinal ganglion cell (RGC) marker[27], in a random subset of 3-5% of total RGCs[24,25]. Prior to dissection, eyes were left at room temperature for 3 hours. Dissection was conducted as described in *Boatright et al.*[26] with one adjustment; the neural retina was not removed and remained intact and attached to the retinal pigment epithelium (RPE). After dissections were complete, samples were washed for 5 minutes in 1X phosphate buffer solution (PBS) (Corning 46-013-CM) with 0.1% V/V Triton X-100 (Sigma) (0.1% PBS-TX). Samples were then blocked in 1X Powerblock solution for 1 hour and then incubated overnight at 4°C with primary antibody. Primary antibodies were diluted to the appropriate concentrations (see Table 1) using 1X PBS and 1X Powerblock. The following day, samples were washed 5 times with 0.1% PBS-

TX solution and then incubated with secondary antibodies (see Table 1) at room temperature for 1-2 hours. Samples were then washed 3 times in 0.1% PBS-TX, once in 0.01% PBS-TX, and once in 1X PBS.

Retinal Pigment Epithelium (RPE) Flatmounts:

Murine eyes were enucleated and placed in zinc + formaldehyde for fixation for 10 minutes at room temperature. Afterwards, the eyes were washed 3X in 1X PBS (Corning 46-013-CM) and stored at 4°C for 1-2 hours before dissection. RPE flatmount dissection were prepared following Boatright *et al.*[26]. Following dissection, RPE flatmounts were individually transferred into a well created by attaching a silicone gasket (Sigma Aldrich #GBL665104-25EA) to a SuperFlost Plus microscope glass slide (Fisher Scientific #12-550-15). Flatmounts were incubated in 300 μL of blocking buffer (1% (W/V) bovine serum albumin (BSA) (Catalog #BP9703-100) and 0.1% (V/V) Triton X-100 (Sigma) in HBSS (Fisher Scientific Catalog # MT21023CV) for 1 hour at room temperature in a humidified chamber. Primary antibodies (see Table 1) were diluted and pre-blocked in the blocking buffer for 1 hour prior to being applied to the flatmounts. Blocking buffer was aspirated from the flatmounts and the flatmounts were incubated overnight at room temperature in primary antibodies. The next day, primary antibodies were aspirated and the flatmounts were rinsed 5X for 2 minutes each with wash buffer (HBSS and 0.1% V/V Triton X-100). Secondary antibodies (see Table 1) were diluted and pre-blocked in blocking buffer for 1 hour at room temperature before being applied to the flatmounts overnight at room temperature. The next day flatmounts were rinsed 5X for 2 minutes with the wash buffer. Afterwards the gasket was removed from the glass slide and the flatmounts were mounted with Fluoromount-G (Southern Biotech; Catalog #0100-01; Birmingham, AL) and covered with a 22X40mm

coverslip (Thermo Fisher #152250).

Confocal Microscopy:

Imaging of the retina sections was performed using a Nikon C1 confocal imaging system with solid-state laser excitation at 488 and 568 nm. Confocal images were stitched together using Adobe Photoshop CS2.

Western blots:

Sample preparation – Retinas were dissected from each eye separately and placed in a round bottom 0.5 ml screwcap tube with both retinas from the same animal pooled in one tube (Eppendorf Catalog #022363344). Homogenization Buffer was prepared from 10mL RIPA Buffer, one tablet of protease inhibitor (compete Mini protein inhibitor Catalog #118361530001) and one tablet of phosphatase inhibitor (Roche PhosSTOP EASypack #04906845001). 75μL of homogenization buffer was added to each pair of retinas along with one 4.7 mm ferric bead in a screw cap tube. The homogenizer was a QIAGEN TissueLyser LT[27]. The retinas were macerated at 50 oscillations per second for 3 minutes at 4 °C. Afterwards, the ferric bead was removed using a magnet and samples were centrifuged at 4 °C for 3 minutes (10,000 ×g) to remove particulate debris. Supernatants were collected and transferred to fresh 500 μL Eppendorf tubes and stored at -80°C until further use.

Protein concentration determination: Overall protein concentration of samples was determined using a Bicinchoninic Acid (BCA) Assay[28]. A 1:10 dilution of the supernatant was prepared with homogenization buffer (described above) for quantification. 10 μL of each diluted sample was pipetted in an individual well of a 96-cell culture plate (Thermo Scientific #165306) in triplicate

along with standards from a Pierce BCA Protein Assay Kit (ThermoFisher Catalog #23227) prepared to manufacturer's instructions. 200 μL of BCA working reagent, also prepared to manufacturer's instructions, was added to each well and the entire culture plate was incubated at 37°C for 30 minutes before absorbance at 562 nm was measured using a Synergy H1 Hybrid Plate Reader (BioTek).

SDS polyacrylamide gel electrophoresis (SDS-PAGE): The sample supernatants were adjusted to a protein concentration of 0.8 mg/mL in 200 μL using 100 μL of 2X Laemelli buffer[29] prepared with 2-mercaptoethanol (ThermoFisher #21985023) (50μL of 14.3 M 2-mercaptoethanol and 950 μL 2X Laemelli buffer[29]) and cold homogenization buffer (described above) and were stored at -20ºC up to a week following preparation. Immediately before electrophoresis samples were heated for 5 minutes at 95ºC in a thermocycler.

Running / staining gel: 30μL of each sample was loaded into individual lanes onto a pre-cast Criterion gel (BioRad TGX Stain Free Gel 4-15% Catalog #567-1083) as well as 10 μL of ladder (BioRad Catalog #1610376) and run at 100 V for 90 min. Samples were then transferred for 7 minutes onto PVDF blotting membrane[30] using Trans-blot turbo pack (BioRad Catalog #170-4157) and Trans-blot Turbo Transfer System (BioRad). The gel was checked pre- and post-transfer to assure that a good transfer of proteins from the gel to the membrane was achieved.

Prior to primary antibody incubation, membranes were blocked for 2 hours at room temperature with 5% (W/V) instant nonfat dry milk (Quality Biological Catalog #A614-1005) in TBST (Tris buffered saline (TBS) (Biorad #1706435) with 0.1% (V/V) Tween 20 (Fisher Scientific BP337-100)). Primary antibodies (see Table 1) were diluted with 5% milk in TBST, and membranes were incubated overnight on a 4°C shaker. The membrane was washed three times for 5 minutes

each using 0.1% TBST. HRP conjugated secondary antibodies (see Table 1) were diluted with 5% milk in TBST and membranes were incubated 1-2 hours at room temperature on a shaker. The membrane was washed three times for 5 minutes each using 0.1% TBST. 10 mL of Luminata Crescendo Western HRP substrate (EMD Millipore Catalog #WBLUR0500) was applied to the membrane for 5 min. The membrane was imaged in chemiluminescence mode using MP ChemiDoc Imaging System (BioRad). Exposure times varied from 30 to 180 seconds. In order to re-probe the same membrane with multiple antibodies, after imaging, 10mL of Restore western blot stripping buffer (Thermo Scientific Catalog #21059) was applied to the blot for 10 minutes, the blot was washed for 5 minutes using 0.1% TBST, and then blocked with 5% milk (W/V) in TBST and incubated with the appropriate primary and secondary antibody as described above.

Western Blot Data Analysis:

Densitometry was conducted on the western blot images using Photoshop CS6. All protein levels were normalized to (divided by) their respective loading control levels (either beta Actin or H3). Mouse retina samples ranged from post-natal day 2 (P2) to post-natal day 330 (P330) for 11 different time points (P2 / P4 / P5 / P6 / P7 / P10 / P14 / P21 / P36 / P121 / P330), and two independent sets of samples were run. In order to determine possible statistical differences in LSD1, H3K4me1, and H3K4me2 across different ages, retina samples ranged from P2 – P36 for 5 different time points (P2 / P7 / P14 / P21 / P36) and 3 independent samples were run for each time point.

Statistical Analysis:

Statistical analysis was conducted using Prism 7 for Mac OS X Version 7 (GraphPad Software, Inc., La Jolla, CA). All data are summarized as mean ± standard deviation (SD) and individual statistical tests are listed in figure legends. P values < 0.05 were considered to be statistically significant. Each sample group member is an independent mouse.

Results

Strong Expression of LSD1 in murine retinas throughout development

LSD1 is highly expressed in late-stage retinal progenitor cells; however, it is not known whether this expression is maintained after development is completed[19]. In order to resolve spatial and temporal expression of LSD1 in more detail, we performed western blot analysis from C57Bl/6J animals starting at post-natal day 2 (P2) during development through maturation at P330 (Figure S1). We probed for LSD1 (S3.1A) and a secondary only control was used to identify any non-specific antibody binding (S3.1B). Single bands were detected when probing for LSD1 and no bands were detected in the secondary-only control blots. Two independent western blots were conducted using independent sets of samples (all from different mice), and quantification of the results for both experiments are shown in Figure S3.1C. In general, LSD1 levels are higher at younger ages, which correspond to the retinoblast stage, and steadily decreased over development.

To determine if there was a significant reduction in LSD1 protein levels as the retina matures, we conducted western blotting on a subset of developmental time points (P2 / P7 / P14 / P21 / P36) using three independent samples (Figure 3.1). We probed for LSD1 (Figure 3.1A), beta-actin

served as a loading control (Figure 3.1B) and a secondary only control determined any non-specific antibody binding. We detected a single band for LSD1 (expected size 107kDa), a single strong band for beta-actin (expected size 42 kDa) with a faint band at 107kDa that likely corresponds to residual LSD1 antibody that remained after the stripping process, and no band in the secondary only control. The western blot results were quantified using densitometry, and LSD1 was normalized to beta-actin for each individual sample. This subset of samples allowed for better resolution of changes in LSD1 protein levels during retinal development. LSD1 is present at P2 and then its expression significantly increases and peaks by P7, which corroborates results from *Popova et al*[21]. LSD1 then decreases significantly from P7 to P21 until reaching a final "basement" level at P36 (Figure 3.1D). This basement level is a plateau corresponding to ~60% of the maximum LSD1 levels observed at P7. A two-way ANOVA analysis shows a statistically significant difference between LSD1 protein levels between P2 and P7, P7 and P14, P7 and P21, P7 and P36, and P21 and P36, and a full list of the statistical tests and their results are listed in Supplemental Table 3.1. Thus, although LSD1 levels decrease after terminal differentiation is complete, it remains present in the retina throughout the lifetime of the mouse.

In order to determine the localization of LSD1 during and after retinal development, we performed immunofluorescence staining for LSD1 in retinal sections from C57BL/6J animals at the same timepoints used in Figure S3.1 (P2 – P330). Throughout the lifetime of the mouse, we observed LSD1 expression solely within the nuclei of cells, which is consistent with its role in demethylating histone proteins (Figure 3.2)[31,32]. We observed high expression of LSD1 throughout the developing retinoblast from P2 to P14. At P21 (weaning age), LSD1 expression remained high; however, the expression pattern began to lose uniformity from one nucleus to the

next in a given cell type. At P36, when retinal maturation is complete, the three nuclear layers showed variation in LSD1 expression from layer to layer and among different cells within a layer. Within the retinal ganglion cell layer (GCL), LSD1 had variable expression among different retinal ganglion cells (RGCs) and displaced amacrine cells, as will be explored later. Within the inner nuclear layer (INL), which consists of amacrine, bipolar, and horizontal cells, there was uniform staining throughout each nucleus regardless of cell type. However, as will be further explained below, in the outer nuclear layer (ONL), there was a distinctly different expression pattern among the photoreceptor cells. This variation of LSD1 expression among different cell types of the GCL and ONL was maintained from P36 until P330. Thus, both the levels and cellular/histological expression patterns of LSD1 changed throughout the lifetime of the mouse, although this does not necessarily equate to altered enzymatic activity.

LSD1 demethylates histone modifications H3K4me1/2 and H3K9me1/2. Like LSD1 it was unclear whether H3K4me1 or H3K4me2 protein levels were changing or not. We conducted western blotting for H3K4me1 and H3K4me2 (Figure 3.3) on the same subset of developmental time-points (P2 / P7 / P14 / P21 / P36) as LSD1 in triplicate to determine if there was a significant reduction in either substrate as the retina matures. Figure 3A and 3E show H3K4me1 and H3K4me2 respectively, and H3 served as an internal loading control for each sample (Figure 3.3B and 3.3F). Unlike LSD1, which peaked at P7, both H3K4me1 and H3K4me2 have equally high levels of expression at P2 and P7 and expression significantly decreases as the retina fully matures. A two-way ANOVA analysis shows a statistically significant difference for H3K4me1 protein levels between P2 and P14, P2 and P21, P7 and P14, and P14 and P21(Figure 3.3D) and a full list of the statistical tests and their results are listed in Supplemental Table 3.2. For

H3K4me2, a two-way ANOVA analysis shows a statistically significant difference between P2 and P14, P2 and P21, P2 and P36, P7 and P14, P7 and P21, and P7 and P36. A full list of the statistical tests results for H3K4me2 is listed in Supplemental Table 3.3. Although both substrate levels decreased after terminal differentiation is complete, they are expressed in the retina throughout the lifetime of the mouse. Changes in H3K4me1 and H3K4me2 are unlikely to be solely influenced by changes in LSD1 levels. Histone methyltransferases such as SET1 can have direct impacts while epigenetic remodelers such as the CHD family can influence the epigenome as a whole by disrupting, moving, and exchanging nucleosomes[33,34]. Those additional epigenetic proteins are likely to be active as the progenitor retinal cells differentiate into their respective terminal cell types thus leading to the observed changes in H3K4me1 and H3K4me2 levels seen in Figure 3.3.

As seen in Figure 3.2, LSD1 localization changes over retinal developmental time. To determine whether similar changes are seen in H3K4me1 and H3K4me2 we performed immunofluorescence at P2 and P36 for these histone modifications (Figure 3.4). Both H3K4me1 and H3K4me2 are uniformly highly expressed throughout all retinal progenitor cells (P2) (Figure 3.4A and 3.4C show H3K4me1 and H3K4me2 alone; Figure 3.4B and 3.4D show H3K4me1 + DAPI nuclear stain and H3K4me2 + DAPI nuclear stain) and all differentiated retinal subtypes (P36) (Figure 3.4E and 3.4G show H3K4me1 and H3K4me2 alone; Figure 3.4F and 3.4H show H3K4me1 + DAPI nuclear stain and H3K4me2 + DAPI nuclear stain). Thus, in contrast to LSD1, both H3K4me1 and H3K4me2 expression remains consistent in all cells across developmental time.

Differential Expression of LSD1 in rod and cone photoreceptors

Within the ONL, only a small subset of cells have LSD1 expression levels that appear to be similar to the expression seen in either the GCL or INL; the majority of the cells appear to display relatively less expression. Because cone photoreceptors make up only 3% of the total cells within the ONL[35], we hypothesized that these relatively highly-expressing LSD1 cells within the ONL are cone photoreceptors. Retinal sections from P36 C57BL/6J mice were stained for LSD1 and short-wavelength cone opsin (S-OPSIN), a marker for cone photoreceptors. Cells in the photoreceptor layer exhibiting high levels of LSD1 immunosignal also exhibited S-OPSIN immunosignal, whereas cells in the photoreceptor layer that exhibited only modest levels of LSD1 immunosignal were not stained for S-OPSIN (Figure 3.5), suggesting that LSD1 is expressed in cone, but not rod, photoreceptors. This difference is even more striking after 3D rendering using Imaris software (Figure 3.6; Imaris, version 9.2; Bitplane USA, Concord, MA). Interestingly, the Imaris images also reveal a difference in the pattern of LSD1 expression between the two types of photoreceptors. Cone photoreceptors have a uniform staining pattern within the nucleus similar to cells in the GCL and INL. However, rod photoreceptors displayed a "ring-like" or "shell-like" staining pattern.

In contrast to the variation in LSD1 expression within the mature murine retina, a mature human retina showed uniform nuclear LSD1 expression in the ONL (Figure 3.7). Qualitatively, there appears to be a general trend whereby all nuclei have roughly the same level of LSD1. While the murine retina showed variability within the retinal ganglion cells and photoreceptors, the human retina does not.

Variable levels of LSD1 within the Ganglion Cell Layer (GCL)

In addition to the variable expression of LSD1 observed among photoreceptor cells in the ONL, LSD1 also showed variable expression among individual cells in the GCL at P36. In Figure 3.8A, the GCL shows obvious differences in LSD1 levels between adjacent cells; these differences are highlighted in Figure 3.8B. There are two major classes of retinal cells found in the GCL, retinal ganglion cells (RGCs) and displaced amacrine cells[36,37]. To determine whether LSD1 expression was isolated to RGCs or not, we stained whole-retina flatmounts from transgenic mice expressing yellow fluorescent protein (YFP) under the control of the pan-RGC marker *Thy1* with LSD1[24]. Using this technique, only 3-5% of RGCs are labeled with YFP, which allows for visualization of the entire dendritic arborization of individual RGCs as well as a single axon projecting to the optic nerve head (Figure 3.8C)[25]. In Figure 3.8D, two RGCs showed fairly equal LSD1 expression as indicated by the amount of yellow color within their nuclei, which represents the overlap between the LSD1 fluorescence in the 488 nm confocal microscope channel and the THY1 expression in the 568 nm channel. Figure 3.8E depicts two adjacent RGCs with varying levels of LSD1 expression. The left RGC had relatively less LSD1 compared to the right RGC. Figure 3.8F shows numerous RGCs with relatively high, intermediate, and low LSD1 levels within the same field of view. Supplemental Figure 3.2 shows LSD1 alone, THY1-YFPH alone, and LSD1 + THY1-YFPH merged for the images shown in Figures 3.8C – 3.8F. Because the THY1-YFPH mice only label 3-5% of the RGC population within a retina, it cannot determine whether LSD1 is expressed in displaced amacrine cells or not. For this, we co-labeled LSD1 with a pan-RGC marker, RPBMS, in P90 C57Bl/6J retinal sections[38]. Figure 3.8G-3.8J shows a peripheral retinal section labeled with LSD1 alone (Figure 3.8G), RPBMS alone (Figure 3.8H), and a merged view (Figure 3.8I). A magnified area in

Figure 3.8J shows 4 individual cells in the GCL. The two cells on the left are RGCs that express LSD1 as indicated by the overlap of 488nm and 568nm fluorescent signal. The third cell from the left only has RPBMS expression, indicating that this is a RGC that does not express LSD1. The cell on the right side only has LSD1 expression, but not RPBMS, indicating that this is a displaced amacrine cell that expresses LSD1. For further clarification, Supplemental Figure 3.3 contains two different areas of P90 C57Bl/6J retina (peripheral and central) with individual channels for DAPI, LSD1, and RPBMS as well as merged views of LSD1 + RPBMS and LSD1 + RPBMS + DAPI (panels S3.3A-S3.3J). Additionally, we have included a displaced amacrine cell marker HPC-1 (syntaxin)[39] co-labeled with LSD1 with individual panels for DAPI, LSD1, and HPC-1 as well as merged views of LSD1 + HPC-1 and LSD1 + HPC-1 + DAPI (panels S3.3K – S3.3O). Overall, these results indicate that LSD1 has variable expression in RGCs and displaced amacrine cells located in the GCL.

LSD1 expression in ocular structures outside the retina

Although the focus of our study was on the expression of LSD1 within the retina, we observed LSD1 expression throughout the entire mature murine eye (Figure 3.9A). At P36, LSD1 is expressed in almost all ocular structures, including the cornea, lens, retina, and retinal pigment epithelium (RPE). In all cases, LSD1 was found only in nuclei based on co-staining of LSD1 with DAPI. At the optic nerve head, LSD1 is expressed in the central retina (Figure 3.9B). In the lens, LSD1 was highly expressed in lens cells near the equatorial region and followed a gradient as the cells round the bow region (Figure 3.9C). This region contains anterior epithelial cells that are beginning to differentiate and elongate into fiber cells, which will eventually lose their nuclei as they complete differentiation[40]. LSD1 levels are very low to nonexistent in the anterior

epithelium. The levels of LSD1 increase in these epithelial cells at the equator, and levels reach a maximum in cells that are undergoing elongation as they morph into fiber cells. In cornea, the central corneal epithelium had higher LSD1 expression compared to the endothelium and stroma and LSD1 is expressed in the iris (Figure 3.9D). Figure 9E shows a 40X retinal pigment epithelium (RPE) flatmount image stained for LSD1 in green and ZO-1, a protein associated with tight junctions, in red to outline the hexagonal borders of the RPE cells. Two white circles with arrows highlight different RPE cells that contain either one or two nuclei. Roughly half of RPE cells are mononuclear and half are binuclear and LSD1 is expressed in all RPE cell nuclei[41]. We did not observe a difference in the level of LSD1 comparing one nucleus to the other in binucleate RPE cells. We also did not observe any differences in LSD1 levels in nuclei located more centrally compared to those in the far periphery of the RPE layer.

Discussion

The purpose of this study was to extend the current understanding of endogenous LSD1 expression spatially and temporally in the retina. The premise of this study is that *Lsd1* is known to play a major role in neuronal maturation and plasticity, specifically through a neuron specific *Lsd1* isoform, neuroLsd1 (*nLsd1*)[42]. The retina is comprised of numerous neuronal cell types; however, the role of *Lsd1* in differentiating retinal progenitor cells (RPCs) into committed neurons is largely unknown. In the developing retina, retinal progenitor cells are actively undergoing mitosis during retinogenesis. As these cells start to commit to various cell lineages and undergo differentiation, gene expression patterns among different cells start to diverge. A small percentage of these changes in gene expression can be accounted for by changes in DNA methylation; however, the vast majority are due to changes in chromatin states via histone

modifications[33,43]. Differences in chromatin state allow for various retinal cell types to be present at distinct levels[33,44].

Lsd1 serves as a key regulator of neural stem cell proliferation via its interactions with the transcription factor TLX[24], which establishes the undifferentiated and self-renewable state of neural stem cells[11,19]. During embryonic stages, the mouse retina develops by first generating ganglion cells followed by the development of cones, horizontal cells and most of the amacrine cells. Postnatally, bipolar cells, Muller glia, the remaining amacrine cells, and rod photoreceptors develop, although there is considerable overlap in the production of different retinal cells types at any specific timepoint[45–47]. Our original hypothesis was that *Lsd1* is critical for the transition between the retinal progenitor state and terminal differentiation. Although it is correlative, our data is consistent with this idea because LSD1 protein levels are highest at P7, when all retinal progenitor cells showed uniform expression, until P21. Although high LSD1 expression is temporally consistent with terminal differentiation of various cell types, expression does not end abruptly in any coincidence with the end of mitotic cell division, differentiation, or synaptic maturation (Fig. 3.1). By P36 the different mature retinal neurons displayed various levels of LSD1 based on their unique subtypes, and LSD1 levels reached a basement maintenance level (Supplement Fig. 3.1) at about 60% of maximum, which is maintained until the oldest age that we tested, P330. These expression pattern changes are also observed in localization changes that occur across developmental time (Figure 3.2). To speculate, this maintenance level may be necessary to maintain the unique chromatin state and gene expression patterns that are distinct between the seven retinal cell subtypes: rod photoreceptors, cone photoreceptors, bipolar, amacrine, horizontal, ganglion, and glial cells, and to maintain biological functions for proper

visual function.

Rod photoreceptor cells have relatively fewer regions of chromatin accessibility and in general, the rod photoreceptor chromatin in nocturnal animals have an inverse architecture compared to those in diurnal animals[48]. Nocturnal animals have chromatin in which the central part of the nucleus is heterochromatin and the surrounding peripheral areas are euchromatin[49]. This inversion occurs through remodeling of the conventional nuclear architecture (euchromatin in the center and heterochromatin in the periphery), due to the lack of the inner nuclear membrane protein lamin B[50] during post-natal differentiation of rod cells[51]. *Popova et. al* demonstrated that pharmacological inhibition of LSD1 stops the development of rod photoreceptors[21]. Our data show that the rod-specific changes of LSD1 nuclear partitioning occurred between P21 and P36, well after mouse retinas become functional by electroretinogram (ERG) signal detection. Nocturnal animals see at light intensities that are a million times lower than those available during the day. Thus, the inverted architecture may optimize light transmission and reduce the scattering of light in the ONL[51,52]. All other retinal cells within nocturnal animals have the conventional architecture, which may explain the difference in LSD1 expression patterns between rod and cone photoreceptor[51] (Figure 3.5). We observe relatively high expression in cone photoreceptors and relatively low expression in rods. Additionally, the "ring-like" staining pattern in the rods matches the peripheral location of euchromatin (Figure 3.6). The inverted rod chromatin organization is only present in nocturnal animals. In diurnal animals, such as humans, the chromatin architecture between their rod and cone photoreceptors are identical, which is consistent with the uniform LSD1 expression pattern we observed (Figure 3.7)[51]. This may be the underlying reason why there is no distinction between cone and rod photoreceptor LSD1

staining in humans.

LSD1 acts upon histone modifications associated with active transcription, such as H3K4 mono- and di-methylation (H3K4me1 and H3K4me2), and these modifications should be located within the nuclear periphery of mouse rod photoreceptors[53]. Furthermore, rod photoreceptor-specific genes accumulate H3K4me2 during retina development in the promoter and gene body[54]. In contrast, H3K4 mono- and di-methylation are located in the central nucleus of cells in the inner parts of the retina[53]. Yet, our immunofluorescence data show H3K4me1 and H3K4me2 located uniformly throughout all cells in the retinoblast and mature retina (Figure 3.4). This contrast between the localization of LSD1 in the mature retina and its substrates H3K4me1 and H3K4me2 may be the result of LSD1 having specific demethylase activity on particular histone protein substrates whereas H3K4me1 and H3K4me2 levels are influenced by a number of different epigenetic writers and erasers. Although, the localization of the substrates in the mature retina differs from LSD1 localization, all three proteins peak in the retinoblast and decrease across retinal developmental time until basement levels at P36, indicating that they are still needed post-development (Figure 3.3).

Unlike the photoreceptors, which show two distinct expression patterns between the two subtypes (rods and cones), we observed variability in LSD1 expression among different RGCs in the mature murine retina (Supplemental Figure 3.2) and in different cells within the ganglion cell layer, including displaced amacrine cells (Figure 3.8 and Supplemental Figure 3.3). RGCs are classically categorized using morphological, physiological, and gene expression profiles. Their soma are located in the GCL with axons that project through the optic nerve to the brain and ~40

subtypes have been identified in the mouse[55–57]. Given the numerous RGCs subtypes and the highly variable LSD1 expression, it can be hypothesized that LSD1 may play a role in the development of different types of RGCs. However, while this hypothesis warrants further investigation, it is outside the scope of the current study.

In addition to its role in neuron differentiation, *Lsd1* also plays a major role in the overall differentiation of embryonic stem cells (ESCs). Homozygous *Lsd1* null mouse embryos are inviable and arrest in their development by embryonic day 7.5[4]. Within the zygote, *Lsd1* expression first appears during the morula stage and by post implantation embryos, expression becomes ubiquitous. Our original hypothesis was that *Lsd1* expression would be relatively low and/or absent in structures outside of the adult retina; however, our results show strong LSD1 expression in all major ocular structures, including optic nerve, lens, cornea, and RPE (Figure 3.9 and Supplemental Figure 3.4).

Despite extensive research on *Lsd1* within the brain, relatively less research has been conducted on its role in the eye. Here, we sought to expand upon and contribute to previous research characterizing the importance of *Lsd1* in the eye. Given the obvious differences in expression between rod and cone photoreceptors as well as the subtle differences between various RGCs, our work highlights the unique role of *Lsd1* in the development of individual retinal subtypes. Additionally, despite the well-established role of *Lsd1* in neuron development, the ubiquitous expression throughout the eye raises interesting questions about its role in epithelial tissues such as cornea or RPE. Future work should investigate the basic mechanisms of how global or cell type specific genetic or pharmacologic inhibition of *Lsd1*, either during or after ocular

development, affects the formation of normal retinal subtypes and ocular tissues.

Lastly, from a translational perspective, inhibition of other epigenetic proteins, such as histone deacetylases, has been shown to have neuroprotective properties in retinal degenerative disorders, such as retinitis pigmentosa[58–60]. Additional studies have looked at inhibition of histone methylation, specifically H3K27me3, and its role in delaying the onset of retinal degeneration[61]. LSD1 inhibitors have long been studied for their potential therapeutic abilities in relation to oncology[7,8] and clinical trials for both acute myeloid leukemia and small cell lung cancer are currently underway. Within the visual system, *Tsutsumi et al.* found potential neuroprotective effects of an LSD1 inhibitor in protecting retinal ganglion cells, which may have implications in glaucoma[22]. Thus, future research is needed to determine the exact role(s) that *Lsd1* plays in ocular development in order to determine its potential as a therapeutic target for retinal diseases or in treating eye tumors.

Table 3.1: List of Antibodies used in these experiments

Antibody	Antibody Type	Catalog Number	Concentration	Application
Rabbit anti-LSD1	Primary antibody - Monoclonal	Abcam ab129195	[1:250]	Sections + Western Blotting + Retina Flatmount + RPE Flatmount
Goat anti-short wavelength cone opsin	Primary antibody - Polyclonal	Santa Cruz sc-14363	[1:250]	Sections
Rabbit anti-H3K4me1	Primary antibody - Polyclonal	Abcam ab205256	[1:1000]	Western Blotting
Rabbit anti-H3K4me2	Primary antibody - Polyclonal	ab7766	[1:1000]	Western Blotting
Rabbit anti H3	Primary antibody - polyclonal	Abcam ab1791	[1:1000]	Western Blotting
Mouse anti beta-actin	Primary antibody - monoclonal	Sigma Aldrich A5441	[1:1000]	Western Blotting
Goat anti-GFP	Primary antibody - Polyclonal	Novus Biologicals NB100-170	[1:750]	Retina Flatmount
Rat anti-ZO1	Primary antibody - Monoclonal	EMD Millipore Catalog #MABt11	[1:100]	RPE Flatmount

Donkey anti-rabbit AF488	Secondary antibody - Polyclonal	Jackson Immunological 711-545-152	[1:1000]	Sections + Retina Flatmount + RPE Flatmount
Donkey anti-goat redX AF568	Secondary antibody - Polyclonal	Jackson Immunological 705-295-147	[1:1000]	Sections + Retina Flatmount
Goat anti-rat AF 568	Secondary antibody - Polyclonal	Life Technologies Catalog #A10042	[1:1000]	RPE Flatmount
Goat anti-mouse IgG-HRP	Secondary antibody	Abcam ab7068	[1:5000]	Western Blotting
Mouse anti-rabbit IgG-HRP	Secondary antibody	Santa Cruz sc-2357	[1:5000]	Western Blotting

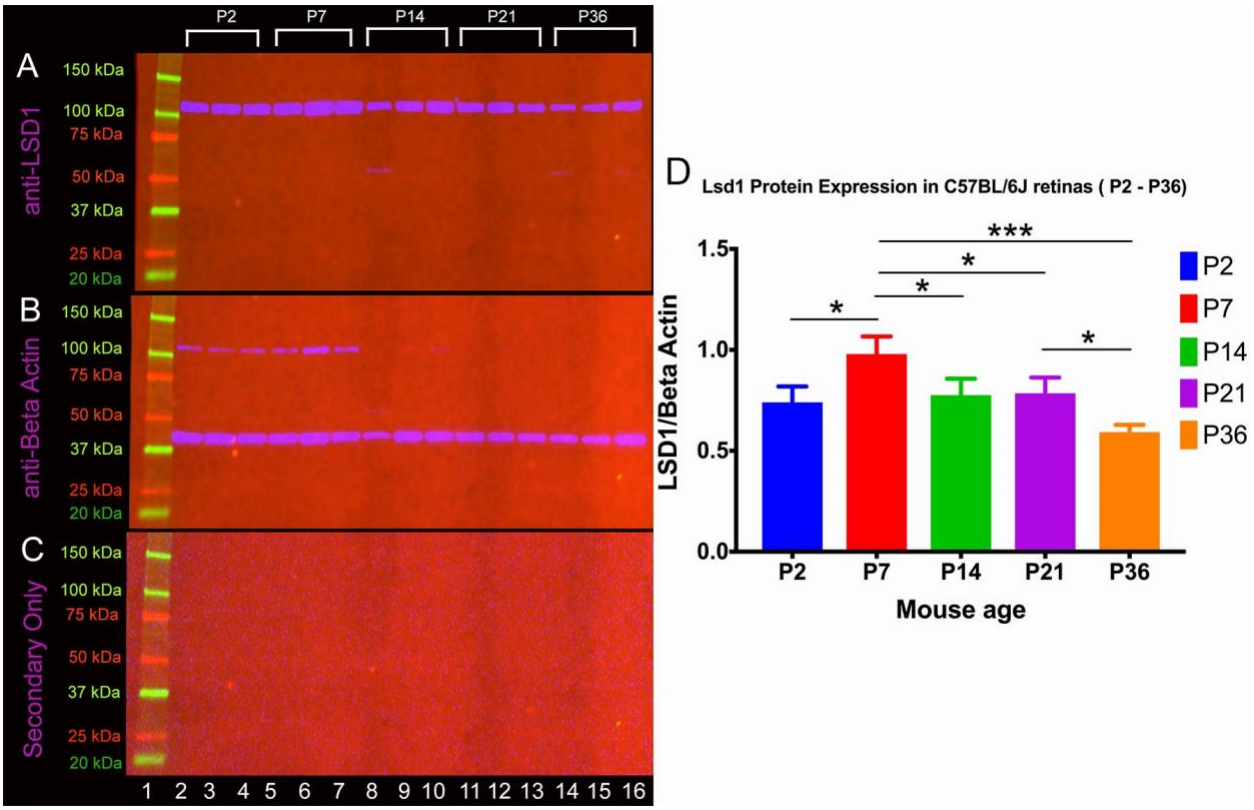

Figure 3.1: LSD1 protein levels peaks at P7. Western blot analysis was conducted on C57BL/6J mouse retina samples at 5 different time-points (P2 / P7 / P14 / P21 / P36) in triplicate. Samples were probed with an anti-LSD1 antibody (single band - expected size: 107 kDa) (panel 3.1A) anti beta-actin (single band – expected size: 43 kDa) served as a loading control (panel 3.1B) and secondary only controls detected no non-specific antibody binding (panel 1C). Quantification of results was achieved using densitometry and LSD1 levels were normalized to beta-actin. A two-way ANOVA with Tukey's multiple comparison test was conducted between the mean expression level in all possible pair combinations. There is a statistically significant decrease in LSD1 protein levels between P2 and P7, P7 and P14, P7 and P21, P7 and P36, and P21 and P36. A full list of comparisons and p values is listed in Supplemental Table 1. * = p value <0.05; ** = p value <0.01; *** = p value < 0.001

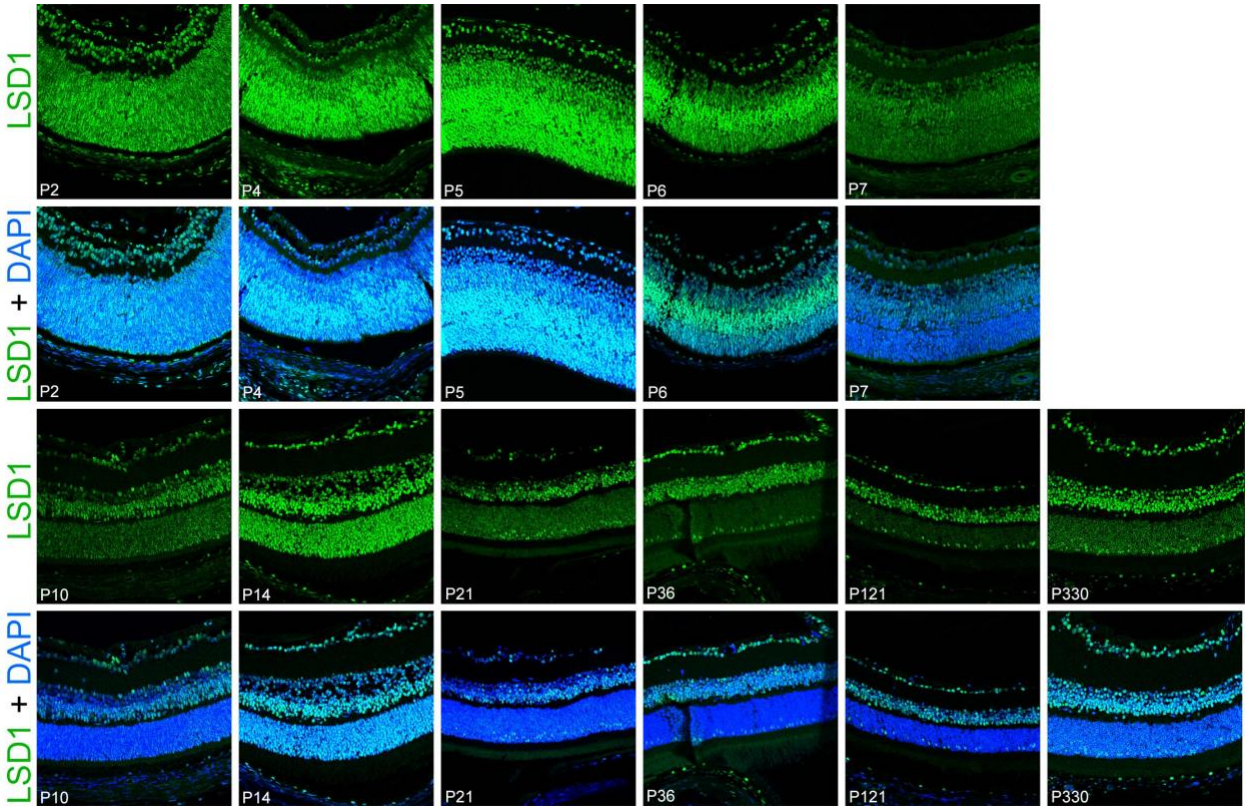

Figure 3.2: LSD1 detected in all retinal cells starting at P2 until P330. Immunofluorescence staining of C57BL/6J mouse retinas for LSD1 alone (green) (top row of images) and LSD1 (green) + DAPI nuclear stain (blue) (bottom row of images). Images were taken using 40X objective lens on a confocal microscope. LSD1 expression was uniformly present in all cells in the retinoblast starting at P2, and this uniform expression was consistent until the retina fully matured at P21. From P36 until P330, LSD1 was present in all three nuclear layers; however, the expression pattern was variable among different retinal subtypes.

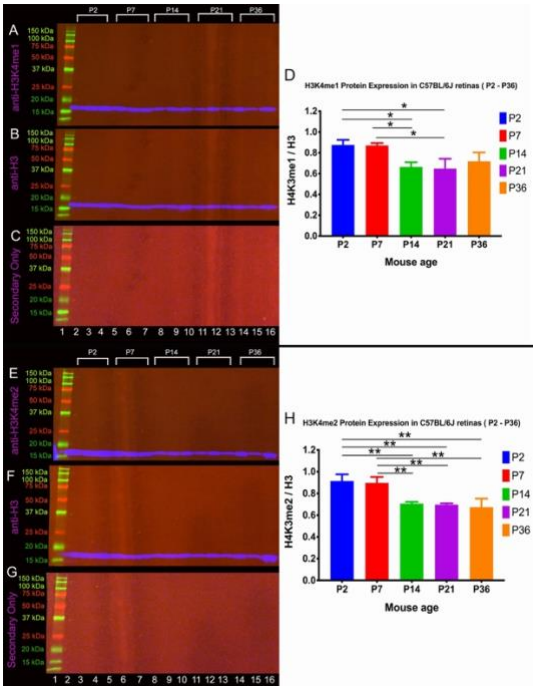

Figure 3.3: LSD1 substrates H3K4me1 and H3K4me2 peak at P2 and significantly decrease across retinal developmental time. Western blot analysis was conducted on C57BL/6J mouse retina samples at 5 different time-points (P2 / P7 / P14 / P21 / P36) in triplicate. Samples were probed with an anti-H3K4me1 (panel 3.3A) or anti-H3K4me2 antibody (panel 3.3E) (single band - expected size: 18kDa) and an anti-H3 antibody (panels 3.3B and 3.3F respectively) (single band - expected size: 18 kDa) served as a loading control. Quantification of results was achieved using densitometry and H3K4me1 / H3K4me2 levels were normalized to H3. A two-way ANOVA with Tukey's multiple comparison test was conducted between the mean expression level in all possible pair combinations. For H3K4me1, there is a statistically significant decrease between P2 and P14, P2 and P21, P7 and P14, and P7 and P21 (panel 3.3D). For H3K4me2, there is a statistically significant decrease between P2 and P14, P2 and P21, P2 and P36, P7 and P14, P7 and P21, and P7 and P36 (panel 3.3H). A full list of comparisons and p values are listed in Supplemental Table 3.2 and Supplemental Table 3.3. * = p value <0.05; ** = p value <0.01; *** = p value <0.001

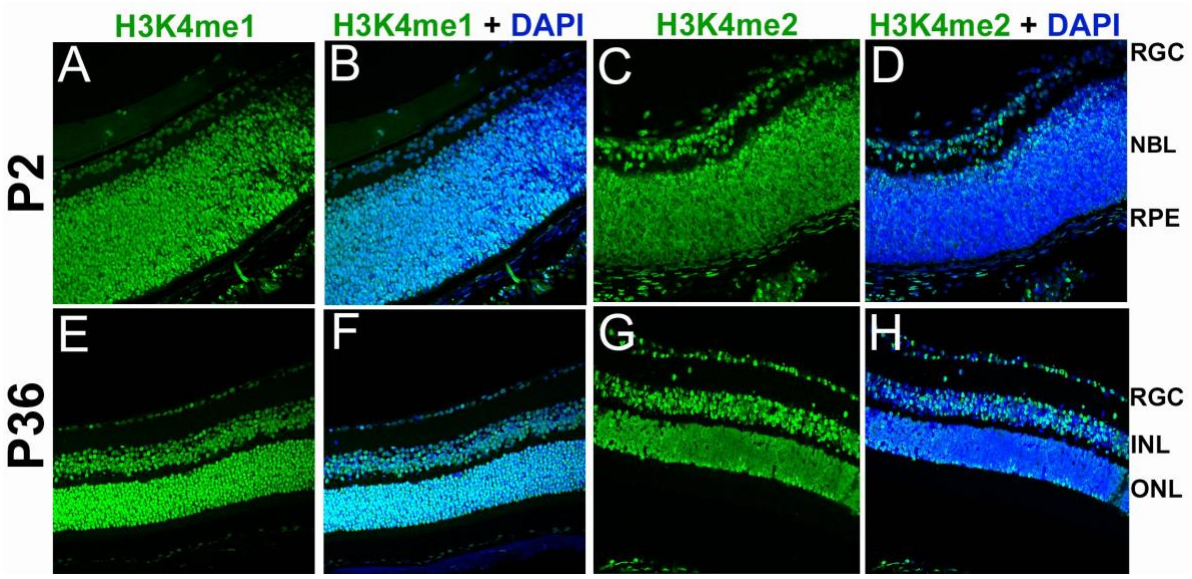

Figure 3.4: LSD1 substrates H3K4me1 and H3K4me2 are expressed throughout the retinoblast and mature retina. Immunofluorescence staining of C57BL/6J mouse retinas at P2 and P36 for H3K4me1 and H3K4me2 (green) with a DAPI nuclear stain (blue). Images were taken using 40X objective lens on a confocal microscope. At P2, H3K4me1 (panels 3.4A-3.4B) and H3K4me2 (panels 3.4C-3.4D) were expressed uniformly in the retinoblast throughout all retinal progenitor cells. At P36 in the mature retina H3K4me1 (panels 3.4E-43.F) and H3K4me2 (panels 3.4G-3.4H) maintain uniform expression in all retinal cell subtypes.

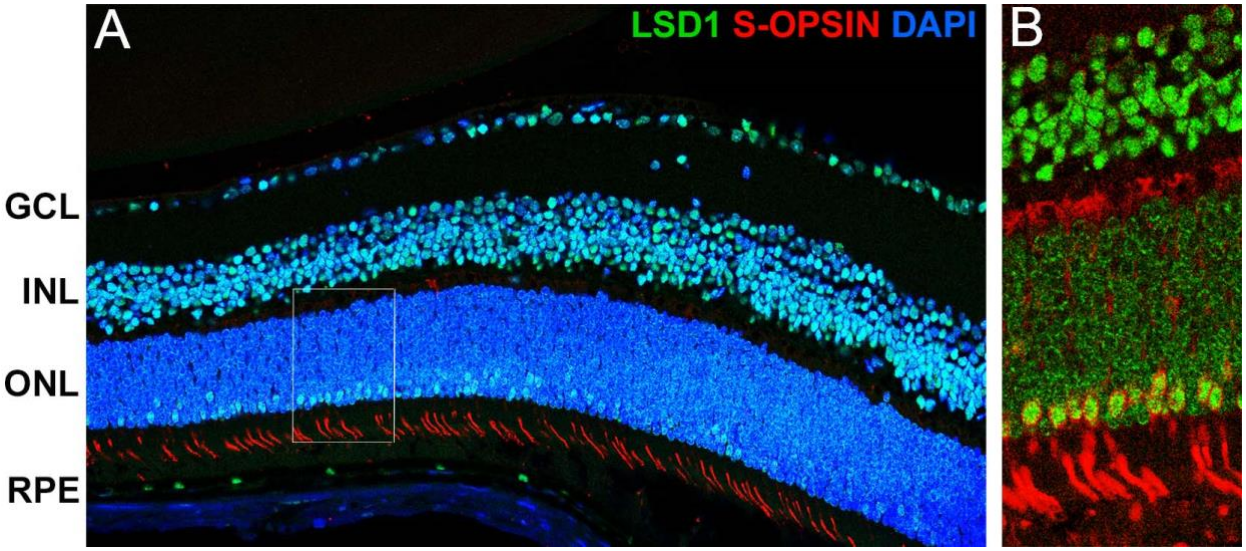

Figure 3.5: High levels of LSD1 in cone photoreceptors but not rods. Immunofluorescence staining of P36 C57BL/6J mouse retinas for LSD1 (green), short wavelength cone opsin (red) and DAPI nuclear stain (blue). 40X merged image taken with confocal microscope show LSD1 expression in all three nuclear layers and short wavelength cone opsin expression in cone photoreceptor outer segments (panel 3.5A). 60X image showing perfect correlation between cells with high LSD1 expression (green) along the outer edge of the ONL and the cone opsin (red) (panel 3.5B).

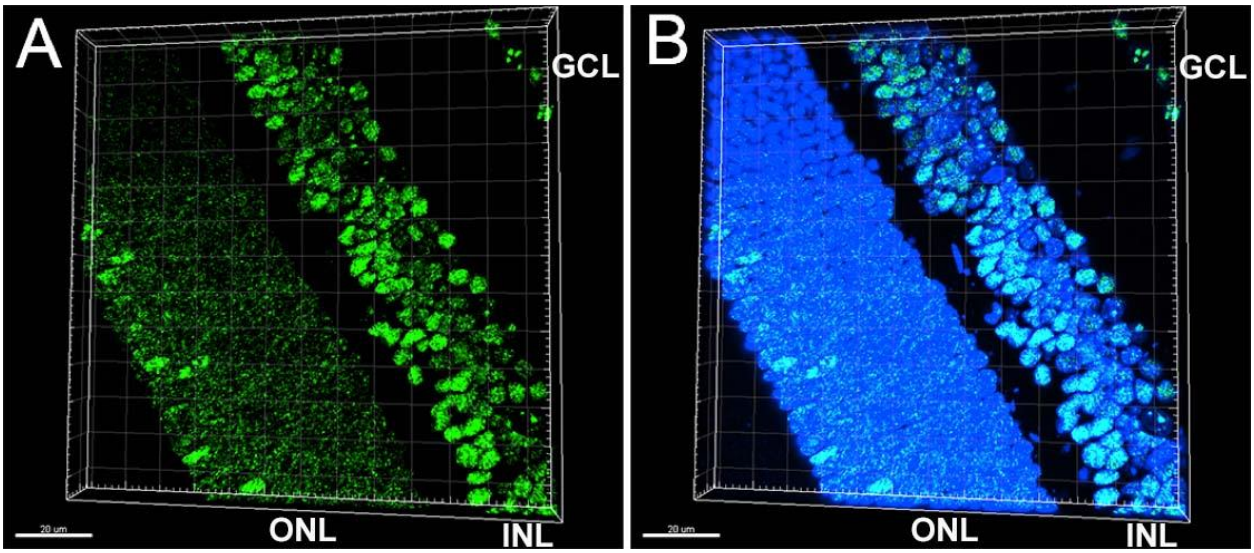

Figure 3.6: 3D rendering in Imaris of P36 C57BL/6J mouse retina section showing LSD1 ring – like staining pattern in rod photoreceptors. 40X confocal images rendered in Imaris software show LSD1 (green) (panel 3.6A) and LSD1 + DAPI nuclear stain (blue) (panel 3.6B). Within the ONL, there is a distinct staining pattern difference between the two photoreceptors subtypes. Rod photoreceptors show a "ring-like" or "shell-like" staining pattern where LSD1 expression is located in the periphery of the nucleus. Cone photoreceptors show a uniform staining pattern which mimics the LSD1 expression found in cell types located in the INL and GCL.

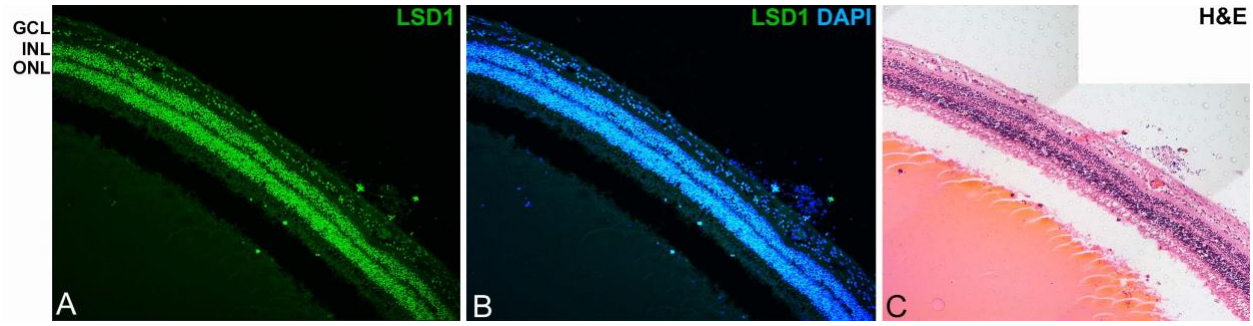

Figure 3.7: LSD1 is uniformly expressed in all retinal cells in a normal human retina

20X confocal images show LSD1 expression alone (green) (panel 3.7A) and LSD1 (green) + DAPI nuclear stain (blue) (3.7B). H&E staining of the same eye (3.7C) highlights location of cell nuclei and the intact morphology of the retinal layers. In contrast to the variable expression seen among retinal cell types in the murine eye, LSD1 is expressed at relatively uniform and equal levels throughout the entire human retina.

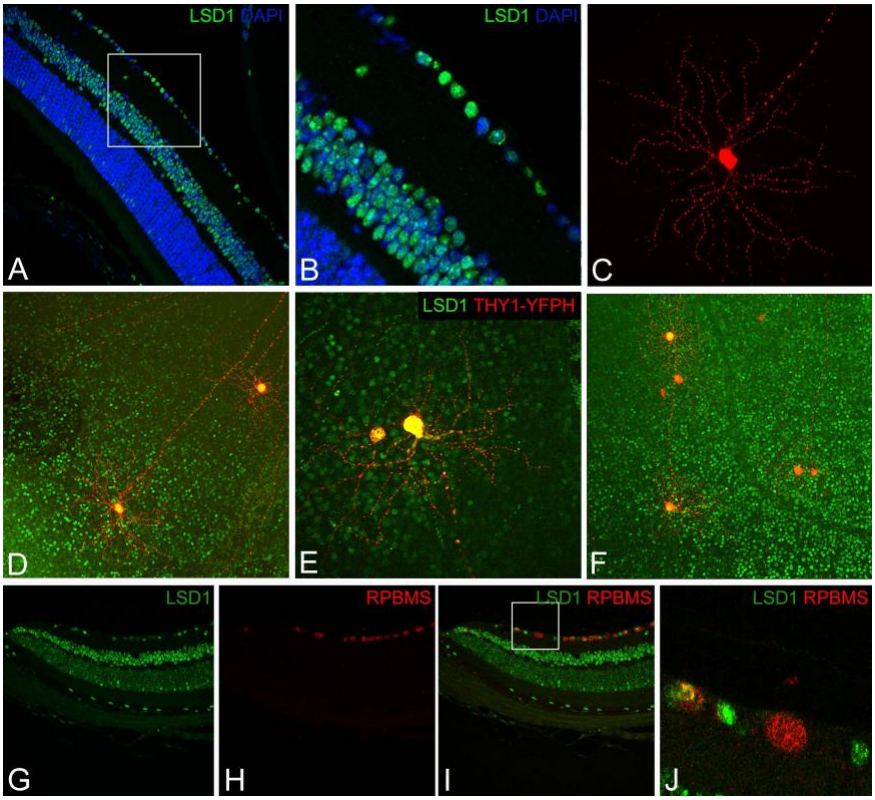

Figure 3.8: LSD1 expression varies among different retinal ganglion cells (RGCs) in the murine retina. Immunofluorescence staining of LSD1 (green) + DAPI nuclear stain (blue) in murine retinal section (panel 3.8A). Magnified image of GCL shows wide variability in the expression of LSD1 in adjacent RGCs (panel 3.8B). Thy1-YFPH expressing RGC stained with anti-GFP antibody (red) shows the dendrite pattern and axon projection of individual RGC (panel 3.8C). Co-localization of LSD1 (green) within Thy-YFPH expressing RGCs (red) in retina flatmounts show variability in relatively high, medium, and low LSD1 expression among adjacent RGCs (panels 3.8D – 3.8F). Co-localization of LSD1 (green) with a pan-RGC marker (RPBMS) shows that both RGCs and displaced amacrine cells in the ganglion cell layer (GCL) can express LSD1 (panels 3.8G – 3.8J).

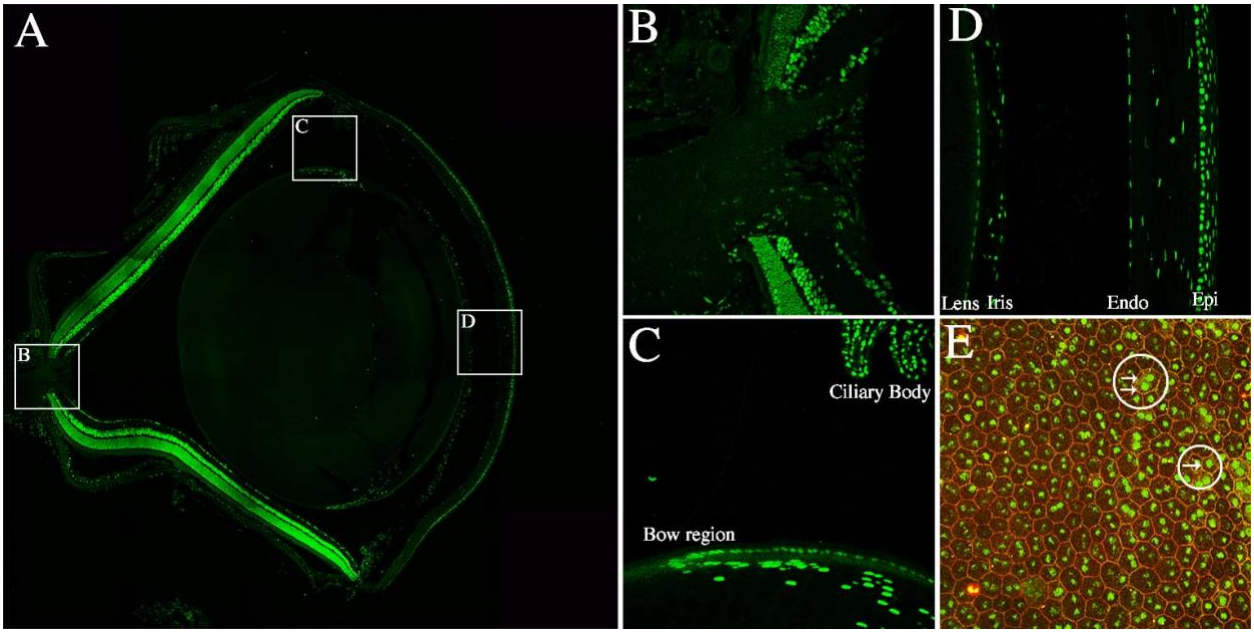

Figure 3.9: LSD1 is expressed throughout the murine eye. Immunofluorescence of LSD1 (green) and DAPI (blue) in P36 C57BL/6J retinal sections and RPE flatmount (panels 3.9A – 3.9E). 20X confocal image of an entire P36 murine eye stained with LSD1 (green) (panel 3.9A) showed LSD1 expression throughout many ocular structures. White boxes indicate areas from which 40X images were taken for Panels 3.9B – 3.9D to focus on various ocular structures outside of the retina including the optic nerve (panel 3.9B), lens (panel 3.9C), and cornea (3.9D). In panel C the bow region of the lens and ciliary body are labeled and in panel D the lens, iris, corneal endothelium and corneal epithelium are labeled. A 40X image from a RPE flatmount showed LSD1 nuclear expression in green and ZO-1 in red (panel 3.9E) to outline all RPE cell borders. Two white circles with arrows highlight different RPE cells that contain either one or two nuclei

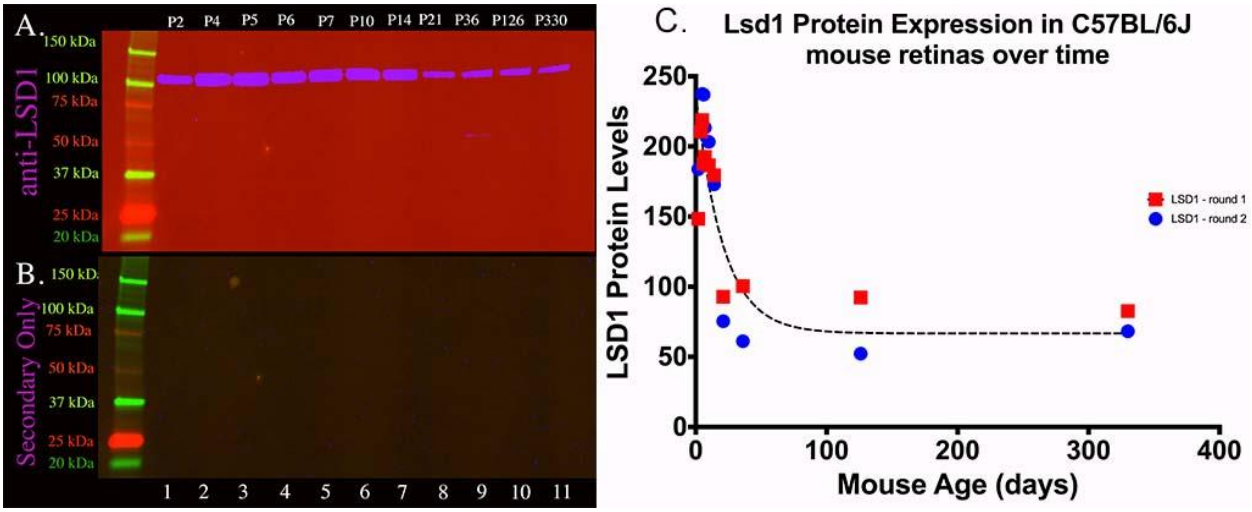

Supplemental Figure 3.1: LSD1 protein levels are highest in the retinoblast and gradually decreased across developmental time. Western blot analysis was conducted on C57BL/6J mouse retina samples from P2 – P330. Samples were probed with an anti-LSD1 antibody (single band - expected size: 107 kDa) (panel S3.1A) and secondary only controls detected no non-specific antibody binding (panel S3.1B). All 11 time points were probed for LSD1 expression using two independent sets of samples. Raw data for one set of samples is shown in S3.1A and data for the other set is not shown. Samples consist of 2 retinas taken from a single mouse and each set consists of 11 individual non-littermate mice. Quantification of results was achieved using densitometry Results from both sets are shown graphed independently (panel S3.1C). Overall, both sets show a similar trend where LSD1 levels peak in the retinoblast and plateau to a basement level by P21.

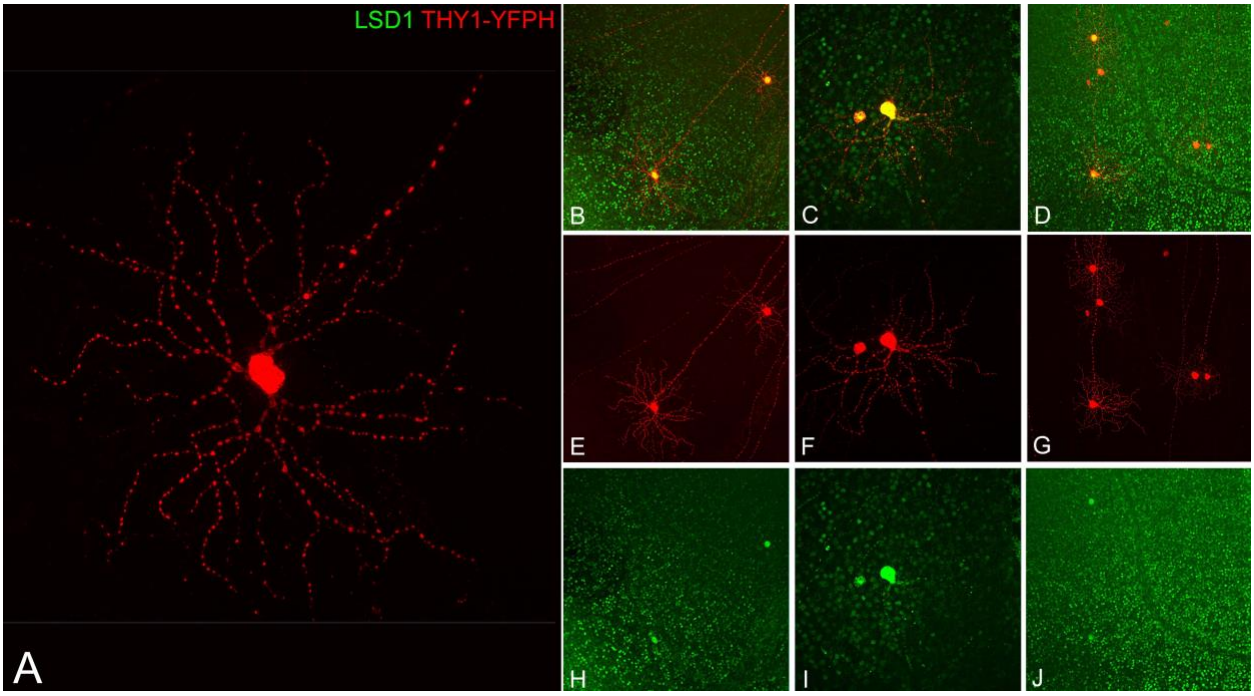

Supplemental Figure 3.2: Individual Channels of variable LSD1 expression among different retinal ganglion cells (RGCs). Immunofluorescence of THY1-YFPH expressing RGC stained with anti-GFP antibody (red) shows the dendrite pattern and axon projection of individual RGC (S3.2A). Individual channels of LSD1 alone (green) (S3.2H, S3.2I, S3.2J) THY1-YFPH alone (red) (S3.2E, S3.2F, S3.2G) and LSD1 + THY1-YFPH merged view (S3.2B, S3.2C, S3.2D).

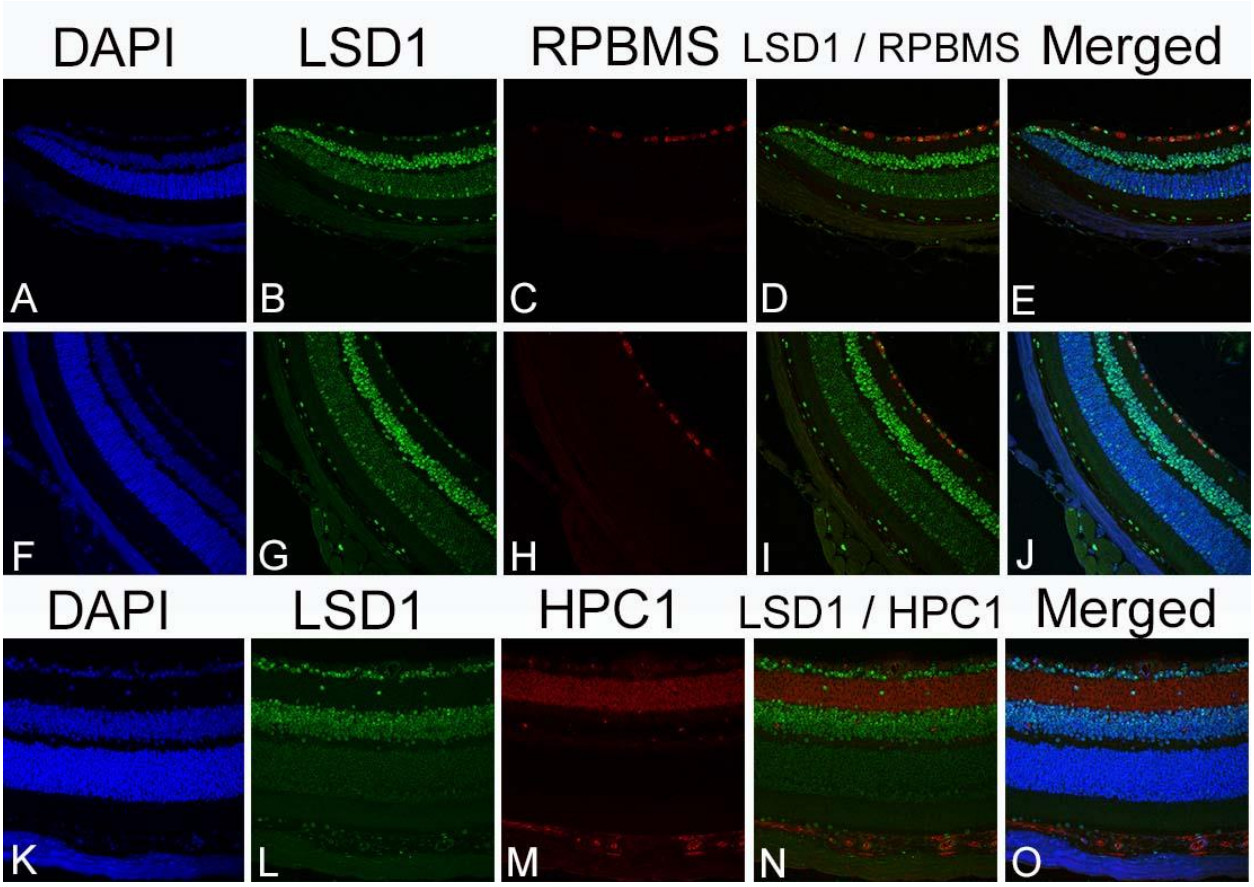

Supplemental Figure 3.3: Individual Channels of LSD1 co-labeled with pan-RGC marker, RPBMS, and displaced amacrine cell marker, HPC-1 (syntaxin). 40X confocal images of P90 C57BL/6J retina stained with DAPI (blue) (S3.3A, S3.3F), LSD1 (green) (S3.3B, S3.3G), and a pan-RGC marker, RPBMS (red) (S3.3C, S3.3H), as well as merged views of LSD1 + RPBMS (S3.3D, S3.3I) and LSD1 + RPBMS + DAPI (panels S3.3E, S3.3J) in both the peripheral retina (panels S3.3A-S3.3E) and central retina (S3.3F-S3.3J). Additional 40X confocal images of P90 C57BL/6J retina include co-labeling of LSD1 with a displaced amacrine cell marker HPC-1 (syntaxin) show individual panels for DAPI (blue) (S3.3K), LSD1 (green) (S3.3L), and HPC-1 (red) (S3.3M) as well as merged views of LSD1 + HPC-1 (S3.3N) and LSD1 + HPC-1 + DAPI (S3.3O).

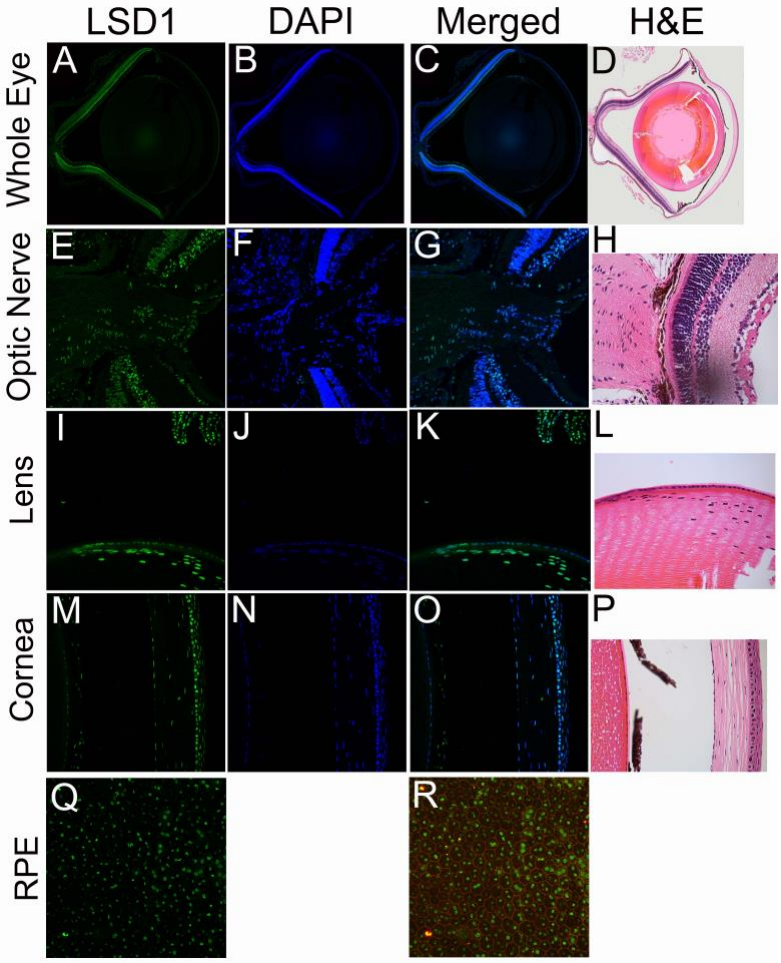

Supplemental Figure 3.4: Individual Channels of LSD1 expression in ocular structures outside of the retina in the murine eye. 20X confocal image of an entire P36 murine eye stained with LSD1 (green) (S3.4A), DAPI nuclear stain (blue) (S3.4B) and LSD1 + DAPI (S3.4C) along with an H&E image (S3.4D). Panels S3.4E-S3.4P are 40X images taken from the same P36 murine eye focused on various ocular structures outside of the retina including the optic nerve (S3.4E – S3.4G), lens (S3.4I – S3.4K), and cornea (S3.4M – S3.4O), along with the corresponding H&E image (S3.4H, S3.4L, S3.4P). A 40X image from a RPE flatmount shows LSD1 nuclear expression in green (S3.4Q), and LSD1 + ZO-1 in red (S3.4R) to outline all RPE cell borders.

Tukey's multiple comparisons test for LSD1 protein levels	Adjusted P Value	Significant?	Summary	Mean Diff.	95.00% CI of diff.
P2 vs. P7	0.0138	Yes	*	-0.2392	-0.4258 to -0.05268
P2 vs. P14	0.9588	No	ns	-0.03589	-0.2224 to 0.1507
P2 vs. P21	0.9129	No	ns	-0.04498	-0.2315 to 0.1416
P2 vs. P36	0.1338	No	ns	0.1476	-0.03894 to 0.3341
P7 vs. P14	0.0329	Yes	*	0.2033	0.01679 to 0.3899
P7 vs. P21	0.0412	Yes	*	0.1942	0.007694 to 0.3808
P7 vs. P36	0.0007	Yes	***	0.3868	0.2003 to 0.5734
P14 vs. P21	0.9998	No	ns	-0.009094	-0.1956 to 0.1774
P14 vs. P36	0.054	No	ns	0.1835	-0.003056 to 0.37
P21 vs. P36	0.043	Yes	*	0.1926	0.006038 to 0.3791

Supplementary Table 3.1: Two-way ANOVA with Tukey's multiple Comparison Test for LSD1 protein levels in the retina over time

* represents p value <0.05; ** represents p value <0.01; *** represents p value <0.001

Tukey's multiple comparisons test for H3K4me1 protein levels	Adjusted P Value	Significant?	Summary	Mean Diff.	95.00% CI of diff.
P2 vs. P7	>0.9999	No	ns	0.005378	-0.1905 to 0.2012
P2 vs. P14	0.0343	Yes	*	0.2116	0.01580 to 0.4075
P2 vs. P21	0.0235	Yes	*	0.2278	0.03191 to 0.4236
P2 vs. P36	0.1275	No	ns	0.157	-0.03885 to 0.3529
P7 vs. P14	0.039	Yes	*	0.2063	0.01042 to 0.4021
P7 vs. P21	0.0266	Yes	*	0.2224	0.02653 to 0.4182
P7 vs. P36	0.1449	No	ns	0.1516	-0.04423 to 0.3475
P14 vs. P21	0.9983	No	ns	0.01611	-0.1797 to 0.2120
P14 vs. P36	0.8639	No	ns	-0.05465	-0.2505 to 0.1412
P21 vs. P36	0.7267	No	ns	-0.07076	-0.2666 to 0.1251

Supplementary Table 3.2: Two-way ANOVA with Tukey's multiple Comparison Test for H3K4me1 protein levels in the retina over time

* represents p value <0.05; ** represents p value <0.01; *** represents p value <0.001

Tukey's multiple comparisons test for H3K4me2 protein levels	Adjusted P Value	Significant?	Summary	Mean Diff.	95.00% CI of diff.
P2 vs. P7	0.9888	No	ns	0.01735	-0.1121 to 0.1468
P2 vs. P14	0.0035	Yes	**	0.2085	0.07906 to 0.3379
P2 vs. P21	0.0026	Yes	**	0.2181	0.08865 to 0.3475
P2 vs. P36	0.0014	Yes	**	0.2404	0.1110 to 0.3698
P7 vs. P14	0.006	Yes	**	0.1911	0.06171 to 0.3206
P7 vs. P21	0.0044	Yes	**	0.2007	0.07131 to 0.3302
P7 vs. P36	0.0023	Yes	**	0.2231	0.09363 to 0.3525
P14 vs. P21	0.9988	No	ns	0.009597	-0.1198 to 0.1390
P14 vs. P36	0.9065	No	ns	0.03192	-0.09752 to 0.1614
P21 vs. P36	0.9719	No	ns	0.02232	-0.1071 to 0.1518

Supplementary Table 3.3: Two-way ANOVA with Tukey's multiple Comparison Test for H3K4me2 protein levels in the retina over time

* represents p value <0.05; ** represents p value <0.01; *** represents p value <0.001

References

1. Fahrner J, Bjornsson H. Mendelian Disorders of the Epigenetic Machinery: Tipping the Balance of Chromatin States. Annu Rev genomics Hum Genet. 2015;510(7503):84-91. doi:10.1038/nature13478.The
2. Li E, Zhang Y. DNA methylation in mammals. Cold Spring Harb Perspect Biol. 2014;6(5). doi:10.1101/cshperspect.a019133
3. Oliver VF, van Bysterveldt KA, Merbs SL. Epigenetics in Ocular Medicine. Med Epigenetics. 2016:391-412. doi:10.1016/B978-0-12-803239-8.00022-3
4. Wang J, Scully K, Zhu X, et al. Opposing LSD1 complexes function in developmental gene activation and repression programmes. Nature. 2007;446(7138):882-887. doi:10.1038/nature05671
5. Laurent B, Ruitu L, Murn J, et al. A Specific LSD1/KDM1A Isoform Regulates Neuronal Differentiation through H3K9 Demethylation. Mol Cell. 2015;57(6):957-970. doi:10.1038/nrg3575.Systems
6. Kalin JH, Wu M, Gomez A V., et al. Targeting the CoREST complex with dual histone deacetylase and demethylase inhibitors. Nat Commun. 2018;9(1). doi:10.1038/s41467-017-02242-4
7. Højfeldt JW, Agger K, Helin K. Histone lysine demethylases as targets for anticancer therapy. Nat Rev Drug Discov. 2013;12(12):917-930. doi:10.1038/nrd4154
8. Zheng Y-C, Ma J, Wang Z, et al. A Systematic Review of Histone Lysine-Specific Demethylase 1 and Its Inhibitors. Med Res Rev. 2015;35(5):1032-1071. doi:10.1002/med
9. Wang J, Hevi S, Kurash JK, et al. The lysine demethylase LSD1 (KDM1) is required for maintenance of global DNA methylation. Nat Genet. 2009;41(1):125-129.

doi:10.1038/ng.268

10. Wang Y, Wu Q, Yang P, et al. LSD1 co-repressor Rcor2 orchestrates neurogenesis in the developing mouse brain. Nat Commun. 2016;7:10481. doi:10.1038/ncomms10481
11. Sun G, Alzayady K, Stewart R, et al. Histone Demethylase LSD1 Regulates Neural Stem Cell Proliferation. Mol Cell Biol. 2010;30(8):1997-2005. doi:10.1128/MCB.01116-09
12. He Y, Zhao Y, Wang L, et al. LSD1 promotes S-phase entry and tumorigenesis via chromatin co-occupation with E2F1 and selective H3K9 demethylation. Oncogene. 2017;(August):1-10. doi:10.1038/onc.2017.353
13. Cho HS, Suzuki T, Dohmae N, et al. Demethylation of RB regulator MYPT1 by histone demethylase LSD1 promotes cell cycle progression in cancer cells. Cancer Res. 2011;71(3):655-660. doi:10.1158/0008-5472.CAN-10-2446
14. Rusconi F, Grillo B, Ponzoni L, et al. LSD1 modulates stress-evoked transcription of immediate early genes and emotional behavior. Proc Natl Acad Sci U S A. 2016;113(13):1511974113-. doi:10.1073/pnas.1511974113
15. Wasson JA, Simon AK, Myrick DA, et al. Maternally provided LSD1/KDM1A enables the maternal-to-zygotic transition and prevents defects that manifest postnatally. Elife. 2016;5(JANUARY2016):1-25. doi:10.7554/eLife.08848
16. Chong JX, Yu J, Lorentzen P, Park KM, Jamal SM, Tabor HK, et al. Gene discovery for Mendelian conditions via social networking: de novo variants in KDM1A cause developmental delay and distinctive facial features. Genet Med 2016;18:788–95. PMCID:26656649.
17. Tunovic S, Barkovich J, Sherr EH, Slavotinek AM. De novo ANKRD11 and KDM1A gene mutations in a male with features of KBG syndrome and Kabuki syndrome. Am J

Med Genet Part A. 2014;164(7):1744-1749. doi:10.1002/ajmg.a.36450

18. Christopher MA, Myrick DA, Barwick BG, et al. LSD1 protects against hippocampal and cortical neurodegeneration. Nat Commun. 2017;8(1):1-13. doi:10.1038/s41467-017-00922-9

19. Islam MM, Zhang C-L. TLX: A master regulator for neural stem cell maintenance and neurogenesis. Biochim Biophys Acta - Gene Regul Mech. 2015;1849(2):210-216. doi:10.1016/j.bbagrm.2014.06.001

20. Yokoyama A, Takezawa S, Schule R, Kitagawa H, Kato S. Transrepressive Function of TLX Requires the Histone Demethylase LSD1. Mol Cell Biol. 2008;28(12):3995-4003. doi:10.1128/MCB.02030-07

21. Popova EY, Pinzon-Guzman C, Salzberg AC, Zhang SS-M, Barnstable CJ. LSD1-Mediated Demethylation of H3K4me2 Is Required for the Transition from Late Progenitor to Differentiated Mouse Rod Photoreceptor. Mol Neurobiol. 2016;53(7):4563-4581. doi:10.1007/s12035-015-9395-8

22. Tsutsumi T, Iwao K, Hayashi H, et al. Potential Neuroprotective Effects of an LSD1 Inhibitor in Retinal Ganglion Cells via p38 MAPK Activity. Investig Opthalmology Vis Sci. 2016;57(14):6461. doi:10.1167/iovs.16-19494

23. Sun N, Shibata B, Hess JF, Fitzgerald PG. An alternative means of retaining ocular structure and improving immunoreactivity for light microscopy studies. Mol Vis. 2015;(April):428-442.

24. Barnstable CJ, Dräger UC. Thy-1 antigen: A ganglion cell specific marker in rodent retina. Neuroscience. 1984;11(4):847-855. doi:10.1016/0306-4522(84)90195-7

25. Feng G, Mellor RH, Bernstein M, et al. Imaging neuronal sets in transgenic mice

expressing multiple spectral variants of GFP. Neuron. 2000;28(1):41-51.

26. Boatright JH, Dalal N, Chrenek MA, et al. Methodologies for analysis of patterning in the mouse RPE sheet. Mol Vis. 2015;21(October 2014):40-60. http://www.ncbi.nlm.nih.gov/pubmed/25593512%5Cnhttp://www.pubmedcentral.nih.gov/articlerender.fcgi?artid=PMC4301600.

27. Gooding SW, Chrenek MA, Ferdous S, Nickerson JM, Boatright JH. Set screw homogenization of murine ocular tissue , including the whole eye. Mol Vis. 2018;(October):690-699.

28. Smith P, Krohn R, Hermanson G, et al. Measurement of Protein Using Bicinchoninic Acid. Anal Biochem. 1985;85:76-85. doi:10.1016/0003-2697(85)90442-7

29. LAEMMLI UK. Cleavage of Structural Proteins during the Assembly of the Head of Bacteriophage T4. Nature. 1970;227:680. http://dx.doi.org/10.1038/227680a0.

30. Towbin H, Staehelin T, Gordon J. Electrophoretic transfer of proteins from polyacrylamide gels to nitrocellulose sheets: procedure and some applications. Proc Natl Acad Sci. 1979;76(9):4350-4354. doi:10.1073/pnas.76.9.4350

31. Shi Y, Lan F, Matson C, et al. Histone demethylation mediated by the nuclear amine oxidase homolog LSD1. Cell. 2004;119(7):941-953. doi:10.1016/j.cell.2004.12.012

32. Jin Y, Kim TY, Kim MS, Kim MA, Park SH, Jang YK. Nuclear import of human histone lysine-specific demethylase LSD1. J Biochem. 2014;156(6):305-313. doi:10.1093/jb/mvu042

33. Aldiri I, Xu B, Wang L, et al. The Dynamic Epigenetic Landscape of the Retina During Development, Reprogramming, and Tumorigenesis. Neuron. 2017;94(3):550-568.e10. doi:10.1016/j.neuron.2017.04.022

34. Hargreaves DC, Crabtree GR. ATP-dependent chromatin remodeling: Genetics, genomics and mechanisms. Cell Res. 2011;21(3):396-420. doi:10.1038/cr.2011.32

35. Carter-Dawson LD, LaVail MM. Rods and cones in the mouse retina. I. Structural analysis using light and electron microscopy. J Comp Neurol. 1979;188(2):245-262. doi:10.1002/cne.901880204

36. Jeon C-J, Strettoi E, Masland RH. The Major Cell Populations of the Mouse Retina. J Neurosci. 1998;18(21):8936-8946. doi:10.1523/jneurosci.18-21-08936.1998

37. Schlamp CL, Montgomery AD, Mac Nair CE, Schuart C, Willmer DJ, Nickells RW. Evaluation of the percentage of ganglion cells in the ganglion cell layer of the rodent retina. Mol Vis. 2013;19(March):1387-1396. http://www.ncbi.nlm.nih.gov/pubmed/23825918%0Ahttp://www.pubmedcentral.nih.gov/articlerender.fcgi?artid=PMC3695759.

38. Rodriguez, Allen R ; Muller, Luis Perez de Sevilla ; Brecha NC. The RNA Binding Protein RBPMS Is a Selective Marker of Ganglion Cells in the Mammalian Retina. Vol 522.; 2015. doi:10.1002/cne.23521.The

39. Barnstable CJ, Hofstein R, Akagawa K. A marker of early amacrine cell development in rat retina. Dev Brain Res. 1985;20(2):286-290. doi:10.1016/0165-3806(85)90116-6

40. Cvekl A, Ashery-Padan R. The cellular and molecular mechanisms of vertebrate lens development. Development. 2014;141(23):4432-4447. doi:10.1242/dev.107953

41. Bodenstein L, Sidman RL. Growth and development of the mouse retinal pigment epithelium. Dev Biol. 1986;121(1):192-204. doi:10.1016/0012-1606(87)90153-9

42. Rusconi F, Grillo B, Toffolo E, Mattevi A, Battaglioli E. NeuroLSD1: Splicing-Generated Epigenetic Enhancer of Neuroplasticity. Trends Neurosci. 2016;xx(1):1-11.

doi:10.1016/j.tins.2016.11.002

43. Hartl D, Krebs AR, Jüttner J, Roska B, Schübeler D. Cis-regulatory landscapes of four cell types of the retina. Nucleic Acids Res. 2017;45(20):11607-11621. doi:10.1093/nar/gkx923

44. Trimarchi JM, Stadler MB, Cepko CL. Individual retinal progenitor cells display extensive heterogeneity of gene expression. PLoS One. 2008;3(2). doi:10.1371/journal.pone.0001588

45. Young R. Cell Proliferation During Postnatal Development of the Retina in the Mouse. Dev brain res. 1985;21:229-239.

46. Young RW. Cell differentiation in the retina of the mouse. Anat Rec. 1985;212:199-205. doi:10.1002/ar.1092120215

47. Bassett EA, Wallace VA. Cell fate determination in the vertebrate retina. Trends Neurosci. 2012;35(9):565-573. doi:10.1016/j.tins.2012.05.004

48. Mo A, Luo C, Davis FP, et al. Epigenomic landscapes of retinal rods and cones. Elife. 2016;5(MARCH2016):1-29. doi:10.7554/eLife.11613

49. Falk M, Feodorova Y, Naumova N, et al. Heterochromatin drives organization of conventional and inverted nuclei. bioRxiv. 2018:1-19.

50. Solovei I, Wang AS, Thanisch K, et al. LBR and lamin A/C sequentially tether peripheral heterochromatin and inversely regulate differentiation. Cell. 2013;152(3):584-598. doi:10.1016/j.cell.2013.01.009

51. Solovei I, Kreysing M, Lanctôt C, et al. Nuclear Architecture of Rod Photoreceptor Cells Adapts to Vision in Mammalian Evolution. Cell. 2009;137(2):356-368. doi:10.1016/j.cell.2009.01.052

52. Sterling P. How Retinal Circuits Optimize the Transfer of Visual Information. (Chalupa L., Werner J., eds.). Cambridge, MA: MIT Press; 2003.

53. Eberhart A, Feodorova Y, Song C, et al. Epigenetics of eu- and heterochromatin in inverted and conventional nuclei from mouse retina. Chromosom Res. 2013;21(5):535-554. doi:10.1007/s10577-013-9375-7

54. Popova EY, Xu X, DeWan AT, et al. Stage and Gene Specific Signatures Defined by Histones H3K4me2 and H3K27me3 Accompany Mammalian Retina Maturation In Vivo. PLoS One. 2012;7(10). doi:10.1371/journal.pone.0046867

55. Levick WR. Receptive Fields And Trigger Features Of Ganglion Cells In The Visual Streak Of The Rabbit's Retina. J Physiol. 1967;188:285-307.

56. Sanes JR, Masland RH. The Types of Retinal Ganglion Cells: Current Status and Implications for Neuronal Classification. Annu Rev Neurosci. 2015;38(1):221-246. doi:10.1146/annurev-neuro-071714-034120

57. Bae JA, Mu S, Kim JS, et al. Digital Museum of Retinal Ganglion Cells with Dense Anatomy and Physiology. Cell. 2018;173(5):1293-1306.e19. doi:10.1016/j.cell.2018.04.040

58. Zhang H, Dai X, Qi Y, He Y, Du W, Pang JJ. Histone deacetylases inhibitors in the treatment of retinal degenerative diseases: Overview and perspectives. J Ophthalmol. 2015;2015(Table 1). doi:10.1155/2015/250812

59. Sancho-Pelluz J, Alavi M V., Sahaboglu A, et al. Excessive HDAC activation is critical for neurodegeneration in the rd1 mouse. Cell Death Dis. 2010;1(2):1-9. doi:10.1038/cddis.2010.4

60. Sancho-Pelluz J., F. P-D. HDAC Inhibition Prevents Rd1 Mouse Photoreceptor

Degeneration. Vol 723.; 2012. doi:10.1007/978-1-4614-0631-0_44

61. Zheng S, Xiao L, Liu Y, et al. DZNep inhibits H3K27me3 deposition and delays retinal degeneration in the rd1 mice article. Cell Death Dis. 2018;9(3). doi:10.1038/s41419-018-0349-8

Chapter IV: Pan-retinal deletion of Lsd1 during retinal development leads to visual function and morphological defects

Salma Ferdous, Isabelle D. Gefke, Micah A. Chrenek, Hans E. Grossniklaus, Jeffrey H. Boatright, John M. Nickerson

Abstract

The purpose of this study was to investigate the role of *Lsd1* in retinal development by deleting *Lsd1* either in a whole body heterozygous manner or in a retina-specific homozygous manner. Lysine specific demethylase 1 (*Lsd1*) is a histone demethylase that can demethylate mono- and di-methyl groups on H3K4 and H3K9. Previously, we have shown that *Lsd1* is ubiquitously expressed throughout the developing retinoblast and in the majority of mature retinal neurons (Ferdous et. al IOVS 2019). Using a *Chx10-Cre* driver line, we generated a novel transgenic mouse line to delete *Lsd1* in the retinoblast lineage. We also tested *Lsd1* +/- heterozygous mice that were received from a collaborator. We hypothesize that because *Lsd1* is important in neuronal development, one or both of these mouse strains will exhibit retina specific functional or morphological defects. We tested adult mice for visual function, using electroretinograms (ERGs), and *in vivo* imaging to obtain SD-OCT and cSLO images. Afterwards, eyes were enucleated and fixed for H&E staining. Although we did not observe any abnormalities in the *Lsd1* +/- animals, we did observe defects in the *Chx10-Cre Lsd1 loxP* animals. We observed a marked reduction in ERGs a- and b- waves in both scotopic and photopic conditions as well as cone flicker responses at P30 and P45 compared to Cre negative littermate controls. This decrease in visual function is corroborated with reductions in total retinal thickness and ONL thickness as observed in both SD-OCT images and H&E stained sagittal sections. Our data supports the notion that *Lsd1* is necessary for neuronal development specifically in the retina as adult *Chx10-Cre Lsd1 loxP* mice show impaired visual function and retinal morphology.

Introduction

Previously, we explored the expression of *Lsd1* in wild-type mice and found that *Lsd1* is expressed in all retinal progenitor cells during retinal development and in the majority of mature retinal neurons after development is complete. We also observed *Lsd1* expression in other major ocular structures, such as the cornea, lens, and retinal pigmented epithelium (RPE)[1]. Based on these observations, we hypothesize that *Lsd1* is important in the development, maintenance and function of ocular structures, especially the retina and that deletion of *Lsd1* will result in abnormalities in the structures. Here we investigated the effects of deleting *Lsd1* globally in a heterozygous manner or by deleting it throughout the entire retina during ocular development.

Total homozygous deletion of *Lsd1* leads to embryonic lethality at ~E.9.5 likely due to cardiac problems[2]. Previously, no gross abnormalities were observed in the *Lsd1* heterozygote deletion mice; however, ocular morphology and function have never been assessed in this strain. Because no gross abnormalities have been observed in the *Lsd1* heterozygous mice, we hypothesize that these mice will show no ocular or visual defects; however, the eye may be uniquely sensitive to the absence of one copy of the *Lsd1* gene therefore testing is warranted. Additionally, we decided to investigate whether homozygous deletion specifically in the retina would have any effects. Using the Cre-Lox system[3], we deleted *Lsd1* in the majority of retinal progenitor cells using a *Chx10-Cre* driver mouse line. *Chx10* was first cloned in 1994 and is a homeobox containing transcription factor that is specifically expressed in the neuroretina, with limited expression in the pons, medulla, and spinal cord[4]. The *Chx10* protein is expressed as early at embryonic day 9.5 (E9.5) in the mouse retina and expression increases by 3-4 fold between post-natal days 0 and 6 (P0-P6)[4]. Expression then begins to decrease around P8 when rod outer

segments start to differentiate[4]. *Chx10* is expressed in the majority of retinal progenitor cells (RPCs) during mouse retinal development, but is absent in almost all post-mitotic retinal cells except bipolar cells and some Muller glial cells[5]. Ectopic expression of *Chx10* in both neonatal mouse and rat retinas induced bipolar cell differentiation at the expense of rod photoreceptor differentation[6].

Mice with the or^{J} allele (*Chx10*$^{orJ/orJ}$ mice) have a nonsense mutation in the *Chx10* gene and these mice have reduced RPC proliferation and an absence of differentiated bipolar cells, ultimately leading to microphthalmia, a cataractous lens, significant retinal thinning, and no optic nerve[5,7]. *Chx10*$^{orJ/orJ}$ mice had misexpression of critical photoreceptor related genes, including *Crx, Rho, Pdeb*, and *Arr3*[8]. The expression of *Chx10* in the adult human is identical to the adult mouse, where expression is limited to the inner nuclear layer (INL), specifically along the outer edge where bipolar cell nuclei are predominant and *Chx10* mutations in humans, like in mice, cause congenital microphthalmia (OMIM 309700)[9,10]. *Chx10* mutations in humans have been independently found in a number of probands with congenital microphthalmia[11–15]; however, *Chx10* mutations are relatively rare among this patient population[16]. Although patients are rarely tested for visual function, in a handful of patients with autosomal recessive congenital microphthalmia, visual function tests showed no detectable ERG or VEP responses. Interestingly, heterozygous carrier patients have been shown to have an inner retinal dystrophy, which is possibly due to semi-dominant expression of a particular *Chx10* mutation[14,15].

In addition to being important for RPC proliferation and neuroretinal cell identity, *Chx10* is also critical for retinal pigment epithelium (RPE) specification by repressing *Mitf*, a transcription

factor that is necessary for RPE cell differentiation[17]. Misexpression of *Chx10* in the chick presumptive RPE can induce and maintain an ectopic neuroretinal-like tissue[18].

The *Chx10* Cre driver mouse line expresses Cre recombinase as early as embryonic day 14.5 (E14.5) in the majority of retinal progenitor cells[19]. We hypothesize that the deletion of *Lsd1* could result in either: 1) Retinal degeneration due to retinal progenitor cells being unable to proliferate and/or cells undergoing apoptosis due to aberrant epigenomic regulation or 2) Improper differentiation of retinal progenitor cells into mature retinal neurons leading to an over- or under-representation of certain neuronal populations, specifically in the photoreceptors. This hypothesis is based on work done by *Popova et al.* where post-natal day 0 (P0) C57Bl/6J mouse retinal explants were treated with a pharmacological *Lsd1* inhibitor, tranylcypromide[20–25]. Based on these experiments, *Popova et al.* proposed the following mechanism where the normal demethylase activity of *Lsd1* on H3K4 methyl modifications inhibits the Notch/Hes1 pathway and allow the majority of retinal progenitor cells to commit and differentiate into rod photoreceptors. The pharmacological inhibition of *Lsd1* allowed the continual expression of the Notch/Hes1 pathway and inhibited rod photoreceptor development (Figure 4.1)[26].

For this project, we generated new transgenic *Chx10-Cre Lsd1 loxP* mice by breeding *Chx10-Cre* mice[19] with *Lsd1* floxed mice[2] to generate litters where half of the mice are *Chx10-Cre* positive (to serve as the experimental group) and half of the mice are *Chx10-Cre* negative (to serve as littermate controls) (Figure 4.2).

Methods

Animal studies: Mouse housing, experiments, and handling were approved by the Emory University Institutional Animal Care and Use Committee, and the studies were conducted in adherence with Association for Research in Vision and Ophthalmology (ARVO) and followed guidance and principles of the Association for Assessment and Accreditation of Laboratory Animal Care (AAALAC). *Lsd1* heterozygous mice (*Lsd1*+/-) were obtained from the Katz Lab at Emory University. These animals were on a mixed 129Sv/C57 background; therefore, they were backcrossed 5 generations to C57Bl/6J animals to reduce variability in genetic background. *Lsd1 loxP* mice were obtained from the Boss Lab at Emory University and *Chx10-Cre* mice were obtained from the Iuvone Lab at Emory University. Both the *Lsd1 loxP* and *Chx10-Cre* mouse lines were on a C57Bl/6J genetic background therefore no backcrossing was necessary. Mice were maintained on a 12-h light/dark cycle at 23°C, and standard mouse chow (Lab Diet 5001; PMI Nutrition Inc., LLC, Brentwood, MO) and water was provided *ad libitum*. The mice were managed and housed by Emory University Division of Animal Resources. Adult mice were euthanized using CO_2 gas asphyxiation for 5 minutes followed by cervical dislocation.

Electroretinograms: Mice were dark-adapted overnight the day before ERGs were performed. Each mouse was anesthetized using intraperitoneal (IP) injections of 100 mg/kg of ketamine and 15 mg/kg xylazine (ketamine; KetaVed from Patterson Veterinary, Greeley, CO; xylazine from Patterson Veterinary, Greeley, CO).

Once anesthetized, proparacaine (1%; Akorn Inc.) and tropicamide (1%; Akorn Inc.) eye drops were administered to reduce eye sensitivity and dilate the pupils. Mice were placed on a heating

pad (39 °C) under dim red light provided by the overhead lamp of the Diagnosys Celeris system (Diagnosys, LLC, Lowell, MA, USA). The light guided electrodes were placed in contact with individual eyes; the corneal electrode for the contralateral eye acts the reference electrode. Full-field ERGs were recorded for the scotopic condition (stimulus intensity: 0.001, 0.005, 0.01, 0.1, 1, and 10 cd s/m^2; flash duration 4 milliseconds). Signals were collected for 0.3 seconds in steps 1 to 5 and 5 seconds for step 6 after light flashes. Scotopic a-, b-, and c-waves were captured and analyzed. After scotopic testing, mice were light-adapted for 10 minutes and then full-field ERGs were recorded for the photopic conditions (stimulus intensity: 3 and 10 cd s/m^2) to capture photopic a- and b-waves as well as cone flicker responses. After recordings, each mouse was placed in its home cage on top of a heating pad (39°C) to recover from anesthesia.

In vivo ocular imaging: Mice were anesthetized using intraperitoneal (IP) injections of 100 mg/kg of ketamine and 15 mg/kg xylazine as above. Once anesthetized, proparacaine and tropicamide eye drops were administered as a topical anesthetic and to dilate the pupils as above. A MicronIV SD-OCT system with fundus camera (Phoenix Research Labs, Pleasanton, CA) was used to obtain both fundus photos and retinal morphology for both eyes. Images were taken after clear visualization of the fundus with a centered optic nerve. Circular scans approximately 100 microns from the optic nerve head were taken and fifty scans were averaged together. The retinal morphology images were analyzed for both total retinal thickness and photoreceptor layer thickness using Photoshop CS6 (Adobe Systems Inc., San Jose, CA) by an individual who was masked to sample identity. The number of pixels were converted into micrometers by multiplying by a conversion factor (1 pixel = 1.3um).

Western blot sample preparation: Retinas were dissected from each eye separately and placed in

a round bottom 0.5 ml screwcap tube with both retinas from the same animal pooled in one tube (Eppendorf Catalog #022363344). Homogenization buffer was prepared from 10mL RIPA Buffer, one tablet of protease inhibitor (compete Mini protein inhibitor Catalog #118361530001) and one tablet of phosphatase inhibitor (Roche PhosSTOP EASypack #04906845001). 75μL of homogenization buffer was added to each pair of retinas along with one 4.7 mm ferric bead in a screw cap tube. The homogenizer was a QIAGEN TissueLyser LT[27]. The retinas were macerated at 50 oscillations per second for 3 minutes at 4 °C. Afterwards, the ferric bead was removed using a magnet and samples were centrifuged at 4 °C for 3 minutes (10,000 ×g) to remove particulate debris. Supernatants were collected and transferred to fresh 500 μL Eppendorf tubes and stored at -80°C until further use.

Protein concentration determination: Overall protein concentration of samples was determined using a Bicinchoninic Acid (BCA) Assay[28]. A 1:10 dilution of the supernatant was prepared with homogenization buffer (described above) for quantification. 10 μL of each diluted sample was pipetted in an individual well of a 96-cell culture plate (Thermo Scientific #165306) in triplicate along with standards from a Pierce BCA Protein Assay Kit (ThermoFisher Catalog #23227) prepared to manufacturer's instructions. 200 μL of BCA working reagent, also prepared to manufacturer's instructions, was added to each well and the entire culture plate was incubated at 37°C for 30 minutes before absorbance at 562 nm was measured using a Synergy H1 Hybrid Plate Reader (BioTek).

SDS polyacrylamide gel electrophoresis (SDS-PAGE): The sample supernatants were adjusted to a protein concentration of 0.8 mg/mL in 200 μL using 100 μL of 2X Laemelli buffer[29] prepared with 2-mercaptoethanol (ThermoFisher #21985023) (50μL of 14.3 M 2-mercaptoethanol and

950 μL 2X Laemelli buffer[29]) and cold homogenization buffer (described above) and were stored at -20ºC up to a week following preparation. Immediately before electrophoresis samples were heated for 5 minutes at 95ºC in a thermocycler.

Running and staining conditions: 30μL of each sample was loaded into individual lanes onto a pre-cast Criterion gel (BioRad TGX Stain Free Gel 4-15% Catalog #567-1083) as well as 10 μL of ladder (BioRad Catalog #1610376) and run at 100 V for 90 min. Samples were then transferred for 7 minutes onto PVDF blotting membrane[30] using Trans-blot turbo pack (BioRad Catalog #170-4157) and Trans-blot Turbo Transfer System (BioRad). The gel was checked pre- and post-transfer to assure that a good transfer of proteins from the gel to the membrane was achieved.

Prior to primary antibody incubation, membranes were blocked for 2 hours at room temperature with 5% (W/V) instant nonfat dry milk (Quality Biological Catalog #A614-1005) in TBST (Tris buffered saline (TBS) (Biorad #1706435) with 0.1% (V/V) Tween 20 (Fisher Scientific BP337-100)). Primary antibodies (anti-LSD1 Abcam 129195 and anti-beta Actin Cell Signaling #4970) were diluted with 5% milk in TBST, and membranes were incubated overnight on a 4°C shaker. The membrane was washed three times for 5 minutes each using 0.1% TBST. HRP conjugated secondary antibodies were diluted with 5% milk in TBST and membranes were incubated 1-2 hours at room temperature on a shaker. The membrane was washed three times for 5 minutes each using 0.1% TBST. 10 mL of Luminata Crescendo Western HRP substrate (EMD Millipore Catalog #WBLUR0500) was applied to the membrane for 5 min. The membrane was imaged in chemiluminescence mode using MP ChemiDoc Imaging System (BioRad). Exposure times varied from 30 to 180 seconds. In order to re-probe the same membrane with multiple antibodies,

after imaging, 10mL of Restore western blot stripping buffer (Thermo Scientific Catalog #21059) was applied to the blot for 10 minutes, the blot was washed for 5 minutes using 0.1% TBST, and then blocked with 5% milk (W/V) in TBST and incubated with the appropriate primary and secondary antibody as described above.

Ocular sectioning and histology: Eyes were enucleated and placed in 10mL of chilled 95% methanol 5% acetic acid for 4 days at -80ºC. Afterwards, samples were dehydrated twice in 100% ethanol for twenty minutes, placed in xylene twice for twenty minutes, and then embedded in paraffin. Sagittal plane sections were cut at 5 micron increments. Sagittal sections containing the optic nerve were selected for further staining to ensure consistency across all samples. Sections were then stained with hematoxylin and eosin (H&E) to visualize retinal morphology. Nuclei in the outer nuclear layer (ONL), inner nuclear layer (INL), and ganglion cell layer (GCL) were counted manually by an individual who was masked to sample identity. Only nuclei within a 100 micron section were counted using Photoshop CS6 at regularly spaced intervals 250 microns apart from the optic nerve in both the inferior and superior directions.

Statistical Analysis: Statistical analysis was conducted using Prism 8.4.2 on Mac OS X (GraphPad Software, Inc., La Jolla, CA, USA). All data are summarized as mean ± standard deviation (SD) and individual statistical tests are listed in figure legends. P values < 0.05 were considered to be statistically significant. Each sample group member is an independent mouse.

Results

We obtained global *Lsd1* heterozygous deletion mice from David Katz' lab at Emory University and backcrossed the mice onto a C57BL/6J background. These mice have a premature STOP codon in exon 13 and this has been verified via polymerase chain reaction (PCR) genotyping of the animals. After genotyping, we determined whether *Lsd1* (+/-) mice had a reduced LSD1 protein level compared with their wild-type littermates. We performed western blotting to examine LSD1 expression using post-natal day 67 (P67) *Lsd1* (+/+) littermate controls and *Lsd1* (+/-) heterozygous mouse retinas. In Figure 4.3, we observe relatively uniform expression of LSD1 and GAPDH loading control across all samples at the correct molecular weights, 107 kDa and 37 kDa respectively (Panel 4.3A). After quantification using densitometry, we observed no significant difference in protein levels between the *Lsd1* (+/+) controls and *Lsd1* (+/-) mice (Panel 4.3B; p-value = 0.2696). Although the protein levels of LSD1 are relatively normal, we wanted to determine whether these mice had any abnormalities in retinal morphology or function. We conducted *in vivo* imaging using the Phoenix MicronIV system to obtain Fundus photos and SD-OCT images from P85 animals. In Figure 4.4, we detected no obvious differences between the retinal layers in *Lsd1* (+/+) controls and *Lsd1* (+/-) mice. All retinal layers were discrete and intact regardless of genotype and the Fundus photos had similar coloration and no obvious signs of damage or mottling. Finally, to observe retinal morphology at higher resolution, we stained P90 mouse retinas from both *Lsd1* (+/+) controls and *Lsd1* (+/-) mice with hematoxylin and eosin (H&E). In Figure 4.5, we observed all intact retinal layers of comparable thickness between the two genotypes. There were no signs of degeneration or abnormalities in the cell morphology or structure. Taken all together, these results indicate that *Lsd1* is

haplosufficient in the eye and one allelic copy of the gene does not result in a reduction of *Lsd1* protein levels and in turn, does not alter retinal structure.

For the *Chx10-Cre Lsd1 loxP* mice, we first tested whether or not we were able to successfully delete Lsd1 from the retina. Retinas were isolated from P30 mice from two control strains, *Chx10-Cre* only and *Lsd1 loxP* only, and one experimental strain *Chx10-Cre Lsd1 loxP*. Western blotting probed for LSD1 protein expression and beta-Actin was used as a loading control (Figure 4.6). In the five *Chx10-Cre* only retinas and five *Lsd1 loxP* retinas, the LSD1 protein bands were at the correct protein size of 107 kDa; however, in all 6 *Chx10-Cre Lsd1 loxP* retinas, a truncated protein was found at ~27 kDa.

Animals were tested at P30 and P45 respectively for visual function using electroretinograms (ERGs) and *in vivo* retinal morphology (SD-OCT and cSLO imaging). ERGs were tested in both scotopic and photopic conditions and measured a-, b-, and c-waves. Raw ERG waveforms in response to a 10 cd s/m^2 light flash showed relatively normal ERG responses in the *Lsd1 loxP* control animals; however, the *Chx10-Cre Lsd1 loxP* animals had almost no visual response (Figure 4.7). In scotopic conditions with increasing light flash intensities, we observed significant decreases in the a- and b-wave of the *Chx10-Cre Lsd1 loxP* animals when compared to littermate controls indicating dysfunction in the rod photoreceptors and rod bipolar cells (Figure 4.8). Additionally, there was a significant decrease in c-wave response after a 10 cd s/m^2 light flash in the experimental animals indicating dysfunction in their retinal pigmented epithelium (RPE) (Figure 4.8). We also observed abnormalities in the ERG waveforms of *Chx10-Cre Lsd1 loxP* mice when compared to their littermate controls in photopic conditions

(Figure 4.9) as well significantly reduced cone flicker amplitudes (Figure 4.10), which suggests functional abnormalities in the cone photoreceptors.

All of the significant visual function defects in the *Chx10-Cre Lsd1 loxP* mice suggest that there were developmental abnormalities in the retinal neurons, specifically the photoreceptors and bipolar cells. To determine whether there were any retinal morphology defects that accounted for the retinal dysfunction, animals were tested at P30 and P45 for *in vivo* retinal morphology. Fundus photos and SD-OCT images were taken, and the total retinal thickness and outer nuclear layer thickness were quantified by a masked individual. In the Fundus photos, we observed a more mottled and speckled appearance in the *Chx10-Cre Lsd1 loxP* animals compared to the controls. The SD-OCT images revealed a dramatically degenerated and hyper-reflective retina in the *Chx10-Cre Lsd1 loxP* animals compared to the controls and there was a significant reduction in total retinal thickness and outer nuclear thickness (Figure 4.11).

After the *in vivo* work, we collected eyes for post-mortem analysis. We first stained five micron thick sagittal retinal sections with hematoxylin & eosin (H&E) to observe retinal morphology in the P30 animals (Figure 4.12). In these sections, we found the same retinal thinning that was seen in the SD-OCT images; however, cell nuclei quantification in the outer nuclear layer (ONL), inner nuclear layer (INL), and retinal ganglion cell layer (RGCL) did not show any significant differences between control and experimental animals.

Discussion

Overall, the goal of this study was to determine the role of *Lsd1* in ocular development through genetic ablation either systemically using a heterozygous global knockout or a homozygous retina specific knockout. We hypothesized that deletion would cause ocular abnormalities which would be observed through visual function tests, *in vivo* imaging, and post-mortem analyses. For the systemic *Lsd1* heterozygous knockout animals, we did not observe any obvious abnormalities in LSD1 protein levels or retinal morphology, both *in vivo* using MicronIV SD-OCT images or post-mortem H&E stained sagittal sections (Figures 4.3-4.5). These results suggest that *Lsd1* is haplosufficient, meaning that 1 genetic copy of *Lsd1* is enough to produce normal *Lsd1* protein levels and provide for proper ocular development. This is not necessarily surprising given that *Lsd1* heterozygous mice have never been reported to have any developmental abnormalities. For the retina specific *Lsd1* knockout using a *Chx10-Cre* driver line to delete *Lsd1* in almost all RPCs, we hypothesized that *Lsd1* ablation could result in either: 1) retinal degeneration due to RPC apoptosis or abnormalities in RPC proliferation or 2) irregularities in the relative proportion of various mature retinal neuron subtypes due to improper differentiation in the RPCs. Through western blotting, we were able to confirm the absence of a canonical wild-type protein (expected band size 107 kDa) and the presence of a truncated *Lsd1* protein (estimated band size ~27 kDa) in only the *Chx10-Cre Lsd1 loxP* animals, not in either of the control groups, *Chx10-Cre* only or *Lsd1 loxP* only. After confirming the deletion of the canonical *Lsd1* protein, we tested the *Chx10-Cre Lsd1 loxP* animals with littermate controls at P30 and P45 for visual function and retinal morphology, both *in vivo* and post-mortem. Our current data showed significant retinal degeneration at both P30 and P45 which resulted in significant decreases in ERG amplitudes both in scotopic and photopic conditions. These decreases in ERG amplitudes suggest

photoreceptor and bipolar cell dysfunction (Figures 4.7-4.10)[27,28]. We also observed significant decreases in total retinal thickness and ONL thickness in SD-OCT images and a more mottled and speckled appearance of Fundus photos in the *Chx10-Cre Lsd1 loxP* animals compared to their littermate controls (Figure 4.11). We did not observe any significant differences in cell nuclei quantification in the outer nuclear layer (ONL), inner nuclear layer (INL), or retinal ganglion cell layer (RGCL) at P30 (Figure 4.12).

One potentially confounding variable in these results is the presence of a Cre ERT2 construct at the Rosa26 locus in the *Lsd1 loxP* mice. Prior to the development of the *Chx10-Cre Lsd1 loxP* mice, we were unaware of this extra Cre ERT2 construct. Unfortunately, the *Lsd1 loxP* mouse line had two copies of Cre ERT2 that was then bred with the *Chx10-Cre* mouse strain. The resulting first generation was then bred together to create the second generation where half of animals are *Chx10-Cre* positive and half were *Chx10-Cre* negative; however due to the presence of the Cre ERT2 construct, half of the *Chx10-Cre* positive animals have one copy of Cre ERT2 while the other half have two copies of Cre ERT2. The same will be true of the *Chx10-Cre* negative animals where half contain one copy of Cre ERT2 and the other half contain two copies.

Cre ERT is a fusion protein between Cre recombinase and a mutated ligand binding domain of the estrogen receptor (ER) that allows for conditional excision of genomic DNA between two loxP sites after tamoxifen injections[29]. The mutated ER ligand can only bind tamoxifen, not endogenous estrogen or progesterone, and in the presence of tamoxifen, the Cre fusion protein is able to translocate from the cytoplasm to the nucleus and complete the genomic excision[3].

Although Cre ERT is unlikely to become active without tamoxifen present, after tamoxifen injection, the efficiency of recombination has been shown to be variable in different tissues[30,31]. Cre ERT2 is an updated ligand-dependent Cre recombinase which is 4-fold more efficiently induced by tamoxifen and is 10-fold more sensitive to tamoxifen induction when compared to the original Cre ERT[32]. The use of Cre ERT and Cre ERT2 have allowed researchers to have both spatial and temporal control during gene deletion; however, issues have arisen where tamoxifen-independent Cre recombinase activity has been observed[33] as well as substantial variability in Cre recombinase activity among individual animals, tissues, and cell types[34]. In particular, after analysis of cytoplasmic and nuclear Cre ERT2 protein levels, it has been noted that Cre ERT2 may not be stable in the absence of the tamoxifen ligand[35].

Given these inconsistencies, the Cre ERT2 construct should only be active after repeated injections of tamoxifen. It is highly unlikely that Cre recombinase will become active without tamoxifen present, and we did not inject any animals with tamoxifen at any point in time. After dividing the animals based on their genotype for the presence or absence of *Chx10-Cre* and the presence of one versus two copies of Cre ERT2, we re-analyzed the ERG data to determine whether the Cre ERT2 construct has any effect on visual function. We have evidence to suggest that the presence of one or two copies of Cre ERT2 does not affect the resulting phenotype (Supplemental Figure 4.1); however, because of the reported issues with the Cre ERT2 construct, we are currently working to breed the Cre ERT2 construct out of the *Lsd1 loxP* animals and to regenerate our *Chx10-Cre Lsd1 loxP* mouse line. Afterwards, we will test those animals using the same parameters as reported here to determine whether the observed phenotype is solely due the *Chx10-Cre* construct deleting *Lsd1* in almost all RPCs.

For now, we are unable to differentiate between our two possible reasons for the retinal degeneration. Whether the retinal degeneration phenotype is due to the inability for RPCs to proliferate, resulting in early cell death, or due to the inability for the RPCs to properly differentiate will be the subject of future studies. We will look at earlier time points during retinal development (between P0 – P21) to determine how the RPCs cope with the epigenetic dysregulation that would occur with the loss of *Lsd1*. RPCs are heterogenous in their individual transcriptome and this allows for multipotency[36–38]. Under the influence of different cell fate determinants, the RPCs become specified and commit to a particular cell fate[39,40]. Therefore, loss of *Lsd1* will likely affect the specification and differentiation of the RPCs. We plan to take sagittal sections from *Chx10-Cre Lsd1 loxP* as well as controls at various timepoints during retinal development and conduct H&E, TUNEL, and immunocytochemistry staining. Future studies can also look at how the epigenome and transcriptome are affected by the loss of *Lsd1* in RPCs by conducting RNA-seq and ChIP-seq experiments. Lastly, *Chx10* expression is maintained in adulthood in retinal bipolar cells; therefore, it is likely that the deletion of *Lsd1* using the *Chx10-Cre* driver may affect the development of either all or specific subtypes of bipolar cells. Recently, single-cell RNA seq has identified 15 different retinal bipolar cells in the adult retina[41] and certain subtypes are shown to express *Lsd1* at relatively higher levels compared to others (Figure 4.13). Therefore, it is imperative to investigate whether or not those specific bipolar cells subtypes, such as cone bipolar cell type BC5D, BC7, or BC8/9, are uniquely affected by the loss of *Lsd1*.

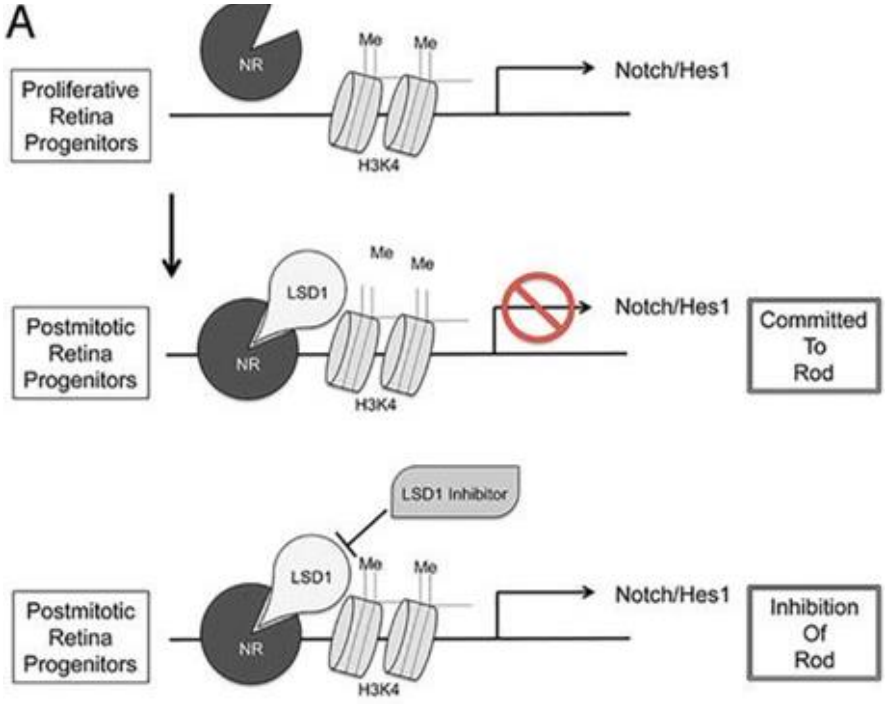

Figure 4.1: Schematic model of the role of LSD1 during retina development. In postmitotic retina progenitor cells, LSD1 inhibits genes that are involved in the Notch/Hes1 pathway, allowing cells to be committed to rod photoreceptors. If pharmacological inhibition of LSD1 occurs in the postmitotic retina progenitors, LSD1 is unable to inhibit the Notch/Hes1 pathway, resulting in inhibition of rod photoreceptors development. (Taken from Popova et al. 2016 Molecular Neurobiology[26]).

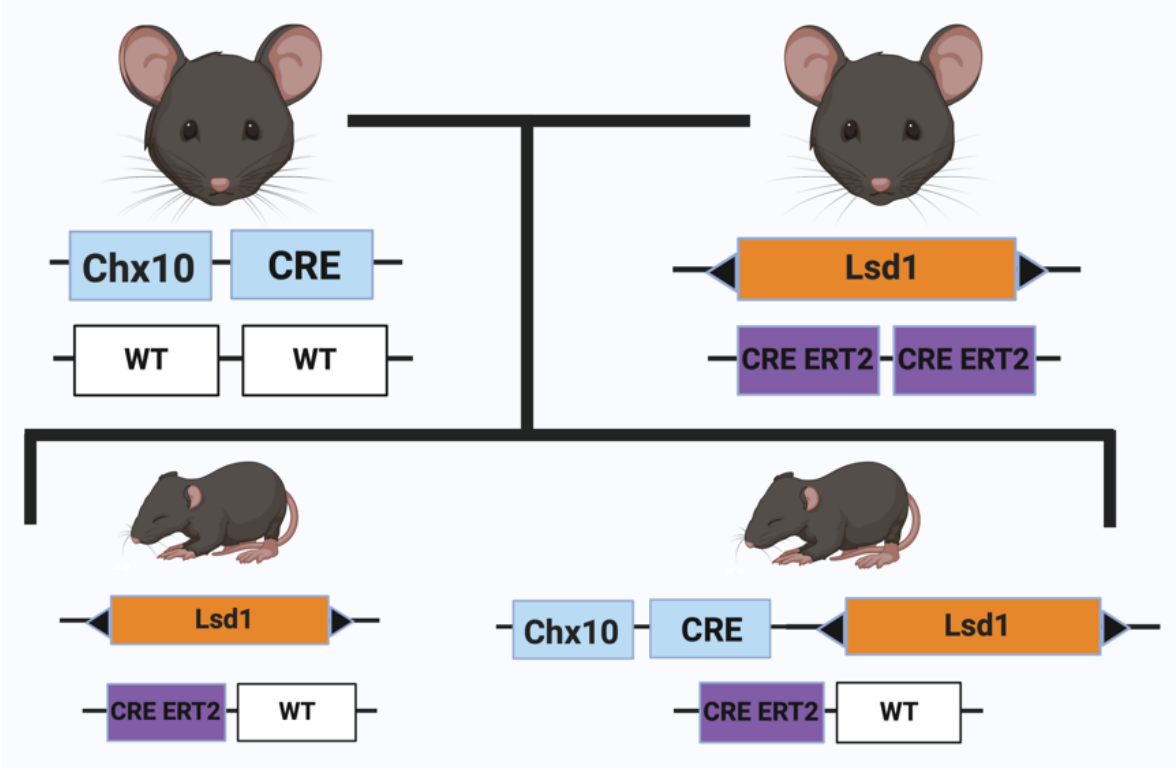

Figure 4.2: Breeding scheme to generate new transgenic *Chx10-Cre Lsd1 loxP* mouse strain with the accidental inclusion of a Cre ERT2 construct.

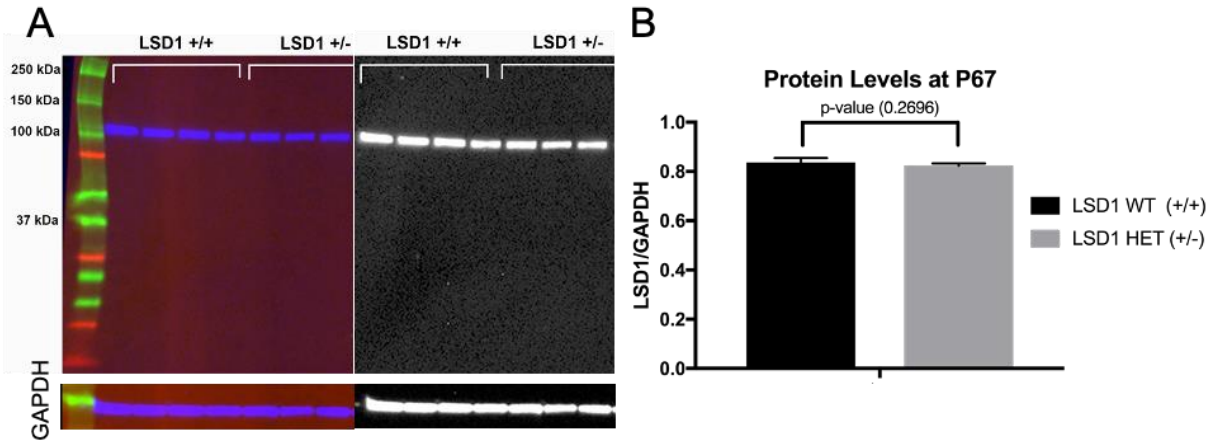

Figure 4.3: Heterozygous *Lsd1* null mice (*Lsd1* +/-) have equal retinal protein levels as littermate controls (*Lsd1* +/+).Western blot analysis on post-natal day 67 (P67) mouse retinas probed for LSD1 and GAPDH protein levels. LSD1 (molecular weight: 107 kDa) and GAPDH (molecular weight: 37kDa) were present in all samples and densitometry analysis showed no significant differences between *Lsd1* protein levels in wild-type littermates (n=4) and heterozygous mice (n=3) (p-value = 0.2696).

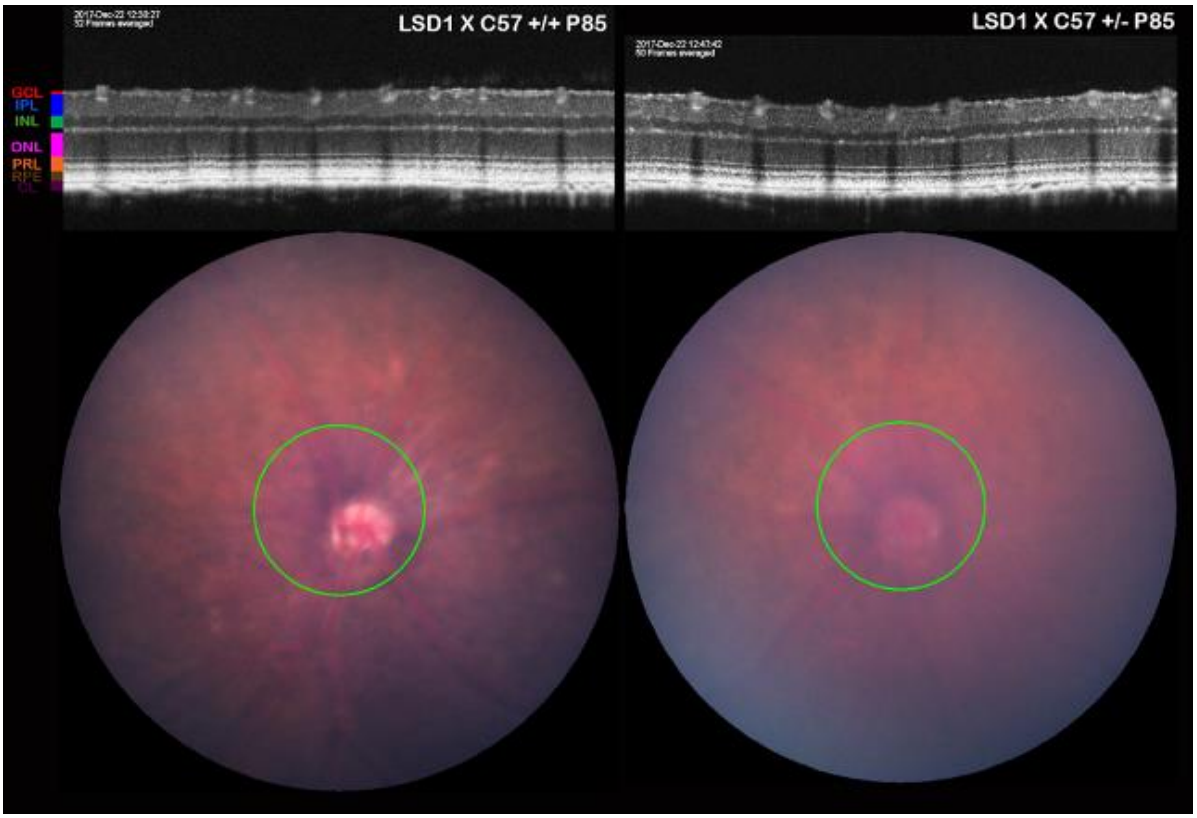

Figure 4.4: MicronIV Fundus and SD-OCT images show comparable *in vivo* retinal morphology between P85 *Lsd1* +/+ littermate controls and *Lsd1* +/- heterozygous mice. There are no obvious differences between the two groups or signs of degeneration in the retinas of the *Lsd1* +/- heterozygous mice.

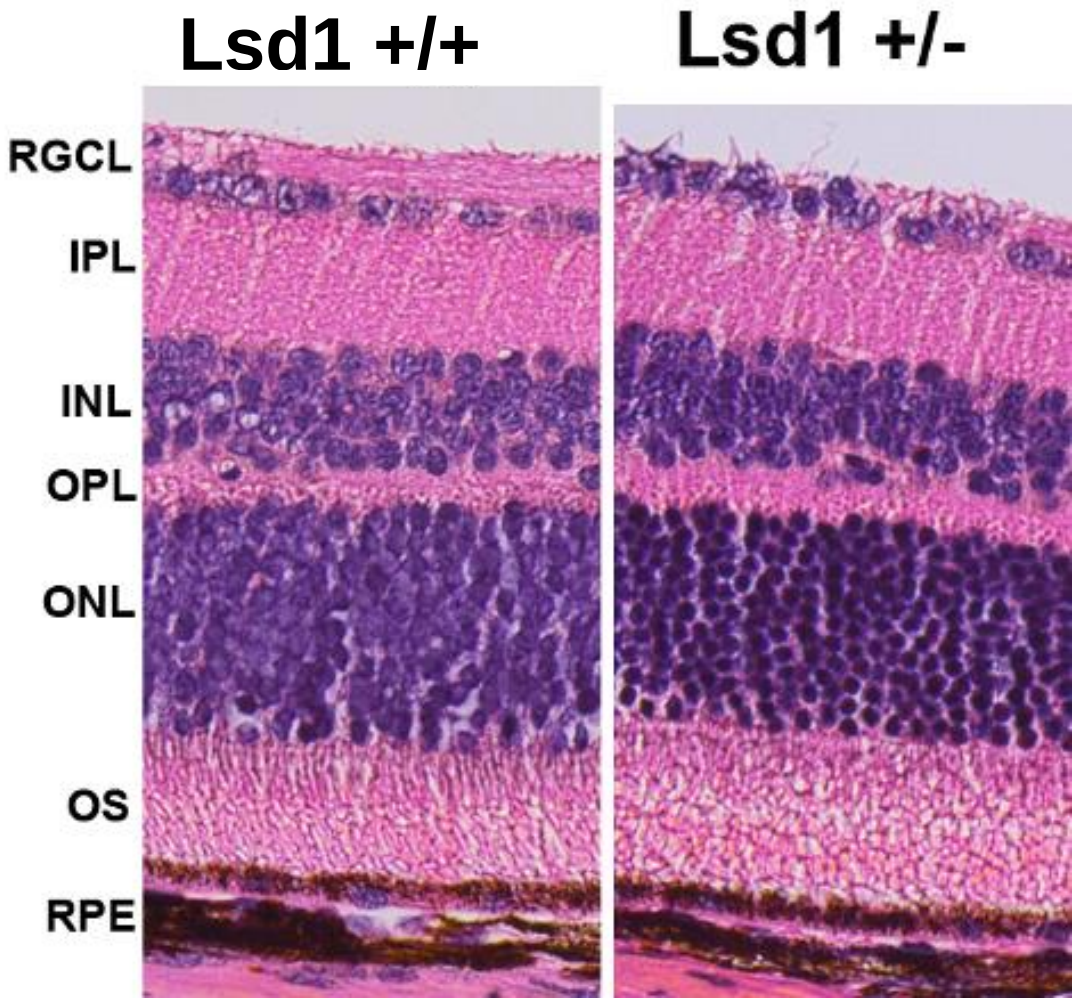

Figure 4.5: Hematoxylin and eosin (H&E) staining of P90 *Lsd1* +/+ littermate controls and *Lsd1* +/- heterozygous mice show comparable post-mortem retinal morphology. There are no obvious morphological defects in the *Lsd1* +/- heterozygous mice.

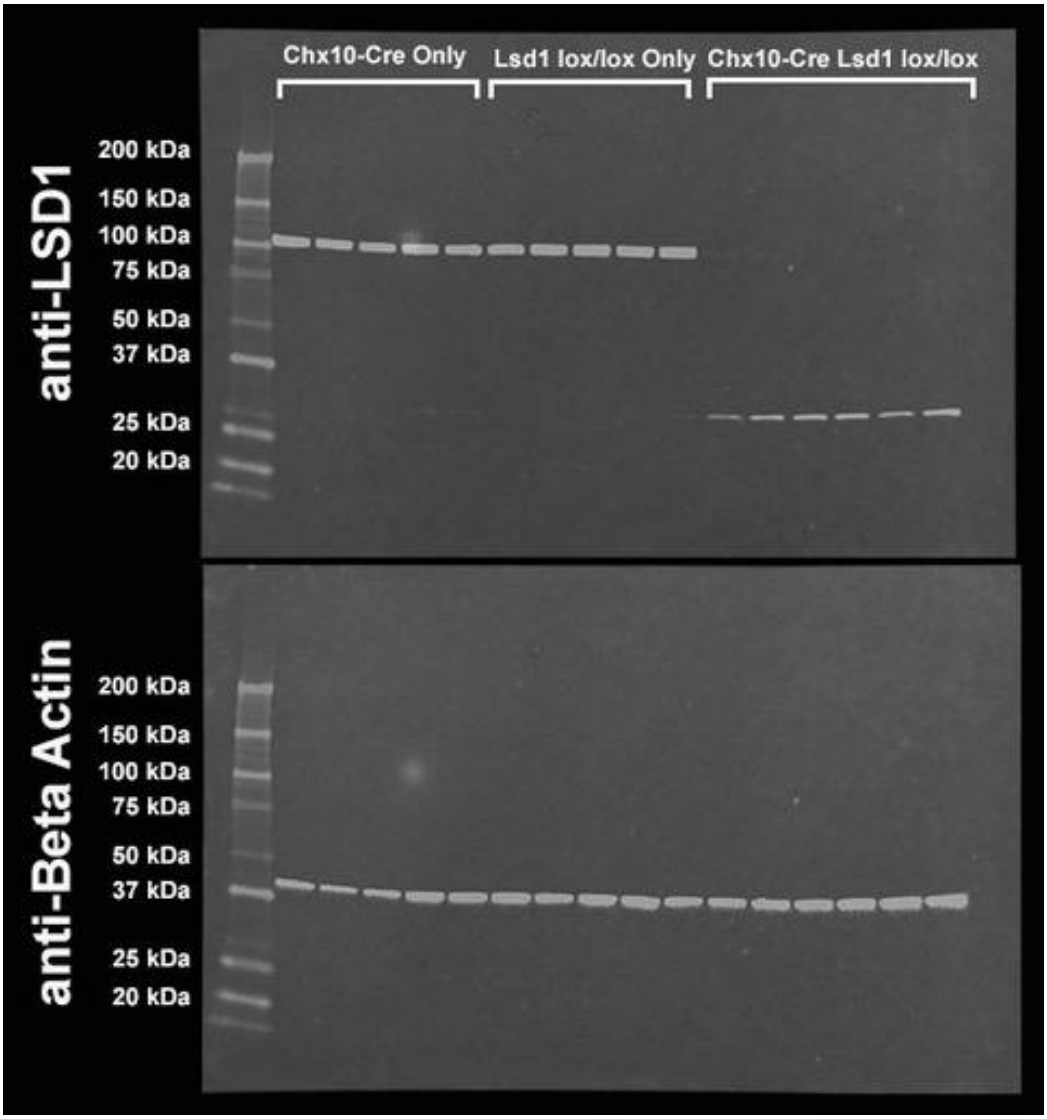

Figure 4.6: Western blot confirming LSD1 Deletion in P30 retinas. Retinas from *Chx10-Cre* only (n=5), *Lsd1 loxP* only (n=5), and *Chx10-Cre Lsd1 loxP* (n=6) probed with an anti-LSD1 antibody [1:1000] and an anti-beta Actin antibody [1:1000] as a loading control. In the two control groups, *Chx10-Cre* only and *Lsd1 loxP* only, the full length LSD1 (molecular weight: 107 kDa) is expressed; however, in the experimental group (*Chx10-Cre Lsd1 loxP*) retinas, there is only expression of a truncated *Lsd1* protein (molecular weight: 27 kDa).

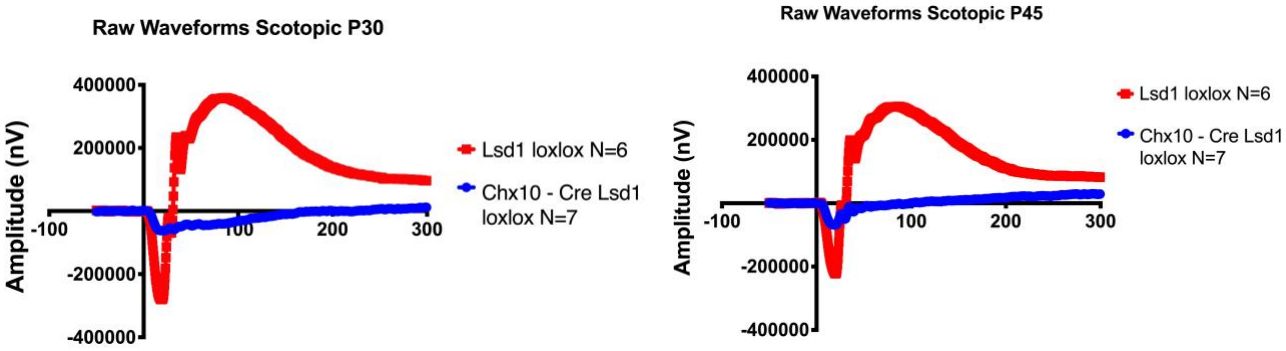

Figure 4.7: *Chx10-Cre Lsd1 loxP* mice have relatively little ERG response in scotopic conditions compared to *Lsd1 loxP* control animals at both P30 and P45. Raw electroretinogram waveforms from *Lsd1 loxP* (controls n=6) and *Chx10-Cre Lsd1 loxP* (experimental n=7) in scotopic conditions after a 1 cd s/m^2 light flash. The littermate control animals (shown in red) have normal ERG responses whereas the experimental animals (shown in blue) have flat ERG responses.

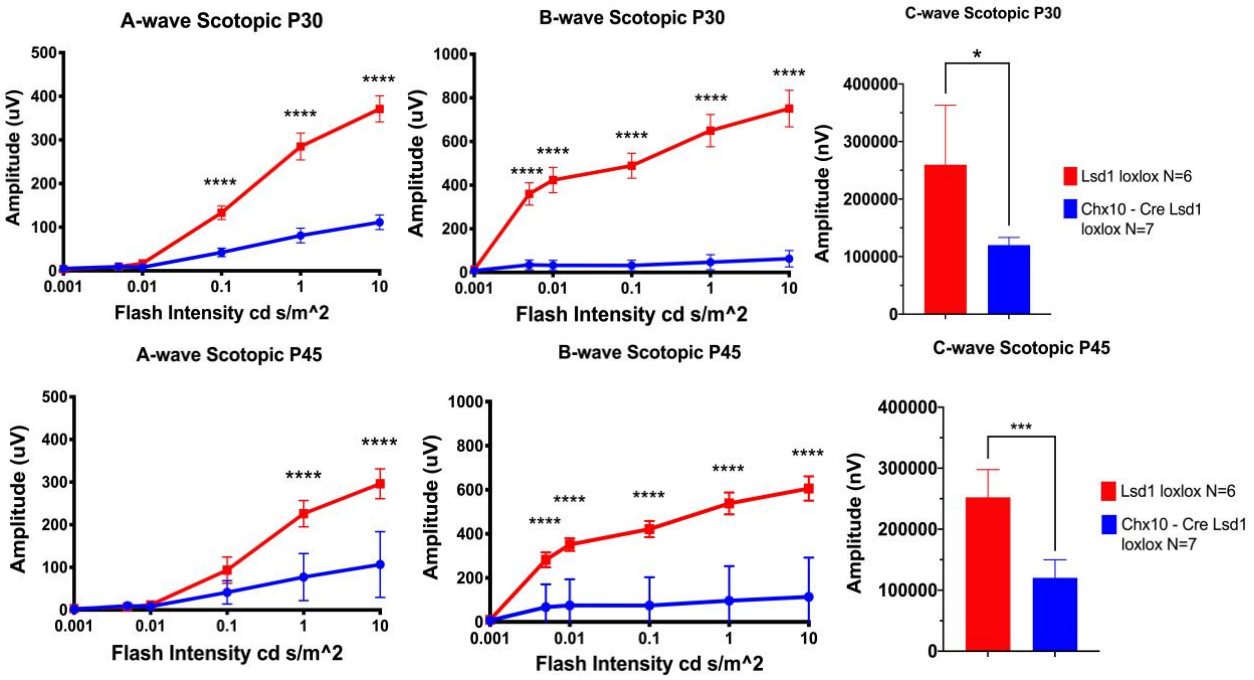

Figure 4.8: *Chx10-Cre Lsd1 loxP* have a significant decrease in a-, b-, and c-waves in scotopic conditions when compared to littermate *Lsd1 loxP* controls at both P30 and P45. Animals were tested in scotopic conditions with increasing flash intensities. *Lsd1 loxP* animals (control group n=6) are shown in red and *Chx10-Cre Lsd1 loxP* animals (experimental group n=7) are shown in blue. *Chx10-Cre Lsd1 loxP* animals show decreased a- and b-wave response at relatively low flash intensities indicating dysfunction in the rod photoreceptors and rod bipolar cells. A significant decrease in c-wave response in the *Chx10 Lsd1 loxP* animals compared to *Lsd1 loxP* animals after a 10 cd s/m^2 flash indicates RPE dysfunction.

* = p value <0.05; ** = p value <0.01; *** = p value < 0.001; **** = p value < 0.0001

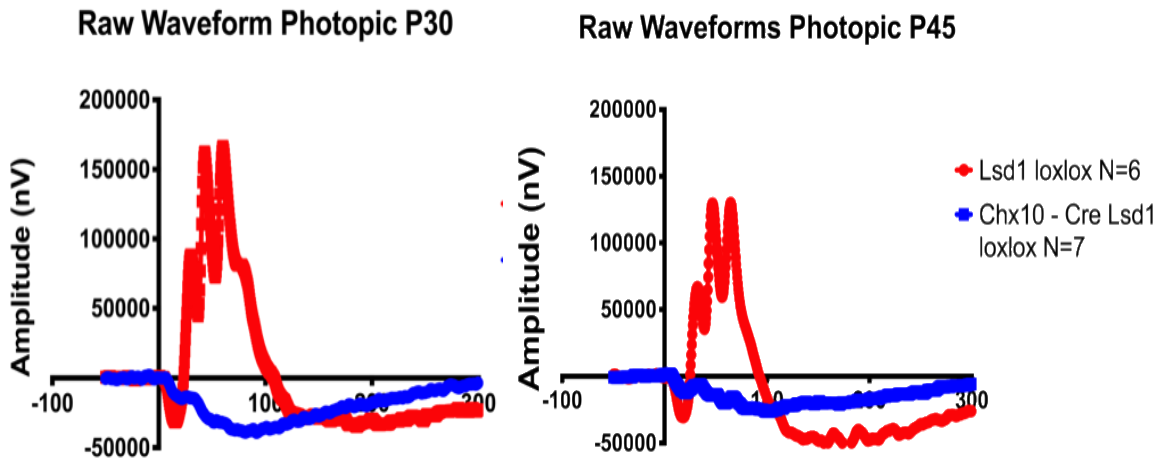

Figure 4.9: *Chx10-Cre Lsd1 loxP* mice have relatively little ERG response in photopic conditions compared to *Lsd1 loxP* control animals. Raw electroretinogram waveforms from *Lsd1 loxP* animals (control group n=6) and *Chx10-Cre Lsd1 loxP* animals (experimental group n=7) at P30 and P45 in photopic conditions after a 10 cd s/m^2 light flash. The littermate control animals (shown in red) have normal ERG responses whereas the experimental animals (shown in blue) have flat ERG responses, indicating cone photoreceptor dysfunction.

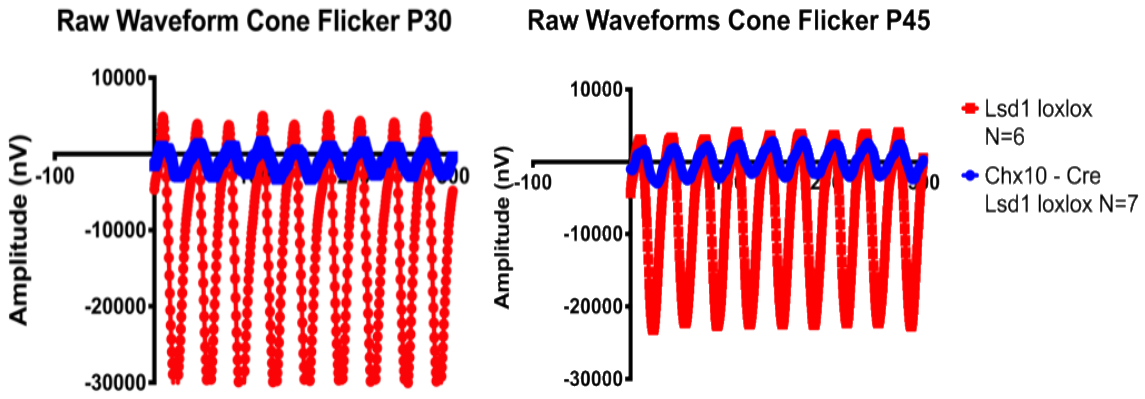

Figure 4.10: *Chx10-Cre Lsd1 loxP* mice have relatively little ERG response in photopic flicker conditions compared to *Lsd1 loxP* control animals. Raw cone flicker electroretinogram waveforms from *Lsd1 loxP* animals (control group n=6) and *Chx10-Cre Lsd1 loxP* animals (experimental group n=7) at P30 and P45 in photopic conditions after the presence of a light flash flicking at 30 Hz. The littermate control animals (shown in red) have normal ERG responses whereas the experimental animals (shown in blue) have flattened ERG responses, indicating cone photoreceptor dysfunction.

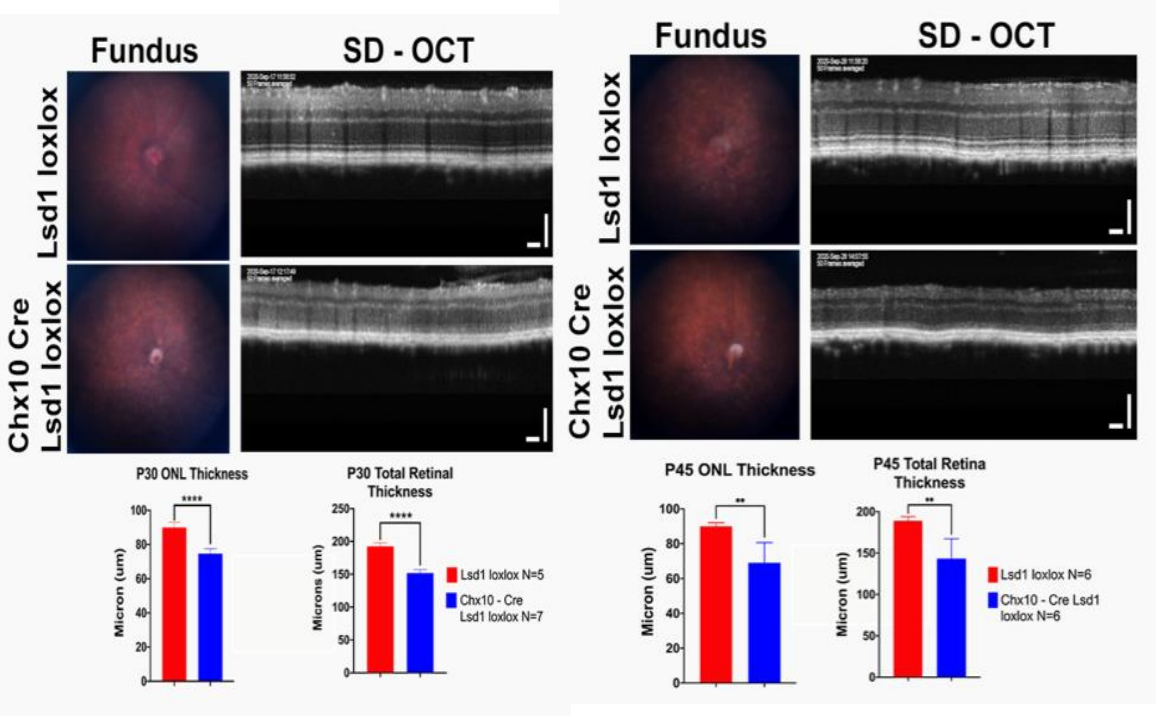

Figure 4.11: *Chx10-Cre Lsd1 loxP* animals show an increased mottled and speckled appearance in Fundus photos compared to their littermate controls as well as thinner retinas and outer nuclear layers (ONL) as measured by SD-OCT images at both P30 and P45. *Chx10-Cre Lsd1 loxP* animals (experimental group n=6-7) have significantly thinner retinas and ONLs compared to their *Lsd1 loxP* littermates (control group n=5-6) indicating retinal degeneration.

* = p value <0.05; ** = p value <0.01; *** = p value < 0.001; **** = p value < 0.0001

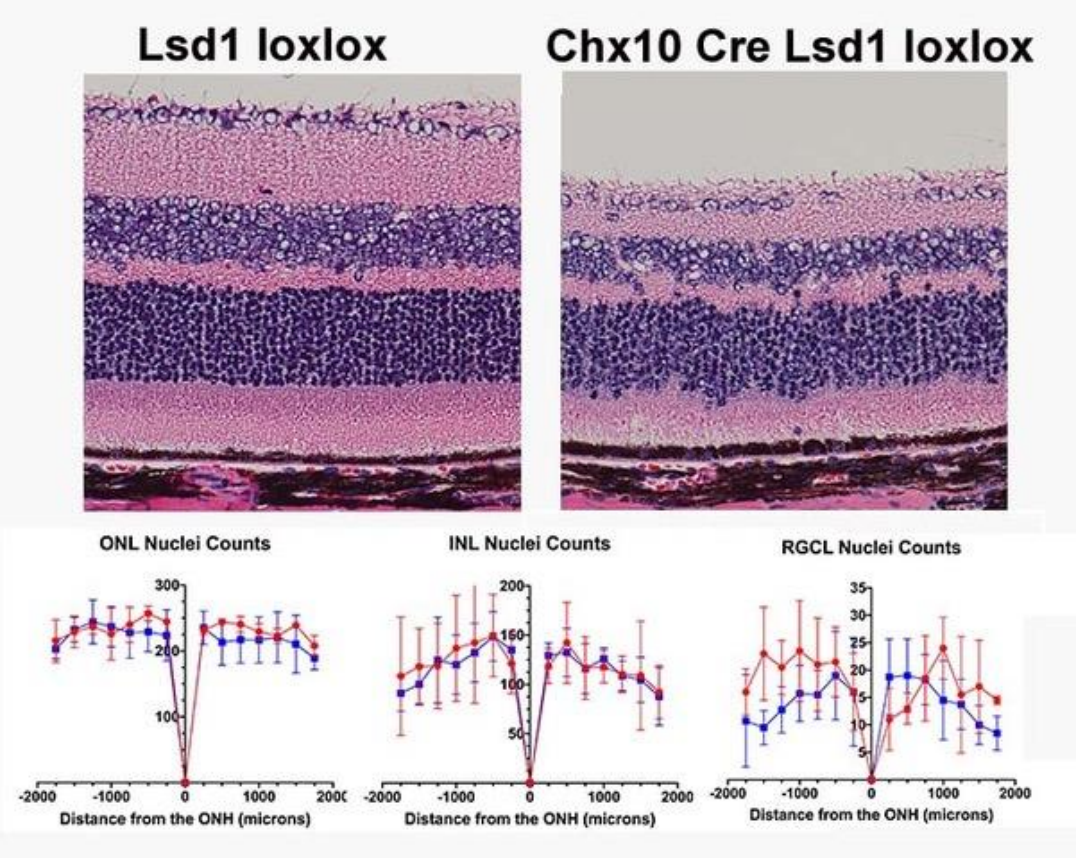

Figure 4.12: *Chx10-Cre Lsd1 loxP* show signs of retinal thinning and irregular morphology in Hematoxylin & Eosin (H&E) staining compared to their littermate controls; however, quantification of cell nuclei in the outer nuclear layer (ONL), inner nuclear layer (INL), or retinal ganglion cell layer (RGCL) did not show any significant changes.

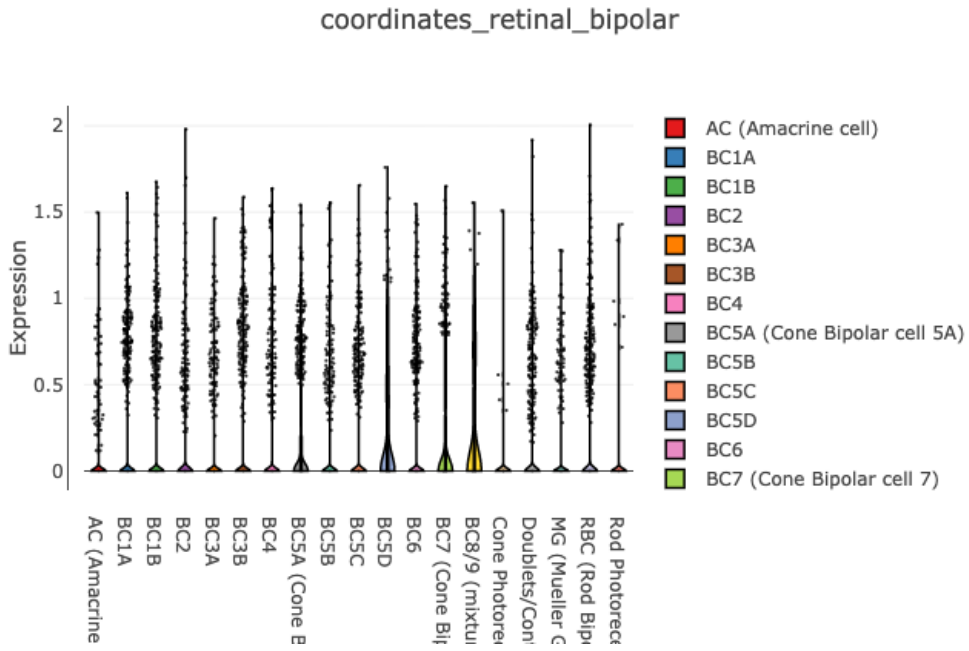

Figure 4.13: Relative expression of *Lsd1* in different retinal ganglion cell subtypes in the adult mouse retina. Data taken from the Single Cell Portal website published by the Broad Institute https://singlecell.broadinstitute.org/single_cell/study/SCP3/retinal-bipolar-neuron-drop-seq#study-visualize

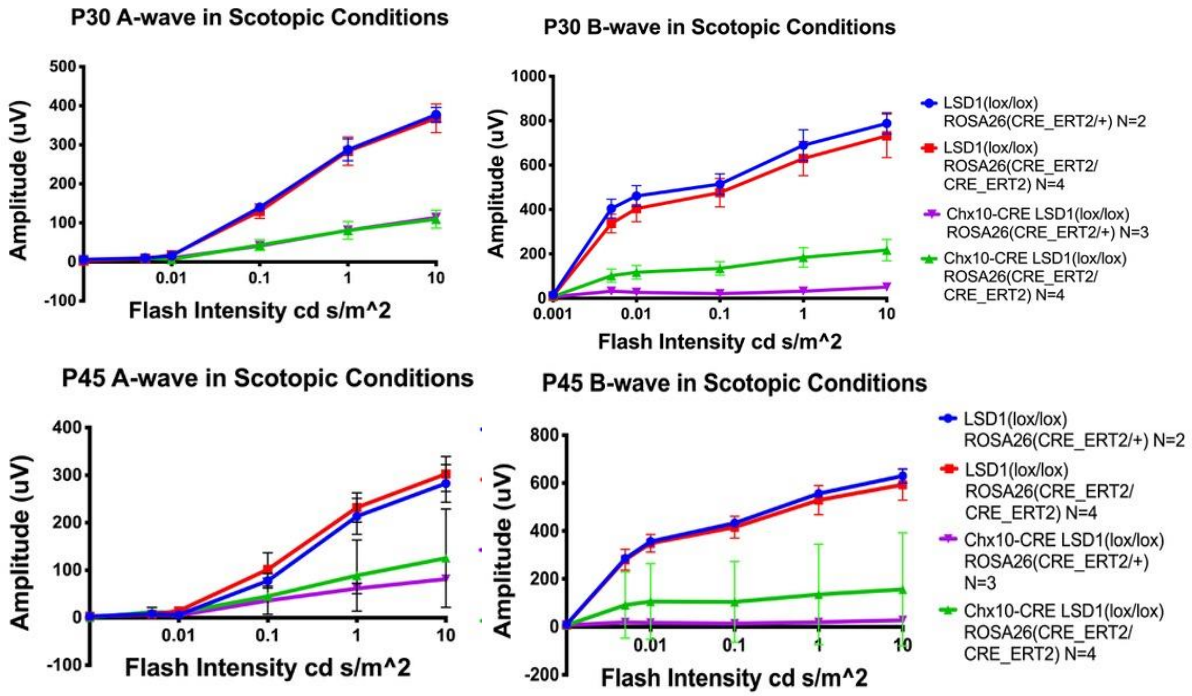

Supplemental Figure 4.1: Scotopic visual function defects observed in the *Chx10-Cre Lsd1 loxP* mice are due to the presence of the *Chx10-Cre* and are not heavily influenced by the presence of one or two Cre ERT2 constructs. Animals were genotyped and grouped based on the presence or absence of Cre recombinase under the control of the *Chx10* promoter as well as the number of Cre ERT2 constructs at the Rosa26 locus. Animals were then tested for ERG visual function at both P30 and P45. Mice without a *Chx10* driven Cre recombinase had normal a- and b-waves regardless of the presence of one Cre ERT2 construct (n=2) or two Cre ERT2 constructs (n=4). Mice with a *Chx10* driven Cre recombinase had greatly reduced a- and b-waves regardless of the presence of one Cre ERT2 construct (n=3) or two Cre ERT2 constructs (n=4).

References:

1 Ferdous S, Grossniklaus HE, Boatright JH, Nickerson JM. Characterization of LSD1 Expression Within the Murine Eye. Invest Ophthalmol Vis Sci 2019;60:4619–31.

2 Wang J, Scully K, Zhu X, Cai L, Zhang J, Prefontaine GG, et al. Opposing LSD1 complexes function in developmental gene activation and repression programs. Nature 2007;446:882–7. PMCID:17392792.

3 Nagy A. Cre recombinase: The universal reagent for genome tailoring. Genesis 2000;26:99–109. PMCID:10686599.

4 Liu ISC, Chen J de, Ploder L, Vidgen D, van der Kooy D, Kalnins VI, et al. Developmental expression of a novel murine homeobox gene (*Chx10*): Evidence for roles in determination of the neuroretina and inner nuclear layer. Neuron 1994;13:377–93.

5 Rowan S, Chen CMA, Young TL, Fisher DE, Cepko CL. Transdifferentiation of the retina into pigmented cells in ocular retardation mice defines a new function of the homeodomain gene *Chx10*. Development 2004;131:5139–52. PMCID:15459106.

6 Livne-Bar I, Pacal M, Cheung MC, Hankin M, Trogadis J, Chen D, et al. *Chx10* is required to block photoreceptor differentiation but is dispensable for progenitor proliferation in the postnatal retina. Proc Natl Acad Sci U S A 2006;103:4988–93. PMCID:16547132.

7 Burmeister M, Novak J, Liang M, Basu S, Ploder L, Hawes NL, et al. Ocular retardation mouse caused by *Chx10* homeobox null allele: impaired retinal progenitor proliferation and bipolar cell differentiation. Nature 1996;12:376–84.

8 Rutherford AD, Dhomen N, Smith HK, Sowden JC. Delayed Expression of the Crx Gene and Photoreceptor Development in the *Chx10*-Deficient Retina. Investig Ophthalmol Vis

Sci 2004;45:375–84. PMCID:14744875.

9 Percin EF, Ploder LA, Yu JJ, Arici K, Horsford DJ, Bapat B, et al. Human microphthalmia associated with mutations in the retinal homeobox gene CHX10. Nature genetics, 25(4), 397–401. https://doi.org/10.1038/78071

10 Horsford DJ, Nguyen MTT, Sellar GC, Kothary R, Arnheiter H, McInnes RR. *Chx10* repression of Mitf is required for the maintenance of mammalian neuroretinal identity. Development 2005;132:177–87. PMCID:15576400.

11 Wang Z, Yasugi S, Ishii Y. *Chx10* functions as a regulator of molecular pathways controlling the regional identity in the primordial retina. Dev Biol 2016;413:104–11. PMCID:27001188.

12 Rowan S, Cepko CL. Genetic analysis of the homeodomain transcription factor *Chx10* in the retina using a novel multifunctional BAC transgenic mouse reporter. Dev Biol 2004;271:388–402.

13 Lee MG, Wynder C, Schmidt DM, McCafferty DG, Shiekhattar R. Histone H3 Lysine 4 Demethylation Is a Target of Nonselective Antidepressive Medications. Chem Biol 2006;13:563–7. PMCID:16793513.

14 Schmidt DMZ, McCafferty DG. trans-2-phenylcyclopropylamine is a mechanism-based inactivator of the histone demethylase LSD1. Biochemistry 2007;46:4408–16.

15 Binda C, Valente S, Romanenghi M, Pilotto S, Cirilli R, Karytinos A, et al. Biochemical, structural, and biological evaluation of tranylcypromine derivatives as inhibitors of histone demethylases LSD1 and LSD2. J Am Chem Soc 2010;132:6827–33.

16 Ji YY, Lin SD, Wang YJ, Su MB, Zhang W, Gunosewoyo H, et al. Tying up tranylcypromine: Novel selective histone lysine specific demethylase 1 (LSD1)

inhibitors. Eur J Med Chem 2017;141:101–12.

17 Niwa H, Umehara T. Structural insight into inhibitors of flavin adenine dinucleotide-dependent lysine demethylases. Epigenetics 2017;12:1–13.

18 Ulrich S, Ricken R, Adli M. Tranylcypromine in mind (Part I): Review of pharmacology. Eur Neuropsychopharmacol 2017;27:697–713. PMCID:28655495.

19 Popova EY, Pinzon-Guzman C, Salzberg AC, Zhang SS-M, Barnstable CJ. LSD1-Mediated Demethylation of H3K4me2 Is Required for the Transition from Late Progenitor to Differentiated Mouse Rod Photoreceptor. Mol Neurobiol 2016;53:4563–81. PMCID:26298666.

20 Granit R. The Components of the retinal action potential in mammals and their relation to the discharge in the optic nerve. J Physiol 1933;77:207–39.

21 Weymouth AE, Vingrys AJ. Rodent electroretinography: Methods for extraction and interpretation of rod and cone responses. Prog Retin Eye Res 2008;27:1–44. PMCID:18042420.

22 Feil R, Brocard J, Mascrez B, Lemeur M, Metzger D, Chambon P. Ligand-activated site-specific recombination in mice. Proc Natl Acad Sci U S A 1996;93:10887–90. PMCID:8855277.

23 Brocard J, Warot X, Wendling O, Messaddeq N, Vonesch JL, Chambon P, et al. Spatio-temporally controlled site-specific somatic mutagenesis in the mouse. Proc Natl Acad Sci U S A 1997;94:14559–63. PMCID:9405652.

24 Vooijs M, Jonkers J, Berns A. A highly efficient ligand-regulated Cre recombinase mouse line shows that. Eur Mol Biol Organ 2001;2:292–7.

25 Indra AK, Warot X, Brocard J, Bornert JM, Xiao JH, Chambon P, et al. Temporally-

controlled site-specific mutagenesis in the basal layer of the epidermis: Comparison of the recombinase activity of the tamoxifen-inducible Cre-ER(T) and Cre-ER(T2) recombinases. Nucleic Acids Res 1999;27:4324–7. PMCID:10536138.

26 Kristianto J, Johnson MG, Zastrow RK, Radcliff AB, Blank RD. Spontaneous recombinase activity of Cre–ERT2 in vivo. Transgenic Res 2017;26:411–7. PMCID:28409408.

27 Heffner CS, Herbert Pratt C, Babiuk RP, Sharma Y, Rockwood SF, Donahue LR, et al. Supporting conditional mouse mutagenesis with a comprehensive cre characterization resource. Nat Commun 2012;3:1218–9. PMCID:23169059.

28 Sandlesh P, Juang T, Safina A, Higgins MJ, Gurova K V. Uncovering the fine print of the CreERT2-LoxP system while generating a conditional knockout mouse model of Ssrp1 gene. PLoS One 2018;13:1–20. PMCID:29953487.

29 Trimarchi JM, Stadler MB, Cepko CL. Individual retinal progenitor cells display extensive heterogeneity of gene expression. PLoS One 2008;3: PMCID:18270576.

30 Bassett EA, Wallace VA. Cell fate determination in the vertebrate retina. Trends Neurosci 2012;35:565–73. PMCID:22704732.

31 Cepko C. Intrinsically different retinal progenitor cells produce specific types of progeny. Nat Rev Neurosci 2014;15:615–27. PMCID:25096185.

32 Cepko CL, Austin CP, Yang X, Alexiades M, Ezzeddine D. Cell fate determination in the vertebrate retina 1996;93:589–95.

33 Livesey FJ, Cepko CL. Vertebrate neural cell-fate determination: Lessons from the retina. Nat Rev Neurosci 2001;2:109–18. PMCID:11252990.

34 Shekhar K, Lapan SW, Whitney IE, Tran NM, Evan Z, Kowalczyk M, et al.

Comprehensive Classification of Retinal Bipolar Neurons by single-cell transcriptomics. Cell 2016;166:1308–23.

Chapter V: Lsd1 is a potential therapeutic target in the treatment of retinoblastoma

Salma Ferdous, Aaron Yeung, Jennifer Rha, Ogul E. Unek, Hans E. Grossniklaus, John M. Nickerson

Abstract

The purpose of this study was to determine whether lysine-specific demethylase 1 (*Lsd1*) is aberrantly expressed in human retinoblastoma (RB) tumors. If LSD1 is aberrantly expressed, it may serve as a potential molecular target for the development of future therapies. Immunofluorescent microscopy for LSD1, Ki67, rhodopsin, and cone opsin was conducted on human and murine formalin-fixed paraffin-embedded eye sections. Additionally, hematoxylin and eosin (H&E) staining was conducted on adjacent human and murine eye sections. We observed relatively uniform expression of LSD1 protein in the intact human retina. Within the RB tumor itself, there was dichotomous expression of LSD1 in different areas of the tumor. The cells with high LSD1 expression corresponded with a proliferation marker, Ki67, and highly differentiated tumor cells, as indicated by cellular morphology through H&E staining. In the transgenic RB mouse line, based on the H&E staining and co-localization of Lsd1 with the photoreceptor markers rhodopsin and cone opsin, the RB tumor is highly proliferative and located in the inner nuclear layer (INL). We have observed high expression of LSD1 and Ki67 in both highly differentiated areas of human RB tumors and transgenic RB mouse tumor. The mouse RB tumor is located in the INL and this differs from human RB tumors which originate from cone precursor cells. Due to these cellular origin differences, future experiments should use RB immortalized cell lines and test whether Lsd1 inhibitors alone or in combination with other drugs are sufficient to kill tumor cells.

Introduction

Retinoblastoma (RB) is the most common primary childhood ocular cancer with an incidence rate of 1 in 14,000 – 20,000 live births[1]. Although survival is the USA is quite high (>90%)[2], current therapeutic options preferentially prioritize saving the patient's life over saving their eye or vision[3]. This can lead to lifelong disability when the child loses vision in one or both eyes. Vision loss can severely affect the patient's quality of life and is often co-morbid with other physical and mental disorders[4], such as depression[5,6] and increased fatigue[7] or loneliness[8]. RB is hypothesized to originate from cone photoreceptor precursors because these cell types are uniquely sensitive to the loss of *Rb1*, the retinoblastoma susceptibility gene, leading to cancerous transformation[9,10]. *Rb1* was the first tumor suppressor gene discovered and is a key regulator of cellular replication[11]. Mutations can result in abnormal gene expression through transcriptional or epigenetic mis-regulation, ultimately leading to uncontrollable cellular division[12].

Aberrant epigenetic changes are a hallmark in many cancer types and lysine specific demethylase 1 (*Lsd1*) mis-expression is observed in many tumors, including gastric, esophageal, oral, breast, lung, colorectal, prostate, and bladder cancers[13–15]. *Lsd1* is an epigenetic protein involved in the demethylation of both H3K4 and H3K9 histone modifications depending on its associated protein complex[16,17]. *Lsd1* can also demethylate non-histone proteins; for example, demethylation of myosin phosphatase target subunit 1 (MYPT1) leads to increased RB1 phosphorylation which stimulates cell cycle progression within cancer cells[18]. *Lsd1* has also been shown to directly interact with and regulate p53 function[19].

During normal retinal development, *Lsd1* is expressed in all retinal progenitor cells and is

maintained even after terminal differentiation, especially in cone photoreceptors[20]. Inhibition of *Lsd1* during development prevents proper rod photoreceptor development[21]. Additionally retinal *Lsd1* overexpression can stabilize hypoxia inducible factor 1a (HIF-1a), leading to increased retinal angiogenesis and tumor vascularization[22]. In Y79 RB cell lines, *Lsd1* interacts with TLX (NR2E1), an orphan nuclear receptor, which regulates retinal stem cell proliferation and differentiation, by controlling the expression of PTEN, a tumor suppressor gene[23–26].

RB is classified as a type of childhood embryonal central nervous system tumor, similar to medulloblastoma (MB) and neuroblastoma (NB)[27,28]. *Lsd1* is overexpressed in human and murine MB tumors and MB cell lines transfected with siRNAs against *Lsd1* showed decreased cell viability and proliferation as well as increased caspase-3 related apoptosis and RE1-Silencing Transcription Factor (REST) related cellular migration[29,30]. MB tumors implanted in mouse flanks that were treated with GSK-LSD1 inhibitors showed decreased tumor size and growth *in vivo*; however no effects were seen on intracranial tumors suggesting insufficient drug accumulation in the brain[31]. Like MB, *Lsd1* shows high expression in undifferentiated NB tumors, and inhibition of *Lsd1* via siRNAs, miR137 and small molecule inhibitors resulted in reduced NB cell growth and increased apoptosis both *in vitro* and *in vivo*[32–34]. These cells likely died from autophagy through the SESN2-dependent pathway or through cooperative interactions of *Lsd1* and MYCN to regulate tumor suppressor genes[35,36].

Overall, there are a few key points for this study. Several hallmark features of retinoblastoma tumors, such as rosettes and fleurettes mimic photoreceptors differentiation and *Lsd1* is involved in the differentiation of those cell types. Additionally, *Lsd1* has been found to be overexpressed

in many different types of cancers including those related to RB, such as MB and NB.

Therefore, we investigated the role of *Lsd1* in human RB tumors, and hypothesized that *Lsd1* would be overexpressed in RB cells and therefore could serve as a therapeutic target in the development of new RB treatments.

Methods

Human studies: Within the records of the L.F. Montgomery Laboratory at the Emory Eye Center, enucleation specimens ranging from January 1940 to August 2017 were identified that contained an intact retina. Many of these samples were enucleated due to a diagnosis of retinoblastoma. For the purposes of this study, only samples that contained a retina with relatively normal morphology and 3 nuclear layers were included for further Lsd1 expression analysis.

Immunohistochemistry: All antibodies are listed in the table below:

Antibody	Antibody Type	Company and Catalog Number	Concentration	Application
Rabbit anti-LSD1	Primary, monoclonal	Abcam ab129195	[1:250]	Human sections
Rabbit anti-Ki67	Primary, monoclonal	Abcam ab16667	[1:250]	Human sections
Mouse Anti-rhodopsin	Primary, monoclonal	Abcam ab98887	[1:250]	Mouse sections
Goat anti-short wavelength cone opsin	Primary, polyclonal	Santa Cruz sc-14363	[1:250]	Mouse sections
Donkey anti-rabbit AF488	Secondary, polyclonal	Jackson Immunological 711-545-152	[1:1000]	Human/mouse sections
Donkey anti-goat redX AF568	Secondary, polyclonal	Jackson Immunological 705-295-147	[1:1000]	Human/mouse sections

Sections: Murine eyes were enucleated and placed in zinc + formaldehyde for fixation for 1 hour

at room temperature. Afterwards the eyes were washed 3X in 1X phosphate buffer solution (PBS) (Corning 46-013-CM), dehydrated using various percentages of ethanol and xylene, and embedded in paraffin. 5 micron sections were cut using a microtome, placed on superfrost glass micro slides (VWR #48311-703) and allowed to dry overnight. The slides were then incubated in xylene for 8 minutes, then 5 minutes, then 2 minutes before being washed in various ethanol percentages for 2 minutes each (100%, 90%, 80% 70%, 60%, 50%) and then twice in 1X PBS for 2 minutes each. Afterwards, antigen retrieval was performed by heating the slides for 30 minutes in citrate buffer (10mM sodium citrate, 0.05% Tween 20, pH 6.0) in a 95°C water bath. The slides were removed from the water bath and allowed to cool to room temperature in a beaker filled with distilled room temperature water for 15 minutes. The slides were then washed one final time for 5 minutes in 1X PBS before being placed in a humidity chamber. A boundary was drawn around each individual retinal section using a pap pen (Research Products International #195505). The slides were incubated in 1X power blocking solution (Fisher Scientific #NC9495720) for 1 hour. Primary antibodies were diluted using 1X power block and 1X PBS. Sections were incubated in primary overnight at 4°C. The next day, slides were washed 3X in 1X PBS for 5 minutes each and then incubated in secondary antibodies for 2 hours at room temperature. The slides were again washed 3X in 1X PBS for 5 minutes each. One drop of DAPI nuclear stain plus fluorshield (Sigma #F6057) was applied on top of each section, a coverslip (Thermo Fisher #152250) was placed on top of the slide and allowed to dry overnight at room temperature before imaging.

Confocal Microscopy: Imaging of the retina sections was performed using a Nikon C1 confocal imaging system with Argon laser excitation at 488 and 568 nm. Confocal images were stitched

together using Adobe Photoshop C2.

Results

Because other studies have observed overexpression of Lsd1 in various cancerous samples, we hypothesized that Lsd1 would also be overexpressed in RB tumors. We obtained human RB tumor sections from the L.F. Montgomery Laboratory at the Emory Eye Center. These eyes were enucleated after being unresponsive to standard treatment procedures, fixed in 4% PFA and then cut into five micron thick sections. Immunocytochemistry was performed using an anti-LSD1 antibody (Figure 5.1). Panels 5.1A and 5.1C show LSD1 expression in green overlapped with a blue DAPI nuclei stain, whereas Panels 5.1B and 5.1D are LSD1 expression only. We observed relatively uniform expression of LSD1 protein in the intact human retina, which corresponds with what we observed previously[20]. Within the RB tumor itself, there is dichotomous expression of LSD1 in different areas of the tumor. Some cells have very high LSD1 expression whereas adjacent cells have little to no expression. This high expression is obvious in Panels 5.1C and 5.1D which are magnified sections from the larger tumor. The high LSD1 expression seems to correlate to areas of the tumor that have rosette and fleurette characteristics and this will be investigated further by looking at H&E stained sections.

We then investigated whether LSD1 expression correlated with particular features of the RB tumors. RB tumors have features that correlate with anaplasia[37]. We cut serial sections of different human tumors and stained them with LSD1, H&E, and Ki67, a cell proliferation marker (Figure 5.2). In different human tumor samples, Lsd1 is expressed in many different tumor cells (Panels 5.2A and 5.2D). When comparing these Lsd1 positive cells to a serial section stained

with H&E, we observe that many of the Lsd1 positive cells are also highly differentiated tumor cells (Panels 5.2B and 5.2E). These cells are also Ki67 positive indicating that they are proliferating (Panels 5.2C and 5.2F).

After looking at the expression and localization of Lsd1 in human RB samples, we wanted to determine whether transgenic RB mouse models showed similar expression patterns. Human RB generally arises from mutations in the RB gene within retinal precursor or cone precursor cells that cause cancerous transformation[9,10]. Mice with only RB mutations do not develop tumors[38]. Although there are a few different transgenic models of RB, one of the most common models is a tri-lateral transgenic RB mouse model[39,40]. It was developed through insertion of a chimeric molecule composed of SV40 Tag driven by the luteinizing hormone beta-subunit promoter[41]. Enucleated eyes from this trilateral RB mouse model were fixed in formaldehyde, cut into five micron thick sections, and stained with LSD1, rhodopsin (a marker for rod photoreceptors), short wavelength cone opsin (a marker for cone photoreceptors), and Ki67 as well as H&E (Figure 5.3). Similar to what we have observed previously, Lsd1 is expressed at varying levels throughout all mouse retinal cells. Based on the H&E staining (Panels 5.3A and 5.3F) and co-localization of Lsd1 with the photoreceptor markers rhodopsin and cone opsin (Panels 5.3B – 5.3I) we can see that the mouse RB tumor is located in the INL. This differs from human RB tumors which originate from cone precursor cells[10]. The mouse RB tumor shows high expression of Lsd1 and these tumors cells are proliferating as indicated by being Ki67 positive (Panel 5.3D and 5.3J).

Discussion

In this study, we investigated whether or not *Lsd1* is overexpressed in RB tumors and therefore could serve as a potential target for future RB therapies. Epigenetic abnormalities play a fundamental role in cancer development and in particular dysregulation of histone demethylases, such as *Lsd1*, have been observed in many different cancers[42]. We observed high expression of LSD1 in human RB tumors (Figure 5.1), specifically in the highly differentiated areas that have rosette and fleurette features (Figure 5.2). Human RB tumors typically arise from mutations either in retinal progenitor cells (RPCs) or cone precursor cells and have photoreceptor – like qualities[1]. A transgenic model of RB develops tumors in the INL, rather than the ONL, indicating that the cellular origins of that tumor are likely different from human RB (Figure 5.3).

Taken together, these data suggests that the overexpression of LSD1 in human RB may be a valuable molecular target for the development of future therapies. Future directions for this project are to test whether or not *Lsd1* inhibitors will be sufficient at killing RB cell lines. Ideally, we will test two different RB cell lines, WERI and Y79. The cell lines are necessary due to the obvious cellular origin differences observed between human RB and the transgenic RB mouse model. WERI cells were established from a 1-year old Caucasian female and have a complete deletion of the *Rb1* gene[12,43]. These WERI cells have similar characteristics as retinal progenitors and can be induced into retinal neuron-like cells which show decreased tumorigenicity compared to the original cell lines[44]. An *in vivo* model of RB can be established when these cells are injected directly into the eyes of nude mice[45]. Y79 cells were established from a 2.5-year old Caucasian female and have a partial *Rb1* deletion[43,46]. They can also be successfully injected intravitreally into nude mice to establish an *in vivo* model[47]. Both cell lines

are well-established RB models and share similar characteristics by growing as a suspension and expressing neuronal and glial markers[48]; however, they differ in growth patterns[49], lipid composition and metabolism[50], and gene expression[51]. Outside of WERI and Y79 cell lines, other less established cell lines, such as the RB116 cell line[52], could also be used.

Previous studies have demonstrated that RB cells are sensitive to treatments that target epigenetic proteins. MicroRNAs and shRNAs that target the histone demethylase HDAC9 and the histone methyltransferase EZH2 successful reduced Y79 derived tumor size and growth[53,54]. HDAC inhibitors, such as vorinostat, can induce growth arrest and apoptosis in both Y79 and WERI by increasing p53 and activated caspase 3, 8, 9 expression as well as regulating c-Myc expression[55,56]. Trans-2-phenylcyclopropylamine (2-PCPA), more commonly known as tranylcypromide (TCP), is an FDA-approved antidepressant that inhibits mono-amine oxidases (MAOs). Due to structural similarities between MAOs and LSD1, TCP can act as an irreversible inhibitor[57–59]. In the laboratory, *Lsd1* inhibitors have been efficacious against many types of cancers and are currently in Phase I/II clinical trials for small-cell lung cancer (SCLC) and acute myeloid leukemia (AML) in both the United States and Europe (ClinicalTrials.gov identifier: NCT02261779 and EudraCT Number: 2012-002154-23 ; identifier: NCT02273102 ; German Clinical Trials Register, DRKS-ID: DRK00006055)[13,60,61]. In addition, new derivates are constantly being synthesized to increase specificity and bioavailability while decreasing off-target effects[62,63].

Lsd1 inhibition alone does not always lead to cancerous cell death, leading to the exploration of effective combinatorial treatment regiments. Simultaneous inhibition of two or more targets by

drug combination can improve therapeutic efficacy. Histone deacetylase (HDAC) inhibitors have been explored as another route of epigenetic regulation. Co-administration of *Lsd1* and HDAC inhibitors showed synergistic effects on Ewing sarcoma[64] and rhabdomyosarcoma[65] cell lines and inhibited cell line and xenograft tumor growth in mouse models of breast cancer[66,67]. Patient-derived glioma stem cells and xenograft GB mouse models responded to *Lsd1* only and *Lsd1* plus HDAC inhibition to reduce cell viability and increase apoptosis[68–70] likely via induction of cellular senescence[71].

Several groups are now developing chimeric agents that target both histone demethylase and histone deacetylases[72–75]. *Kalin et al.* developed a synthetic hybrid agent that is effective in slowing tumor growth in a mouse xenograft model of melanoma[73]. *Duan et al.* also developed dual LSD1/HDAC inhibitors that inhibited growth in 5 different cancerous cell lines including gastric, breast, colorectal, prostate, and lung cancer[74]. These hybrid molecules will hopefully allow for increased therapeutic efficacy while decreasing harmful side effects for patients.

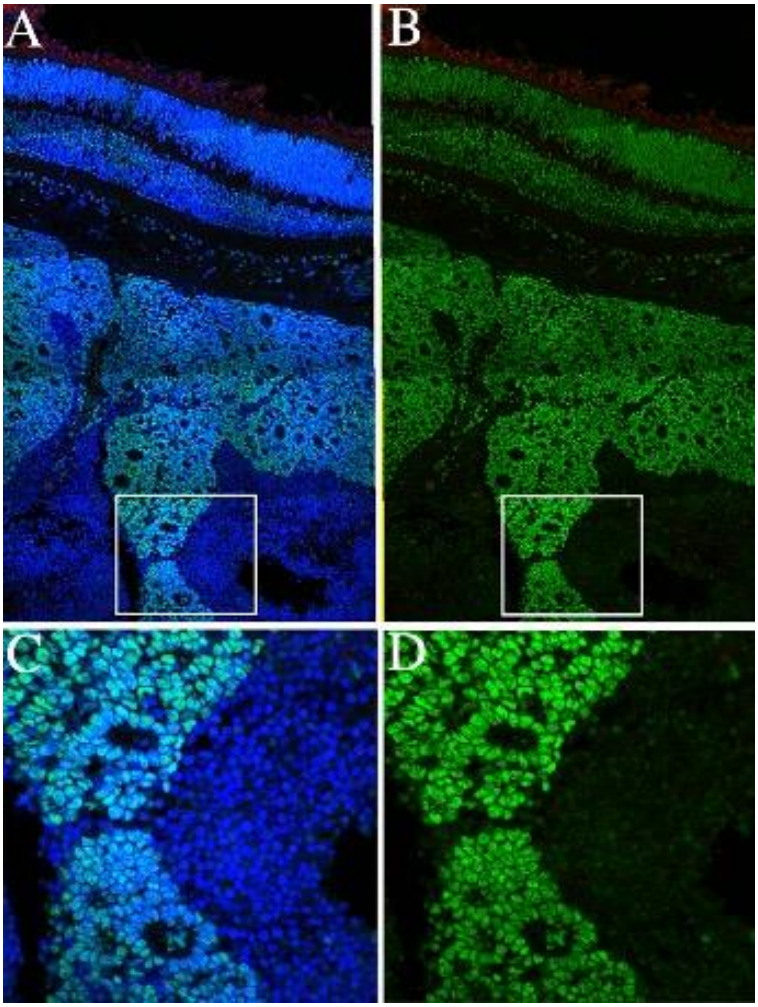

Figure 5.1: LSD1 expression in human retinoblastoma tumors. Photo merged 60X confocal microscope images of LSD1 expression (green), short wavelength cone opsin S-OPSIN (red), and DAPI nuclear stain (blue) containing both an intact retina (upper area of the panel) and tumor (bottom area) (Panel A). LSD1 expression (green) and S-OPSIN (red) are shown in Panel B. A single 60X image taken from Panels A and B, indicated by the white box, with DAPI nuclear stain (Panel C) and without nuclear stain (Panel D), highlights adjacent areas of the tumor that have high LSD1 expression directly bordering areas that have very low/no LSD1 expression.

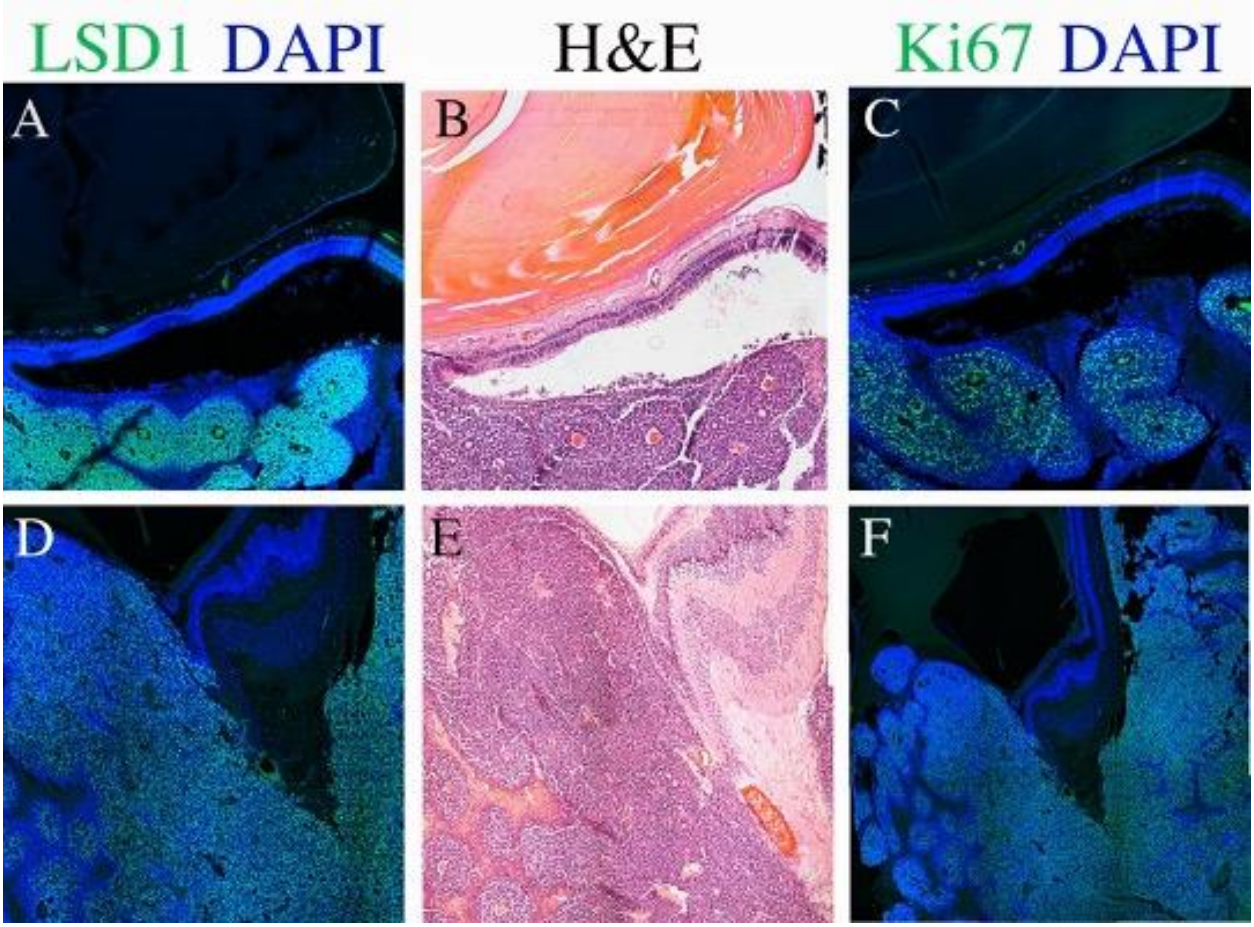

Figure 5.2: LSD1 is highly expressed in human retinoblastoma tumors in cells that are proliferating. 10X confocal images of immunohistochemistry on different human retinoblastoma tumors for LSD1 expression (green) and DAPI nuclear stain (blue) show very high LSD1 expression in specific areas of the tumor and very low/no LSD1 expression in other areas (Panels A and D). H&E staining of the tumor areas confirmed that the LSD1 expression correlated with highly differentiated areas of the tumors (generally defined by features such as rosettes) and very low/no LSD1 expression in undifferentiated areas (Panels B and E). Ki67+ cells indicate tumor areas that are proliferating and are generally located in the same cells that express high levels of LSD1 (Panels C and F).

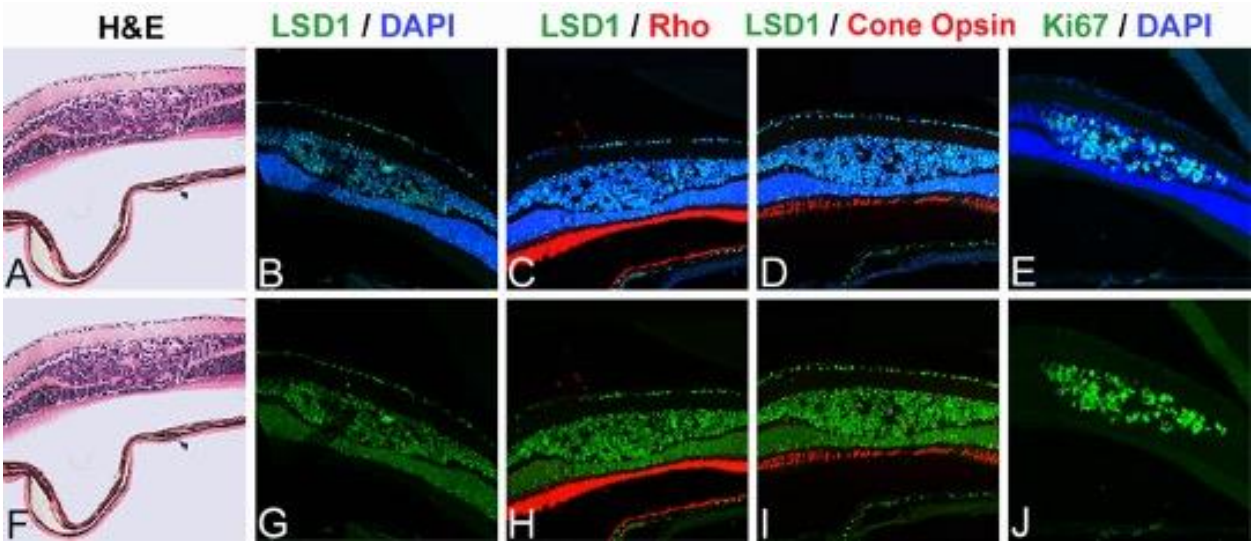

Figure 5.3: Retinoblastoma tumors in one common tri-lateral transgenic mouse model are located in the inner nuclear layer (INL) rather than outer nuclear layer (ONL) cells in human RB indicating differences in cellular origins. H&E staining shows the tissue structure of the RB mouse tumor (Panel A and F). The top row of 20X confocal images show a blue DAPI nuclear stain overlapping with LSD1 and various photoreceptor markers (Panels B – D) or Ki67 (Panel E). The bottom row of 20X confocal images show LSD1 alone (Panel G), LSD1 + rhodopsin (Panel H), LSD1 + short wavelength cone opsin (Panel I) and Ki67 alone (Panel J).

References

1 Mendoza PR, Grossniklaus HE. The Biology of Retinoblastoma. Prog Mol Biol Transl Sci. 2015;134:503-16. doi: 10.1016/bs.pmbts.2015.06.012. Epub 2015 Jul 14. PMID: 26310174

2 Broaddus E, Topham A, Singh AD. Survival with retinoblastoma in the USA: 1975-2004. Br J Ophthalmol 2009;93:24–7. PMCID:18718969.

3 Mendoza PR, Grossniklaus HE. Therapeutic Options for Retinoblastoma. Cancer Control 2016;23:99–109. PMCID:25661903.

4 Court H, McLean G, Guthrie B, Mercer SW, Smith DJ. Visual impairment is associated with physical and mental comorbidities in older adults: a cross-sectional study. BMC Med 2014;12:1–8.

5 Morse AR. Addressing the Maze of Vision and Depression. JAMA Ophthalmol 2019;137:832–3.

6 Osaba M, Doro J, Liberal M, Lagunas J, Kuo IC, Reviglio VE. Relationship Between Legal Blindness and Depression. Med Hypothesis, Discov Innov Ophthalmol J 2019;8:306–11.

7 Schakel W, Van Der Aa HPA, Bode C, Hulshof CTJ, Van Rens GHMB, Van Nispen RMA. The economic burden of visual impairment and comorbid fatigue: A cost-of-illness study (from a societal perspective). Investig Ophthalmol Vis Sci 2018;59:1916–23.

8 Brunes A, Hansen MB, Heir T. Loneliness among adults with visual impairment: Prevalence, associated factors, and relationship to life satisfaction. Health Qual Life Outcomes 2019;17:1–7. PMCID:30709406.

9 Bremner R, Sage J. Cancer: The origin of human retinoblastoma. Nature. 2014 Oct 16;514(7522):312-3. doi: 10.1038/nature13748. Epub 2014 Sep 24. PMID: 25252972; PMCID: PMC5438154

10 Xu XL, Singh HP, Wang L, Qi D-L, Poulos BK, Abramson DH, et al. Rb suppresses human cone precursor-derived retinoblastoma tumors. Nature 2014;514:385–8. PMCID:25252974.

11 Friend SH, Bernards R, Rogelj S, Weinberg RA, Rapaport JM, Albert DM, et al. A human DNA segment with properties of the gene that predisposes to retinoblastoma and osteosarcoma. Nature 1986;323:643–6. PMCID:2877398.

12 Bookstein R, Lee EYHP, To H, Young LJ, Sery TW, Hayes RC, et al. Human retinoblastoma susceptibility gene: Genomic organization and analysis of heterozygous intragenic deletion mutants. Proc Natl Acad Sci U S A 1988;85:2210–4.

13 Zheng Y-C, Ma J, Wang Z, Li J, Jiang B, Zhou W, et al. A Systematic Review of Histone Lysine-Specific Demethylase 1 and Its Inhibitors. Med Res Rev 2015;35:1032–71. PMCID:20099266.

14 Hayami S, Kelly JD, Cho HS, Yoshimatsu M, Unoki M, Tsunoda T, et al. Overexpression of LSD1 contributes to human carcinogenesis through chromatin regulation in various cancers. Int J Cancer 2011;128:574–86. PMCID:20333681.

15 Ismail T, Lee HK, Kim C, Kwon T, Park TJ, Lee HS. KDM1A microenvironment, its oncogenic potential, and therapeutic significance. Epigenetics and Chromatin 2018;11:1–15.

16 Shi Y, Lan F, Matson C, Mulligan P, Whetstine JR, Cole PA, et al. Histone demethylation mediated by the nuclear amine oxidase homolog LSD1. Cell

2004;119:941–53. PMCID:15620353.

17 Wang J, Scully K, Zhu X, Cai L, Zhang J, Prefontaine GG, et al. Opposing LSD1 complexes function in developmental gene activation and repression programs. Nature 2007;446:882–7. PMCID:17392792.

18 Cho HS, Suzuki T, Dohmae N, Hayami S, Unoki M, Yoshimatsu M, et al. Demethylation of RB regulator MYPT1 by histone demethylase LSD1 promotes cell cycle progression in cancer cells. Cancer Res 2011;71:655–60. PMCID:21115810.

19 Huang J, Sengupta R, Espejo AB, Lee MG, Dorsey JA, Richter M, et al. p53 is regulated by the lysine demethylase LSD1. Nature 2007;449:105–8. PMCID:17805299.

20 Ferdous S, Grossniklaus HE, Boatright JH, Nickerson JM. Characterization of LSD1 Expression Within the Murine Eye. Invest Ophthalmol Vis Sci 2019;60:4619–31.

21 Popova EY, Pinzon-Guzman C, Salzberg AC, Zhang SS-M, Barnstable CJ. LSD1-Mediated Demethylation of H3K4me2 Is Required for the Transition from Late Progenitor to Differentiated Mouse Rod Photoreceptor. Mol Neurobiol 2016;53:4563–81. PMCID:26298666.

22 Kim Y, Nam HJ, Lee J, Park DY, Kim C, Yu YS, et al. Methylation-dependent regulation of HIF-1α stability restricts retinal and tumour angiogenesis. Nat Commun 2016;7:10347. PMCID:26757928.

23 Yokoyama A, Takezawa S, Schule R, Kitagawa H, Kato S. Transrepressive Function of TLX Requires the Histone Demethylase LSD1. Mol Cell Biol 2008;28:3995–4003. PMCID:18391013.

24 Islam MM, Zhang C-L. TLX: A master regulator for neural stem cell maintenance and neurogenesis. Biochim Biophys Acta - Gene Regul Mech 2015;1849:210–6.

25 Li J, Yen C, Liaw D, Podsypanina K, Bose S, Wang SI, et al. PTEN, a Putative Protein Tyrosine Phosphatase Gene Mutated in Human Brain, Breast, and Prostate Cancer. Science (80-) 1997;275:1943–7. PMCID:9072974.

26 Yin Y, Shen WH. PTEN: A new guardian of the genome. Oncogene 2008;27:5443–53. PMCID:18794879.

27 Capper D, Jones DTW, Sill M, Hovestadt V, Schrimpf D, Sturm D, et al. DNA methylation-based classification of central nervous system tumours. Nature. 2018 Mar 22;555(7697):469-474. doi: 10.1038/nature26000. Epub 2018 Mar 14. PMID: 29539639; PMCID: PMC6093218.

28 Kohe SE, Bennett CD, Gill SK, Wilson M, McConville C, Peet AC. Metabolic profiling of the three neural derived embryonal pediatric tumors retinoblastoma, neuroblastoma and medulloblastoma, identifies distinct metabolic profiles. Oncotarget 2018;9:11336–51.

29 Pajtler KW, Weingarten C, Thor T, Künkele A, Heukamp LC, Büttner R, et al. The KDM1A histone demethylase is a promising new target for the epigenetic therapy of medulloblastoma. Acta Neuropathol Commun 2014;2:1–13.

30 Callegari K, Maegawa S, Bravo-Alegria J, Gopalakrishnan V. Pharmacological inhibition of LSD1 activity blocks REST-dependent medulloblastoma cell migration. Cell Commun Signal 2018;16:1–13.

31 Lee C, Rudneva VA, Erkek S, Zapatka M, Chau LQ, Tacheva-Grigorova SK, et al. Lsd1 as a therapeutic target in Gfi1-activated medulloblastoma. Nat Commun 2019;10:332.

32 Gupta S, Doyle K, Mosbruger TL, Butterfield A, Weston A, Ast A, et al. Reversible LSD1 inhibition with HCI-2509 induces the p53 gene expression signature and disrupts the MYCN signature in high-risk neuroblastoma cells. Oncotarget 2018;9:9907–24.

33 Schulte JH, Lim S, Schramm A, Friedrichs N, Koster J, Versteeg R, et al. Lysine-specific demethylase 1 is strongly expressed in poorly differentiated neuroblastoma: Implications for therapy. Cancer Res 2009;69:2065–71. PMCID:19223552.

34 Althoff K, Beckers A, Odersky A, Mestdagh P, Köster J, Bray IM, et al. MiR-137 functions as a tumor suppressor in neuroblastoma by downregulating KDM1A. Int J Cancer 2013;133:1064–73.

35 Ambrosio S, Saccà CD, Amente S, Paladino S, Lania L, Majello B. Lysine-specific demethylase LSD1 regulates autophagy in neuroblastoma through SESN2-dependent pathway. Oncogene 2017;36:6701–11.

36 Amente S, Milazzo G, Sorrentino MC, Ambrosio S, Palo G Di, Lania L, et al. Lysine-specific demethylase (LSD1/KDM1A) and MYCN cooperatively repress tumor suppressor genes in neuroblastoma. Oncotarget 2015;6:14572–83. PMCID:26062444.

37 Pia R. Mendoza Charles S. Specht. Histopathologic Grading of Anaplasia in Retinoblastoma. Am J Ophthalmol 2015;159:764-776.e3.

38 Williams BO, Schmitt EM, Remington L, Bronson RT, Albert DM, Weinberg RA, et al. Extensive contribution of Rb-deficient cells to adult chimeric mice with limited histopathological consequences. EMBO J 1994;13:4251–9. PMCID:7925270.

39 Mills MD, Windle JJ, Albert DM. Retinoblastoma in Transgenic Mice: Models of Hereditary Retinoblastoma. Surv Ophthalmol 1999;43:508–18.

40 Nair RM, Vemuganti GK. Transgenic Models in Retinoblastoma Research. Ocul Oncol Pathol 2015;1:207–13.

41 Windle JJ, Albert DM, O'Brien JM, Marcus DM, Disteche CM, Bernards R, et al. Retinoblastoma in transgenic mice. Nature 1990;343:665–9.

42 Lim S, Metzger E, Schle R, Kirfel J, Buettner R. Epigenetic regulation of cancer growth by histone demethylases. Int J Cancer 2010;127:1991–8.

43 Reid TW, Albert DM, Rabson AS, Russell P, Craft J, Chu EW, et al. Characteristics of an established cell line of retinoblastoma. J Natl Cancer Inst 1974;53:347–60.

44 Hu HL, Deng F, Liu Y, Chen MF, Zhang XL, Sun XR, et al. Characterization and retinal neuron differentiation of WERI-Rb1 cancer stem cells. Mol Vis 2012;18:2388–97.

45 Liu Y, Hu H, Liang M, Xiong Y, Li K, Chen M, et al. Regulated differentiation of WERI-Rb-1 cells into retinal neuron-like cells. Int J Mol Med 2017;40:1172–84.

46 McFall R, Sery TW, Makadon M. Characterization of a New Continuous Cell Line Derived from a Human Retinoblastoma. Cancer Res 1977;37:1003–10.

47 Tschulakow A V., Schraermeyer U, Rodemann HP, Julien-Schraermeyer S. Establishment of a novel retinoblastoma (Rb) nude mouse model by intravitreal injection of human Rb Y79 cells - Comparison of in vivo analysis versus histological follow up. Biol Open 2016;5:1625–30.

48 Jiang Q, Lim R, Blodi FC. Dual properties of cultured retinoblastoma cells: Immunohistochemical characterization of neuronal and glial markers. Exp Eye Res 1984;39:207–15.

49 Busch M, Philippeit C, Weise A, Dünker N. Re-characterization of established human retinoblastoma cell lines. Histochem Cell Biol 2014;143:325–38.

50 Yorek MA, Figard PH, Kaduce TL, Spector AA. A comparison of lipid metabolism in two human retinoblastoma cell lines. Investig Ophthalmol Vis Sci 1985;26:1148–54.

51 Sur I, Taipale J. Systematic variation in gene expression patterns in human cancer cell lines [see comments]. Nat Rev Cancer 2016;24:227–35.

52 Bejjani A, Choi MR, Cassidy L, Collins DW, Brien JMO, Murray T, et al. RB116 : An RB1 + retinoblastoma cell line expressing primitive markers. Mol Vis 2012;18:2805–13. PMCID:23233783.

53 Zhang Y, Wu D, Xia F, Xian H, Zhu X, Cui H, et al. Downregulation of HDAC9 inhibits cell proliferation and tumor formation by inducing cell cycle arrest in retinoblastoma. Biochem Biophys Res Commun 2016;473:600–6.

54 Jin Q, He W, Chen L, Yang Y, Shi K, You Z. MicroRNA-101-3p inhibits proliferation in retinoblastoma cells by targeting EZH2 and HDAC9. Exp Ther Med 2018;16:1663–70.

55 Poulaki V, Mitsiades CS, Kotoula V, Negri J, McMullan C, Miller JW, et al. Molecular sequelae of histone deacetylase inhibition in human retinoblastoma cell lines: Clinical implications. Investig Ophthalmol Vis Sci 2009;50:4072–9. PMCID:19387079.

56 Yu N, Chen P, Wang Q, Liang M, Qiu J, Zhou P, et al. Histone deacetylase inhibitors differentially regulate c-Myc expression in retinoblastoma cells. Oncol Lett 2020;19:460–8.

57 Schmidt DMZ, McCafferty DG. trans-2-phenylcyclopropylamine is a mechanism-based inactivator of the histone demethylase LSD1. Biochemistry 2007;46:4408–16.

58 Lee MG, Wynder C, Schmidt DM, McCafferty DG, Shiekhattar R. Histone H3 Lysine 4 Demethylation Is a Target of Nonselective Antidepressive Medications. Chem Biol 2006;13:563–7. PMCID:16793513.

59 Niwa H, Umehara T. Structural insight into inhibitors of flavin adenine dinucleotide-dependent lysine demethylases. Epigenetics 2017;12:1–13.

60 Morera L, Lübbert M, Jung M. Targeting histone methyltransferases and demethylases in clinical trials for cancer therapy. Clin Epigenetics 2016;8:57. PMCID:27222667.

61 Fiskus W, Sharma S, Shah B, Portier BP, Devaraj SGT, Liu K, et al. Highly effective combination of LSD1 (KDM1A) antagonist and pan-histone deacetylase inhibitor against human AML cells. Leukemia 2014;28:2155–64.

62 Binda C, Valente S, Romanenghi M, Pilotto S, Cirilli R, Karytinos A, et al. Biochemical, structural, and biological evaluation of tranylcypromine derivatives as inhibitors of histone demethylases LSD1 and LSD2. J Am Chem Soc 2010;132:6827–33.

63 Ji YY, Lin SD, Wang YJ, Su MB, Zhang W, Gunosewoyo H, et al. Tying up tranylcypromine: Novel selective histone lysine specific demethylase 1 (LSD1) inhibitors. Eur J Med Chem 2017;141:101–12.

64 Welch D, Kahen E, Fridley B, Brohl AS, Cubitt CL, Reed DR. Small molecule inhibition of lysine-specific demethylase 1 (LSD1) and histone deacetylase (HDAC) alone and in combination in Ewing sarcoma cell lines. PLoS One 2019;14:1–17.

65 Haydn T, Metzger E, Schuele R, Fulda S. Concomitant epigenetic targeting of LSD1 and HDAC synergistically induces mitochondrial apoptosis in rhabdomyosarcoma cells. Cell Death Dis 2017;8:1–12.

66 Huang Y, Vasilatos SN, Boric L, Shaw PG, Davidson NE. Inhibitors of histone demethylation and histone deacetylation cooperate in regulating gene expression and inhibiting growth in human breast cancer cells. Breast Cancer Res Treat 2012;131:777–89.

67 Cao C, Wu H, Vasilatos SN, Chandran U, Qin Y, Oesterreich S, et al. HDAC5-LSD1 Axis Regulates Antineoplastic Effect of Natural HDAC Inhibitor Sulforaphane in Human Breast Cancer Cells 2018;143:1388–401.

68 Sareddy GR, Nair BC, Krishnan SK, Gonugunta VK, Zhang Q guang, Suzuki T, et al.

KDM1 is a novel therapeutic target for the treatment of gliomas. Oncotarget 2013;4:18–28.

69 Singh MM, Manton CA, Bhat KP, Tsai WW, Aldape K, Barton MC, et al. Inhibition of LSD1 sensitizes glioblastoma cells to histone deacetylase inhibitors. Neuro Oncol 2011;13:894–903. PMCID:21653597.

70 Singh MM, Johnson B, Venkatarayan A, Flores ER, Zhang J, Su X, et al. Preclinical activity of combined HDAC and KDM1A inhibition in glioblastoma. Neuro Oncol 2015;17:1463–73. PMCID:25795306.

71 Sacca CD, Gorini F, Ambrosio S, Amente S, Faicchia D, Matarese G, et al. Inhibition of lysine-specific demethylase LSD1 induces senescence in Glioblastoma cells through a HIF-1α-dependent pathway. Gene Regul Mech 2019;41:535–46.

72 Stazi G, Fioravanti R, Mai A, Mattevi A, Valente S. Histone deacetylases as an epigenetic pillar for the development of hybrid inhibitors in cancer. Curr Opin Chem Biol 2019;50:89–100.

73 Kalin JH, Wu M, Gomez A V., Song Y, Das J, Hayward D, et al. Targeting the CoREST complex with dual histone deacetylase and demethylase inhibitors. Nat Commun 2018;9: PMCID:29302039.

74 Duan YC, Ma YC, Qin WP, Ding LN, Zheng YC, Zhu YL, et al. Design and synthesis of tranylcypromine derivatives as novel LSD1/HDACs dual inhibitors for cancer treatment. Eur J Med Chem 2017;140:392–402.

75 Engel M, Gee YS, Cross D, Maccarone A, Heng B, Hulme A, et al. Novel dual-action prodrug triggers apoptosis in glioblastoma cells by releasing a glutathione quencher and lysine-specific histone demethylase 1A inhibitor. J Neurochem 2019;149:535–50. PMCID:30592774.

Chapter VI: Age-related ocular changes in wildtype C57Bl/6J mice between 2 and 32 months

Salma Ferdous, Kristie L. Liao, Isabelle D. Gefke, Vivian R. Summers, Wenfei Wu, Kevin J. Donaldson, Yong-Kyu Kim, Jana Sellers, Jendayi Dixon, Debresha A. Shelton, Shanu Markand, Somin M. Kim, Nan Zhang, Jeffrey H. Boatright, John M. Nickerson

Currently under review at Investigative Ophthalmology and Visual Sciences (IOVS)

Abstract

The purpose of this study was to extend our understanding of how aging affects normal retina function and morphology in wild-type C57BL/6J mice, by analyzing electrophysiological recordings and in vivo and postmortem anatomy. Electroretinograms (ERGs), Spectral Domain Optical Coherence Tomography (SD-OCT) and confocal scanning laser ophthalmoscope (cSLO) in vivo images were obtained from mice between the ages of 2 and 32 months in four groups: Group 1 (<0.5 years), Group 2 (1.0 - 1.5 years), Group 3 (1.5 - 2.0 years), Group 4 (>2.0 years). Afterwards, mouse bodies and eyes were weighed. Eyes were stained with hematoxylin & eosin (H&E) and cell nuclei were quantified. With aging, mice showed a significant reduction in both a- and b-wave ERG amplitudes in scotopic and photopic conditions. Additionally, total retina and ONL thickness, as measured by SD-OCT images, were significantly reduced in older groups. cSLO images showed an increase in auto-fluorescence at the photoreceptor-RPE interface as age increases. H&E cell nuclei quantification showed significant reduction in the ONL in older ages, but no differences in the INL or GCL. By using multiple age groups and extending the upper age limit of our animals to ~2.65 years (P970), we found that natural aging causes negative effects on retinal function and morphology in a gradual, rather than abrupt, process. Future studies should investigate the exact mechanisms that contribute to these gradual declines in order to discover pathways that could potentially serve as therapeutic targets.

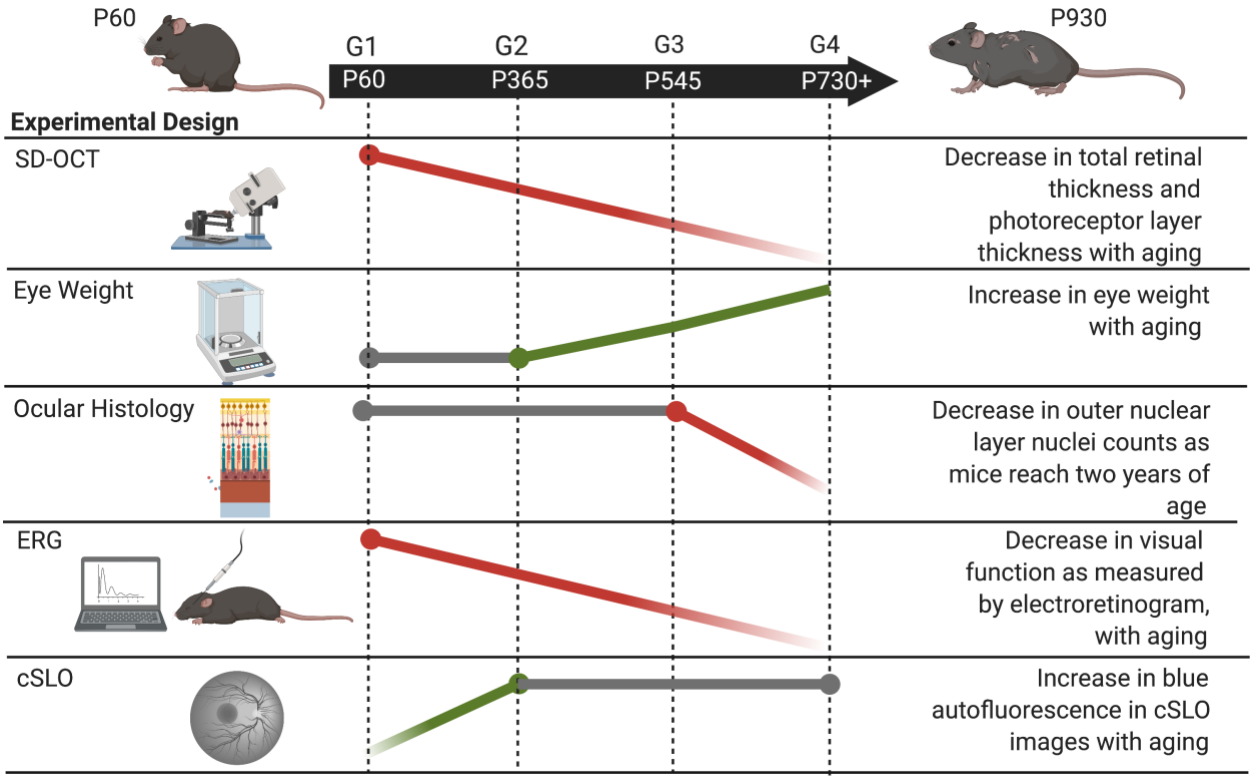

Graphical Abstract: Age-related retinal changes that occur in C57BL/6J mice between 2 and 32 months. Overall, across all ages there is a gradual decline in retinal and photoreceptor layer thickness as measured by OCT and visual function as measured by ERG. There is a relatively stable number of cell nuclei in the ONL until mice reach P545 then a decline is observed. Lastly, there is an increase in eye weight and auto-fluorescence at the ONL-RPE junction as measured on cSLO images taken by the Heidelberg Spectralis HRA + OCT. (Created with BioRender.com)

Introduction

Age-related visual impairment affects the physical, psychological and social function of older adults[1] and is a major risk factor for many prevalent ophthalmic disorders[2]. Even healthy patients have structural retinal changes with age, including decreased retinal nerve fiber layer and mean central retinal thickness[3], as well as decreased thickness of individual retinal layers, such as the ganglion cell layer (GCL), inner plexiform layer (IPL), and inner nuclear layer (INL)[4]. These changes in retinal layer thickness are accompanied by decreased rod photoreceptor density[5], altered retinal microvasculature[6,7], mitochondrial dysfunction with increased reactive oxygen species (ROS) generation[8], and para-inflammation[9]. The morphological and physiological changes likely cause exponential decreases in rod and cone amplitudes and increased implicit times in both photopic and scotopic conditions[10,11]. Outside of the retina, aging can cause stiffening of lens fibers and zonules, leading to presbyopia, and the loss of transparency in lens crystallin, leading to cataracts[2]. Additionally, as age increases, macrophages and microglia infiltrate the photoreceptor-retinal pigment epithelium (RPE) interface[12,13], there is an increase in lipofuscin and drusen[14,15] and Bruch's membrane thickens partially due to depositions of lipids[16].

Animal studies evaluating age-related changes in the visual system have observed gross structural, morphological, and functional changes in both the retina and RPE and explored underlying mechanisms. Aging studies in rats showed gradual decreases in a- and b-wave electroretinogram (ERG) responses and significant thinning was observed in the inner plexiform layer (IPL), outer plexiform layer (OPL), inner nuclear layer (INL), and outer nuclear layer (ONL)[17,18]. In mice, similar decreases in ERG responses were observed between 1.5 and 18 months of age which correlated with metabolic changes in the retina, RPE/choroid, optic nerve,

and lens[19].

Many aging studies in rodents compare relatively young animals (< 6 months) to "aged" animals, which range from roughly 1-2 years old. Although useful as a general comparison, investigating the differences between 1 "young" group and 1 "aged" group does not provide information on the overall progression of ocular changes due to aging. Therefore, we included multiple age groups in our current study to identify a general age when these ocular changes occur as well as extend the upper age limit to include animals that are at the maximum life expectancy of mice. The purpose of this study was to build upon and extend our understanding of how aging affects normal retina function and morphology by analyzing electrophysiological recordings and *in vivo* and *postmortem* anatomical data collected from wild-type C57BL/6J animals aged 2 – 32 months.

Methods

Animals: Mouse housing, experiments, and handling were approved by the Emory University Institutional Animal Care and Use Committee. Studies were conducted in adherence with Association for Research in Vision and Ophthalmology (ARVO) and followed guidance and principles of the Association for Assessment and Accreditation of Laboratory Animal Care (AAALAC). C57BL/6J (WT) mice were maintained on a 12-h light/dark cycle at 22C, and standard mouse chow (Lab Diet 5001; PMI Nutrition Inc., LLC, Brentwood, MO) and water were provided *ad libitum*. Animals were either purchased from Jackson Laboratories (JAX) directly or bred in-house for 3 generations or less from JAX breeding pairs. The mice in each group represent multiple different litters and all of the mice used in this study are independent

from one another (i.e., no mouse was included in multiple groups); therefore, we expect no batch effects. The mice were managed and housed by Emory University Division of Animal Resources. Adult mice were euthanized using CO_2 gas asphyxiation for 5 minutes followed by cervical dislocation. All mice used for this study were divided up into the following groups: Group 1 (post-natal day 60 – 180); Group 2 (post-natal day 365 – 544); Group 3 (post-natal day 545 – 729); Group 4 (post-natal day 730+). There is a fair distribution of genders in all groups. See Table 1.

Electroretinograms (ERGs): Mice were dark-adapted overnight the day before ERGs were assessed. Each mouse was anesthetized using intraperitoneal (IP) injections of 100 mg/kg of ketamine and 15 mg/kg xylazine (ketamine; KetaVed from Patterson Veterinary, Greeley, CO; xylazine from Patterson Veterinary, Greeley, CO).

Once anesthetized, proparacaine (1%; Akorn Inc., Ann Arbor, MI) and tropicamide (1%; Akorn Inc.) eye drops were administered as a topical anesthetic and to dilate the pupils. Mice were placed on a heating pad inside of a Faraday cage directly in front of the desktop Bigshot LED Ganzfeld stimulator (LKC Technologies, Gaithersburg, MD). Custom-made platinum wire fiber electrodes were placed in contact with each individual cornea. Refresh tears (Allergan) were added to form a "bubble" on each eye in order to maintain conductivity with the electrode fibers. 1-centimeter reference electrodes (LKC) were inserted into each cheek pad and a ground electrode (LKC) was placed in the tail. ERGs were recorded for the scotopic condition (0.00039 – 137 cd s/m^2 with 3 – 10 flash stimuli increasing in time intervals ranging from 4.1 to 62.6 seconds) and for the photopic condition (0.16 – 79.65 cd s/m^2 with 25 flash stimuli at time

intervals of 0.476 seconds). Afterwards, mice were injected with reversal agent (0.5 mg/mL atipamezole, injection volume 5 µL per gram mouse weight; Patterson Veterinary, Greeley, CO) and placed individually in cages on top of heated water pads until fully awake.

In vivo ocular imaging: Mice were anesthetized using intraperitoneal (IP) injections of 100 mg/kg of ketamine and 15 mg/kg xylazine as above. Once anesthetized, proparacaine and tropicamide eye drops were administered as a topical anesthetic and to dilate the pupils as above. A MicronIV SD-OCT system with fundus camera (Phoenix Research Labs, Pleasanton, CA) was used to obtain fundus photos and retinal morphology for both eyes. Images were taken after clear visualization of the fundus with the optic nerve centered was obtained. Circular SD-OCT scans approximately 100 microns from the optic nerve head were taken and fifty scans were averaged together. The retinal morphology images were analyzed for both total retinal thickness and photoreceptor layer thickness using Photoshop CS6 (Adobe Systems Inc., San Jose, CA) by two individuals who were masked to sample identity. The number of pixels was converted into micrometers by multiplying by a conversion factor (1 pixel = 1.3 µm).

Afterwards, a rigid contact lens was placed on the eye (BOZR: 1.7 mm, Diameter: 3.2 mm, power: Plano), and confocal scanning laser ophthalmoscopy (cSLO) blue autofluorescence (488nm excitation wavelength) imaging was conducted using the Spectralis HRA+OCT (Heidelberg Engineering) instrument. Various images were taken en face at fairly discrete depths using intraocular landmarks. For the purposes of this study, we are showing images from the “farthest”/deepest layer, which we believe to be at the level of the photoreceptor-RPE cells. During imaging and anesthetic recovery, the mice were kept on water-circulating heat pads to

maintain their body temperature. Quantification of these images was achieved using densitometry analysis. Briefly, all images were cropped to 1440 pixels X 1440 pixels to remove extraneous static around the edge of the raw images. These cropped images were then opened in Photoshop CS6 and then the magnetic lasso tool was used to demarcate different sections of the image that excluded blood vessels to measure the densitometry. The different sections were summed for each individual image. Depending on whether one or both eyes were successfully imaged from an individual mouse, each sample consists of either one quantified image or two quantified images that were averaged together.

Ocular Section Histology: Eyes were enucleated and placed in 10 mL of chilled 95% methanol 5% acetic acid for 4 days at -80ºC. Afterwards, samples were dehydrated twice in 100% ethanol for twenty minutes, placed in xylene twice for twenty minutes, and then embedded in paraffin. Sagittal plane sections were cut at 5 micron increments. Sagittal sections containing the optic nerve were selected for further staining to ensure consistency across all samples. Sections were then stained with hematoxylin and eosin (H&E) to visualize retinal morphology. Nuclei in the outer nuclear layer (ONL), inner nuclear layer (INL), and ganglion cell layer (GCL) were counted manually by two individuals who were masked to sample identity. Only nuclei within a 100 micron section were counted using Photoshop CS6 at regularly spaced intervals 250 microns apart from the optic nerve in both the superior and inferior directions.

Eye and Body Weight: Mouse body-weight measurements were taken using a scale (Escali Corporation Model L600, Burnsville, MN, USA). Eyes were enucleated and fat and extra ocular muscle were removed using forceps under a dissecting microscope. Individual eyes were then

weighed (Denver Instrument Company Model A-160, Bohemia, NY, USA).

Statistical Analysis: Statistical analysis was conducted using Prism 8.4.2 on Mac OS X Version 7 (GraphPad Software, Inc., La Jolla, CA, USA). All data are summarized as mean □ standard deviation (SD) and individual statistical tests are listed in figure legends. P values □ 0.05 were considered to be statistically significant. Each sample group member is an independent mouse and sample sizes for each figure are listed in Table 1.

Results

We first assessed how retinal function changes with age by recording a- and b- waves in both scotopic and photopic conditions across a series of increasing flash intensities. Overall, both bar and line graphs of a- and b-wave amplitudes showed significant decreases in retinal function across different age groups regardless of condition (Supplemental Figure 6.1). These differences were most evident when looking at the raw average ERG waveforms from the youngest animals (Group 1) and the oldest animals (Group 4) (Supplemental Figure 6.2). At low flash intensities in both scotopic and photopic conditions, there was little difference between the two groups; however, at medium and high flash intensities in both scotopic and photopic conditions, the differences became much more apparent. At the highest flash intensities (137 cd s/m^2 for scotopic conditions or 79.65 cd s/m^2 for photopic conditions), there were significant differences among the youngest group (Group 1) and the three older groups (Group 2, Group 3, and Group 4) (Figure 6.1). There were significant differences among Group 1 and the remaining three groups (Group 2, Group 3, and Group 4) in the scotopic a-wave. No differences were observed among Group 2, 3, and 4. The same pattern was observed for the scotopic b-waves and photopic

b-waves. Photopic a-waves only showed significant differences between Group 1 and Group 2, not among the older groups. The full list of statistical comparisons for a- and b-wave ERG results in both scotopic and photopic conditions at increasing flash intensities is available in Supplemental Tables 6.1 – 6.4.

Morphological changes were seen with age in Fundus and SD-OCT images. Qualitatively, as age increases, there was an increasingly mottled appearance in the C57BL/6J fundus photos (Supplemental Figure 6.3). Additionally, there are also opacities evident in the older animals that could be indicative of increased cataract development or complications of incomplete iris dilation. We have highlighted some, but not all, of these features with white arrows in both Figure 6.2 and Supplemental Figure 6.3. Quantification of the total retinal thickness and ONL from SD-OCT images showed significant decreases as age increased (Figure 6.2). For total retinal thickness, there were significant decreases among Group 1 and the remaining three groups (Group 2, Group 3 and Group 4). There was also a significant decrease in total retinal thickness between Group 2 and Group 3. When specifically looking at the ONL, a significant decrease was observed among Group 1 and the remaining groups (Group 2, Group 3 and Group 4) as well as between Group 2 and Group 4. A full list of statistical comparisons for total retinal thickness and photoreceptor layer thickness is available in Supplemental Tables 6.5 and 6.6, respectively.

In addition to the thickness changes seen in the retina, changes were also observed in representative cSLO images from the layer of cells at the photoreceptor-RPE interface (Figure 6.3). In the youngest animals (Group 1), no abnormalities were observed in the fundus autofluorescence images; however, numerous discrete small punctate spots became apparent by

one year of age (Group 2) and remained constant and pronounced up to 2+ years of age (Group 4). Densitometry quantification of the autofluorescence further illustrated the statistically significant increase in autofluorescence among Group 1 and the three remaining groups.

After ERGs and *in vivo* imaging were collected, the eyes were enucleated and weighed. Eye weights increased gradually, but significantly with age among Group 1 and the remaining three groups (Group 2, Group 3, and Group 4) (Figure 6.4). However, when the eye weight is adjusted for the body weight of the animal, there is only a significant difference between Group 1 and Group 4, and between Group 3 and 4. A full list of statistical comparisons for eye weight and eye weight adjusted for body weight is available in Supplemental Tables 6.7 and 6.8 respectively.

Finally, H&E staining provided a more detailed overview of the morphological changes that occur during aging. We show one representative whole eye, retina, and photoreceptor – RPE interface image for each group (Figure 6.5). Overall, we did not observe any obvious morphological changes in the retina as age increases. In Group 4, there were some subtle irregularities in the inner and outer segments and the RPE sheet was slightly bumpy with small amounts of irregular thinning and elevation in patches, which we hypothesize to correspond with the mottling that was observed in the Fundus images (Supplemental Figure 6.4). Alas, we are unable to prove or disprove this hypothesis until better alignment and registration can be achieved. Quantification of cell nuclei number at 250 micron intervals from the optic nerve head both in the superior and inferior direction for the ONL, INL, and GCL showed consistent significant decreases in the ONL, but not the INL or GCL (Figure 6.5). In the ONL, there were significant decreases in the number of nuclei at the majority of intervals between Group 1 and

Group 4; however, no significant differences were observed among Group 1, Group 2 and Group 3. In the INL and GCL, while there were certain intervals that had significant decreases, they were not consistent among particular groups or at particular intervals; therefore, they were likely not biologically meaningful. A full list of statistical comparisons for nuclei counts in the ONL, INL, and GCL is available in Supplemental Tables 9 – 11 respectively.

Discussion

The purpose of this study was to expand our current understanding of how natural aging affects retinal function and morphology. Here we sought to understand if vision changes due to natural aging occur gradually or abruptly. Whereas the majority of aging studies in the visual system compare one "young" group of animals to another "old" group, one that is generally 1-2 years old, our study has multiple age groups and extends the upper age limit of our animals to ~2.65 years (P970). Although the relationship between mouse and human age is not directly correlated due to differences in development, the upper age limit of 2.65 years for mice is close to the maximum life expectancy of a laboratory mouse and thus may represent people who are centenarians (100+ years old) or supercentenarians (110+ years old)[20].

When assessing retinal function through ERGs (Figure 6.1), there were significant differences among the "young" group (<0.5 years) and the three older groups for scotopic a- and b-waves and photopic b-waves. Photopic a-waves only showed significant differences between Group 1 and Group 2, not with the older groups. This is likely due to the large variation in responses in older animals, suggesting that cone functionality may be more sensitive and variable in aging compared to rod photoreceptors or the inner retinal neurons. Additionally, cone photoreceptors

make up a very small percentage of mouse retinal neurons (<3%); therefore, small differences in cone death or dysfunction in individual mice could have a large impact on the group's variation. When assessing retinal morphology through SD-OCT and Fundus images (Figure 6.2), the Fundus images show a clear increase in mottling with age. This mottling may be due to a number of different causes, including, but not limited to, the loss and/or reorganization of RPE cells or changes in the structures underneath the retina, including the subretinal space, RPE, or choroid. The exact cause of the mottling is beyond the scope of this present study but should be noted. The SD-OCT images show gradual and significant decreases in total retinal thickness and photoreceptor layer thickness were observed. For total retinal thickness, there were significant decreases among Group 1 and the remaining three age groups, but also between Group 2 and Group 3. This suggests that between the ages of 2 months and 2 years, there was likely a loss of neuronal cell bodies or synapses; however, after 2 years of age the total retinal thickness stabilizes. The ONL followed a similar trend where the thickness significantly decreased among Group 1 and the remaining three age groups. Additionally, significant differences were also seen between Groups 2 and 4, not Group 2 and 3, suggesting that the overall ONL thickness stabilized across 1 year of age, but then decreased again at 2 years of age. One technical limitation in our SD-OCT image methodology is that our images are obtained from a ring approximately 100 microns from the optic nerve head; therefore, any changes outside of this immediate area, including those in peripheral areas as well as those in the nasal-temporal or equatorial orientations would be missed. Age-related increases in mottling and lens opacities were observed in fundus images. The white/blue opacities could be indicative of increased cataract formation or due to incomplete iris dilation. Changes in the clarity of the optical media, whether via corneal opacity, lens opacity, or any other disturbances, will lead to a scattering of light. Less light

hitting the back of the eye will reduce the intensity of the Fundus, SD-OCT, and auto fluorescence images and may contribute to a reduction in contrast and detail in the images, including gray spots on the color Fundus photos or “dark” areas on the auto fluorescent images. cSLO data also showed increased optical aberrations in the blue – autofluorescence among Group 1 and the remaining three older groups; however, these aberrations remained relatively stable after 1 year of age (Figure 6.3). The auto fluorescent aberrations observed in the cSLO images could be photoreceptor cell rosettes / tubulations resulting from age-related degeneration of the ONL[21]. This degeneration can lead to the accumulation of bisretinoid compounds that are transferred to the RPE during photoreceptor outer segment membrane shedding and phagocytosis[22,23]. This intracellular lipofuscin is a hallmark of aging[24] and contains fluorophores such as A2E[25,26]. Lipofuscin is known to be a major source of fundus autofluorescence and its accumulation is mostly observed in many different retinal degeneration and detachment models[27,28]. In addition to lipofuscin, we hypothesize that some of the autofluorescence may be contributed by surveilling and activated microglia that are eating cellular debris, including lipofuscin. Auto fluorescent granule deposits have been observed in Iba1+ positive microglia found in both the perivasculature and subretinal space in 12- and 18-month old mice[29]. This increase in microglial presence would correspond with changes in gene expression related to immune activation in the aging retina[30,31]. A technical limitation that may contribute to the sudden increase in autofluorescence in the cSLO images between Group 1 and the remaining groups is automatic normalization by the Spectralis software. The Spectralis equipment normalizes the overall intensity of different cSLO images; therefore, as fluorescent agents accumulate with increasing age, a threshold of fluorescence will be reached that the equipment can detect and produce an image with sufficient detail. This can make intensity comparisons

between individual mice and different ages difficult to interpret. The changes seen in lens opacity corroborated eye weight data, which showed increasing eye weight as age increases, even when adjusted for the body weight of the individual mouse (Figure 6.4). The lens continuously grows throughout life when new epithelial cells differentiate into fiber cells and then lay down over existing cells to form distinctive layers[32]. Finally, cell nuclei quantification taken from H&E stained sagittal cross-sections of the retina showed significant decreases in the ONL, but not in the INL or GCL, between Group 1 and Group 4 at the majority of the intervals; however, there were no significant differences among Group 1, Group 2 and Group 3. This differs from observations by *in vivo* SD-OCT imaging, where differences among Group 1 and the other three group were observed in the ONL. This discrepancy is likely due to the cell nuclei counts being done within 100 micron sections along the length of the entire retina in contrast to the OCT images, which were taken at a central area near the optic nerve head.

Aging is a biological process that affects all organ systems, tissues, and cell types and factors such as genetics, nutrition, and physical activity can modulate its effects on health[33]. Aging affects different biological processes such as mitochondrial function, proteostasis, autophagy, and cellular senescence via alterations in genomic stability, epigenetics, and transcription[34–38]. Resources, such as the Age Phenome Knowledgebase, and animal models of aging highlight how this process affects all organ systems and tissues, including the eye[39,40]. Age remains one of the major risk factors for various ophthalmic disorders, most notably cataracts, glaucoma, and AMD[41–43]. Yet, despite this vast wealth in knowledge, there is little information about the rate of vision loss over time or how specific biological processes affect the rate of visual decline.

Overall, our study aligns with and builds upon previous literature studying the effects of aging on the visual system. One limitation of our study is our focus on only one mouse strain, C57BL/6J. Although these highly inbred mice are considered "wild-type" and many genetic mutant strains are made or studied on this background, there are many other "wild-type" inbred mouse strains that represent substantially different genetic backgrounds. Thus, the changes that we observed may be specific to a particular genetic background and will likely be influenced by allelic or SNP (single nucleotide polymorphism) differences that are unique to that particular strain. Another limitation in this current study is our focus on the retina only, not on other ocular tissues, such as the cornea or RPE, which are also known to undergo natural changes related to aging. Specifically, in AMD, the RPE becomes dysfunctional and is no longer able to perform its synergistic role in nourishing and protecting photoreceptors. In addition to this synergistic role, the RPE also performs other critical functions including forming the blood-retina barrier, transporting nutrients, retinoids, and waste products, and phagocytosis of outer segments[44]. Future studies need to assess the natural effects of aging on these structures, especially at the extreme ages (2+ years) that represent the upper limit of life expectancy.

	ERG	Fundus and SD-OCT images	HRA cSLO	Eye Weights	H&E
Group 1	N = 10	N =13	N = 12	N = 10	N = 4
	Female = 3 ; Male = 7	Female = 3 ; Male = 10	Female = 4 ; Male = 8	Female = 3 ; Male = 7	Female = 2 ; Male = 2
Group 2	N = 7	N = 12	N = 11	N = 4	N = 3
	Female = 6 ; Male = 1	Female = 3 ; Male = 9	Female = 5 ; Male = 6	Female = 4 ; Male = 0	Female = 1 ; Male = 2
Group 3	N =5	N = 9	N = 10	N = 6	N = 4
	Female = 2 ; Male = 3	Female = 6 ; Male = 3	Female = 8 ; Male = 2	Female = 4 ; Male = 2	Female = 3 ; Male = 1
Group 4	N =3	N =8	N = 5	N =6	N =3
	Female = 3 ; Male =0	Female = 4 ; Male = 4	Female = 2 ; Male = 3	Female = 3 ; Male = 3	Female = 1 ; Male = 2

Table 1: Sample Sizes for each group per technique

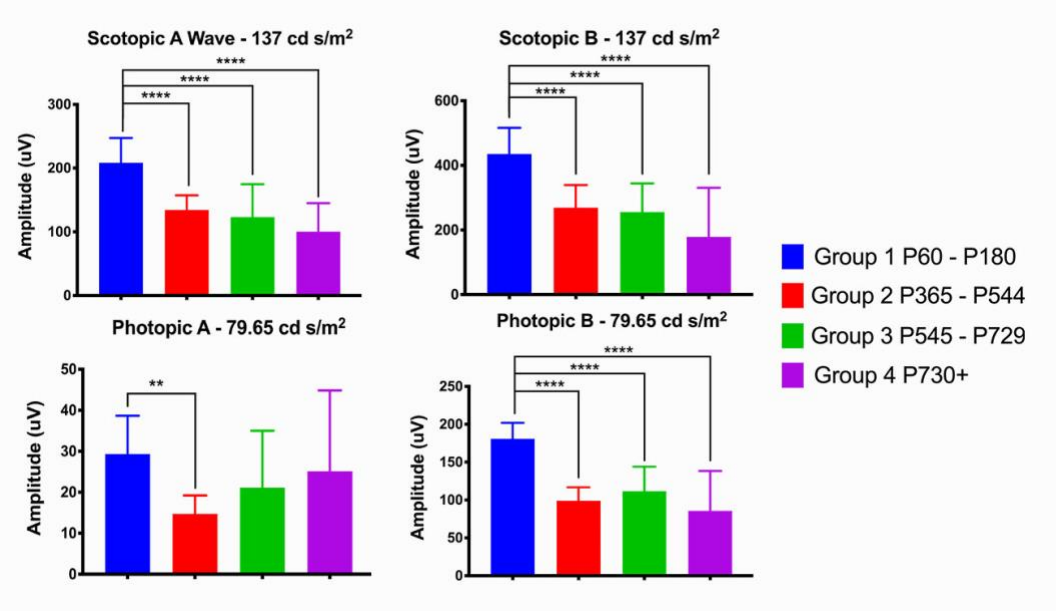

Figure 6.1: Electroretinogram recordings of a- and b-waves show decreased retinal function in both scotopic and photopic conditions as age increases. Bar graphs show the amplitude of a-waves and b-waves for both scotopic conditions and photopic conditions at the highest flash intensities (137 cd s/m^2 or 79.65 cd s/m^2 respectively). In all four conditions, there are significant decreases in retinal function as age increases. For scotopic a-waves, there are significant differences among Group 1 and the remaining three groups (Group 2, Group 3, and Group 4). No differences were observed among Group 2, 3, and 4. The same pattern is observed for the scotopic b-waves, photopic a-waves, and photopic b-waves. A two-way ANOVA with Tukey's multiple comparisons test was conducted between the mean amplitudes in all possible pair combinations across all four conditions. A full list of comparisons and p-values is listed in Supplemental Figure 1 and Supplemental Tables 1 - 4. Sample sizes Group 1 (<0.5 years) n = 10 (3F / 7M); Group 2 (1.0 – 1.5 years) n = 7 (6F /1M); Group 3 (1.5 – 2.0 years) n = 5 (2F / 3M); Group 4 (>2.0 years) n = 3 (3F) * = p value <0.05; ** = p value <0.01; *** = p value < 0.001; **** = p value < 0.0001

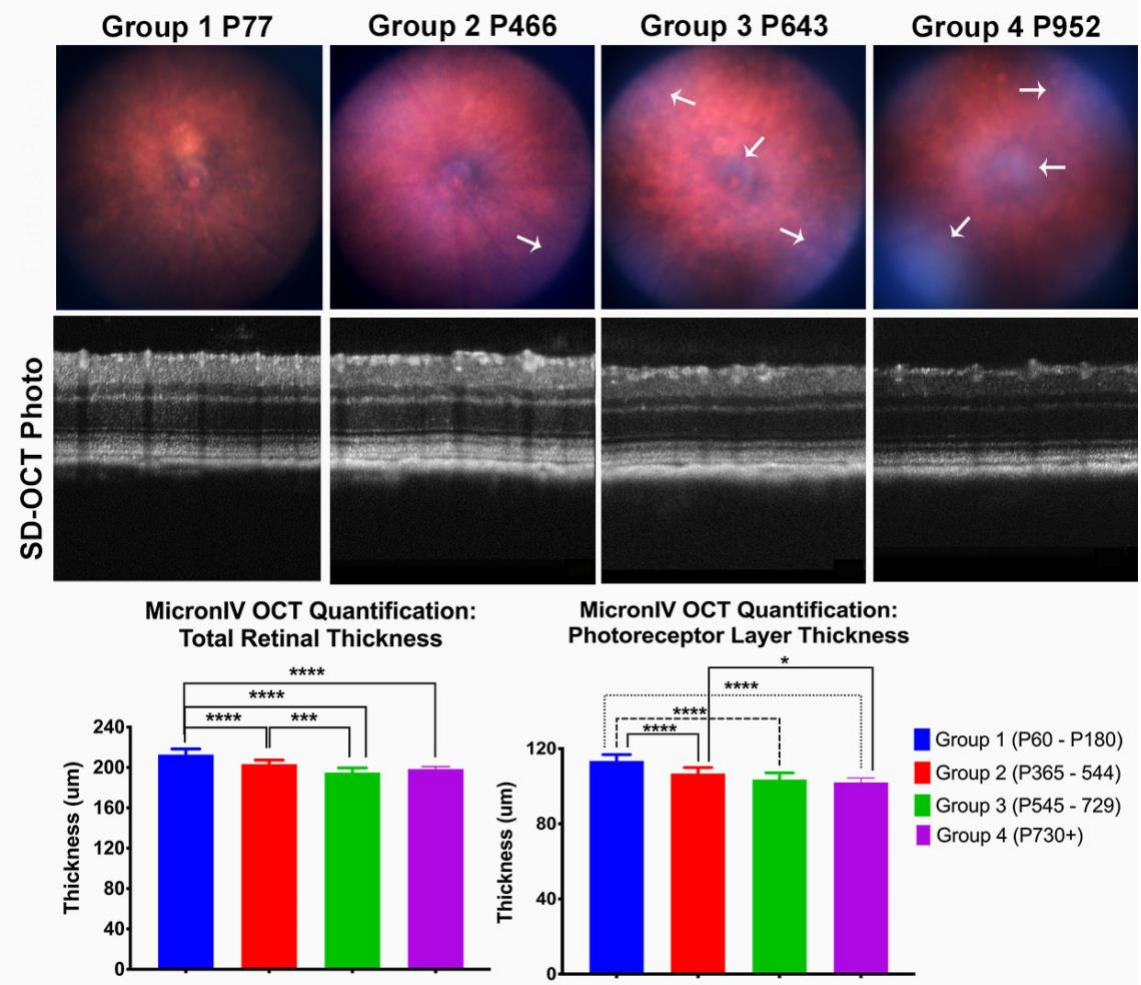

Figure 6.2: In vivo imaging of C57BL/6J retinas shown significant decreases in total retinal thickness and photoreceptor layer thickness over time. SD-OCT images show total retinal thickness and photoreceptor layer thickness decrease over time. Micron IV Fundus photography shows an increased mottled or dappled appearance in C57BL/6J eyes with aging (additional images available in Supplemental Figure 2). There are also opacities and uneven illumination evident in the older animals that could be indicative of increased cataract development or incomplete iris dilation. These features have been highlighted by white arrows. Additionally, quantification of SD-OCT images, circular scans taken approximately 100 microns from the optic nerve head, show a significant decrease in total retinal thickness among Group 1 and Group 2, Group 3 and Group 4. There was also a significant decrease in total retinal thickness between

Group 2 and Group 3. When specifically looking at the ONL (photoreceptor layer), a significant decrease was observed among Group 1 and Group 2, Group 3 and Group 4 as well as between Group 2 and Group 4. A one-way ANOVA with Tukey's multiple comparisons test was conducted between the mean thickness measurements in all possible pair combinations. A full list of comparisons and p-values is listed in Supplemental Table 5 (Total Retinal Thickness) or Supplemental Table 6 (Total Photoreceptor Layer Thickness). Sample sizes Group 1 (<0.5 years) n = 13 (3F / 10M); Group 2 (1.0 – 1.5 years) n = 12 (3F / 9M); Group 3 (1.5 – 2.0 years) n = 9 (6F / 3M); Group 4 (>2.0 years) n = 8 (4F / 4M).

* = p value <0.05; ** = p value <0.01; *** = p value < 0.001; **** = p value < 0.0001.

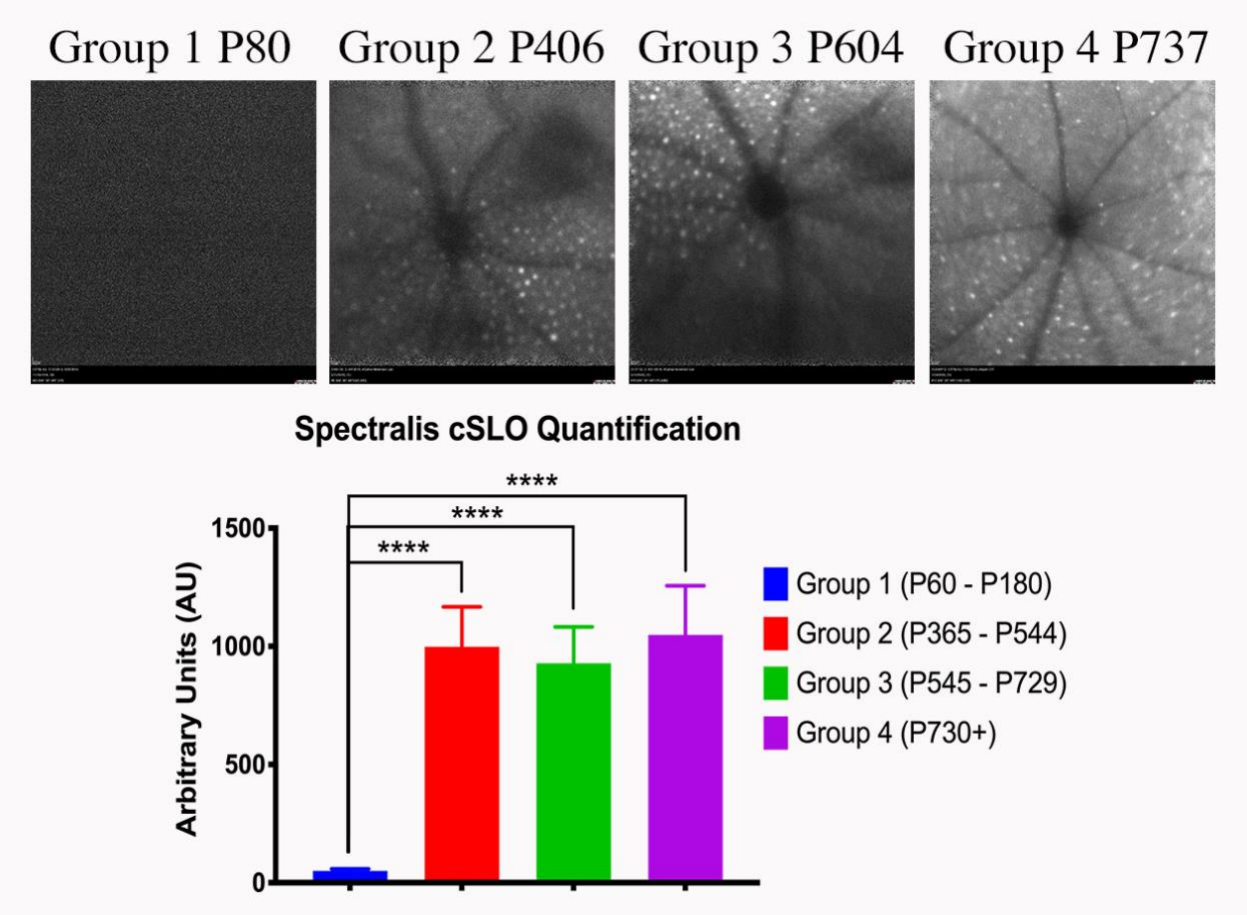

Figure 6.3: Heidelberg Spectralis cSLO images show increased blue auto-fluorescence at the photoreceptor-RPE junction as age increases. Quantification of images using densitometry shows a significant increase in auto-fluorescence among Group 1 and the remaining three groups (Group 2, Group 3, and Group 4). Sample sizes Group 1 (<0.5 years) n = 12 (4F / 8M); Group 2 (1.0 – 1.5 years) n = 11 (5F / 6M); Group 3 (1.5 – 2.0 years) n = 10 (8F / 2M); Group 4 (>2.0 years) n = 5 (2F / 3M).

* = p value <0.05; ** = p value <0.01; *** = p value < 0.001; **** = p value < 0.0001

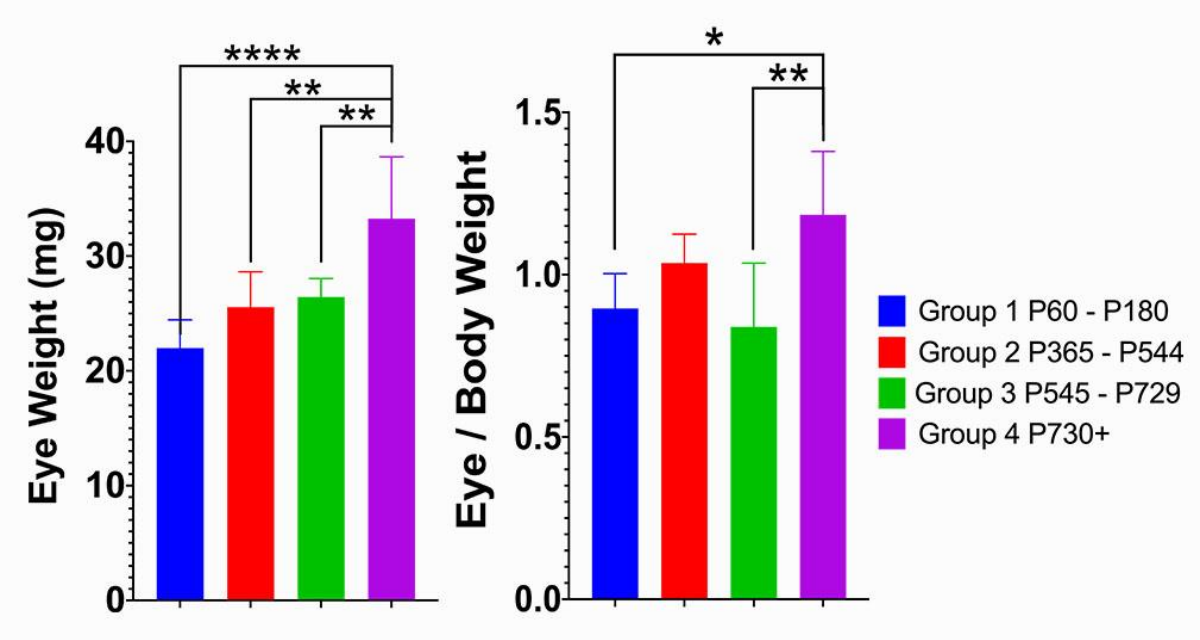

Figure 6.4: Eye weights increase with age. Raw eye weight data show a gradual and significant increase between Group 1 and Group 4, Group 2 and Group 4, and Group 3 and Group 4. When the eye weight is adjusted for the body weight of the animal, there remains a significant difference between Group 1 and Group 4 as well as Group 3 and Group 4. Sample sizes Group 1 (<0.5 years) n = 10 (3F / 7M); Group 2 (1.0 – 1.5 years) n = 4 (4F); Group 3 (1.5 – 2.0 years) n = 6 (4F / 2M); Group 4 (>2.0 years) n = 6 (3F / 3M).

* = p value <0.05; ** = p value <0.01; *** = p value < 0.001; **** = p value < 0.0001

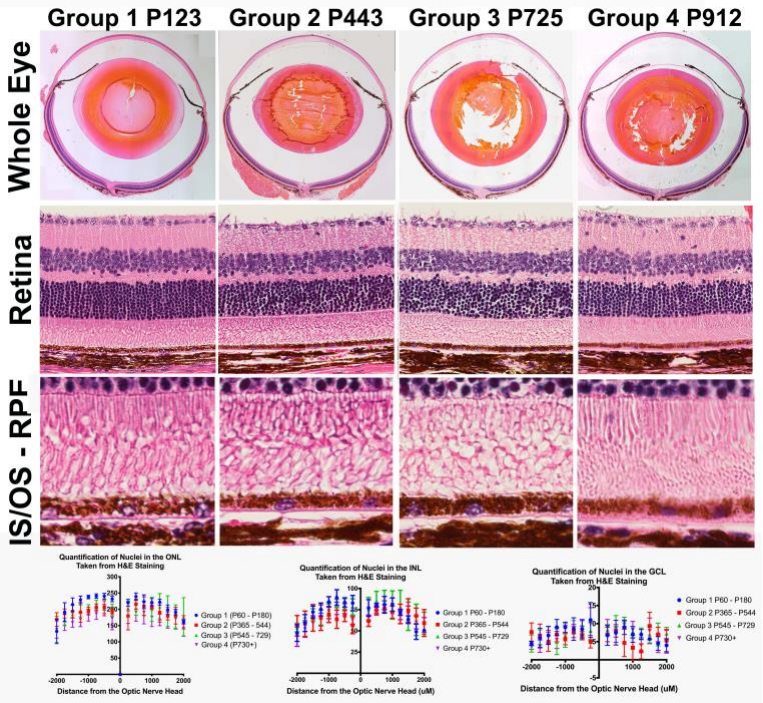

Figure 6.5: Postmortem retinal morphology shows decreasing cell nuclei counts in the outer nuclear layer (ONL) with increasing age whereas inner nuclear layer (INL) and ganglion cell layer (GCL) remain relatively equal. Representative images of H&E staining of the whole eye and retinal sections from all four groups shows gross changes in retinal morphology. Quantification of cell nuclei counts at 250 micron intervals from the optic nerve head both in the superior and inferior direction in the ONL show statistically significant decreases between Group 1 and Group 4 at the majority of the intervals; however, no significant differences among Group 1, Group 2 and Group 3. A two-way ANOVA with Tukey's multiple comparisons test was conducted between the mean nuclei counts in all possible pair combinations. A full list of comparisons and p-values is listed for the ONL, INL, and GCL in Supplemental Tables 9 – 11 respectively. Sample sizes Group 1 (<0.5 years) n = 4 (2F / 2M); Group 2 (1.0 – 1.5 years) n = 3 (1F / 2M); Group 3 (1.5 – 2.0 years) n = 4 (3F / 1M); Group 4 (>2.0 years) n = 3 (1F / 2M)

* = p value <0.05; ** = p value <0.01; *** = p value < 0.001; **** = p value < 0.0001

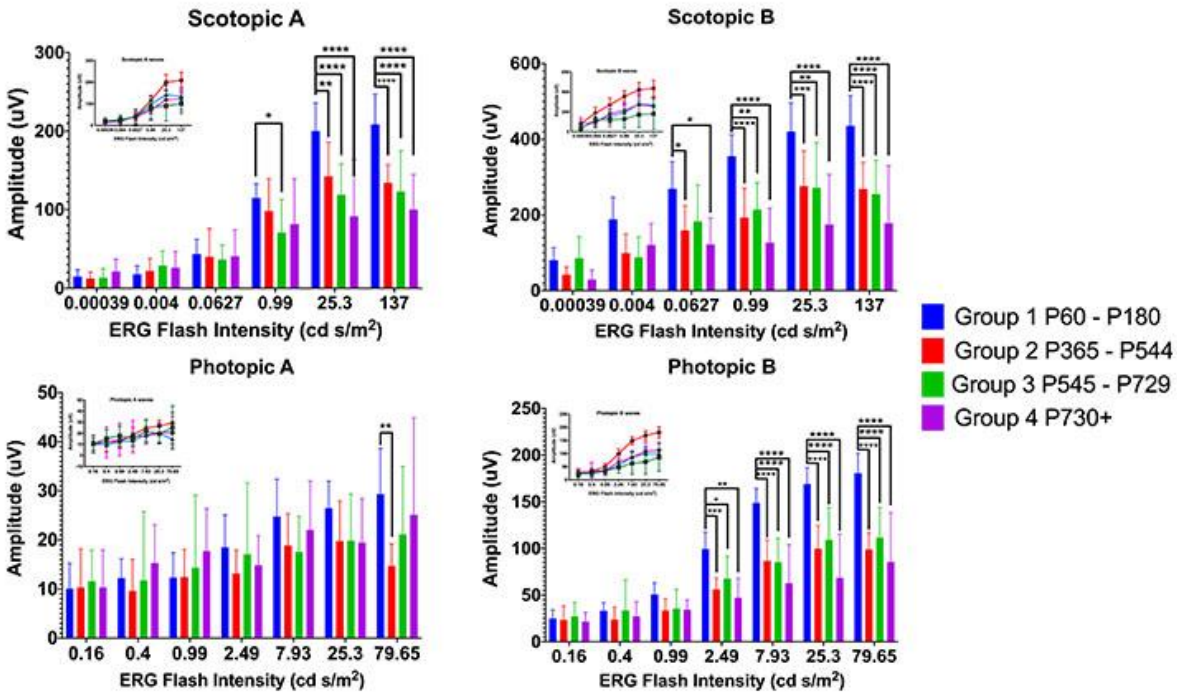

Supplemental Figure 6.1: Electroretinogram recordings of a- and b-waves show decreased visual function in both scotopic and photopic conditions as age increases. Line graphs depict waveform amplitudes in response to increasing flash intensity (0.00039 to 137 cd s/m^2 for scotopic conditions and 0.16 to 79.65 cd s/m^2 for photopic conditions). In general waveform amplitudes increased in response to the increasing flash intensity, however there are significant decreases in retinal function as age increases. A two-way ANOVA with Tukey's multiple comparisons test was conducted between the mean amplitudes in all possible pair combinations across all four conditions. A full list of comparisons and p-values is listed in Supplemental Tables 1 - 4. Sample sizes Group 1 (<0.5 years) n = 10; Group 2 (1.0 – 1.5 years) n = 7; Group 3 (1.5 – 2.0 years) n = 5; Group 4 (>2.0 years) n = 3

* = p value <0.05; ** = p value <0.01; *** = p value < 0.001; **** = p value < 0.0001

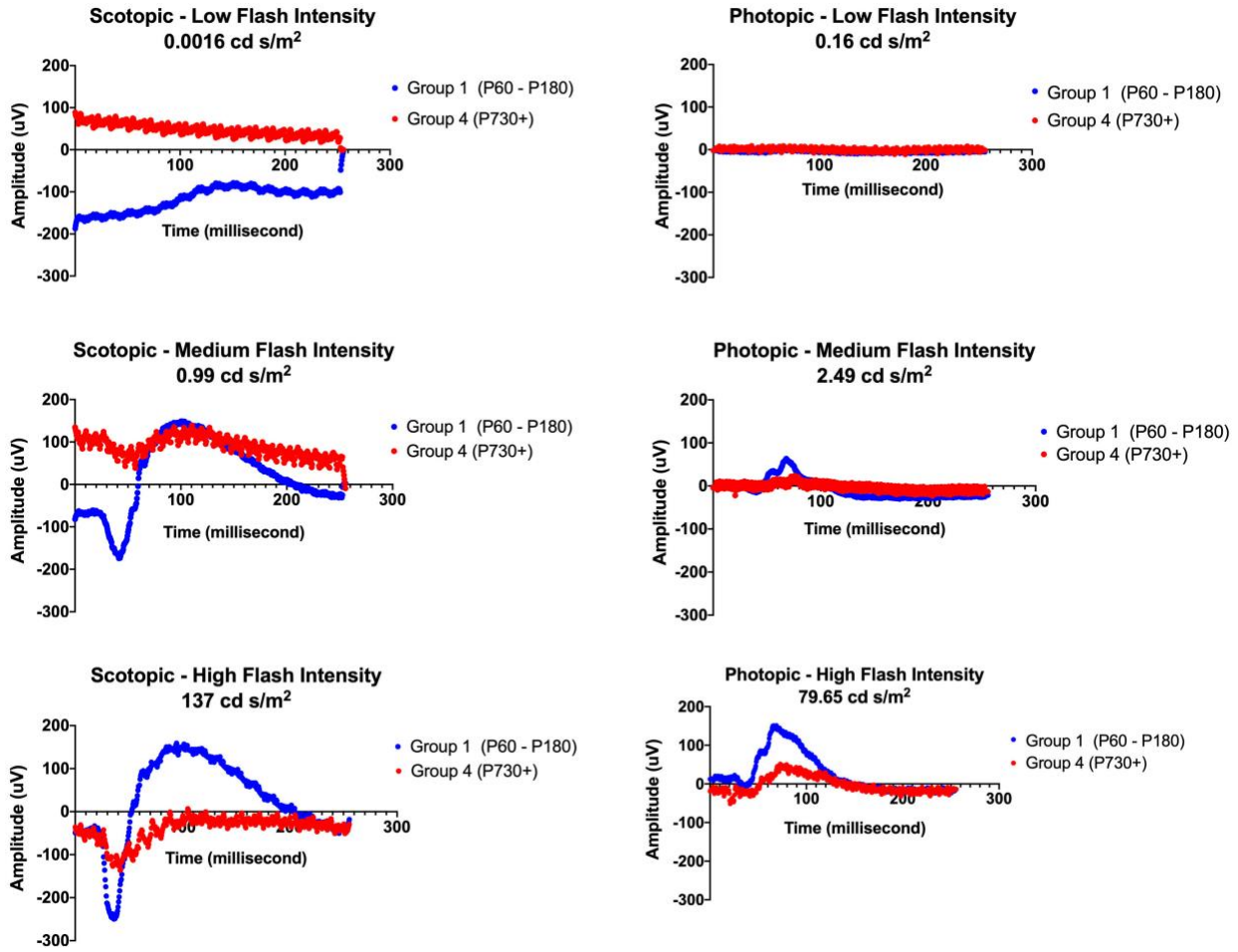

Supplemental Figure 6.2: Representative average electroretinogram waveforms show a significant decline in visual function in both scotopic and photopic conditions between Group 1 and Group 4 animals. At low light flash intensities, both age groups show little retinal response; however, at medium and high flash intensities, Group 1 animals respond normally with a characteristic a- and b- waveform while Group 4 animals show little response. Sample sizes Group 1 (<0.5 years) n = 10; Group 4 (>2.0 years) n = 3. Scotopic conditions: Low Flash Intensity (0.0016 cd s/m^2), Medium Flash Intensity (0.99 cd s/m^2), High Flash Intensity (137 cd s/m^2). Photopic conditions: Low Flash Intensity (0.16 cd s/m^2), Medium Flash Intensity (2.49 cd s/m^2), High Flash Intensity (79.65 cd s/m^2).

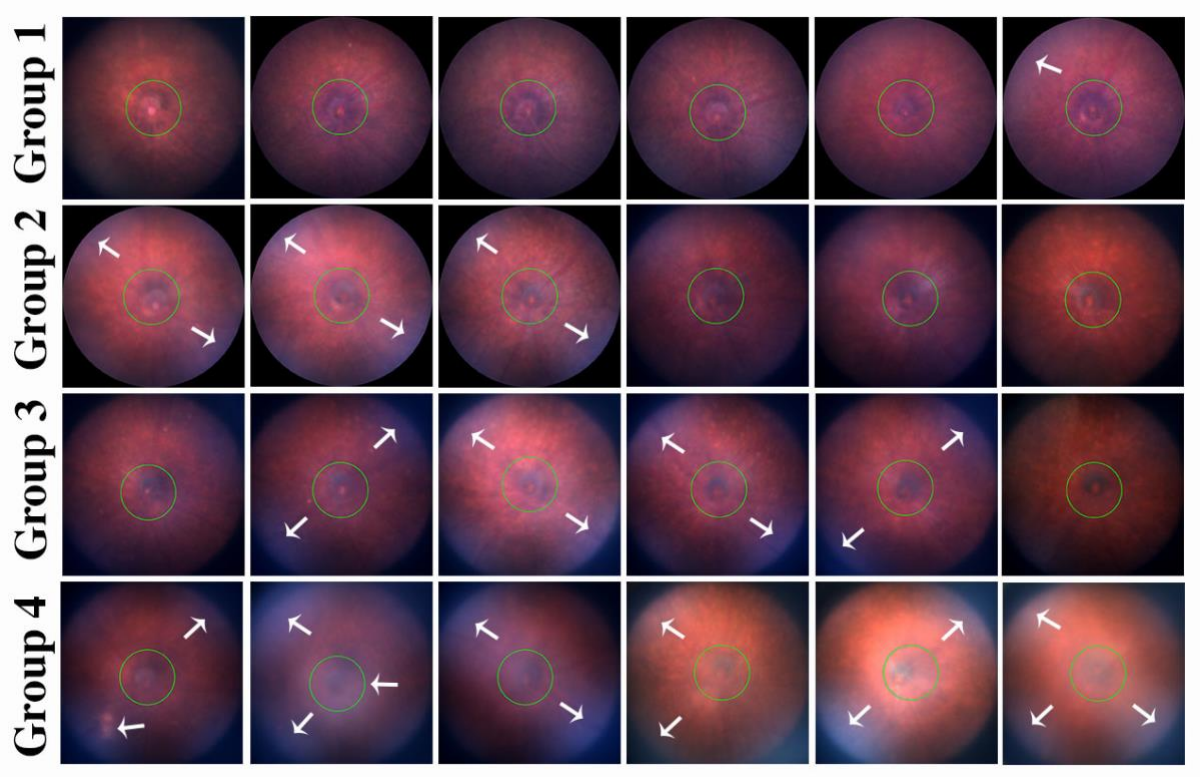

Supplemental Figure 6.3: Color Fundus photographs from six individual mice per group show an increase in mottled appearance and opacity as age increases. Total sample sizes for OCT retinal images: Group 1 (<0.5 years) n = 13; Group 2 (1.0 – 1.5 years) n = 12; Group 3 (1.5 – 2.0 years) n = 9; Group 4 (>2.0 years) n = 8.

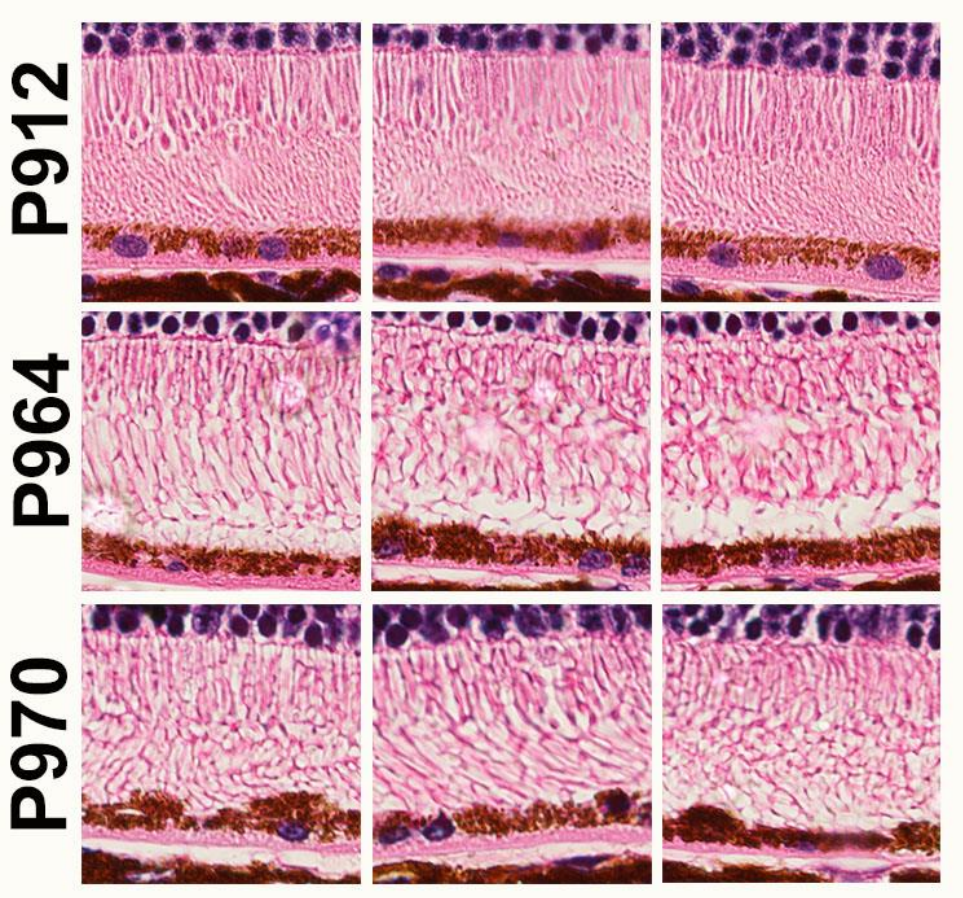

Supplemental Figure 4: 60X High Magnification Brightfield Images of the inner segment - outer segment - RPE interface from 3 different independent mouse samples in different areas of the retina.

Two-way ANOVA with Tukey's multiple comparisons test - Scotopic A wave	Adjusted P Value	Significant?	Summary
0.00039			
Group 1 P60 - P180 - vs. Group 2 P365 - P544 -	0.9981	No	ns
Group 1 P60 - P180 - vs. Group 3 P545 - P729	0.9997	No	ns
Group 1 P60 - P180 - vs. Group 4 P730+	0.9892	No	ns
Group 2 P365 - P544 - vs. Group 3 P545 - P729	>0.9999	No	ns
Group 2 P365 - P544 - vs. Group 4 P730+	0.9741	No	ns
Group 3 P545 - P729 vs. Group 4 P730+	0.9849	No	ns
0.004			
Group 1 P60 - P180 - vs. Group 2 P365 - P544 -	0.9925	No	ns
Group 1 P60 - P180 - vs. Group 3 P545 - P729	0.9175	No	ns
Group 1 P60 - P180 - vs. Group 4 P730+	0.9774	No	ns
Group 2 P365 - P544 - vs. Group 3 P545 - P729	0.9829	No	ns
Group 2 P365 - P544 - vs. Group 4 P730+	0.9976	No	ns
Group 3 P545 - P729 vs. Group 4 P730+	0.9994	No	ns
0.0627			
Group 1 P60 - P180 - vs. Group 2 P365 - P544 -	0.9965	No	ns
Group 1 P60 - P180 - vs. Group 3 P545 - P729	0.9775	No	ns
Group 1 P60 - P180 - vs. Group 4 P730+	0.9992	No	ns

Group 2 P365 - P544 - vs. Group 3 P545 - P729	0.9972	No	ns
Group 2 P365 - P544 - vs. Group 4 P730+	>0.9999	No	ns
Group 3 P545 - P729 vs. Group 4 P730+	0.9977	No	ns
0.99			
Group 1 P60 - P180 - vs. Group 2 P365 - P544 -	0.6807	No	ns
Group 1 P60 - P180 - vs. Group 3 P545 - P729	0.0487	Yes	*
Group 1 P60 - P180 - vs. Group 4 P730+	0.3563	No	ns
Group 2 P365 - P544 - vs. Group 3 P545 - P729	0.4369	No	ns
Group 2 P365 - P544 - vs. Group 4 P730+	0.8659	No	ns
Group 3 P545 - P729 vs. Group 4 P730+	0.9643	No	ns
25.3			
Group 1 P60 - P180 - vs. Group 2 P365 - P544 -	0.0012	Yes	**
Group 1 P60 - P180 - vs. Group 3 P545 - P729	<0.0001	Yes	****
Group 1 P60 - P180 - vs. Group 4 P730+	<0.0001	Yes	****
Group 2 P365 - P544 - vs. Group 3 P545 - P729	0.567	No	ns
Group 2 P365 - P544 - vs. Group 4 P730+	0.0835	No	ns
Group 3 P545 - P729 vs. Group 4 P730+	0.6137	No	ns
137			
Group 1 P60 - P180 - vs. Group 2 P365 - P544 -	<0.0001	Yes	****
Group 1 P60 - P180 - vs. Group 3 P545 - P729	<0.0001	Yes	****

Group 1 P60 - P180 - vs. Group 4 P730+	<0.0001	Yes	****
Group 2 P365 - P544 - vs. Group 3 P545 - P729	0.9261	No	ns
Group 2 P365 - P544 - vs. Group 4 P730+	0.3818	No	ns
Group 3 P545 - P729 vs. Group 4 P730+	0.7398	No	ns

Supplementary Table 6.1: Two-way ANOVA with Tukey's multiple Comparison Test for Scotopic A Wave Electroretinogram

Two-way ANOVA with Tukey's multiple comparisons test - Photopic A wave	Adjusted P Value	Significant?	Summary
0.16			
Group 1 P60 - P180 - vs. Group 2 P365 - P544 -	>0.9999	No	ns
Group 1 P60 - P180 - vs. Group 3 P545 - P729	0.988	No	ns
Group 1 P60 - P180 - vs. Group 4 P730+	>0.9999	No	ns
Group 2 P365 - P544 - vs. Group 3 P545 - P729	0.9939	No	ns
Group 2 P365 - P544 - vs. Group 4 P730+	>0.9999	No	ns
Group 3 P545 - P729 vs. Group 4 P730+	0.997	No	ns
0.4			
Group 1 P60 - P180 - vs. Group 2 P365 - P544 -	0.9173	No	ns
Group 1 P60 - P180 - vs. Group 3 P545 - P729	0.9996	No	ns
Group 1 P60 - P180 - vs. Group 4 P730+	0.9426	No	ns
Group 2 P365 - P544 - vs. Group 3 P545 - P729	0.9711	No	ns
Group 2 P365 - P544 - vs. Group 4 P730+	0.7507	No	ns
Group 3 P545 - P729 vs. Group 4 P730+	0.9353	No	ns
0.99			
Group 1 P60 - P180 - vs. Group 2 P365 - P544 -	>0.9999	No	ns
Group 1 P60 - P180 - vs. Group 3 P545 - P729	0.9716	No	ns
Group 1 P60 - P180 - vs. Group 4 P730+	0.7507	No	ns

Group 2 P365 - P544 - vs. Group 3 P545 - P729	0.9793	No	ns
Group 2 P365 - P544 - vs. Group 4 P730+	0.7848	No	ns
Group 3 P545 - P729 vs. Group 4 P730+	0.9407	No	ns
2.49			
Group 1 P60 - P180 - vs. Group 2 P365 - P544 -	0.5547	No	ns
Group 1 P60 - P180 - vs. Group 3 P545 - P729	0.9892	No	ns
Group 1 P60 - P180 - vs. Group 4 P730+	0.905	No	ns
Group 2 P365 - P544 - vs. Group 3 P545 - P729	0.8483	No	ns
Group 2 P365 - P544 - vs. Group 4 P730+	0.9913	No	ns
Group 3 P545 - P729 vs. Group 4 P730+	0.9818	No	ns
7.93			
Group 1 P60 - P180 - vs. Group 2 P365 - P544 -	0.4618	No	ns
Group 1 P60 - P180 - vs. Group 3 P545 - P729	0.38	No	ns
Group 1 P60 - P180 - vs. Group 4 P730+	0.9579	No	ns
Group 2 P365 - P544 - vs. Group 3 P545 - P729	0.9933	No	ns
Group 2 P365 - P544 - vs. Group 4 P730+	0.9425	No	ns
Group 3 P545 - P729 vs. Group 4 P730+	0.8775	No	ns
25.3			
Group 1 P60 - P180 - vs. Group 2 P365 - P544 -	0.353	No	ns
Group 1 P60 - P180 - vs. Group 3 P545 - P729	0.4605	No	ns

Group 1 P60 - P180 - vs. Group 4 P730+	0.5692	No	ns
Group 2 P365 - P544 - vs. Group 3 P545 - P729	>0.9999	No	ns
Group 2 P365 - P544 - vs. Group 4 P730+	>0.9999	No	ns
Group 3 P545 - P729 vs. Group 4 P730+	0.9999	No	ns
79.65			
Group 1 P60 - P180 - vs. Group 2 P365 - P544 -	0.0023	Yes	**
Group 1 P60 - P180 - vs. Group 3 P545 - P729	0.2668	No	ns
Group 1 P60 - P180 - vs. Group 4 P730+	0.8637	No	ns
Group 2 P365 - P544 - vs. Group 3 P545 - P729	0.5432	No	ns
Group 2 P365 - P544 - vs. Group 4 P730+	0.2613	No	ns
Group 3 P545 - P729 vs. Group 4 P730+	0.9102	No	ns

Supplementary Table 6.2: Two-way ANOVA with Tukey's multiple Comparison Test for Photopic A Wave Electroretinogram

Two-way ANOVA with Tukey's multiple comparisons test - Scotopic B wave	Adjusted P Value	Significant?	Summary
0.00039			
Group 1 P60 - P180 - vs. Group 2 P365 - P544 -	0.7096	No	ns
Group 1 P60 - P180 - vs. Group 3 P545 - P729	0.9993	No	ns
Group 1 P60 - P180 - vs. Group 4 P730+	0.7127	No	ns
Group 2 P365 - P544 - vs. Group 3 P545 - P729	0.7403	No	ns
Group 2 P365 - P544 - vs. Group 4 P730+	0.9944	No	ns
Group 3 P545 - P729 vs. Group 4 P730+	0.7191	No	ns
0.004			
Group 1 P60 - P180 - vs. Group 2 P365 - P544 -	0.0707	No	ns
Group 1 P60 - P180 - vs. Group 3 P545 - P729	0.0649	No	ns
Group 1 P60 - P180 - vs. Group 4 P730+	0.499	No	ns
Group 2 P365 - P544 - vs. Group 3 P545 - P729	0.9935	No	ns
Group 2 P365 - P544 - vs. Group 4 P730+	0.975	No	ns
Group 3 P545 - P729 vs. Group 4 P730+	0.9293	No	ns
0.0627			
Group 1 P60 - P180 - vs. Group 2 P365 - P544 -	0.0144	Yes	*
Group 1 P60 - P180 - vs. Group 3 P545 - P729	0.1432	No	ns
Group 1 P60 - P180 - vs. Group 4 P730+	0.0144	Yes	*

Group 2 P365 - P544 - vs. Group 3 P545 - P729	0.9437	No	ns
Group 2 P365 - P544 - vs. Group 4 P730+	0.8834	No	ns
Group 3 P545 - P729 vs. Group 4 P730+	0.6642	No	ns
0.99			
Group 1 P60 - P180 - vs. Group 2 P365 - P544 -	<0.0001	Yes	****
Group 1 P60 - P180 - vs. Group 3 P545 - P729	0.0033	Yes	**
Group 1 P60 - P180 - vs. Group 4 P730+	<0.0001	Yes	****
Group 2 P365 - P544 - vs. Group 3 P545 - P729	0.9601	No	ns
Group 2 P365 - P544 - vs. Group 4 P730+	0.5575	No	ns
Group 3 P545 - P729 vs. Group 4 P730+	0.3623	No	ns
25.3			
Group 1 P60 - P180 - vs. Group 2 P365 - P544 -	0.0006	Yes	***
Group 1 P60 - P180 - vs. Group 3 P545 - P729	0.0017	Yes	**
Group 1 P60 - P180 - vs. Group 4 P730+	<0.0001	Yes	****
Group 2 P365 - P544 - vs. Group 3 P545 - P729	0.9995	No	ns
Group 2 P365 - P544 - vs. Group 4 P730+	0.1898	No	ns
Group 3 P545 - P729 vs. Group 4 P730+	0.273	No	ns
137			
Group 1 P60 - P180 - vs. Group 2 P365 - P544 -	<0.0001	Yes	****
Group 1 P60 - P180 - vs. Group 3 P545 - P729	<0.0001	Yes	****

Group 1 P60 - P180 - vs. Group 4 P730+	<0.0001	Yes	****
Group 2 P365 - P544 - vs. Group 3 P545 - P729	0.989	No	ns
Group 2 P365 - P544 - vs. Group 4 P730+	0.2849	No	ns
Group 3 P545 - P729 vs. Group 4 P730+	0.4807	No	ns

Supplementary Table 6.3: Two-way ANOVA with Tukey's multiple Comparison Test for Scotopic B Wave Electroretinogram

Two-way ANOVA with Tukey's multiple comparisons test – Photopic B wave	Adjusted P Value	Significant?	Summary
0.16			
Group 1 P60 - P180 - vs. Group 2 P365 - P544 -	0.9991	No	ns
Group 1 P60 - P180 - vs. Group 3 P545 - P729	0.9965	No	ns
Group 1 P60 - P180 - vs. Group 4 P730+	0.9954	No	ns
Group 2 P365 - P544 - vs. Group 3 P545 - P729	0.9891	No	ns
Group 2 P365 - P544 - vs. Group 4 P730+	0.9993	No	ns
Group 3 P545 - P729 vs. Group 4 P730+	0.9822	No	ns
0.4			
Group 1 P60 - P180 - vs. Group 2 P365 - P544 -	0.7886	No	ns
Group 1 P60 - P180 - vs. Group 3 P545 - P729	>0.9999	No	ns
Group 1 P60 - P180 - vs. Group 4 P730+	0.9731	No	ns
Group 2 P365 - P544 - vs. Group 3 P545 - P729	0.8466	No	ns
Group 2 P365 - P544 - vs. Group 4 P730+	0.9943	No	ns
Group 3 P545 - P729 vs. Group 4 P730+	0.9758	No	ns
0.99			
Group 1 P60 - P180 - vs. Group 2 P365 - P544 -	0.3448	No	ns
Group 1 P60 - P180 - vs. Group 3 P545 - P729	0.5521	No	ns
Group 1 P60 - P180 - vs. Group 4 P730+	0.627	No	ns

Group 2 P365 - P544 - vs. Group 3 P545 - P729	0.9983	No	ns
Group 2 P365 - P544 - vs. Group 4 P730+	>0.9999	No	ns
Group 3 P545 - P729 vs. Group 4 P730+	0.9997	No	ns
2.49			
Group 1 P60 - P180 - vs. Group 2 P365 - P544 -	0.0002	Yes	***
Group 1 P60 - P180 - vs. Group 3 P545 - P729	0.0304	Yes	*
Group 1 P60 - P180 - vs. Group 4 P730+	0.0012	Yes	**
Group 2 P365 - P544 - vs. Group 3 P545 - P729	0.7719	No	ns
Group 2 P365 - P544 - vs. Group 4 P730+	0.9301	No	ns
Group 3 P545 - P729 vs. Group 4 P730+	0.5374	No	ns
7.93			
Group 1 P60 - P180 - vs. Group 2 P365 - P544 -	<0.0001	Yes	****
Group 1 P60 - P180 - vs. Group 3 P545 - P729	<0.0001	Yes	****
Group 1 P60 - P180 - vs. Group 4 P730+	<0.0001	Yes	****
Group 2 P365 - P544 - vs. Group 3 P545 - P729	0.9995	No	ns
Group 2 P365 - P544 - vs. Group 4 P730+	0.3437	No	ns
Group 3 P545 - P729 vs. Group 4 P730+	0.4459	No	ns
25.3			
Group 1 P60 - P180 - vs. Group 2 P365 - P544 -	<0.0001	Yes	****
Group 1 P60 - P180 - vs. Group 3 P545 - P729	<0.0001	Yes	****

Group 1 P60 - P180 - vs. Group 4 P730+	<0.0001	Yes	****
Group 2 P365 - P544 - vs. Group 3 P545 - P729	0.869	No	ns
Group 2 P365 - P544 - vs. Group 4 P730+	0.1368	No	ns
Group 3 P545 - P729 vs. Group 4 P730+	0.0421	Yes	*
79.65			
Group 1 P60 - P180 - vs. Group 2 P365 - P544 -	<0.0001	Yes	****
Group 1 P60 - P180 - vs. Group 3 P545 - P729	<0.0001	Yes	****
Group 1 P60 - P180 - vs. Group 4 P730+	<0.0001	Yes	****
Group 2 P365 - P544 - vs. Group 3 P545 - P729	0.7278	No	ns
Group 2 P365 - P544 - vs. Group 4 P730+	0.7843	No	ns
Group 3 P545 - P729 vs. Group 4 P730+	0.3179	No	ns

Supplementary Table 6.4: Two-way ANOVA with Tukey's multiple Comparison Test for Photopic B Wave Electroretinogram

One-way ANOVA with Tukey's multiple comparisons test - Total Retinal Thickness as measured through MicronIV SD-OCT	Significant?	Summary	Adjusted P Value
Group 1 (P60 - P180) vs. Group 2 (P365 - 544)	Yes	****	<0.0001
Group 1 (P60 - P180) vs. Group 3 (P545 - 729)	Yes	****	<0.0001
Group 1 (P60 - P180) vs. Group 4 (P730+)	Yes	****	<0.0001
Group 2 (P365 - 544) vs. Group 3 (P545 - 729)	Yes	***	0.0008
Group 2 (P365 - 544) vs. Group 4 (P730+)	No	ns	0.0937
Group 3 (P545 - 729) vs. Group 4 (P730+)	No	ns	0.4022

Supplemental Table 6.5: One-way ANOVA with Tukey’s multiple Comparison Test for Total Retinal Thickness as measured through MicronIV SD-OCT

One-way ANOVA with Tukey's multiple comparisons test - Photoreceptor Layer Thickness as measured through MicronIV SD-OCT	Significant?	Summary	Adjusted P Value
Group 1 (P60 - P180) vs. Group 2 (P365 - 544)	Yes	****	<0.0001
Group 1 (P60 - P180) vs. Group 3 (P545 - 729)	Yes	****	<0.0001
Group 1 (P60 - P180) vs. Group 4 (P730+)	Yes	****	<0.0001
Group 2 (P365 - 544) vs. Group 3 (P545 - 729)	No	ns	0.119
Group 2 (P365 - 544) vs. Group 4 (P730+)	Yes	*	0.0119
Group 3 (P545 - 729) vs. Group 4 (P730+)	No	ns	0.7545

Supplemental Table 6.6: One-way ANOVA with Tukey’s multiple Comparison Test for Photoreceptor Layer Thickness as measured through MicronIV SD-OCT

One-way ANOVA with Tukey's multiple comparisons test - Eye Weight Data	Adjusted P Value	Significant?	Summary
Group 1 (P60 - P180) vs. Group 2 (P365 - 544)	0.2912	No	ns
Group 1 (P60 - P180) vs. Group 3 (P545 - 729)	0.0719	No	ns
Group 1 (P60 - P180) vs. Group 4 (P730+)	<0.0001	Yes	****
Group 2 (P365 - 544) vs. Group 3 (P545 - 729)	0.9757	No	ns
Group 2 (P365 - 544) vs. Group 4 (P730+)	0.0081	Yes	**
Group 3 (P545 - 729) vs. Group 4 (P730+)	0.0088	Yes	**

Supplementary Table 6.7: One-way ANOVA with Tukey’s multiple Comparison Test for Eye Weight Data

One-way ANOVA with Tukey's multiple comparisons test for Eye Weight / Body Weight Data	Adjusted P Value	Significant?	Summary
Group 1 (P60 - P180) vs. Group 2 (P365 - 544)	0.4007	No	ns
Group 1 (P60 - P180) vs. Group 3 (P545 - 729)	0.8794	No	ns
Group 1 (P60 - P180) vs. Group 4 (P730+)	0.017	Yes	*
Group 2 (P365 - 544) vs. Group 3 (P545 - 729)	0.2003	No	ns
Group 2 (P365 - 544) vs. Group 4 (P730+)	0.4976	No	ns
Group 3 (P545 - 729) vs. Group 4 (P730+)	0.0084	Yes	**

Supplementary Table 6.8: One-way ANOVA with Tukey’s multiple Comparison Test for Eye Weight / Body Weight Data

Two-way ANOVA with Tukey's multiple comparisons test - Cell nuclei quantification in the ONL	Adjusted P Value	Significant?	Summary
Row 1 (-2000uM from ONH)			
Group 1 (P60 - P180) vs. Group 2 (P365 - 544)	0.1821	No	ns
Group 1 (P60 - P180) vs. Group 3 (P545 - 729)	0.9819	No	ns
Group 1 (P60 - P180) vs. Group 4 (P730+)	0.9858	No	ns
Group 2 (P365 - 544) vs. Group 3 (P545 - 729)	0.3379	No	ns
Group 2 (P365 - 544) vs. Group 4 (P730+)	0.3233	No	ns
Group 3 (P545 - 729) vs. Group 4 (P730+)	>0.9999	No	ns
Row 2 (-1750uM from ONH)			
Group 1 (P60 - P180) vs. Group 2 (P365 - 544)	0.9956	No	ns
Group 1 (P60 - P180) vs. Group 3 (P545 - 729)	0.5027	No	ns
Group 1 (P60 - P180) vs. Group 4 (P730+)	0.0491	Yes	*
Group 2 (P365 - 544) vs. Group 3 (P545 - 729)	0.7133	No	ns
Group 2 (P365 - 544) vs. Group 4 (P730+)	0.1343	No	ns
Group 3 (P545 - 729) vs. Group 4 (P730+)	0.6264	No	ns
Row 3 - (-1500uM from ONH)			
Group 1 (P60 - P180) vs. Group 2 (P365 - 544)	0.6448	No	ns

Group 1 (P60 - P180) vs. Group 3 (P545 - 729)	0.2682	No	ns
Group 1 (P60 - P180) vs. Group 4 (P730+)	0.0054	Yes	**
Group 2 (P365 - 544) vs. Group 3 (P545 - 729)	0.9566	No	ns
Group 2 (P365 - 544) vs. Group 4 (P730+)	0.2195	No	ns
Group 3 (P545 - 729) vs. Group 4 (P730+)	0.4203	No	ns
Row 4 - (-1250uM from ONH)			
Group 1 (P60 - P180) vs. Group 2 (P365 - 544)	0.148	No	ns
Group 1 (P60 - P180) vs. Group 3 (P545 - 729)	0.176	No	ns
Group 1 (P60 - P180) vs. Group 4 (P730+)	0.0021	Yes	**
Group 2 (P365 - 544) vs. Group 3 (P545 - 729)	0.9953	No	ns
Group 2 (P365 - 544) vs. Group 4 (P730+)	0.6124	No	ns
Group 3 (P545 - 729) vs. Group 4 (P730+)	0.394	No	ns
Row 5 - (-1000uM from ONH)			
Group 1 (P60 - P180) vs. Group 2 (P365 - 544)	0.0821	No	ns
Group 1 (P60 - P180) vs. Group 3 (P545 - 729)	0.1374	No	ns
Group 1 (P60 - P180) vs. Group 4 (P730+)	0.0054	Yes	**
Group 2 (P365 - 544) vs. Group 3 (P545 - 729)	0.9799	No	ns
Group 2 (P365 - 544) vs. Group 4 (P730+)	0.8933	No	ns
Group 3 (P545 - 729) vs. Group 4 (P730+)	0.6359	No	ns
Row 6 - (-750uM from ONH)			

Group 1 (P60 - P180) vs. Group 2 (P365 - 544)	0.2121	No	ns
Group 1 (P60 - P180) vs. Group 3 (P545 - 729)	0.3519	No	ns
Group 1 (P60 - P180) vs. Group 4 (P730+)	0.0065	Yes	**
Group 2 (P365 - 544) vs. Group 3 (P545 - 729)	0.9755	No	ns
Group 2 (P365 - 544) vs. Group 4 (P730+)	0.6907	No	ns
Group 3 (P545 - 729) vs. Group 4 (P730+)	0.3602	No	ns
Row 7 - (-500uM from ONH)			
Group 1 (P60 - P180) vs. Group 2 (P365 - 544)	0.2333	No	ns
Group 1 (P60 - P180) vs. Group 3 (P545 - 729)	0.3769	No	ns
Group 1 (P60 - P180) vs. Group 4 (P730+)	0.0511	No	ns
Group 2 (P365 - 544) vs. Group 3 (P545 - 729)	0.977	No	ns
Group 2 (P365 - 544) vs. Group 4 (P730+)	0.9598	No	ns
Group 3 (P545 - 729) vs. Group 4 (P730+)	0.763	No	ns
Row 8 - (-250uM from ONH)			
Group 1 (P60 - P180) vs. Group 2 (P365 - 544)	0.1239	No	ns
Group 1 (P60 - P180) vs. Group 3 (P545 - 729)	0.1708	No	ns
Group 1 (P60 - P180) vs. Group 4 (P730+)	0.0025	Yes	**
Group 2 (P365 - 544) vs. Group 3 (P545 - 729)	0.99	No	ns
Group 2 (P365 - 544) vs. Group 4 (P730+)	0.6907	No	ns
Group 3 (P545 - 729) vs. Group 4 (P730+)	0.4292	No	ns

Row 9 - (0uM from ONH)			
Group 1 (P60 - P180) vs. Group 2 (P365 - 544)	>0.9999	No	ns
Group 1 (P60 - P180) vs. Group 3 (P545 - 729)	>0.9999	No	ns
Group 1 (P60 - P180) vs. Group 4 (P730+)	>0.9999	No	ns
Group 2 (P365 - 544) vs. Group 3 (P545 - 729)	>0.9999	No	ns
Group 2 (P365 - 544) vs. Group 4 (P730+)	>0.9999	No	ns
Group 3 (P545 - 729) vs. Group 4 (P730+)	>0.9999	No	ns
Row 10 - (+250uM from ONH)			
Group 1 (P60 - P180) vs. Group 2 (P365 - 544)	0.1084	No	ns
Group 1 (P60 - P180) vs. Group 3 (P545 - 729)	0.7282	No	ns
Group 1 (P60 - P180) vs. Group 4 (P730+)	0.042	Yes	*
Group 2 (P365 - 544) vs. Group 3 (P545 - 729)	0.5565	No	ns
Group 2 (P365 - 544) vs. Group 4 (P730+)	0.9975	No	ns
Group 3 (P545 - 729) vs. Group 4 (P730+)	0.3685	No	ns
Row 11 - (+500uM from ONH)			
Group 1 (P60 - P180) vs. Group 2 (P365 - 544)	0.5477	No	ns
Group 1 (P60 - P180) vs. Group 3 (P545 - 729)	0.1511	No	ns
Group 1 (P60 - P180) vs. Group 4 (P730+)	0.0198	Yes	*
Group 2 (P365 - 544) vs. Group 3 (P545 - 729)	0.9205	No	ns
Group 2 (P365 - 544) vs. Group 4 (P730+)	0.5094	No	ns
Group 3 (P545 - 729) vs. Group 4 (P730+)	0.8491	No	ns

Row 12 - (+750uM from ONH)			
Group 1 (P60 - P180) vs. Group 2 (P365 - 544)	0.8681	No	ns
Group 1 (P60 - P180) vs. Group 3 (P545 - 729)	0.9269	No	ns
Group 1 (P60 - P180) vs. Group 4 (P730+)	0.1924	No	ns
Group 2 (P365 - 544) vs. Group 3 (P545 - 729)	0.9972	No	ns
Group 2 (P365 - 544) vs. Group 4 (P730+)	0.7019	No	ns
Group 3 (P545 - 729) vs. Group 4 (P730+)	0.5121	No	ns
Row 13 - (+1000uM from ONH)			
Group 1 (P60 - P180) vs. Group 2 (P365 - 544)	0.9057	No	ns
Group 1 (P60 - P180) vs. Group 3 (P545 - 729)	0.5692	No	ns
Group 1 (P60 - P180) vs. Group 4 (P730+)	0.0316	Yes	*
Group 2 (P365 - 544) vs. Group 3 (P545 - 729)	0.9544	No	ns
Group 2 (P365 - 544) vs. Group 4 (P730+)	0.2392	No	ns
Group 3 (P545 - 729) vs. Group 4 (P730+)	0.4563	No	ns
Row 14 - (+1250uM from ONH)			
Group 1 (P60 - P180) vs. Group 2 (P365 - 544)	0.2882	No	ns
Group 1 (P60 - P180) vs. Group 3 (P545 - 729)	0.8197	No	ns
Group 1 (P60 - P180) vs. Group 4 (P730+)	0.0065	Yes	**
Group 2 (P365 - 544) vs. Group 3 (P545 - 729)	0.7671	No	ns
Group 2 (P365 - 544) vs. Group 4 (P730+)	0.5831	No	ns

Group 3 (P545 - 729) vs. Group 4 (P730+)	0.077	No	ns
Row 15 - (+1500uM from ONH)			
Group 1 (P60 - P180) vs. Group 2 (P365 - 544)	0.716	No	ns
Group 1 (P60 - P180) vs. Group 3 (P545 - 729)	0.9931	No	ns
Group 1 (P60 - P180) vs. Group 4 (P730+)	0.4563	No	ns
Group 2 (P365 - 544) vs. Group 3 (P545 - 729)	0.8512	No	ns
Group 2 (P365 - 544) vs. Group 4 (P730+)	0.99	No	ns
Group 3 (P545 - 729) vs. Group 4 (P730+)	0.6264	No	ns
Row 16 - (+1750uM from ONH)			
Group 1 (P60 - P180) vs. Group 2 (P365 - 544)	0.9354	No	ns
Group 1 (P60 - P180) vs. Group 3 (P545 - 729)	0.8041	No	ns
Group 1 (P60 - P180) vs. Group 4 (P730+)	0.6074	No	ns
Group 2 (P365 - 544) vs. Group 3 (P545 - 729)	0.9948	No	ns
Group 2 (P365 - 544) vs. Group 4 (P730+)	0.9459	No	ns
Group 3 (P545 - 729) vs. Group 4 (P730+)	0.9875	No	ns
Row 17 - (+2000uM from ONH)			
Group 1 (P60 - P180) vs. Group 2 (P365 - 544)	0.9997	No	ns
Group 1 (P60 - P180) vs. Group 3 (P545 - 729)	0.7961	No	ns
Group 1 (P60 - P180) vs. Group 4 (P730+)	0.6074	No	ns
Group 2 (P365 - 544) vs. Group 3 (P545 - 729)	0.7826	No	ns

Group 2 (P365 - 544) vs. Group 4 (P730+)	0.7216	No	ns
Group 3 (P545 - 729) vs. Group 4 (P730+)	0.1419	No	ns

Supplementary Table 6.9: One-way ANOVA with Tukey's multiple Comparison Test for Outer Nuclear Layer (ONL) Nuclei Quantification from Manual Counting of H&E Stained Sections

Two-way ANOVA with Tukey's multiple comparisons test - Cell nuclei quantification in the INL	Adjusted P Value	Significant?	Summary
Row 1 (-2000uM from ONH)			
Group 1 P60 - P180 vs. Group 2 P365 - P544	0.6614	No	ns
Group 1 P60 - P180 vs. Group 3 P545 - P729	0.7796	No	ns
Group 1 P60 - P180 vs. Group 4 P730+	0.9259	No	ns
Group 2 P365 - P544 vs. Group 3 P545 - P729	0.9931	No	ns
Group 2 P365 - P544 vs. Group 4 P730+	0.3167	No	ns
Group 3 P545 - P729 vs. Group 4 P730+	0.4009	No	ns
Row 2 (-1750uM from ONH)			
Group 1 P60 - P180 vs. Group 2 P365 - P544	0.9993	No	ns
Group 1 P60 - P180 vs. Group 3 P545 - P729	0.7167	No	ns
Group 1 P60 - P180 vs. Group 4 P730+	0.7382	No	ns
Group 2 P365 - P544 vs. Group 3 P545 - P729	0.6889	No	ns
Group 2 P365 - P544 vs. Group 4 P730+	0.845	No	ns
Group 3 P545 - P729 vs. Group 4 P730+	0.1652	No	ns
Row 3 (-1500uM from ONH)			

Group 1 P60 - P180 vs. Group 2 P365 - P544	0.7871	No	ns
Group 1 P60 - P180 vs. Group 3 P545 - P729	0.9648	No	ns
Group 1 P60 - P180 vs. Group 4 P730+	0.2048	No	ns
Group 2 P365 - P544 vs. Group 3 P545 - P729	0.9601	No	ns
Group 2 P365 - P544 vs. Group 4 P730+	0.8115	No	ns
Group 3 P545 - P729 vs. Group 4 P730+	0.4439	No	ns
Row 4 (-1250uM from ONH)			
Group 1 P60 - P180 vs. Group 2 P365 - P544	0.5693	No	ns
Group 1 P60 - P180 vs. Group 3 P545 - P729	0.4439	No	ns
Group 1 P60 - P180 vs. Group 4 P730+	0.34	No	ns
Group 2 P365 - P544 vs. Group 3 P545 - P729	0.9997	No	ns
Group 2 P365 - P544 vs. Group 4 P730+	0.9939	No	ns
Group 3 P545 - P729 vs. Group 4 P730+	0.9979	No	ns
Row 5 (-1000uM from ONH)			
Group 1 P60 - P180 vs. Group 2 P365 - P544	0.1875	No	ns
Group 1 P60 - P180 vs. Group 3 P545 - P729	0.5112	No	ns
Group 1 P60 - P180 vs. Group 4 P730+	0.4439	No	ns
Group 2 P365 - P544 vs. Group 3 P545 - P729	0.8846	No	ns

Group 2 P365 - P544 vs. Group 4 P730+	0.9224	No	ns
Group 3 P545 - P729 vs. Group 4 P730+	0.9995	No	ns
Row 6 (-750uM from ONH)			
Group 1 P60 - P180 vs. Group 2 P365 - P544	0.0039	Yes	**
Group 1 P60 - P180 vs. Group 3 P545 - P729	0.7592	No	ns
Group 1 P60 - P180 vs. Group 4 P730+	0.2505	No	ns
Group 2 P365 - P544 vs. Group 3 P545 - P729	0.0574	No	ns
Group 2 P365 - P544 vs. Group 4 P730+	0.3112	No	ns
Group 3 P545 - P729 vs. Group 4 P730+	0.8183	No	ns
Row 7 (-500uM from ONH)			
Group 1 P60 - P180 vs. Group 2 P365 - P544	0.1603	No	ns
Group 1 P60 - P180 vs. Group 3 P545 - P729	0.9782	No	ns
Group 1 P60 - P180 vs. Group 4 P730+	0.7167	No	ns
Group 2 P365 - P544 vs. Group 3 P545 - P729	0.3167	No	ns
Group 2 P365 - P544 vs. Group 4 P730+	0.6823	No	ns
Group 3 P545 - P729 vs. Group 4 P730+	0.9135	No	ns
Row 8 (-250uM from ONH)			
Group 1 P60 - P180 vs. Group 2 P365 - P544	0.0031	Yes	**

Group 1 P60 - P180 vs. Group 3 P545 - P729	0.9135	No	ns
Group 1 P60 - P180 vs. Group 4 P730+	0.0232	Yes	*
Group 2 P365 - P544 vs. Group 3 P545 - P729	0.0211	Yes	*
Group 2 P365 - P544 vs. Group 4 P730+	0.8286	No	ns
Group 3 P545 - P729 vs. Group 4 P730+	0.1215	No	ns
Row 10 (+250uM from ONH)			
Group 1 P60 - P180 vs. Group 2 P365 - P544	0.168	No	ns
Group 1 P60 - P180 vs. Group 3 P545 - P729	0.9963	No	ns
Group 1 P60 - P180 vs. Group 4 P730+	0.34	No	ns
Group 2 P365 - P544 vs. Group 3 P545 - P729	0.247	No	ns
Group 2 P365 - P544 vs. Group 4 P730+	0.9551	No	ns
Group 3 P545 - P729 vs. Group 4 P730+	0.466	No	ns
Row 11 (+500uM from ONH)			
Group 1 P60 - P180 vs. Group 2 P365 - P544	0.8339	No	ns
Group 1 P60 - P180 vs. Group 3 P545 - P729	0.8702	No	ns
Group 1 P60 - P180 vs. Group 4 P730+	0.8702	No	ns
Group 2 P365 - P544 vs. Group 3 P545 - P729	0.4096	No	ns
Group 2 P365 - P544 vs. Group 4 P730+	0.9991	No	ns

Group 3 P545 - P729 vs. Group 4 P730+	0.4222	No	ns
Row 12 (+750uM from ONH)			
Group 1 P60 - P180 vs. Group 2 P365 - P544	0.9332	No	ns
Group 1 P60 - P180 vs. Group 3 P545 - P729	0.8702	No	ns
Group 1 P60 - P180 vs. Group 4 P730+	>0.9999	No	ns
Group 2 P365 - P544 vs. Group 3 P545 - P729	0.5616	No	ns
Group 2 P365 - P544 vs. Group 4 P730+	0.9431	No	ns
Group 3 P545 - P729 vs. Group 4 P730+	0.8538	No	ns
Row 13 (+1000uM from ONH)			
Group 1 P60 - P180 vs. Group 2 P365 - P544	0.619	No	ns
Group 1 P60 - P180 vs. Group 3 P545 - P729	0.9999	No	ns
Group 1 P60 - P180 vs. Group 4 P730+	>0.9999	No	ns
Group 2 P365 - P544 vs. Group 3 P545 - P729	0.6614	No	ns
Group 2 P365 - P544 vs. Group 4 P730+	0.619	No	ns
Group 3 P545 - P729 vs. Group 4 P730+	0.9999	No	ns
Row 14 (+1250uM from ONH)			
Group 1 P60 - P180 vs. Group 2 P365 - P544	0.9954	No	ns
Group 1 P60 - P180 vs. Group 3 P545 - P729	0.7796	No	ns

Group 1 P60 - P180 vs. Group 4 P730+	0.9648	No	ns
Group 2 P365 - P544 vs. Group 3 P545 - P729	0.6823	No	ns
Group 2 P365 - P544 vs. Group 4 P730+	0.9971	No	ns
Group 3 P545 - P729 vs. Group 4 P730+	0.4885	No	ns
Row 15 (+1500uM from ONH)			
Group 1 P60 - P180 vs. Group 2 P365 - P544	0.4703	No	ns
Group 1 P60 - P180 vs. Group 3 P545 - P729	0.9372	No	ns
Group 1 P60 - P180 vs. Group 4 P730+	0.7796	No	ns
Group 2 P365 - P544 vs. Group 3 P545 - P729	0.7994	No	ns
Group 2 P365 - P544 vs. Group 4 P730+	0.94	No	ns
Group 3 P545 - P729 vs. Group 4 P730+	0.9834	No	ns
Row 16 (+1750uM from ONH)			
Group 1 P60 - P180 vs. Group 2 P365 - P544	0.0606	No	ns
Group 1 P60 - P180 vs. Group 3 P545 - P729	0.1777	No	ns
Group 1 P60 - P180 vs. Group 4 P730+	0.38	No	ns
Group 2 P365 - P544 vs. Group 3 P545 - P729	0.9224	No	ns
Group 2 P365 - P544 vs. Group 4 P730+	0.7296	No	ns
Group 3 P545 - P729 vs. Group 4 P730+	0.972	No	ns

Row 17 (+2000uM from ONH)			
Group 1 P60 - P180 vs. Group 2 P365 - P544	0.6335	No	ns
Group 1 P60 - P180 vs. Group 3 P545 - P729	0.6035	No	ns
Group 1 P60 - P180 vs. Group 4 P730+	0.7796	No	ns
Group 2 P365 - P544 vs. Group 3 P545 - P729	>0.9999	No	ns
Group 2 P365 - P544 vs. Group 4 P730+	0.9892	No	ns
Group 3 P545 - P729 vs. Group 4 P730+	0.9914	No	ns

Supplementary Table 6.10: One-way ANOVA with Tukey's multiple Comparison Test for Inner Nuclear Layer (INL) Nuclei Quantification from Manual Counting of H&E Stained Sections

Two-way ANOVA with Tukey's multiple comparisons test - Cell nuclei quantification in the GCL	Adjusted P Value	Significant?	Summary
Row 1 (-2000uM from ONH)			
Group 1 P60 - P180 vs. Group 2 P365 - P544	0.3102	No	ns
Group 1 P60 - P180 vs. Group 3 P545 - P729	>0.9999	No	ns
Group 1 P60 - P180 vs. Group 4 P730+	0.9349	No	ns
Group 2 P365 - P544 vs. Group 3 P545 - P729	0.3102	No	ns
Group 2 P365 - P544 vs. Group 4 P730+	0.107	No	ns
Group 3 P545 - P729 vs. Group 4 P730+	0.9349	No	ns
Row 2 (-1750uM from ONH)			
Group 1 P60 - P180 vs. Group 2 P365 - P544	0.9832	No	ns
Group 1 P60 - P180 vs. Group 3 P545 - P729	0.9989	No	ns
Group 1 P60 - P180 vs. Group 4 P730+	0.5464	No	ns
Group 2 P365 - P544 vs. Group 3 P545 - P729	0.9957	No	ns
Group 2 P365 - P544 vs. Group 4 P730+	0.3838	No	ns
Group 3 P545 - P729 vs. Group 4 P730+	0.4545	No	ns
Row 3 (-1500uM from ONH)			
Group 1 P60 - P180 vs. Group 2 P365 - P544	0.7744	No	ns
Group 1 P60 - P180 vs. Group 3 P545 - P729	0.9989	No	ns

Group 1 P60 - P180 vs. Group 4 P730+	0.991	No	ns
Group 2 P365 - P544 vs. Group 3 P545 - P729	0.6944	No	ns
Group 2 P365 - P544 vs. Group 4 P730+	0.9035	No	ns
Group 3 P545 - P729 vs. Group 4 P730+	0.9709	No	ns
Row 4 (-1250uM from ONH)			
Group 1 P60 - P180 vs. Group 2 P365 - P544	0.6944	No	ns
Group 1 P60 - P180 vs. Group 3 P545 - P729	0.0886	No	ns
Group 1 P60 - P180 vs. Group 4 P730+	0.1685	No	ns
Group 2 P365 - P544 vs. Group 3 P545 - P729	0.6944	No	ns
Group 2 P365 - P544 vs. Group 4 P730+	0.8451	No	ns
Group 3 P545 - P729 vs. Group 4 P730+	0.991	No	ns
Row 5 (-1000uM from ONH)			
Group 1 P60 - P180 vs. Group 2 P365 - P544	0.2676	No	ns
Group 1 P60 - P180 vs. Group 3 P545 - P729	0.5464	No	ns
Group 1 P60 - P180 vs. Group 4 P730+	0.991	No	ns
Group 2 P365 - P544 vs. Group 3 P545 - P729	0.935	No	ns
Group 2 P365 - P544 vs. Group 4 P730+	0.4122	No	ns
Group 3 P545 - P729 vs. Group 4 P730+	0.7304	No	ns
Row 6 (-750uM from ONH)			
Group 1 P60 - P180 vs. Group 2 P365 - P544	0.9689	No	ns

Group 1 P60 - P180 vs. Group 3 P545 - P729	0.991	No	ns
Group 1 P60 - P180 vs. Group 4 P730+	>0.9999	No	ns
Group 2 P365 - P544 vs. Group 3 P545 - P729	0.8863	No	ns
Group 2 P365 - P544 vs. Group 4 P730+	0.9689	No	ns
Group 3 P545 - P729 vs. Group 4 P730+	0.991	No	ns
Row 7 (-500uM from ONH)			
Group 1 P60 - P180 vs. Group 2 P365 - P544	0.7496	No	ns
Group 1 P60 - P180 vs. Group 3 P545 - P729	0.9709	No	ns
Group 1 P60 - P180 vs. Group 4 P730+	0.991	No	ns
Group 2 P365 - P544 vs. Group 3 P545 - P729	0.935	No	ns
Group 2 P365 - P544 vs. Group 4 P730+	0.5812	No	ns
Group 3 P545 - P729 vs. Group 4 P730+	0.8817	No	ns
Row 8 (-250uM from ONH)			
Group 1 P60 - P180 vs. Group 2 P365 - P544	0.0068	Yes	**
Group 1 P60 - P180 vs. Group 3 P545 - P729	0.291	No	ns
Group 1 P60 - P180 vs. Group 4 P730+	0.9349	No	ns
Group 2 P365 - P544 vs. Group 3 P545 - P729	0.3594	No	ns
Group 2 P365 - P544 vs. Group 4 P730+	0.0347	Yes	*
Group 3 P545 - P729 vs. Group 4 P730+	0.64	No	ns
Row 10 (+250uM from ONH)			

Group 1 P60 - P180 vs. Group 2 P365 - P544	0.9991	No	ns
Group 1 P60 - P180 vs. Group 3 P545 - P729	0.8125	No	ns
Group 1 P60 - P180 vs. Group 4 P730+	0.5464	No	ns
Group 2 P365 - P544 vs. Group 3 P545 - P729	0.9035	No	ns
Group 2 P365 - P544 vs. Group 4 P730+	0.6944	No	ns
Group 3 P545 - P729 vs. Group 4 P730+	0.9709	No	ns
Row 11 (+500uM from ONH)			
Group 1 P60 - P180 vs. Group 2 P365 - P544	0.9928	No	ns
Group 1 P60 - P180 vs. Group 3 P545 - P729	0.7304	No	ns
Group 1 P60 - P180 vs. Group 4 P730+	0.991	No	ns
Group 2 P365 - P544 vs. Group 3 P545 - P729	0.9035	No	ns
Group 2 P365 - P544 vs. Group 4 P730+	0.9474	No	ns
Group 3 P545 - P729 vs. Group 4 P730+	0.5464	No	ns
Row 12 (+750uM from ONH)			
Group 1 P60 - P180 vs. Group 2 P365 - P544	0.0875	No	ns
Group 1 P60 - P180 vs. Group 3 P545 - P729	0.8125	No	ns
Group 1 P60 - P180 vs. Group 4 P730+	0.9709	No	ns
Group 2 P365 - P544 vs. Group 3 P545 - P729	0.0092	Yes	**
Group 2 P365 - P544 vs. Group 4 P730+	0.0308	Yes	*
Group 3 P545 - P729 vs. Group 4 P730+	0.9709	No	ns

Row 13 (+1000uM from ONH)			
Group 1 P60 - P180 vs. Group 2 P365 - P544	0.1899	No	ns
Group 1 P60 - P180 vs. Group 3 P545 - P729	0.9709	No	ns
Group 1 P60 - P180 vs. Group 4 P730+	0.8817	No	ns
Group 2 P365 - P544 vs. Group 3 P545 - P729	0.0779	No	ns
Group 2 P365 - P544 vs. Group 4 P730+	0.039	Yes	*
Group 3 P545 - P729 vs. Group 4 P730+	0.991	No	ns
Row 14 (+1250uM from ONH)			
Group 1 P60 - P180 vs. Group 2 P365 - P544	0.0557	No	ns
Group 1 P60 - P180 vs. Group 3 P545 - P729	0.991	No	ns
Group 1 P60 - P180 vs. Group 4 P730+	0.291	No	ns
Group 2 P365 - P544 vs. Group 3 P545 - P729	0.0268	Yes	*
Group 2 P365 - P544 vs. Group 4 P730+	0.7982	No	ns
Group 3 P545 - P729 vs. Group 4 P730+	0.1685	No	ns
Row 15 (+1500uM from ONH)			
Group 1 P60 - P180 vs. Group 2 P365 - P544	0.2088	No	ns
Group 1 P60 - P180 vs. Group 3 P545 - P729	0.8817	No	ns
Group 1 P60 - P180 vs. Group 4 P730+	0.5464	No	ns
Group 2 P365 - P544 vs. Group 3 P545 - P729	0.5812	No	ns
Group 2 P365 - P544 vs. Group 4 P730+	0.8863	No	ns
Group 3 P545 - P729 vs. Group 4 P730+	0.9349	No	ns

Row 16 (+1750uM from ONH)			
Group 1 P60 - P180 vs. Group 2 P365 - P544	0.5223	No	ns
Group 1 P60 - P180 vs. Group 3 P545 - P729	0.4545	No	ns
Group 1 P60 - P180 vs. Group 4 P730+	>0.9999	No	ns
Group 2 P365 - P544 vs. Group 3 P545 - P729	>0.9999	No	ns
Group 2 P365 - P544 vs. Group 4 P730+	0.5223	No	ns
Group 3 P545 - P729 vs. Group 4 P730+	0.4545	No	ns
Row 17 (+2000uM from ONH)			
Group 1 P60 - P180 vs. Group 2 P365 - P544	0.8863	No	ns
Group 1 P60 - P180 vs. Group 3 P545 - P729	0.2242	No	ns
Group 1 P60 - P180 vs. Group 4 P730+	0.9349	No	ns
Group 2 P365 - P544 vs. Group 3 P545 - P729	0.7208	No	ns
Group 2 P365 - P544 vs. Group 4 P730+	0.9979	No	ns
Group 3 P545 - P729 vs. Group 4 P730+	0.5464	No	ns

Supplementary Table 6.11: One-way ANOVA with Tukey's multiple Comparison Test for Ganglion Cell Layer (GCL) Nuclei Quantification from Manual Counting of H&E Stained Sections

References

1. Swenor BK, Lee MJ, Varadaraj V, Whitson HE, Ramulu PY. Aging with Vision Loss: A Framework for Assessing the Impact of Visual Impairment on Older Adults. Gerontologist. 2019;10(10):1-7. doi:10.1093/geront/gnz117
2. Lin JB, Tsubota K, Apte RS. A glimpse at the aging eye. npj Aging Mech Dis. 2016;2(1):1-7. doi:10.1038/npjamd.2016.3
3. Ryoo NK, Ahn SJ, Park KH, et al. Thickness of retina and choroid in the elderly population and its association with Complement Factor H polymorphism: KLoSHA Eye study. PLoS One. 2018;13(12):1-15. doi:10.1371/journal.pone.0209276
4. Chauhan BC, Vianna JR, Sharpe GP, et al. Differential Effects of Aging in the Macular Retinal Layers, Neuroretinal Rim and Peripapillary Retinal Nerve Fibre Layer. Ophthalmology. 2019:1-9. doi:10.1016/j.ophtha.2019.09.013
5. Curcio CA, Millican CL, Allen KA, Kalina RE. Aging of the human photoreceptor mosaic: Evidence for selective vulnerability of rods in central retina. Investig Ophthalmol Vis Sci. 1993;34(12):3278-3296.
6. Lin Y, Jiang H, Liu Y, et al. Age-related alterations in retinal tissue perfusion and volumetric vessel density. Investig Ophthalmol Vis Sci. 2019;60(2):685-693. doi:10.1167/iovs.18-25864
7. Orlov N V., Coletta C, van Asten F, et al. Age-related changes of the retinal microvasculature. PLoS One. 2019;14(5):1-17. doi:10.1371/journal.pone.0215916
8. Eells JT. Mitochondrial dysfunction in the aging retina. Biology (Basel). 2019;8(2). doi:10.3390/biology8020031
9. Xu H, Chen M, Forrester J V. Para-inflammation in the aging retina. Prog Retin Eye Res.

2009;28(5):348-368. doi:10.1016/j.preteyeres.2009.06.001

10. Birch DG, Anderson J. Standardized Full-Field Electroretinography. Arch Ophthalmol. 1992;110:1571-1576.
11. Weleber RG. The effect of age on human cone and rod ganzfeld electroretinograms. Investig Ophthalmol Vis Sci. 1981;20(3):392-399.
12. Damani MR, Zhao L, Fontainhas AM, Amaral J, Fariss RN, Wong WT. Age-related Alterations in the Dynamic Behavior of Microglia. Aging Cell. 2008;10(2):263-276. doi:10.1038/jid.2014.371
13. Telegina D V., Kozhevnikova OS, Kolosova NG. Changes in Retinal Glial Cells with Age and during Development of Age-Related Macular Degeneration. Biochem. 2018;83(9):1009-1017. doi:10.1134/S000629791809002X
14. Tarau I-S, Berlin A, Curcio CA, Ach T. The Cytoskeleton of the Retinal Pigment Epithelium: from Normal Aging to Age-Related Macular Degeneration. Int J Mol Sci. 2019;20(14):3578. doi:10.3390/ijms20143578
15. Delori C, Goger DG, Dorey CK. Age-Related Accumulation and Spatial Distribution of Lipofuscin in RPE of Normal Subjects. 2001;42(8).
16. Presley JB, Chimento MF, Curcio CA. Comparison of Morphology of Human Macular and Peripheral Bruch's Membrane in Older Eyes. Curr Eye Res. 2008;32(9):791-799. doi:10.1080/02713680701550660.Comparison
17. Nadal-Nicolás FM, Vidal-Sanz M, Agudo-Barriuso M. The aging rat retina: from function to anatomy. Neurobiol Aging. 2018;61:146-168. doi:10.1016/j.neurobiolaging.2017.09.021
18. Cano J, Machado A, Reinoso-Suárez F. Morphological changes in the retina of ageing

rats. Arch Gerontol Geriatr. 1986;5(1):41-50. doi:10.1016/0167-4943(86)90006-3

19. Wang Y, Grenell A, Zhong F, et al. Metabolic signature of the aging eye in mice. Neurobiol Aging. 2018;71:223-233. doi:10.1016/j.neurobiolaging.2018.07.024

20. Dutta S, Sengupta P. Men and mice: Relating their ages. Life Sci. 2016;152:244-248. doi:10.1016/j.lfs.2015.10.025

21. Flynn E, Ueda K, Auran E, Sullivan JM, Sparrow JR. Fundus autofluorescence and photoreceptor cell rosettes in mouse models. Investig Ophthalmol Vis Sci. 2014;55(9):5643-5652. doi:10.1167/iovs.14-14136

22. Sparrow JR, Yoon KD, Wu Y, Yamamoto K. Interpretations of fundus autofluorescence from studies of the bisretinoids of the retina. Investig Ophthalmol Vis Sci. 2010;51(9):4351-4357. doi:10.1167/iovs.10-5852

23. Secondi R, Kong J, Blonska AM, Staurenghi G, Sparrow JR. Fundus autofluorescence findings in a mouse model of retinal detachment. Investig Ophthalmol Vis Sci. 2012;53(9):5190-5197. doi:10.1167/iovs.12-9672

24. STREHLER BL, MARK DD, MILDVAN AS. Rate and magnitude of age pigment accumulation in the human myocardium. J Gerontol. 1959;14:430-439. doi:10.1093/geronj/14.4.430

25. Ben-Shabat S, Parish CA, Vollmer HR, et al. Biosynthetic studies of A2E, a major fluorophore of retinal pigment epithelial lipofusein. J Biol Chem. 2002;277(9):7183-7190. doi:10.1074/jbc.M108981200

26. Sparrow JR, Kim SR, Wu Y. Experimental approaches to the study of A2E, a bisretinoid lipofuscin chromophore of retinal pigment epithelium. Methods Mol Biol. 2010;652:315-327. doi:10.1007/978-1-60327-325-1_18

27. Wang NK, Fine HF, Chang S, et al. Cellular origin of fundus autofluorescence in patients and mice with a defective NR2E3 gene. Br J Ophthalmol. 2009;93(9):1234-1240. doi:10.1136/bjo.2008.153577

28. Mata NL, Weng J, Travis GH. Biosynthesis of a major lipofuscin fluorophore in mice and humans with ABCR-mediated retinal and macular degeneration. Proc Natl Acad Sci U S A. 2000;97(13):7154-7159. doi:10.1073/pnas.130110497

29. Xu H, Chen M, Manivannan A, Lois N, Forrester J V. Age-dependent accumulation of lipofuscin in perivascular and subretinal microglia in experimental mice. Aging Cell. 2008;7(1):58-68. doi:10.1111/j.1474-9726.2007.00351.x

30. Yoshida S, Yashar BM, Hiriyanna S, Swaroop A. Microarray analysis of gene expression in the aging human retina. Investig Ophthalmol Vis Sci. 2002;43(8):2554-2560.

31. Chen M, Muckersie E, Forrester J V., Xu H. Immune activation in retinal aging: A gene expression study. Investig Ophthalmol Vis Sci. 2010;51(11):5888-5896. doi:10.1167/iovs.09-5103

32. Augusteyn RC. Growth of the eye lens: I. Weight accumulation in multiple species. Mol Vis. 2014;20(October 2013):410-426.

33. Partridge L, Deelen J, Slagboom PE. Facing up to the global challenges of ageing. Nature. 2018;561(7721):45-56. doi:10.1038/s41586-018-0457-8

34. Ferrucci L, Gonzalez-Freire M, Fabbri E, et al. Measuring biological aging in humans: A quest. Aging Cell. 2019;(July):1-21. doi:10.1111/acel.13080

35. Pagiatakis C, Musolino E, Gornati R, Bernardini G, Papait R. Epigenetics of aging and disease: a brief overview. Aging Clin Exp Res. 2019;(0123456789). doi:10.1007/s40520-019-01430-0

36. López-Otín C, Blasco MA, Partridge L, Serrano M, Kroemer G. The hallmarks of aging. Cell. 2013;153(6):1194. doi:10.1016/j.cell.2013.05.039

37. Van Deursen JM. The role of senescent cells in ageing. Nature. 2014;509(7501):439-446. doi:10.1038/nature13193

38. Wang C, Jurk D, Maddick M, Nelson G, Martin-ruiz C, Von Zglinicki T. DNA damage response and cellular senescence in tissues of aging mice. Aging Cell. 2009;8(3):311-323. doi:10.1111/j.1474-9726.2009.00481.x

39. Mitchell SJ, Scheibye-Knudsen M, Longo DL, de Cabo R. Animal Models of Aging Research: Implications for Human Aging and Age-Related Diseases. Annu Rev Anim Biosci. 2015;3(1):283-303. doi:10.1146/annurev-animal-022114-110829

40. Geifman N, Rubin E. The mouse age phenome knowledgebase and disease-specific inter-species age mapping. PLoS One. 2013;8(12). doi:10.1371/journal.pone.0081114

41. Lambert NG, Singha MK, ElShelmani H, et al. Risk Factors and Biomarkers of Age-Related Macular Degeneration. Prog Retin Eye Res. 2016;54(1):64-102. doi:doi:10.1016/j.preteyeres.2016.04.003.

42. Al-Zamil WM, Yassin SA. Recent developments in age-related macular degeneration: A review. Clin Interv Aging. 2017;12:1313-1330. doi:10.2147/CIA.S143508

43. Chakravarthy U, Wong TY, Fletcher A, et al. Clinical risk factors for age-related macular degeneration: A systematic review and meta-analysis. BMC Ophthalmol. 2010;10(1):31. doi:10.1186/1471-2415-10-31

44. Boulton M, Dayhaw-barker P. The role of the retinal pigment epithelium: topographical variation and ageing changes. Nature, Eye. 2001;15:384-389.

Chapter VII: Discussion

Summary

Overall, the main goals of this dissertation were to investigate the role of *Lsd1* in proper retinal development and the potential for *Lsd1* to be a therapeutic target for retinoblastoma. Secondarily, we also chose to investigate how natural aging affects the retina between 2 and 32 months of age in wild-type C57Bl/6J animals.

Lsd1 is known to be crucial for the proper development and differentiation of neurons in the brain, partially due to the presence of a neuron specific *Lsd1* isoform, n*Lsd1*. n*Lsd1* is an isoform that contains a micro-exon (E8a) that encodes a tetrapeptide Asp-Thr-Val-Lys[1]. This n*Lsd1* isoform is able to regulate neuronal differentiation via H3K9 demethylation[2–4]. In retinal explants, pharmacological inhibition of *Lsd1* prevents the proper differentiation of rod photoreceptors[5]. Taken together, this collective body of work summarized in Chapter 2 provided sufficient premise to investigate the role of *Lsd1* in proper retinal development.

First, we investigated the endogenous expression of *Lsd1* and its substrates H3K4me1 and H3K4me2 during and after retinal development in a wild-type mouse strain, C57Bl/6J. These findings were published in the journal *Investigative Ophthalmology and Vision Science (IOVS)* in 2019 and are included as Chapter 3 of this dissertation[6]. In summary, we found that *Lsd1* is expressed as early as post-natal day 2 in the vast majority of cells in the developing retinoblast. This pattern of expression is the same for its substrates H3K4me1 and H3K4me2. As the retina begins to differentiate, the pattern of *Lsd1* expression starts to vary among different mature retinal subtypes. By post-natal day 36, there is a distinct pattern of expression where *Lsd1* is relatively highly expressed in cone photoreceptors and inner nuclear layer cells, such as

amacrine, bipolar, and horizontal cells. In contrast rod photoreceptors have relatively low *Lsd1* expression, partially due to their unique inverted chromatin organization[7]. Retinal ganglion cells have a continuous expression pattern whereby adjacent cells can either have low, medium, or high *Lsd1* levels.

Given these results, we hypothesized that *Lsd1* must play an important role in the development or maintenance of specific mature neuronal subtypes in the retina. Therefore, to test this hypothesis, we tested mice with either global heterozygous deletion of *Lsd1* or a homozygous retina-specific deletion. Those findings are detailed in Chapter 4 of this dissertation. In summary, we found no obvious ocular defects in the *Lsd1* heterozygous animals, implying that *Lsd1* is haplosufficient in the eye. For the homozygous retina-specific deletion, we used the Cre-Lox system[8] to generate a new transgenic line by breeding *Chx10-Cre* mice (JAX Stock No. 005105) to *Lsd1 loxP* animals (gift from Dr. Jeremy Boss, Emory University). By using the *Chx10-Cre* driver line we deleted *Lsd1* in the majority of retinal progenitor cells[9]. These animals showed signs of retinal degeneration in adulthood (both post-natal day 30 and 45) as indicated by a variety of techniques including electroretinogram (ERG), *in vivo* Fundus and SD-OCT images, and post-mortem morphology. *Chx10-Cre Lsd1 loxP* animals had a significant reduction in a- and b-waves both in scotopic and photopic conditions, indicating abnormalities in rod photoreceptor, rod bipolar cell, cone photoreceptor, and cone bipolar cell function[10,11]. These animals also had a significant reduction in their total retinal thickness and outer nuclear layer thickness compared to their littermate controls as measured by SD-OCT images.

One potential confound for these results is the presence of a Cre ERT2 construct at the ROSA26

locus in the *Lsd1 loxP* animals. Cre ERT2 allows for conditional knockout of a gene in the presence of the tamoxifen; however, none of our experiments included tamoxifen injections. We have data suggesting that the presence of one or two copies of the Cre ERT2 allele in either the *Chx10-Cre* positive or *Chx10-Cre* negative animals has no effect on the resulting phenotype; however, there have been reported issues with tamoxifen-independent Cre recombinase activity and high variability among individual animals, tissues, and cell types[12,13]. Therefore, we are currently working to bred out this construct from these mouse strain and will test the new animals once they become available to validate this retinal degeneration phenotype.

Outside of retinal development, we also investigated the potential for *Lsd1* to act as a biomarker and subsequent therapeutic target in retinoblastoma (RB). Aberrant epigenetic changes are frequently observed in different types of cancers[14–17]. Specifically, mis-expression of *Lsd1* has been found in many cancers[18–21] including related cancers such as medulloblastoma and neuroblastoma[22,23]. In human and murine medulloblastoma, *Lsd1* is overexpressed in tumors and siRNA inhibition decreased tumor cell viability and proliferation[24,25]. In neuroblastoma, *Lsd1* is overexpressed in undifferentiated tumors and *Lsd1* inhibition via siRNA, microRNAs such as miR137, and small molecule inhibitors result in reduced tumor cell growth and increased apoptosis both *in vitro* and *in vivo*[26–28]. Inhibition of *Lsd1* specifically in the retina can stabilize HIF-1a which can lead to retinal angiogenesis and tumor vascularization[29]. With this premise, we investigated the expression of *Lsd1* in human RB sections and RB transgenic murine sections in Chapter 5 of this dissertation. In the human and murine sections, we observed overexpression of *Lsd1* in highly differentiated Ki67 positive tumor cells; however, given that the cellular origins of the murine RB cells are likely different from human RB, we believe that the transgenic RB

mouse is not a valid animal model for our purposes[30,31] and that xenograft models would be more appropriate[32–35].

Lastly, in Chapter 6 of this dissertation, we investigated the effect of natural aging on normal retinal function and morphology in the wild-type mouse strain, C57Bl/6J. Using four groups of animals, Group 1 (<0.5 years), Group 2 (1.0 – 1.5 years), Group 3 (1.5 – 2.0 years), and Group 4 (>2.0 years), we tested for visual function using electroretinograms (ERGs), and retinal morphology, both *in vivo* and post-mortem, using cSLO, SD-OCT, and H&E stained sagittal sections. With aging, mice showed a significant reduction in both a- and b-wave ERG amplitudes at various light flash intensities both in scotopic and photopic conditions. Additionally, total retinal thickness and outer nuclear layer thickness, as measured by *in vivo* SD-OCT images, were significantly reduced in the older groups. cSLO images show an increase in auto-fluorescence at the photoreceptor-RPE interface as age increases. A similar result was observed in H&E stained sections where the number of cell nuclei in the outer nuclear layer were significantly reduced in the older ages; however, there were no differences in cell nuclei counts in the inner nuclear layer or retinal ganglion cell layer. This work is currently under review at the journal *Investigative Ophthalmology and Visual Sciences (IOVS).*

Future Directions

Although this dissertation has addressed some key scientific questions regarding the role of *Lsd1* is the retina and retinoblastoma, there are still many unanswered questions that should be addressed in future studies.

One future direction that is needed is to investigate how the presence and absence of *Lsd1* affects the epigenome and transcriptome of retinal cells during and after retinal development. This can be achieved by first conducting ChIP-seq in C57Bl/6J wild type animals at discrete timepoints for *Lsd1* and its substrates, such as H3K4 mono- and di-methyl and H3K9 mono- and di-methyl, to determine where in the genome *Lsd1* may be acting. Afterwards, in the *Chx10-Cre Lsd1 loxP* animals and littermate controls, the same ChIP-seq experiment can be conducted to determine how the deletion of *Lsd1* affects the epigenome. The transcriptome can also be investigated using RNA-seq, either canonical RNA-seq or single cell RNA – seq (scRNA-seq). Due to the unique function of *Lsd1* to act as both a transcriptional activator and repressor depending on its' associated protein complex and its importance in neuronal development, we expect that there are dramatic shifts in the epigenetic environment in these cells, leading to transcriptional and proteomic dysregulation. In the *Chx10-Cre Lsd1 loxP* mouse strain, because of the deletion of *Lsd1* in the majority of retinal progenitor cells, future studies can also investigate how retinal development in these animals is disrupted. In the adult animals, both post-natal day 30 and 45, there is evidence of retinal degeneration due to reductions in visual function and retinal morphology; however, it is unclear whether this phenotype is due to the lack of proliferation in the retinal progenitor cells or due to apoptosis in the developing retina. In order to distinguish between these two possibilities, morphological studies can be conducted on experimental and controls animals between post-natal day 0 and 21. These studies should look for markers for proliferation and apoptosis as well as markers for mature retinal subtypes to determine how *Lsd1* deletion leads to retinal developmental abnormalities.

In addition to continued characterization of the *Chx10-Cre Lsd1 loxP* mouse line, it is crucial to

determine the role of *Lsd1* in the differentiation of specific mature retinal subtypes. Rod photoreceptors are of particular interest due to work from *Popova et al.* Their work showed that pharmacological inhibitor of *Lsd1* using tranylcypromide in committed rod photoreceptor precursor cells result in aberrant cone photoreceptor gene expression[5]. These experiments were done *ex vivo* using retinal explants that were treated with tranylcypromide. To determine whether the same transcriptional dysfunction would be seen *in vivo*, our lab is actively generating a new transgenic mouse line using a Cre recombinase under the control of the rhodopsin promoter (Rho-iCre75 JAX Stock No. 15850) to delete *Lsd1* specifically in rod precursor cells (*Rho-iCre75 Lsd1 loxP*). The *Rho-iCre75* mouse line expresses Cre recombinase as early as at post-natal day 7 with peak expression at post-natal day 18[36]. We hypothesize that the adult retinas of these animals will not show any signs of retinal degeneration or cell loss but will have an abnormal ratio of rod-to-cone photoreceptors. We hypothesize that rod photoreceptors will be relatively underrepresented and cone photoreceptors will be relatively overrepresented. This abnormal ratio of photoreceptors could result in a proportional decrease in visual function in scotopic conditions and a proportional increase in photopic conditions. The overall morphology of the retina would likely be unchanged; however, immunocytochemistry staining with rod specific markers such as rhodopsin and cone specific markers such as cone arrestin would show a decrease in rods and increase in cones. One potential issue that may arise is the relatively late expression of the Cre recombinase under the rhodopsin promoter. Rod photoreceptors make up a majority of the cells in the retina and rhodopsin is the first known marker of this cell type; yet, rods are one of the last retinal neuronal subtypes to be born[37,38]. Therefore, by the peak of Cre recombinase expression at post-natal day 18, *Lsd1* may have already fulfilled its role. This transgenic mouse line deletion of *Lsd1* would differ greatly from the *Popova et al.* study, which

started pharmacological inhibition of *Lsd1* at post-natal day 0 (P0)[5].

In addition to generating a rod photoreceptor specific *Lsd1* knockout, deletion in other cells types, such as cone photoreceptors, or other ocular structures, such as the retinal pigmented epithelium (RPE), would also be interesting. We have previously observed relatively high expression of *Lsd1* in both of these cell types[6] and are working to generate these knockout mice. Unlike rod photoreceptors which are the most abundant cell type in the human and murine retinas (~75%), cone photoreceptors make up a much smaller percentage (~3%)[37]. This is due to the multipotent nature of retinal progenitor cells and their ability to undergo asymmetric mitotic divisions[38]. The asymmetric divisions allow one progenitor cell to produce two daughter cells that differentiate into two different cell types[39]. Cone photoreceptors have relatively higher expression of *Lsd1* compared to rod photoreceptors; therefore, *Lsd1* may be important for their development. We are generating a new transgenic mouse line deleting *Lsd1* with a cone specific Cre driver line (*Hrgp-Cre* JAX Stock No. 032911). We hypothesize that *Lsd1* deletion in this cell type may result in their complete lack of development and/or death. The RPE is a structure underneath the retina that helps to perform critical functions including forming the blood-retina barrier, transporting nutrients, retinoids, and waste products, and phagocytosis of outer segments[40]. *Lsd1* is expressed in both mono- and bi-nucleate adult mouse RPE cells[6]. Using a *Best1-Cre* driver or *RPE-65 Cre* driver line, we can generate a transgenic RPE specific knockout mouse of *Lsd1*. We hypothesize that deleting *Lsd1* in the RPE will result in the death of RPE cells, which could secondarily cause retina degeneration.

For the potential of *Lsd1* to serve as a therapeutic target in retinoblastoma, future studies should

test *Lsd1* inhibitors alone and in combination with HDAC inhibitors on RB cell lines, such as Y79 and WERI. MicroRNAs, shRNAs, and pharmacological agents that target histone demethylases and methyltransferases have previously been shown to reduce tumor cell growth and increase apoptosis in these cell lines[41–43]. Given the high expression of *Lsd1* that we observed in human and mouse retinoblastoma tumors[6], we hypothesize that pharmacological inhibition of *Lsd1* will result in either the direct death of these cells or will make them more sensitive to other chemotherapy agents.

Overall Impact

Overall, this work adds to our general understanding of the importance of epigenetic proteins, such as *Lsd1*, in the development and maintenance of the retina and their role in ocular cancers, such as retinoblastoma. Yet, in general, the ocular epigenetics field remains relatively small and there is a lack of knowledge about the role of the epigenome in ocular development and ocular diseases, both genetic and multifactorial. On the other hand, the transcriptome and individual genes that are necessary for general ocular development, such as Pax6[44–46], and those specific for particular neuronal subtypes, such as Nrl for rod photoreceptors[47–50], have been extensively studied. It has only been in the last 20 years or so that the vision science field has started to investigate the general role of the epigenome in retinal development[51,52] and specific retinal cell types, such as photoreceptors[53]. Advances in technologies such as ChIP-seq[54–56], CUT&RUN[57,58], RNA-seq[59–62], and single cell RNA[63–66] have pushed the ocular epigenetics field forward in just the last two decades[67]. Now the general epigenetic landscape of the developing retina[51] is being investigated and specific forms of epigenetics, such as histone lysine methylation[68] and DNA methylation[69,70] are gaining attention.

Even in specific cell types, such as photoreceptors, important roles for DNA methylation[70] and histone acetylation[71] have been studied. Outside of the importance of investigating the epigenome in retinal development, the increasing importance of epigenetic abnormalities in ocular diseases is being realized[72–74]. Complex diseases such as glaucoma[75], diabetic retinopathy (DR)[76–78], age-related macular degeneration (AMD)[79–81], and retinoblastoma (RB)[51], as well as genetic retinal degeneration diseases can result in aberrant epigenomes. Inhibitors of specific epigenetic proteins, such as histone deacetylases[82,83] and histone methyltransferases[84], have started to show some efficacy as treatment options. Now, researchers are beginning to combine knowledge of the transcriptome and epigenome in retinal cell types to gain a more complete understanding of its complexity on a systems biology level[51,85,86]. While the general retinal epigenome is being studied, an in-depth understanding of the role of specific epigenetic proteins is lacking. Some epigenetic proteins have been studied such as Ezh2 and Jmjd2, among others. Ezh2 is a methyltransferase that acts on H3K27[87,88]. Ezh2 has been shown to be required for proper retinal progenitor cell proliferation and deletion during retinal development can alter the normal distribution of retinal cells, including ganglion cells, amacrine cells, and Muller glial cells[89]. Jmjd3 is a demethylase that acts on H3K27[90,91]. Jmjd3 is expressed as early as embryonic day 15 (E15) in the mouse retina and knockdown of Jmj3 in retinal explants affected the proper development of rod ON bipolar cells[92].

Although *Lsd1* has been extensively studied in brain neuronal development and many different cancers types, there is a severe dearth of knowledge within the visual system. To our knowledge, there are less than 10 manuscripts on the role of *Lsd1* in the eye. These manuscripts have shown that *Lsd1* plays a significant role in the development of mouse rod photoreceptors[5], and that *Lsd1*

is upregulated in diabetic retinopathy rat retinas[93].*Lsd1* inhibition was protective against oxidative stress or NMDA-induced excitotoxicity[94] and prevented retinal endothelial cell apoptosis, mitochondrial damage, and reactive oxygen species generation in a diabetic retinopathy rat model[95]. We hope that the work contained in this dissertation will help set the foundation for the role of *Lsd1* in the eye and contribute to this small, but growing, area of research.

Ultimately, epigenetic mechanisms have been shown to play a substantial role in neurodevelopmental and neurodegeneration disorders and it should be expected that the same is true for the retina[96]. Therefore, understanding these mechanisms is vital for the visual science field in order to move towards developing treatments and possible cures for blinding diseases. Specifically, future research is needed to determine the exact role(s) that *Lsd1* plays in ocular development in order to determine its potential as a therapeutic target for retinal diseases and eye tumors.

References

1 Zibetti C, Adamo A, Binda C, Forneris F, Toffolo E, Verpelli C, *et al.* Alternative splicing of the histone demethylase LSD1/KDM1 contributes to the modulation of neurite morphogenesis in the mammalian nervous system. *J Neurosci* 2010;30:2521–32. PMCID:20164337.

2 Toffolo E, Rusconi F, Paganini L, Tortorici M, Pilotto S, Heise C, *et al.* Phosphorylation of neuronal Lysine-Specific Demethylase 1LSD1/KDM1A impairs transcriptional repression by regulating interaction with CoREST and histone deacetylases HDAC1/2. *J Neurochem* 2014;128:603–16. PMCID:24111946.

3 Laurent B, Ruitu L, Murn J, Hempel K, Ferrao R, Xiang Y, *et al.* A Specific LSD1/KDM1A Isoform Regulates Neuronal Differentiation through H3K9 Demethylation. *Mol Cell* 2015;57:957–70. PMCID:26928661.

4 Rusconi F, Grillo B, Toffolo E, Mattevi A, Battaglioli E. NeuroLSD1: Splicing-Generated Epigenetic Enhancer of Neuroplasticity. *Trends Neurosci* 2016;40:1–11. PMCID:27986293.

5 Popova EY, Pinzon-Guzman C, Salzberg AC, Zhang SS-M, Barnstable CJ. LSD1-Mediated Demethylation of H3K4me2 Is Required for the Transition from Late Progenitor to Differentiated Mouse Rod Photoreceptor. *Mol Neurobiol* 2016;53:4563–81. PMCID:26298666.

6 Ferdous S, Grossniklaus HE, Boatright JH, Nickerson JM. Characterization of LSD1 Expression Within the Murine Eye. *Invest Ophthalmol Vis Sci* 2019;60:4619–31.

7 Solovei I, Kreysing M, Lanctôt C, Kösem S, Peichl L, Cremer T, *et al.* Nuclear Architecture of Rod Photoreceptor Cells Adapts to Vision in Mammalian Evolution. *Cell*

2009;137:356–68. PMCID:19379699.

8 Nagy A. Cre recombinase: The universal reagent for genome tailoring. *Genesis* 2000;26:99–109. PMCID:10686599.

9 Rowan S, Cepko CL. Genetic analysis of the homeodomain transcription factor *Chx10* in the retina using a novel multifunctional BAC transgenic mouse reporter. *Dev Biol* 2004;271:388–402.

10 Granit R. The Components of the retinal action potential in mammals and their relation to the discharge in the optic nerve. *J Physiol* 1933;77:207–39.

11 Weymouth AE, Vingrys AJ. Rodent electroretinography: Methods for extraction and interpretation of rod and cone responses. *Prog Retin Eye Res* 2008;27:1–44. PMCID:18042420.

12 Kristianto J, Johnson MG, Zastrow RK, Radcliff AB, Blank RD. Spontaneous recombinase activity of Cre–ERT2 in vivo. *Transgenic Res* 2017;26:411–7. PMCID:28409408.

13 Heffner CS, Herbert Pratt C, Babiuk RP, Sharma Y, Rockwood SF, Donahue LR, *et al.* Supporting conditional mouse mutagenesis with a comprehensive cre characterization resource. *Nat Commun* 2012;3:1218–9. PMCID:23169059.

14 Lim S, Metzger E, Schle R, Kirfel J, Buettner R. Epigenetic regulation of cancer growth by histone demethylases. *Int J Cancer* 2010;127:1991–8.

15 Højfeldt JW, Agger K, Helin K. Histone lysine demethylases as targets for anticancer therapy. *Nat Rev Drug Discov* 2013;12:917–30. PMCID:24232376.

16 Morera L, Lübbert M, Jung M. Targeting histone methyltransferases and demethylases in clinical trials for cancer therapy. *Clin Epigenetics* 2016;8:57. PMCID:27222667.

17 Stazi G, Fioravanti R, Mai A, Mattevi A, Valente S. Histone deacetylases as an epigenetic pillar for the development of hybrid inhibitors in cancer. *Curr Opin Chem Biol* 2019;50:89–100.

18 Hayami S, Kelly JD, Cho HS, Yoshimatsu M, Unoki M, Tsunoda T, *et al.* Overexpression of LSD1 contributes to human carcinogenesis through chromatin regulation in various cancers. *Int J Cancer* 2011;128:574–86. PMCID:20333681.

19 He Y, Zhao Y, Wang L, Bohrer LR, Pan Y, Wang L, *et al.* LSD1 promotes S-phase entry and tumorigenesis via chromatin co-occupation with E2F1 and selective H3K9 demethylation. *Oncogene* 2018;37:534–43.

20 Ismail T, Lee HK, Kim C, Kwon T, Park TJ, Lee HS. KDM1A microenvironment, its oncogenic potential, and therapeutic significance. *Epigenetics and Chromatin* 2018;11:1–15.

21 Karakaidos P, Verigos J, Magklara A. Lsd1/kdm1a, a gate-keeper of cancer stemness and a promising therapeutic target. *Cancers (Basel)* 2019;11:1–22.

22 Capper D, Jones DTW, Sill M, Hovestadt V, Schrimpf D, Sturm D, *et al.* DNA methylation-based classification of central nervous system tumours. Nature. 2018 Mar 22;555(7697):469-474. doi: 10.1038/nature26000. Epub 2018 Mar 14. PMID: 29539639; PMCID: PMC6093218.

23 Kohe SE, Bennett CD, Gill SK, Wilson M, McConville C, Peet AC. Metabolic profiling of the three neural derived embryonal pediatric tumors retinoblastoma, neuroblastoma and medulloblastoma, identifies distinct metabolic profiles. *Oncotarget* 2018;9:11336–51.

24 Pajtler KW, Weingarten C, Thor T, Künkele A, Heukamp LC, Büttner R, *et al.* The

KDM1A histone demethylase is a promising new target for the epigenetic therapy of medulloblastoma. *Acta Neuropathol Commun* 2014;2:1–13.

25 Callegari K, Maegawa S, Bravo-Alegria J, Gopalakrishnan V. Pharmacological inhibition of LSD1 activity blocks REST-dependent medulloblastoma cell migration. *Cell Commun Signal* 2018;16:1–13.

26 Schulte JH, Lim S, Schramm A, Friedrichs N, Koster J, Versteeg R, *et al.* Lysine-specific demethylase 1 is strongly expressed in poorly differentiated neuroblastoma: Implications for therapy. *Cancer Res* 2009;69:2065–71. PMCID:19223552.

27 Althoff K, Beckers A, Odersky A, Mestdagh P, Köster J, Bray IM, *et al.* MiR-137 functions as a tumor suppressor in neuroblastoma by downregulating KDM1A. *Int J Cancer* 2013;133:1064–73.

28 Gupta S, Doyle K, Mosbruger TL, Butterfield A, Weston A, Ast A, *et al.* Reversible LSD1 inhibition with HCI-2509 induces the p53 gene expression signature and disrupts the MYCN signature in high-risk neuroblastoma cells. *Oncotarget* 2018;9:9907–24.

29 Kim Y, Nam HJ, Lee J, Park DY, Kim C, Yu YS, *et al.* Methylation-dependent regulation of HIF-1α stability restricts retinal and tumour angiogenesis. *Nat Commun* 2016;7:10347. PMCID:26757928.

30 O'Brien JM, Marcus DM, Niffenegger, Arysol S, Bernards R, Carpenter JL, Windle JJ, *et al.* Retinoblastoma in transgenic mice. *Nature* 1990;343:665–9.

31 Bremner R, Sage J. Cancer: The origin of human retinoblastoma. Nature. 2014 Oct 16;514(7522):312-3. doi: 10.1038/nature13748. Epub 2014 Sep 24. PMID: 25252972; PMCID: PMC5438154

32 del Cerro M, Notter MF, Seigel G, Lazar E, Chader G, del Cerro C. Intraretinal

xenografts of differentiated human retinoblastoma cells integrate with the host retina. *Brain Res* 1992;583:12–22. PMCID:1504822.

33 Mendoza PR, Grossniklaus HE. The Biology of Retinoblastoma. Prog Mol Biol Transl Sci. 2015;134:503-16. doi: 10.1016/bs.pmbts.2015.06.012. Epub 2015 Jul 14. PMID: 26310174

34 Tschulakow A V., Schraermeyer U, Rodemann HP, Julien-Schraermeyer S. Establishment of a novel retinoblastoma (Rb) nude mouse model by intravitreal injection of human Rb Y79 cells - Comparison of in vivo analysis versus histological follow up. *Biol Open* 2016;5:1625–30.

35 Liu Y, Hu H, Liang M, Xiong Y, Li K, Chen M, *et al.* Regulated differentiation of WERI-Rb-1 cells into retinal neuron-like cells. *Int J Mol Med* 2017;40:1172–84.

36 Li S, Chen D, Sauvé Y, McCandless J, Chen YJ, Chen CK. Rhodopsin-iCre transgenic mouse line for Cre-mediated rod-specific gene targeting. *Genesis* 2005;41:73–80.

37 Young RW. Cell differentiation in the retina of the mouse. *Anat Rec* 1985;212:199–205. PMCID:6501608.

38 Cepko CL, Austin CP, Yang X, Alexiades M, Ezzeddine D. Cell fate determination in the vertebrate retina 1996;93:589–95.

39 Livesey FJ, Cepko CL. Vertebrate neural cell-fate determination: Lessons from the retina. *Nat Rev Neurosci* 2001;2:109–18. PMCID:11252990.

40 Boulton M, Dayhaw-barker P. The role of the retinal pigment epithelium: topographical variation and ageing changes. *Nature, Eye* 2001;15:384–9.

41 Poulaki V, Mitsiades CS, Kotoula V, Negri J, McMullan C, Miller JW, *et al.* Molecular sequelae of histone deacetylase inhibition in human retinoblastoma cell lines: Clinical

implications. *Investig Ophthalmol Vis Sci* 2009;50:4072–9. PMCID:19387079.

42 Zhang Y, Wu D, Xia F, Xian H, Zhu X, Cui H, *et al.* Downregulation of HDAC9 inhibits cell proliferation and tumor formation by inducing cell cycle arrest in retinoblastoma. *Biochem Biophys Res Commun* 2016;473:600–6.

43 Jin Q, He W, Chen L, Yang Y, Shi K, You Z. MicroRNA-101-3p inhibits proliferation in retinoblastoma cells by targeting EZH2 and HDAC9. *Exp Ther Med* 2018;16:1663–70.

44 Hill RE, Favort J, Hogan BLM, Ton CCT, Saunders GF, Hanson IM, *et al.* Mouse Small eye results from mutations in a paired-like homeobox-containing gene. *Nature* 1991;354:522–5.

45 Glaser T, Walton D, Maas RL, Hughes H. Genomic structure, evolutionary conservation and aniridia mutations in the human PAX6 gene. *Nature* 1992;2:232–9.

46 Gehring WJ, Ikeo K. Pax 6: Mastering eye morphogenesis and eye evolution. *Trends Genet* 1999;15:371–7. PMCID:10461206.

47 Mears AJ, Kondo M, Swain PK, Takada Y, Bush RA, Saunders TL, *et al.* Nrl is required for rod photoreceptor development. *Nat Genet* 2001;29:447–52. PMCID:11694879.

48 Swain PK, Hicks D, Mears AJ, Apel IJ, Smith JE, John SK, *et al.* Multiple Phosphorylated Isoforms of NRL Are Expressed in Rod Photoreceptors. *J Biol Chem* 2001;276:36824–30.

49 Mears AJ, Swaroop A, Williams DS, Jr ENP. Features of the Photoreceptors of the Nrl Knockout Mouse 2015;46:2156–67.

50 Yu W, Mookherjee S, Chaitankar V, Hiriyanna S, Kim JW, Brooks M, *et al.* Nrl knockdown by AAV-delivered CRISPR/Cas9 prevents retinal degeneration in mice. *Nat Commun* 2017;8:1–15. PMCID:28291770.

51 Aldiri I, Xu B, Wang L, Chen X, Hiler D, Griffiths L, *et al.* The Dynamic Epigenetic Landscape of the Retina During Development, Reprogramming, and Tumorigenesis. *Neuron* 2017;94:550-568.e10.

52 Corso-Diaz X, Jaeger C, Chaitankar V, Swaroop A. Epigenetic Control of Gene Regulation during Devleopment and Disease: A View from the Retina. *Prog Mol Biol Transl Sci* 2018;65:1–27.

53 Mo A, Luo C, Davis FP, Mukamel EA, Henry GL, Nery JR, *et al.* Epigenomic landscapes of retinal rods and cones. *Elife* 2016;5:1–29. PMCID:26949250.

54 Barski A, Cuddapah S, Cui K, Roh TY, Schones DE, Wang Z, *et al.* High-Resolution Profiling of Histone Methylations in the Human Genome. *Cell* 2007;129:823–37. PMCID:17512414.

55 Mikkelsen TS, Ku M, Jaffe DB, Issac B, Lieberman E, Giannoukos G, *et al.* Genome wide maps of chromatin state in pluripotent and lineage-committed cells. *Nature* 2007;448:553–60. PMCID:1000000221.

56 Park PJ. ChIP-seq: Advantages and challenges of a maturing technology. *Nat Rev Genet* 2009;10:669–80. PMCID:19736561.

57 Skene PJ, Henikoff S. An efficient targeted nuclease strategy for high-resolution mapping of DNA binding sites. *Elife* 2017:1–35.

58 He C, Bonasio R. Chromatin mapping: A cut above. *Elife* 2017:1–3.

59 Lister R, O'Malley RC, Tonti-Filippini J, Gregory BD, Berry CC, Millar AH, *et al.* Highly Integrated Single-Base Resolution Maps of the Epigenome in Arabidopsis. *Cell* 2008;133:523–36. PMCID:18423832.

60 Nagalakshmi U, Wang Z, Waern K, Shou C, Raha D, Gerstein M, *et al.* The

transcriptional landscape of the yeast genome defined by RNA sequencing. *Science (80-)* 2008;320:1344–9. PMCID:18451266.

61 Mortazavi A, Williams BA, McCue K, Schaeffer L, Wold B. Mapping and quantifying mammalian transcriptomes by RNA-Seq. *Nat Methods* 2008;5:621–8. PMCID:18516045.

62 Wang Z, Gerstein M, Snyder M. RNA-Seq: a revolutionary tool for transcriptomics. *Nat Rev Genet* 2009;10:57–63.

63 Macosko EZ, Basu A, Satija R, Nemesh J, Goldman M, Tirosh I, *et al.* Highly parallel genome-wide expression profiling of individual cells using nanoliter droplets. *Cell* 2016;161:1202–14.

64 Hwang B, Lee JH, Bang D. Single-cell RNA sequencing technologies and bioinformatics pipelines. *Exp Mol Med* 2018;50: PMCID:30089861.

65 Chen G, Ning B, Shi T. Single-cell RNA-seq technologies and related computational data analysis. *Front Genet* 2019;10:1–13.

66 Ding J, Adiconis X, Simmons SK, Kowalczyk MS, Hession CC, Marjanovic ND, *et al.* Systematic comparison of single-cell and single-nucleus RNA-sequencing methods. *Nat Biotechnol* 2020;38:737–46. PMCID:32341560.

67 Chaitankar V, Karakülah G, Ratnapriya R, Giuste FO, Brooks MJ, Swaroop A. Next generation sequencing technology and genome wide data analysis: Perspectives for retinal research. *Prog Retin Eye Res* 2016;55:1–31. PMCID:27297499.

68 Raoss RC, Tchedre KT, Malik MTA, Coleman N, Fang Y, Marquez VE, *et al.* Dynamic patterns of histone lysine methylation in the Developing Retina. *Investig Ophthalmol Vis Sci* 2010;51:6784–92. PMCID:20671280.

69 Otteson DC. Eyes on DNA methylation: Current evidence for DNA methylation in ocular

development and disease. *J Ocul Biol Dis Infor* 2011;4:95–103.

70 Singh RK, Mallela RK, Hayes A, Dunham NR, Hedden ME, Enke RA, *et al.* Dnmt1, Dnmt3a and Dnmt3b cooperate in photoreceptor and outer plexiform layer development in the mammalian retina. *Exp Eye Res* 2017;159:132–46.

71 Ferreira RC, Popova EY, James J, Briones MRS, Zhang SS, Barnstable CJ. Histone deacetylase 1 is essential for rod photoreceptor differentiation by regulating acetylation at histone H3 lysine 9 and histone H4 lysine 12 in the mouse retina. *J Biol Chem* 2017;292:2422–40. PMCID:28028172.

72 Li W, Liu J, Galvin JA. Epigenetics and common ophthalmic diseases. *Yale J Biol Med* 2016;89:597–600. PMCID:28018148.

73 Oliver VF, van Bysterveldt KA, Merbs SL. Epigenetics in Ocular Medicine. *Med Epigenetics* 2016:391–412.

74 Moos WH, Faller D V., Glavas IP, Harpp DN, Irwin MH, Kanara I, *et al.* Epigenetic Treatment of Neurodegenerative Ophthalmic Disorders: An Eye Toward the Future. *Biores Open Access* 2017;6:169–81.

75 Gauthier AC, Liu J. Epigenetics and Signaling Pathways in Glaucoma. *Biomed Res Int* 2017;2017:

76 Agardh E, Lundstig A, Perfilyev A, Volkov P, Freiburghaus T, Lindholm E, *et al.* Genome-wide analysis of DNA methylation in subjects with type 1 diabetes identifies epigenetic modifications associated with proliferative diabetic retinopathy. *BMC Med* 2015;13:1–9.

77 Zorrilla-Zubilete MA, Yeste A, Quintana FJ, Toiber D, Mostoslavsky R, Silberman DM. Epigenetic control of early neurodegenerative events in diabetic retinopathy by the

histone deacetylase SIRT6. *J Neurochem* 2018;144:128–38.

78 Shafabakhsh R, Aghadavod E, Ghayour-Mobarhan M, Ferns G, Asemi Z. Role of histone modification and DNA methylation in signaling pathways involved in diabetic retinopathy. *J Cell Physiol* 2019;234:7839–46. PMCID:30515789.

79 Oliver VF, Jaffe AE, Song J, Wang G, Zhang P, Branham KE, *et al.* Differential DNA methylation identified in the blood and retina of AMD patients. *Epigenetics* 2015;10:698–707.

80 Xu Z, Ruan Z, Huang X, Liu Q, Li Z, Zhou X, *et al.* Identification of aberrantly methylated differentially expressed genes in age-related macular degeneration. *Medicine (Baltimore)* 2019;98:e15083.

81 Gemenetzi M, Lotery AJ. Epigenetics in age-related macular degeneration: new discoveries and future perspectives. *Cell Mol Life Sci* 2020;77:807–18.

82 Zhang H, Dai X, Qi Y, He Y, Du W, Pang JJ. Histone deacetylases inhibitors in the treatment of retinal degenerative diseases: Overview and perspectives. *J Ophthalmol* 2015;2015: PMCID:24488694.

83 Fan J, Alsarraf O, Chou CJ, Yates PW, Goodwin NC, Rice DS, *et al.* Ischemic preconditioning, retinal neuroprotection and histone deacetylase activities. *Exp Eye Res* 2016;146:269–75. PMCID:24655651.

84 Zheng S, Xiao L, Liu Y, Wang Y, Cheng L, Zhang J, *et al.* DZNep inhibits H3K27me3 deposition and delays retinal degeneration in the rd1 mice article. *Cell Death Dis* 2018;9: PMCID:29472543.

85 Hartl D, Krebs AR, Jüttner J, Roska B, Schübeler D. Cis-regulatory landscapes of four cell types of the retina. *Nucleic Acids Res* 2017;45:11607–21. PMCID:29059322.

86 Olivares AM, Jelcick AS, Reinecke J, Leehy B, Haider A, Morrison MA, *et al.* Multimodal Regulation Orchestrates Normal and Complex Disease States in the Retina /631/114/2114. *Sci Rep* 2017;7:1–16. PMCID:28386079.

87 Cao R, Wang L, Wang H, Xia L, Erdjument-Bromage H, Tempst P, *et al.* Role of histone H3 lysine 27 methylation in polycomb-group silencing. *Science (80-)* 2002;298:1039–43. PMCID:12351676.

88 Kuzmichev A, Nishioka K, Erdjument-Bromage H, Tempst P, Reinberg D. Histone methyltransferase activity associated with a human multiprotein complex containing the enhancer of zeste protein. *Genes Dev* 2002;16:2893–905. PMCID:12435631.

89 Zhang J, Taylor RJ, La Torre A, Wilken MS, Cox KE, Reh TA, *et al.* Ezh2 maintains retinal progenitor proliferation, transcriptional integrity, and the timing of late differentiation. *Dev Biol* 2015;403:128–38.

90 Hong S, Cho Y, Yu L, Yu H, Veenstra TD, Ge K. Identification of JmjC domain-containing UTX and JMJD3 as histone H3 lysine 27 demethylases. *Pnas* 2007;104:18439–44.

91 Xiang Y, Zhu Z, Han G, Lin H, Xu L, Chen CD. JMJD3 is a histone H3K27 demethylase. *Cell Res* 2007;17:850–7. PMCID:17923864.

92 Iida A, Iwagawa T, Kuribayashi H, Satoh S, Mochizuki Y, Baba Y, *et al.* Histone demethylase Jmjd3 is required for the development of subsets of retinal bipolar cells. *Proc Natl Acad Sci U S A* 2014;111:3751–6. PMCID:24572572.

93 Zhong Q, Kowluru RA. Epigenetic modification of Sod2 in the development of diabetic retinopathy and in the metabolic memory: Role of histone methylation. *Investig Ophthalmol Vis Sci* 2013;54:244–50. PMCID:23221071.

94 Tsutsumi T, Iwao K, Hayashi H, Kirihara T, Kawaji T, Inoue T, *et al.* Potential Neuroprotective Effects of an LSD1 Inhibitor in Retinal Ganglion Cells via p38 MAPK Activity. *Investig Opthalmology Vis Sci* 2016;57:6461. PMCID:27893888.

95 Zhong Q, Kowluru RA. Regulation of matrix metalloproteinase-9 by epigenetic modifications and the development of diabetic retinopathy. *Diabetes* 2013;62:2559–68. PMCID:23423566.

96 Jakovcevski M, Akbarian S. Epigenetic mechanisms in neurodevelopmental and neurodegenerative disease. *Nat Med* 2013;18:1194–204.